UNIVERZITET U NOVOM SADU
FAKULTET TEHNIČKIH NAUKA U NOVOM SADU

Danka Labus Zlatanović

Friction stir spot welding of ultrathin sheets made of aluminium – magnesium alloy

PhD Thesis

Tačkasto zavarivanje trenjem sa mešanjem ultratankih limova od legure aluminijuma i magnezijuma

DOKTORSKA DISERTACIJA

Novi Sad, 2020.

УНИВЕРЗИТЕТ У НОВОМ САДУ ● **ФАКУЛТЕТ ТЕХНИЧКИХ НАУКА**
21000 НОВИ САД, Трг Доситеја Обрадовића 6

КЉУЧНА ДОКУМЕНТАЦИЈСКА ИНФОРМАЦИЈА

Редни број, **РБР**:		
Идентификациони број, **ИБР**:		
Тип документације, **ТД**:		Монографска документација
Тип записа, **ТЗ**:		Текстуални штампани материјал
Врста рада, **ВР**:		Докторска дисертација
Аутор, **АУ**:		Данка Лабус Златановић
Ментор, **МН**:		Др Себастиан Балош, ванредни професор Др Жан Пијер Бергман, редовни професор
Наслов рада, **НР**:		Тачкасто заваривање трењем са мешањем ултратанких лимова од легуре алуминијума и магнезијума
Језик публикације, **ЈП**:		Српски
Језик извода, **ЈИ**:		Српски / Енглески
Земља публиковања, **ЗП**:		Република Србија
Уже географско подручје, **УГП**:		Војводина
Година, **ГО**:		2020
Издавач, **ИЗ**:		Ауторски репринт
Место и адреса, **МА**:		Нови Сад, Трг Доситеја Обрадовића 6
Физички опис рада, **ФО**:		7/148/194/12/112
Научна област, **НО**:		Машинско Инжењерство
Научна дисциплина, **НД**:		Материјали и технологије спајања
Предметна одредница/Кључне речи, **ПО**:		Легура AA 5754-H11,тачкасто заваривање трењем са мешањем, деформационо ојачавање, термичко омекшавање, међуконтактна површина
УДК		
Чува се, **ЧУ**:		Библиотеци Факултета техничких наука
Важна напомена, **ВН**:		
Извод, **ИЗ**:		У оквиру ове докторске дисертације испитивано је тачкасто заваривање трењем са мешањем ултратанких лимова дебљине 0.3 mm од легуре AA 5754 – H111 (AlMg3). Утицај геометрије алата и параметара као што су угаона брзина и аксијално оптерећење су детаљно анализирани уз помоћ бројних техника. Установљено је да приликом заваривања ниским угаоним брзинама долази до деформационог ојачавања, док на високим угаоним брзинама долази до термичког омекшавања зоне завара. Код узорка завареног са најмањим бројем обртаја долази до формирања комплексног слоја на међуконтактној површини који изазива деламинацију приликом испитивања механичких особина.
Датум прихватања теме, **ДП**:		11.07.2019
Датум одбране, **ДО**:		
Чланови комисије, **КО**:	Председник:	Др Лепосава Шиђанин, професор емеритус
	Члан:	Др Саурав Гоел, ванредни професор
	Члан:	Др Драган Рајновић, доцент
	Члан, ментор:	Др Себастиан Балош, ванредни професор
	Члан, ментор:	Др Жан Пијер Бергман, редовни професор

Потпис ментора

UNIVERSITY OF NOVI SAD ● **FACULTY OF TECHNICAL SCIENCES**
21000 NOVI SAD, Trg Dositeja Obradovića 6

KEY WORDS DOCUMENTATION

Accession number, **ANO**:		
Identification number, **INO**:		
Document type, **DT**:		Monographic publication
Type of record, **TR**:		Textual material, printed
Contents code, **CC**:		PhD Thesis
Author, **AU**:		Danka Labus Zlatanović
Mentor, **MN**:		Dr Sebastian Baloš, Associate Professor Dr Jean Pierre Bergmann, Full Professor
Title, **TI**:		Friction stir spot welding of ultrathin sheets made of aluminium – magnesium alloy
Language of text, **LT**:		Serbian
Language of abstract, **LA**:		Serbian / English
Country of publication, **CP**:		Republic of Serbia
Locality of publication, **LP**:		Vojvodina
Publication year, **PY**:		2020
Publisher, **PB**:		Author's reprint
Publication place, **PP**:		Novi Sad, Trg Dositeja Obradovića 6
Physical description, **PD**: (chapters/pages/ref./tables/pictures/graphs/appendixes)		7/148/194/12/112
Scientific field, **SF**:		Mechanical Engineering
Scientific discipline, **SD**:		Materials and Joining Technologies
Subject/Key words, **S/KW**:		AA 5754-H11 alloy, Friction Stir Spot Welding, strain hardening, thermal softening, weld faying interface
UC		
Holding data, **HD**:		Library of the Faculty of Technical Sciences, Novi Sad
Note, **N**:		
Abstract, **AB**:		Within the framework of presented PhD, friction stir spot welding (FSSW) of multiple ultrathin sheets of AA 5754 – H111 (AlMg3) alloy 0.3 mm thick, was studied. The influence of tool geometry and process parameters such as rotational speed and axial load have been analysed using numerous techniques. It has been understood that during the welding at low rotational speeds weld zone undergoes strain hardening, while at high rotational speeds weld zone undergoes thermal softening. It was observed that during FSSW at low rotational speeds a complex layer at weld interface is present, which causes delamination when welded samples are subjected to load.
Accepted by the Scientific Board on, **ASB**:		11.07.2019
Defended on, **DE**:		
Defended Board, **DB**:	President:	Dr Leposava Šiđanin, Professor Emeritus
	Member:	Dr Saurav Goel, Associate Professor
	Member:	Dr Dragan Rajnović, Assistant Professor
	Member, Mentor:	Dr Sebastian Baloš, Associate Professor
	Member, Mentor:	Dr Jean Pierre Bergmann, Full Professor

Mentor's signature

Abstract

Friction stir spot welding (FSSW) is a solid-state joining process that uses a non-consumable rotational pin or pin-less tool. It is an emerging technology in the automotive and aerospace industry which is receiving significant attention from researchers because of its potential to reduce cost and to improve throughput.

In this study, FSSW using two convex pin-less tools with different radiuses was used to weld multiple ultrathin sheets (0.3 mm thickness) of aluminium AA 5754 grade alloy. The process parameters, namely, rotational speed, axial load and penetration depth were varied and the influence of these on key mechanisms like strain hardening, thermal softening, material's microstructure and strength of the weld joints was studied. As a priori to the main experiments, a series of dummy trials were made to know the range of the axially applied load. Accordingly, an axial load of 2 kN was used for batch I (tool T1) and 4 kN for batch II (tool T2). The penetration depth was set as 0.25 mm for both batches. The most influential parameter, rotational speed, was varied from 1500 to 3500 RPM for the processing of batch I and from 1000 to 4500 RPM for batch II.

It was interesting to observe that an increase of the tool radius from 15 to 22.5 mm reduced the dwell time by approximately three times, bringing the weld time to under 1 s. The rotational speed was found to have a significant influence on the mechanical properties, the topography of the weld, dwell time and stress distribution governing the joining mechanism. At lower RPM, surface microhardness was higher compared with that of the base material. By contrast, using higher RPM made the surface softer. An increase in the RPM lead to an increase in the strain rate which resulted in an increased temperature. It was concluded that low RPM during FSSW make strain hardening to be dominate mechanism whereas higher RPM caused thermal softening. In both cases, dislocation tangle inside the grains caused the formation of several subgrain structures.

Post-weld Scanning Acoustic Microscopy (SAM) was used for non-destructive testing of the weld faying interfaces (WFI) across the thickness to determine if there were other defects which had not been observed. It was found that delamination in the last interface is dependent on RPM. A Small Punch Test (SPT) was used to assess the weld-joint strength. It revealed a layer 1.7 μm to 4.2 μm thick within rupture in specimen after SPT that had been welded with 1000 RPM from batch II. From SEM micrographs, it seemed that this layer was responsible for delamination during SPT tests. To better understand these atomistic mechanisms governing the delamination, an analysis was performed using transmission electron microscopy (TEM), nanoindentation, and nanoelectromechanical analysis was performed on an Atomic Force Microscope (AFM).

A detailed analysis using these techniques revealed that the fracture of the samples during the SPT at WFI was caused by dynamic precipitation. Also, an entrapped oxide layer mixed in the nano pits on the surface was seen at the middle of the weld faying interface. Together, these led to the initiation or the nucleation of cracks with the crack path growing to the outer line of the weld faying interface leaving a ductile rupture on its path. Weld faying interface seen from the TEM was between approximately 1.6 to 2.05 μm thick, which correlated well with the SEM results. The methods used in this work provide a pathway to obtain defect-free weld joints in ultrathin multiple sheets with FSSW by using convex pin-less tools.

Резиме

У новије време све је већа потреба за употребом лаких легура у аутомобилској и авио индустрији, због све већих захтева за смањењем укупне масе возила и њихове цене. Сходно томе, све је чешћа употреба алуминијумских легура као замена за легуре које имају већу специфичну масу као што су бакар, челик и сл. Употреба алуминијума уместо бакра је све чешћа како за проводнике тако и за фолије и лимове у батеријама и другим компонентама возила, и то не само због уштеде на тежини, већ и због тога што алуминијум на тржишту има знатно нижу и стабилнију цену. Такође, један од захтева сваког производног процеса је и да обезбеди производ са задовољавајућим механичким особинама уз минимални утрошак енергије, а самим тим и уз минималне трошкове. Тренутно најактуелније технике за преклопно спајање лимова од алуминијума и његових легура су електро-отпорно тачкасто заваривање, специјални поступак заваривања у заштити гаса (*Cold Metal Transfer Spot Welding*), тачкасто заваривање ласером, ултразвучно тачкасто заваривање, закивање (S*elf-Piercing Riveting*), и различите изведбе тачкастог заваривања трењем са мешањем – ТЗТМ (*Friction Stir Spot Welding – FSSW*). За сада је електроотпорно тачкасто заваривање најчешће коришћен поступак од наведених, захваљујући великој продуктивности и могућности приступа радном предмету. Међутим, због високе температуре у току процеса заваривања у завареним узорцима често долази до појаве дефеката као што су порозност, смањење механичких особина у завареном споју у односу на основни материјал, заостали напони, могуће испаравање појединих легирајућих елемената, прслине, напонска корозија и слично. Такође, потрошња енергије је велика што неповољно утиче на цену финалног производа.

Тачкасто заваривање трењем са мешањем је релативно нови поступак заснован на принципу заваривања трењем са мешањем (ЗТМ). То је поступак за заваривање у чврстом стању, који је први пут развијен 1991 године на институту за заваривање у Великој Британији (*The Welding Institute, UK*). У току ЗТМ процеса не долази до топљења материјала што веома поједностављује поступак. Поступак има низ предности као што су: мала деформација завареног споја, механичке особине завареног споја су сличне или боље у односу на основни материјал, уједначена микроструктура, технологија нема лош утицај на животну средину што је посебно значајно код заваривања легура алуминијума.

Основни принцип је крајње једноставан. Ротирајући алат са посебно дизајнираним трном и раменом улази у горњу површину припремљеног обратка, затим се спушта на доле, све док и раме не додирне горњу површину обратка. Процес траје док не дође до динамичке рекристализације, која настаје као последица високог степена деформације око трна, услед великог трења и високе температуре узроковане тим истим трењем. Затим се алат повлачи из завареног споја, на чијем месту остаје рупа која смањује механичке особине завареног споја. Да би се превазишао овај проблем предложено је неколико различити модификација овог поступка.

Тачкасто заваривање с мешањем са попуном излазне рупе (*Refill Friction Stir Spot Welding-RFSSW*) је поступак ТЗТМ који омогућава заваривање са алатом без трна али захтева

сложену опрему. Примена алата без трна је такође решење које обезбеђује добијање узорака без рупе узроковано повлачењем трна алата. Постоје различите изведбе алата без трна, тј. различите геометрије површине чела алата могу бити изведене. Овај поступак се у литератури такође појављује и под називом хибридно дифузионо заваривање трењем - ХДЗТ (*Hybrid Friction Diffusion Bonding – HFDB*). Као главни механизми одговорни за спајање приликом ХДЗТ предложени су дифузија и динамичка рекристализација. Овај поступак се од конвенционалног ТЗТМ разликује по томе што алат улази само у први лим до дефинисане дубине. Захваљујући унесеној енергији у току процеса долази до динамичке рекристализације испод површине алата праћене дифузијом на слободним површинама између лимова. Недостатак овог поступка је то што део материјала испод алата бива истиснут на површину лима, па је потребна накнадно поравнати узорке, што неповољно утиче због додатног времена потребног за финализовање производа, па самим тим и на пораст цене поступка. Такође, сматра се да је овим поступком немогуће или тешко заваривати танке лимове или фолије. Према доступној литератури, заваривање ултра-танких лимова испод 0,8 mm дебљине се углавном не изводи ТЗТМ.

Још један веома значајан недостатак приликом преклопног заваривања појединих легура је присуство површинског оксида, као што је рецимо код легура алуминијума, које поседују веома танак заштитни слој алуминијум-оксида (Al_2O_3). Овај слој, због високе температуре топљења (~2072 °C) се не разлаже у току поступка заваривања, а истовремено представља снажну баријеру дифузији на међуконтактној површини између лимова који се заварују. Ово је први пут примећено у току поступка дифузионог заваривања, међутим и приликом ТЗТМ са алатом без трна овај проблем је такође присутан, али у значајно мањој мери. Уколико се површина узорка притисне одређеном силом долази и до савијања међуконтактне површине услед чега се крта фаза Al_2O_3 ломи и раздваја се у мање сегменте, између којих долази до дифузије. Што су сегменти ситнији и боље умешани то је квалитетнији заварени спој. Ако се дода и ротација алата поступак уситњавања је још израженији. Међутим, оксид ће остати заробљен у завареном споју у виду честица или сегмената и може представљати иницијално место за појаву прслина уколико дође до прекомерног оптерећења завареног споја.

Да би се процес ТЗТМ успешно применио за заваривање компоненти батерија, конектора и да би се користио за заваривање компоненти у електроници, неопходно је развити поступак погодан за заваривање ултратанких лимова и фолија. Због високог степена деформације и загревања трењем приликом ТЗТМ ултра танких лимова и фолија, долази до кидања (цепања) фолија или ултратанких лимова између спољне контуре алата и незавареног дела лима. Неопходно је конструисати алат који ће уз адекватан однос параметрара обезбедити заварени спој без дефеката у завареној зони као и без оштећења лима на прелазу између заварене и не заварене зоне.

Идеја у оквиру ове докторске дисертације је била да се развије алат који ће обезбедити постепен унос деформације и загревања трењем у четири преклопљена лима од легуре AlMg3 (AA 5754 – H111) дебљине 0,3 mm, како би се наведени проблеми превазишли. Хипотетички посматрано, оваква конструкција алата би такође омогућила постепено и равномерно савијање међуконтактних површина, што би могло да обезбеди бољу

дифузију на међуконтактној површини. Такође, да би поступак ТЗТМ био оправдан, тј. да би био конкурентан ултразвучном заваривању и тачкастом електроотпорном заваривању, поред адекватне геометрије алата, неопходно је изабрати и адекватне параметре процеса који би могли да обезбеде да време заваривања буде минимално уз адекватну микроструктуру, односно механичке особине завареног споја.

Да би се испунили сви наведени захтеви конструисана су два алата без трна са конвексном контактном површином. Коришћени пречник оба алата је 12 mm, међутим радијус контактне површине се разликује. Алат који је коришћен за заваривање узорака у серији I израђен је са радијусом контактне површине од 15 mm док је алат у серији II израђен са радијусом контактне површине 22,5 mm. Промена величине радијуса утиче на степен деформације и температуру унесену у радни предмет, утичући тако и на време заваривања. Приликом избора параметара дубина продирања алата и аксијално оптерећење су одабрани да буду константе док је угаона брзина варирана, као најутицајнији параметар у току процеса.

Дубина продирања алата је дефинисана тако да представља минималну дубину при којој је могуће постићи заварени спој између четири лима. У обе серије је дубина продирања алата подешена да буде 0,25 mm. С друге стране, аксијално оптерећење је одабрано тако да буде максимално оптерећење са којим је могуће остварити спој између четири лима. Ако би се сила додатно смањила време заваривања би се повећало, с обзиром да је уређај за заваривање са контролом силе, што значи да време трајања процеса зависи од подешене дубине продирања алата, механичких особина основног материјала, задате угаоне брзине и аксијалног оптерећења. Другим речима, време заваривања ће у том случају бити време потребно да алат достигне задату дубину тако што ће савладати отпор материјала са предефинисаном угаоном брзином и оптерећењем.

Након дефинисања свих наведених параметара добијене су две серије узорака:

Серија I: са алатом T1 са радијусом контактне површине 15 mm, спој између сва четири лима је остварен код узорака заварених са угаоним брзинама 1500, 2000, 2500, 3000 и 3500 o/min.

Серија II: са алатом T2 са радијусом контактне површине 22.5 mm, заварени спој између сва четири лима је остварен код узорака са угаоним брзинама 1000, 1500, 2000, 2500, 3000, 3500, 4000 и 4500 o/min.

Испод 1500 o/min (серија I) и испод 1000 o/min (серија II) време заваривања би било преко 5 s, што је ван опсега машине. Преко 3500 o/mm (серија I) и преко 4500 o/min (серија II) није било могуће заварити више од три лима.

Захваљујући подацима добијеним са уређаја за заваривање као што су моменат, сила и време трајања поступка израчунати су смицајни и нормални напони као и коефицијент трења у зависности од времена заваривања. Такође, захваљујући постављању термо пара на дну узорка омогућено је мерење температуре при различитим угаоним брзинама. Анализом добијених резултата установљено је да у зависности од угаоне брзине као и геометрије алата, вредности температуре, смицајног напона и коефицијента трења

значајно варирају. Последично, установљено је да у току процеса заваривања са малим бројевима обртаја смицајни напон осцилује у границама између вредности које одговарају почетку деформационог ојачавања и затезне чврстоће код основног материјала, што доводи до деформационог ојачавања у зони завара. У току заваривања са великим угаоним брзинама напон непосредно након почетка процеса достиже максималну вредност која прелази вредност затезне чврстоће основног материјала да би затим нагло опао и до краја процеса био нижи од вредности која одговара почетку деформационог ојачавања, што доводи до термичког омекшавања завара. Из вредности напона и коефицијента трења током процеса може се констатовати да у току поступка ТЗТМ долази до симултаног деформационог ојачавања и термичког омекшавања. У узорцима завареним са малим угаоним брзинама доминантно је деформационо ојачавање у односу на термичко омекшавање док је у узорцима завареним са великим угаоним брзинама доминантно термичко омекшавање.

Из напонске анализе такође се могу уочити два различита стадијума у току заваривања. У првом стадијуму (*stick-slip)* нормални напон је доминантан у односу на смицајни напон. Непосредно након тренутка када смицајни напон постане доминантан у односу на нормални напон почиње други стадијум (*steady state weld*). У првом стадијуму, алат успоставља контакт са радним предметом и материјал се креће према центру завареног споја, да би у другом стадијуму тек дошло до локалног пуцања материјала (када се превазиђе затезна чврстоћа). Услед пуцања материјала долази до ослобађања одређене количине топлоте која помаже локалном омекшавању материјала и доводи до течења материјала према периферији алата.

У зависности од угаоне брзине, средња температура изазвана низом фактора, као што су трење, локално пуцање материјала итд. у највећој мери зависи од угаоне брзине алата, док геометрија алата, аксијално оптерећење и време заваривања имају далеко мањи утицај. Такође је установљено, да за узорке заварене са 1500 o/min у обе серије, иако се време заваривања разликује тј. време заваривања у серији I је скоро три пута веће у односу на серију II, пораст температуре је незнатан. Према томе, време заваривања има незнатан утицај на загревање трењем у току процеса ТЗТМ. За скоро све узорке из обе серије, криве температура се скоро подударају, међутим, са порастом угаоне брзине, у обе серије, долази до значајног пораста температуре.

Након заваривања, узорци су испитани са методом без разарања за детекцију дефеката у завареном споју – скенирајућим акустичним микроскопом (Scanning Acoustic Microscopy – SAM). Ова метода омогућава скенирање целог узорка по дубини и на тај начин утврђивање да ли постоје дефекти као што су деламинација, оксиди и слично, било где у завареном споју. Захваљујући SAM-у установљено је да до појаве деламинације долази само на последњој међуконтактној површини (између трећег и четвртог лима).

Анализом резултата добијених на SAM-у у виду Ц-скенова установљени је да са порастом броја обртаја расте и површински удео деламинације. Такође, са порастом броја обртаја се смањује површина завареног споја на последњој међуконтактној површини. SAM Б-скен анализом у попречном пресеку, посебно код узорка завареном са 1000 o/min уочена

је танка линија на првој и другој међуконтактној површини која би могла да представља заробљени слој оксида.

Након заваривања узорци су припремљени за детаљнију анализу завареног споја уз помоћ метода карактеризације микроструктуре као што су: светлосна микроскопија (*Light Microscopy* – LM), скенирајућа електронска микроскопија (*Scanning Electron Microscopy* – SEM), трансмисиона електронска микроскопија (*Transmision Electron Microscopy* – TEM) са могућношћу енергетске дисперзионе спектрофотометријске анализе (*Energy Dispersive X-ray Analysis* – EDX) анализе и микроскопија атомских сила са Келвиновом сондом са модулацијом фреквенције (*Frequency-Modulated Kelvin Probe Force Microscopy* – FM-KPFM). Такође, заварени спојеви су подвргнути методама за одређивање механичких особина материјала као што су: испитивање микротврдоће попречног пресека завареног споја; испитивање заварених спојева пробојним тестом са трном (*small punch test* – SPT) испитивање међуконтактне површине са уређајем за испитивање нано тврдоће (*In situ-Scanning Probe Microscope* - SPM).

Макроиспитивањем, површине завареног споја одозго могу се уочити две различите зоне: (i) зона крзања обрађене површине и (ii) зона стабилног контакта. Зона стабилног контакта представља зону непосредно испод алата, док је зона крзања обрађене површине зона на периферији алата. У тој зони је алат у контакту са горњим лимом непланирано Радијалне силе настале као последица чврсте везе између прибора за стезање радног предмета са једне стране и алата са друге стране доводе до савијања горњег лима у подручју између прибора и алата. Савијени лим додирује алат по периферији, где иначе не би требало да буде у контакту са њим. На тај начин услед малих сила и великог трења долази до крзања периферне зоне завареног споја. Зона крзања обрађене површине је у облику прстена који окружује зону стабилног контакта испод које се налази зона завара.

У обе серије се однос зоне крзања обрађене површине и зоне стабилног контакта између алата и радног предмета мења са променом угаоне брзине алата. Са порастом угаоне брзине алата тај однос расте. У теоријским условима овај однос не би требао да зависи од угаоне брзине већ само од геометрије алата. Међутим, с обзиром да у току заваривања на нижим угаоним брзинама долази до деформационог ојачавања материјала, површина непосредно испод алата ће након заваривања поднети еластично враћање па ће заварени спој на крају процеса имати дебљину већу него задату. У случају велике угаоне брзине услед термичког омекшавања и велике центрифугалне силе материјал уместо да преноси оптерећење према дну узорка, биће потиснут на горе, према периферији алата. Код ових узорака је примећена мања дебљина узорка након заваривања а шира зона стабилног контакта, што значи да је дошло до истискивања веће запремине материјала у односу на узорке заварене са малим угаоним брзинама. Такође, због промене радијуса алата овај однос је већи у серији II у поређењу са серијом I.

Услед разлике у понашању материјала приликом заваривања са малим и великим угаоним брзинама дошло је и до разлике у облику и запремини завареног споја. Као што је већ споменуто, с обзиром да приликом заваривања са великим угаоним брзинама материјал нагло омекшава непосредно испод алата, аксијално оптерећење које је примењено на

радни предмет се не преноси на нижи део узорка, него тежи да већ омекшани материјал истисне према периферији алата. Због тога је облик зоне завара узорака заварених са великом брзинама обртаја конусан. Површина последње заварене међуконтактне површине је значајно мања у односу на површину прве међуконтактне површине. С друге стране код узорака заварених са ниским угаоним брзинама услед деформационог ојачавања оптерећење се преноси по дубини, па је разлика између површине прве и последње међуконтактне површине далеко мања, док облик зоне завара тежи ка цилиндричном облику. Ова тренд је исти у обе серије.

Након анализе попречног пресека нагрижених узорака са светлосним микроскопом, установљено је да се на разликују поједине зоне као што су: зона завара (грумен), зона термо-механичког утицаја (ЗТМУ), зона утицаја топлоте (ЗУТ) и основни материјал (ОМ). Такође, у обе серије може се приметити да угаона брзина има највећи утицај на величину и облик ових зона, као и на величину, облик и оријентацију зрна унутар ових зона.

Зона завара представља највећу зону која је настала као последица утицаја загревања трењем и пластичне деформације изазваних аксијалним оптерећењем и ротацијом алата. Захваљујући високој деформацији и повишеној температури испуњени су услови за динамичку рекристализацију и дифузију између лимова. Последично, финозрна структура је постигнута код свих узорака. Међутим, у зависности од угаоне брзине величина зрна и оријентација се разликују. Величина зрна у зони завара расте са порастом угаоне брзине. Просечна величина зрна основног материјала је 69 μm, док је величина зрна у зони завара узорка завареног са 4500 o/min (серија II) у просеку 24 μm а код узорка завареног са 1000 o/min (серија II) просечна величина зрна је 5 μm. Разлика у величини зрна у зависности од угаоне брзине се такође доводе у везу са различитим понашањем материјала при различитим односима деформационог ојачавања и термичког омекшавања. При малим угаоним брзинама услед високе деформације, ниског степена деформације и релативно ниске температуре долази до реакције мобилних дислокација са раствореним атомима магнезијума и талозима унутар зрна. На тај начин долази до формирања граница субзрна унутар зрна основног материјала. При интензивној пластичној деформацији субзрна ротирају и постају полигонална зрна (високоугаона субзрна). Приликом заваривања са већим угаоним брзинама услед повишене температуре након формирања нових зрна ротацијом субзрна, долази и до динамичког опорављања које изазива додатни раст новонасталих зрна. Током динамичког опорављања раст зрна се доводи у везу са понирањем дислокација у границе зрна и миграцијом граница.

ЗТМУ је јединствена прелазна зона која се налази између зоне завара и зоне утицаја топлоте. Карактерише је високо деформисана структура са углавном издуженим зрнима која прате спољну контуру зоне завара. Међутим, ова зона не подлеже динамичкој рекристализацији услед ниског степена деформације. Величина саме ЗТМУ као и величина и облик зрна унутар зоне не зависе од облика алата, тј. сличан тренд је уочен у обе серије. Међутим ширина ЗТМУ као и величина и облик зрна значајно се мењају у зависности од угаоне брзине. Тако приликом заваривања са малим угаоним брзинама (нпр. 1000 o/min) ЗТМУ је уска са издуженим зрнима просечне величине 21 μm док са

порастом угаоне брзине расте ширина ЗТМУ, зрна мењају облик од издуженог ка приближно кружном облику и величина зрна расте. Тако је величина зрна у ЗТМУ у узорку завареном са 4500 o/min 36 μm. Према томе, микроструктура узорака заварених са великим угаоним брзинама показује мању анизотропију у поређењу са узорцима завареним са малим угаоним брзинама.

ЗУТ је зона која се налази између ЗТМУ и ОМ. Сматра се да је ово зона у којој не долази до пластичне деформације, већ само долази до промена микроструктуре изазваних утицајем температуре. Облик зрна у ЗУТ одговара облику зрна у основном материјалу, међутим величина зрна се разликује. Зрна која се налазе у ЗУТ су већа у односу на зрна у ЗТМУ (у узорцима завареним са 1000 и 4500 o/min просечна величина зрна унутар ЗУТ је 43 μm) а мања у односу на зрна основног материјала.

Да би се установио утицај геометрије алата, аксијалног оптерећења и угаоне брзине на квалитет завареног споја извршено је испитивање микротврдоће попречног пресека свих узорака из обе серије. Резултати испитивања су потврдили теорију о деформационом ојачавању/термичком омекшавању у току поступка ТЗТМ. У узорцима завареним са ниским угаоним брзинама (1500 и 2000 o/min у серији I и 1000 o/min у серији II) дошло је до значајног пораста тврдоће у зони завара у поређењу са основним материјалом. Са порастом угаоне брзине тврдоћа у зони завара је опала, да би у узорцима са највишим угаоним брзинама у обе серије дошло до омекшавања зоне завара у односу на основни материјал услед динамичког опорављања. Овај пораст тврдоће са смањењем броја обртаја се такође може довести у везу са Хол-Печовом једначином. Услед тога што су зрна у узорцима завареним са малом угаоном брзином значајно мања у односу на зрна основног материјала, према Хол-Печевој једначини са смањењем величине зрна долази до пораста чврстоће и тврдоће.

Приликом поређења микротврдоће узорака из серије I и II утврђено је да геометрија алата и аксијално оптерећење утичу на механичке особине завареног споја, с обзиром да је за исте угаоне брзине (1500 и 2000 o/min) у серији I дошло до деформационог ојачавања а у серији II до термичког омекшавања. Ово може довести до закључка да са снижавањем аксијалног оптерећења са 4 kN у серији II на 2 kN у серији I узорак пролази трансформацију од термичког омекшавања до деформационог ојачавања.

У свим узорцима завареним у обе серије уочено је да тврдоћа опада од врха узорка (непосредно испод алата) ка дну узорка. Ово се такође доводи у везу са Хал-Печевом једначином јер у свим узорцима долази до раста зрна од врха узорка (где је најситније зрно) према дну где је уочена и ЗТМУ са значајним порастом зрна у последњем лиму. Чак и у узорцима у којим је дошло до термичког омекшавања примећена је повећана тврдоћа непосредно испод алата.

SPT је изведен да би се боље разумео утицај геометрије алата, аксијалног оптерећења и угаоне брзине на механичке особине материјала зоне завара као и да би се установио механизам лома и разлог појаве деламинације. Установљено је да резултати добијени овим тестом потврђују резултате добијене испитивањем микротврдоће. Највеће оптерећење које је било потребно да дође до појаве прслине је уочено у узорцима

завреним са малим угаоним брзинама (1500 o/min у серији I и 1000 o/min у серији II). У оба случаја максимално оптерећење је било веће у поређењу са максималним оптерећењем потребним да се изазове појава прслине у узорцима израђеним од основном материјала. Код свих осталих узорака до лома је дошло на нижим оптерећењима у поређењу са основним материјалом. Тако је ефикасност заваривања највећа код узорка завареног са 1500 o/min из серије I и износи 106,1 % док је најнижа код узорка завареног са 4500 o/min из серије II и износи 87,4 %.

Показало се да су сви узорци из серије I издржали већа оптерећења у поређењу са узорцима из серије II. То се може довести у везу са деламинацијом која је примећена у узорцима из серије II након SPT-а. Код свих узорака из серије I уочена је ободно оријентисана кружна прслина под углом од 45° у односу на осу дејства оптерећења, која је каратеристична приликом испитивања SPT-ом. Ни у једном узорку у серији I није примећена појава деламинације. Међутим, у узорцима из серије II примећена је деламинација код већине узорака.

Установљено је да је најутицајнији параметар на појаву деламинације време заваривања. С обзиром да на контактним површинама лимова који се заварују постоји високо-постојани оксидни слој који не дозвољава да дође до дифузије, неопходно је тај слој разбити у ситне сегменте или честице и умешати довољно да би било омогућено дифузији да се оствари између њих. Према томе да би се обезбедило добро умешавање оксидног слоја главну улогу има време заваривања.

У узорку заваремон са 1500 o/min из серије I просечно време заваривања је 4.6 s, док је у узорку завареном са истом угаоном брзином из серије II то време у просеку 1.4 s. С обзиром да у првом случају није дошло до појаве деламинације, а да је у другом случају дошло до појаве деламинације на две последње међуконтактне површине, установљено је да време заваривања значајно утиче на квалитет умешавања оксидног слоја а самим тим и на дифузију између лимова у току процеса заваривања.

Након SPT, карактеризација преломљене површине је изведена методом SEM. Установљено је да се између две преломљене површине налази заробљен слој који варира у дебљини од 1.72 до 4.23 μm. Преломљене површине које окружују овај слој су јамичасте, дуктилног карактера.

Макроструктуре узорака након SPT као и стањивање узорка и максимални ход пробе у току SPT сугеришу да се у зависности од угаоне брзине мења и дуктилност завареног споја. Стога, најмање стањивање узорка након SPT-а и најмањи ход пробе у току SPT па самим тим и најмања дуктилност у поређењу са основним материјалом, је уочена код узорака заварених са ниским угаоним брзинама, као последица деформационог ојачавања, док је при заваривању са већим угаоним брзинама услед динамичког опорављања дошло до пораста дуктилности у поређењу са основним материјалом.

Да би се утврдио утицај на механичке особине, хемијски састав и морфологија слоја који је пронађен на месту прслине између лимова, извршена је детаљнија анализа саме међуконтактне површине.

Након испитивања међуконтактне површине са SPM на основу добијених мапа тврдоће и модула еластичности утврђено је да у зони међуконтактне површине као и у околини (20 × 20 μm) није дошло до промене механичких особина поредећи међуконтактну површину и зону завара која је окружује. Међутим, с обзиром да је резолуција уређаја за испитивање са одабраном пробом око 200 nm а дебљина оксидног слоја до 50 nm могуће је да оскидни слој није детектован. Ипак, међуконтактна површина чија дебљина варира од 1.72 до 4.23 μm према измереним вредностима на SEM-у након SPT-а сигурно јесте.

Посматрајући мапе добијене на SPM-у могу се уочити три различита кластера тврдоће и модула еластичности. Два кластера одговарају механичким особинама зоне завара. С обзиром да је тестиран само један узорак заварен са 1500 o/min из серије I, велики удео акумулираних дислокација је очекиван. Разлика између кластера просечне тврдоће 2,2 GPa и модула еластичности 103,37 GPa и кластера просечне тврдоће 1,87 GPa и модула еластичности 88,25 GPa је настала као последица акумулације дислокација у појединим зрнима. Тврдоће измерене у кластеру са просечном тврдоћом 2,12 GPa одговарају местима где је дошло до нагомилавања дислокација и формирања субзрна, док други кластер одговара околном материјалу. Трећи кластер са просечном тврдоћом 10,23 GPa и модулом еластичности од 154,63 GPa одговара интерметалној фази $Al_6(FeMn)$ која је карактеристична за легуру AA 5754.

Добијене мапе тврдоће и модула еластичности су у корелацији са резултатима добијеним на TEM. Резултати са TEM указују на присуство акумулираних дислокација која формирају субзрна унутар полигоналних зрна зоне завара, што је потврђено и са дифракционом сликом која указује на присуство дислокација, на тај начин што дислокације локално мењају кристалну оријентацију, што изазива дифракционе тачке да буду издужене. Ови резултати представљају још једну потврду теорије о деформационом ојачавању као и да је финозрна микроструктура настала као последица континуалне динамичке рекристализације тј. да је главни механизам формирања нових зрна последица ротације субзрна која су настала као последица акумулације дислокација.

Анализом резултата добијених на TEM, на узорку завареном са 1000 o/min из серије I јасно се може уочити разлика између зоне завара и међуконтактне површине. Интересантно је приметити да међуконтактна површина представља комплексну зону која се разликује од зоне завара али осим оксидног слоја који је био очекиван, разликује се и по величини зрна, као и по величини, морфологији и количини талога који се ту налазе. Дебљина међуконтактне површине се креће од 1,67 до 2,02 μm што одговара дебљини слоја уоченог на SEM-у између преломљених површина узорка након SPT-а.

Примећено је такође да се у међуконтактној површини облик и величина зрна разликују у поређењу са зоном завара. Облик и величина зрна на међуконтактној површини су последица додатне микро-деформације настале као последица интеракције храпавих лимова који су у контакту. Просечна величина ових зрна је 0,92 μm у поређењу са зоном завара где је просечна величина зрна 4,90 μm. Додатно смањење величине зрна, у поређењу са зрнима у зони завара, је последица микро-деформације која је изазвала додатну акумулацију дислокација и формирање већег броја ситнијих зрна. Такође, зрна

на међуконтактној површини, имају издужен облик који прати правац вектора смицајног напона, што је последица пластичне микро-деформације храпавих површина у смеру ротације алата.

На међуконтактној површини уочена су три различите групе талога чији су хемијски састави потврђени методом EDX. У прву групу спадају $Al_6(FeMn)$ карактеристични за легуру AA 5754. Могу се наћи како на границама зрна тако и унутар зрна и могу бити различитих величина и облика. У другу групу спадају Al_3Mg_2 који су такође карактеристични за легуру алуминијума са 3% магнезијума, јер је растворљивост магнезијума у алуминијуму на собној температури испод 1% па је очекивано да ће остатак магнезијума бити излучен у виду талога Al_3Mg_2 по границама зрна. Међутим, ако се упореди количина талога излучених на међуконтактној површини и талога излучених у зони завара уочава се да их има много више на међуконтактној површини. Такође, може се уочити и да је највећи број тих талога излучен на границама између зрна међуконтактне површине и зоне завара. Просечна величина ових талога је 0,09 μm. С обзиром да је након SPT установљено да је преломљена површина јамичаста и да дебљина слоја пронађеног између преломљених површина одговара дебљини међуконтактне површине уочене на TEM, закључује се да су Al_3Mg_2 који се налазе на прелазу између међуконтактне површине и зоне завара заправо иницијална места на којим је дошло до деламинације. Већа количина талога на међуконтактној површини последица је динамичког таложења, које је настало услед високог степена деформације на релативно ниским температурама.

У трећу групу талога спадају такође талози чији је хемијски састав компатибилан са талозима Al_3Mg_2, међутим, ови талози су излучени унутар зрна и морфолошки се разликују од талога излучених по границама зрна. Ови талози су у облику штапића оријентисаних у два правца нормална један у односу на други. Просечна дужина ових штапића је 0,076 ±0,016 μm док је просечна дебљина 0,042 ±0,009 μm. С обзиром да се и ови талози могу наћи само на међуконтактној површини унутар издужених зрна, може се сматрати да су они настали као последица динамичког таложења. Део будућег истраживања биће посвећен одређивању механизма који доводи до динамичког таложења како унутар зрна тако и на граничним површинама.

У средини комплексне међуконтактне површине, на самој граничној површини лимова које заварујемо уочен је такође и већ поменути заробљени оксидни слој, као и нано-јамице окружене у потпуности са оксидним слојем. Два типа оксида су уочена и хемијски анализирана: (i) Al_2O_3 који у потпуности окружује микро-јамицу и (ii) MgO који је уочен у различитим зонама како око нано-јамица тако и на месу споја где је дошло до потпуног заваривања.

Присуство оксида око микро-јамице је потврђено и са FM – KPFM-ом. На основу добијене мапе функције рада (*work function*) установљено је да је међуконтактна површина засићена честицама чија функција рада одговара функцији рада алуминијум-оксида или магнезијум оксида. Такође, на основу морфологије уочених оксида верификована је теорија о савијању оксидног слоја и уситњавању у мање сегменте што дозвољава појаву дифузије и добијање квалитетног завареног споја. Међутим, на основу свих изведених

анализа је установљено да је за деламинацију ипак одговорно динамичко таложење на прелазу између међуконтактне површине и зоне завара.

Након свеобухватне анализе изведене у оквиру ове дисертације, утврђено је да се поступком ТЗТМ могу успешно преклопно заваривати ултратанки лимови од легуре алуминијума са магнезијумом, што отвара могућности да овај поступак добије своју примену у електроници и уопштено за заваривање компоненти проводника у ауто-, авио индустрији и др. Технологија ТЗТМ се показала као продуктивна технологија заваривања, код које време заваривања иде испод 1 s, која омогућава добијање заварених спојева високих механичких особина, односно, чврстоће која може превазићи основни материјал. Висока продуктивност, мали утрошак енергије, релативно јефтина опрема, одсуство заштитног гаса и додатног материјала и чињеница да је ТЗТМ поступак без икаквих штетних последица по животну средину, чини ТЗТМ перспективном технологијом у будућности.

Acknowledgment

During the long and exciting process of PhD studies I had the opportunity to enrich myself personally and professionally and to expand my scientific knowledge thanks to the people who invested their time and trust in my ideas. I absolutely need to mention those special individuals for giving their invaluable guidance, motivation and moral support.

At the outset, I would like to thank my PhD committee comprising of my supervisor Dr Sebastian Baloš, PhD advisor Prof Dr Leposava Šiđanin, committee member Dr Dragan Rajnović at Faculty of Technical Sciences, Novi Sad, Serbia and two co-supervisors Prof Dr Jean Pierre Bergmann at Ilmenau University of Technology from Germany and Dr Saurav Goel from Cranfield University/London South Bank University from the United Kingdom, for guiding me in the writing of my thesis.

I would like to express my heartfelt thanks to my primary supervisor Dr Sebastian Baloš who has continuously supported me with patience and helped keep me focused throughout my PhD. I'm especially grateful for our deep discussions and the advice and critiques he gave me, all of which fuelled and fostered my scientific and spiritual maturity. I would also like to express my immense appreciation to my co-supervisors Professor Jean Pierre Bergmann and Dr Saurav Goel for facilitating me with the required research platforms and experimental facilities without which this PhD research work would not have been possible. They welcomed me to their laboratories, helped me with focusing my ideas and gave me countless suggestions. My gratitude to them exceeds words.

I would like to add my sincere thanks to my PhD advisor and my inspirational role model Professor Leposava Šiđanin for motivating me through extended meetings and discussions. Most of all, she has my appreciation for encouraging me to search beyond the borders. Her rich scientific background and endless love for science motivated me to become what I am today. Words would be few to describe my admiration and respect for her.

The list of people and organizations who also have contributed to my work during this PhD is far exhaustive. Every individual in this journey has helped me to learn something new and to move my research forward. Words would be few to express my gratitude to them. Therefore, I will try to mention all organizations and people without whom this work would not be the same.

First of all I would like to show my appreciation for various funders such as Deutscher Akademischer Austauschdienst (DAAD), European Cooperation in Science and Technology (COST) especially COST Action CA15102 and Henry Royce Institute (HRI) in the UK for providing me the generous financial support via grants and scholarships to allow me to access cutting-edge facilities across the EU.

I would also like to thank all colleagues in the Department of Production Engineering at Novi Sad University, Serbia, who showed understanding and support. Thanks to Mr. Miloš Bokorov at University Centre for Electron Microscopy, University of Novi Sad, Serbia for conducting the work at Scanning Electron Microscope (SEM). Also, I would extend my gratitude to all my colleagues at the Department of Production Technologies working at Ilmenau, Germany especially to Ms. Franziska Petzoldt for her unreserved friendship. She not only trained me to use the equipment but also helped me organize my family's social life during our stay in Germany. Furthermore, my sincere gratitude goes to Dr Stefan Rasche, Mr. Michael Grätzel, and Mr. Tobias Köhler for continuously supporting my work and as well to all other colleagues that have contributed my work and living in Germany.

My heartfelt appreciation goes to colleagues from Cranfield University, UK (Precision Engineering Institute in the School of Aerospace, Transport and Manufacturing) for their hospitality and help during my stay at Cranfield, as well. I especially want to thank Dr Claudiu Giusca who contributed to my experimental work in surface characterization of the weld surface. Also, I would like to thank to Mr. Alan Heaume for his hospitality, trainings and technical support related to my work. I am

also thankful to the Dean of the School of Engineering at London South Bank University, Prof Asa Barber for extending the use of their Scanning Acoustic Microscope (SAM) as well as providing travel support for additional training at PVA Tepla in West Hausen, Germany. At the same time, special thanks to Dr Tatjana Djuric-Rissner and Mr. Bugra Birki from company PvA TePla for training me to use the SAM.

My sincere appreciation goes to colleagues Dr David Stanley, Dr John Walmsley and Dr Giorgio Divitini at Henry Royce Institute and Cambridge University from the UK for providing me facilities and possibility to work with them which had helped me with characterisation of my samples. Also, I would like to thank Dr Vishal Panchal and Mr. Stephen Lewandowski at Bruker company from Coventry, UK for their unreserved help with finding the right methods and performing extended characterisation of my samples using a wide range of nanotechnology tools.

I would also like to mention people who have contributed to my work like Dr Pavel Hanus from Technical University of Liberec, Czech Republic who facilitated SEM related research, Dr Janez Zavašnik at Jožef Stefan Institute from Slovenia for conducting preliminary TEM research essential for my work and to Mr. Ivan Zabunov, Director of Proficut company in Serbia for providing me with the facilities for conducting experimental research on ultrasonic welding which is essential for future work in this area. My high appreciation goes to my dear friend Diane Vuković for proofreading my PhD thesis.

However, all my efforts would be worthless if I would not dedicate it to special individuals. Those individuals are my daughters Magdalena and Tara, my husband Siniša Zlatanović, my parents and my friends. I hope they will forgive me for all the hours I took from them to contribute to this work and I also hope this work will be a great motivation for my daughters during their intellectual and spiritual development. Finally, I would like to express my highest gratitude, love and dedication to my husband for continuous understanding, support and love he had for me during the entire process.

Prof. Associate dr Sebastian Baloš
Prof. Emeritus dr Leposava Šiđanin
and to all colleagues from Chair
of Material and Joining Technologies

Prof. Associate dr Saurav Goel
Prof. dr Asa Barber
Sr. Lecturer dr Claudiu Giusca
Mr. Alan Heaume
and to all colleagues from
SATM, Cranfield

Dr Vishal Panchal
Mr. Stephen Lewandowski

Dr Janez Zavašnik

Mr. Miloš Bokorov,
University Centre for
Electron Microscopy Novi Sad

Short Term Scientific Missions
(STSM) supported from
Cost Action CA 15102

Prof. Dr.-Ing. habil. Jean Pierre Bergmann
Ms. Franziska Petzoldt
Dr Stefan Rasche
Mr. Michael Grätzel
Mr. Tobias Köhler
and to all colleagues from
Department of Production Technology

Dr David Stanley
Dr John Walmsley
Dr Giorgio Divitini

Dr Tatjana Djuric-Rissner
Mr. Bugra Birki

Dr Pavel Hanus

Mr. Ivan Zabunov,
Director at Proficut d.o.o.

Short Term Research
Scholarship (6 months)

Contents

Abbreviations

BF	Bright field
BM	Base material
CDRX	Continuous dynamic recrystallisation
CoF	Coefficient of friction
CFSW	Conventional friction stir welding
CFSSW	Conventional friction stir spot welding
CSOL	Continuous surface oxide layer
DB	Diffusion bonding
DRX	Dynamic recrystallisation
DSA	Dynamic strain ageing
DS-FSW	Double-side friction stir welding
EBSD	Electron backscatter diffraction
ECAP	Equal-channel angular pressing
EDX	Energy-dispersive X-ray spectroscopy
FE	Finite element
FE-SEM	Field emission scanning electron microscope
FFSSW	Flat friction stir spot welding
FIB	Focused ion beam
FM-KPFM	Frequency-modulated Kelvin probe force microscopy
FSAMP	Friction stir assisted manufacturing processes
FSC	Friction stir channelling
FSP	Friction stir processing
FSR	Friction stir riveting
FSS	Friction stir surfacing
FSBR	Friction stir blind riveting
FSCl	Friction surface cladding
FSIF	Friction stir incremental forming HD
FSSVW	Friction stir spot vibration welding
FSSW	Friction stir spot welding
FSW	Friction stir welding
GKSS	Helmholtz-Zentrum Geesthacht
HAADF	High-angle annular dark-field imaging
HAGB	High angle grain boundary
HAZ	Heat affected zone
HD	Hook defects
HFDB	Hybrid friction diffusion bonding
HFSC	Hybrid friction stir channelling
HR-TEM	High resolution transmission electron microscope
IL-FSSW	Intermediate layer friction stir spot welding
In-situ SPM	In-situ scanning probe microscopy
IR	Infrared
KB	Kissing bond
LAGB	Low angle grain boundary
LEDS	Low energy dislocation structure

LM	Light microscopy
MFSC	Modified friction stir channelling
MSL	Mixed subsurface layer
nSRS	Negative strain rate sensitivity
RFSSW	Refill friction stir spot welding
RPM	Revolutions per minute
RSW	Resistance spot welding
PB	Partial bonding
PFSSW	Protrusion friction stir spot welding
PLC	Portevin-Le Chatelier effect
PLT-FSSW	Friction stir spot welding with pin-less tool
PMB	Partial metallurgical bond
RSZ	Recrystalised stir zone
SADP	Selected area diffraction pattern
SAM	Scanning acoustic microscope
SEM	Scanning electron microscope
SFSSW	Swing friction stir spot welding
SFSW	Submerged friction stir welding
SIF	Stress intensity factor
SP	Surface potential
SPM	Scanning probe microscopy
SPT	Small punch test
SR-FSW	Self-reacting (bobbin) stir welding
STEM	Scanning transmission electron microscope
SZ	Stir zone
TEM	Transmission electron microscopy
TMAZ	Thermomechanical affected zone
TSFL	Tensile shear failure load
TWI	The welding institute
USW	Ultrasonic spot welding
UW	Ultrasonic welding
WFSSW	Walking friction stir spot welding
WFI	Weld faying interface
XPM	High speed property maps
μFSW	Micro friction stir welding

Nomenclature

A_c	Projected contact area
d	Grain diameter
dA	Contact surface element
d/D	Ratio of the bottom diameter of the SZ and top diameter of the SZ
dF_r	Resistance force for element
e	Charge of an electron
E_S	Weld efficiency
F_N	Axial load
$Fmax$	Rupture load
$Fmax_{weld}$	Rupture load of weld
$Fmax_{BM}$	Rupture load of base material
H	Axial height of the joint in the centre of the weld
H_{IT}	Indentation hardness
k_1	Strength of the cell boundary
L_e	Effective (average) depth
m	Exponent
n	Rotational speed
$p(r)$	Axial stress
P_{max}	Peak force
R	Outer radius
r	Radius
r_e	Effective (average) radius
r/R	Ratio of the radius of the edge-chipping area and stable process-pressure area
Rm	Average material flow rate
Rm_{BM}	Ultimate strength of base material
Rm_{weld}	Ultimate strength of weld
S_{max}	Maximum punch displacement
T	Torque
α	Taper angle of the stir zone
ΔV_{CPD}	Contact potential difference
μ	Coefficient of friction
σ	Yield strength
σ_n	Normal stress
σ_o	Frictional stress
τ	Shear stress
Φ_{probe}	Work function of the probe
Φ_{sample}	Work function of the sample
ω	Angular velocity
$\dot{\varepsilon}$	Material flow strain rate

1. INTRODUCTION

1.1 Background and motivation

The growing demand in the automotive and aerospace industry for low-weight components has made aluminium and its alloys popular in modern manufacturing. Economic reasons, market demands and, most of all, the drive for weight reduction have pushed for copper (8.96 g/cm^3) to be substituted by aluminium (2.7 g/cm^3). This push for substitution is especially seen in battery components and strand-terminal connectors as aluminium achieves the same conductivity as copper while weighing nearly half. Consequently, there is a pressing international need to establish acceptable joining technologies and weld characteristics for aluminium and its alloys [1–4].

Currently, the most frequently applied technique for spot welding of aluminium is resistance spot welding (RSW) [5], followed by laser spot welding [6] and cold metal transfer spot welding [7]. However, all of these techniques are based on the melting of the base material. Due to the presence of a transient liquid phase, different kind of defects can occur, including pores, poor weld strength, brittle solidification, distortion due to residual stress, hot cracking, stress corrosion. Consequently, various solid-state welding techniques were developed like diffusion bonding (DB) [8], ultrasonic welding (UW) [9] and friction stir spot welding (FSSW) [10]. The main advantages of these techniques over conventional welding techniques are low process temperature, higher mechanical properties of welds and relatively moderate energy consumption. However, the welding of aluminium with solid-state welding techniques is challenging due to a tenacious and chemically stable aluminium oxide layer formed at the interfaces of welded sheets. Aluminium reacts with oxygen in the atmosphere forming a stable oxygen layer which becomes entrapped in the interface between sheets after welding [11–13]. This layer impedes the diffusion between the sheets and thus hampers the bonding process necessary for joining. To overcome this issue, many approaches were proposed. One of them is the imposition of macroscopic plastic deformation during the process by using sheets with rough surfaces. In this approach, a substantial level of plastic deformation is induced in the workpiece. Metal to metal contact is thus promoted because of local disruption of the oxide film on both faying surfaces. However, this approach only produces a partially welded interface with limited mechanical properties [14]. This problem has been overcome in UW and FSSW by utilizing vibration (in UW) and rotation (in FSSW) to introduce a high level of deformation in the workpiece during welding. However, due to the complex tool geometry, UW leaves the surface of welds rough which can lead to corrosion. Also, undesirable mechanical properties of welds after UW were observed [15].

The main reason why resistance spot welding still has a leading role in the automotive industry is because of its short dwell time (range from 0.01 to 0.63 s depending on the thickness of the metal). Even though FSSW is more energy-efficient compared with RSW and produces joints with higher mechanical properties, due to its relatively long dwell time (range approximately

from 1 to 5 s depending on the thickness) it is still not a preferable technique, especially in batch and mass production.

Friction stir welding was developed in 1991 at The Welding Institute (TWI) of the UK [16]. Primarily, it was developed as a welding technique but, over the years, the technique gained popularity for use in different areas of manufacturing for processes like surface property enhancement, channelling, riveting and forming. The series of developments in different fields have led to an increase in the number of processes that are based on harnessing the principle of friction stir welding.

Conventional friction stir spot welding (CFSSW) is a spot-welding technique for lap joining initially developed for the automotive industry. The technology was firstly developed by the German research centre (*Helmholtz – Zentrum Geesthacht* – HGZ). Mazda reported the first application of CFSSW in 2003 in the mass-produced RX-8 car [17]. The entire aluminium rear door was friction stir spot welded. They claim large energy savings and capital investment gains compared with using RSW (~90 % energy saving and 40 % investment reduction). CFSSW consumes low energy and, because of being a solid-state process, can provide superior weld properties compared with those of the other methods mentioned above. It is suitable for producing spot-like joints with minimum or no material loss. Unlike FSW, FSSW can be considered as a transient process due to its short dwell (cycle) time of up to a few seconds. However, CFSSW uses a tool that leaves a keyhole behind. It causes a reduction of the effective cross-section area of the joint and leads to the formation of the so-called hook defects (HD) due to a thin oxide film present in the interface between two sheets. During the welding, the hook defects are formed due to an upper bending of the welding interface caused by the penetration of the tool pin into the bottom sheet [18,19]. To overcome this disadvantage, Bakavos *et al.* [20] proposed the use of friction stir spot welding with a pin-less tool (PLT-FSSW) which managed to obtain higher shear strength compared with that of CFSSW. Thereafter, Chiou *et al.* [21] found that using a pin-less tool provides higher mechanical properties of the weld than those obtained with the conventional tool. It has led to PLT-FSSW becoming a very attractive technology for welding thin sheets (1-2 mm). However, for welding of ultrathin sheets (from 0.2 to 0.65 mm) or foils (less than 0.2 mm), using a flat tool was not suitable due to a tendency to tear the uppermost sheets at the contact edge of the tool [22]. Therefore, it seems plausible that the flat tool, creating the uniform pressure along the entire radius of the tool, is unsuitable for welding multiple aluminium ultra-thin sheets with FSSW. Considering this, the presented thesis aims to provide an improved understanding of friction stir spot welding of multiple ultrathin sheets.

1.2 Aim and objectives of the research

As the welding of multiple ultrathin sheets with FSSW represents a grand challenge, a profound analysis of all influencing parameters is required. The main aim is to obtain lap joints of multiple thin sheets of AA 5754-H111 alloy with mechanical properties of the joint in the range of the base material or higher.

To address this aim, the following objectives were set:

(i) Review the existing literature to develop an understanding of the previous work and identify critical research gaps.
(ii) Design a suitable tool geometry to achieve the targeted stress state for enabling FSSW of multiple thin sheets.
(iii) Implement a well-factored process parameter array by varying rotational speed, plunge depth and axial load. It is expected that different combinations of these parameters and tool geometries will produce joints with different mechanical properties. It is also important to identify the key parameters which are most influential in governing the joint quality.
(iv) Detailed analysis of the stress-temperature state during the welding process. Calculation of directional stresses and coefficient of friction (CoF).
(v) Analyse the weld interface to develop a bottom-up understanding of the nature of defects such as oxides and high-pressure phases affecting the joint strength.

A flowchart depicting the summary of this thesis is illustrated in **Fig. 1.1**.

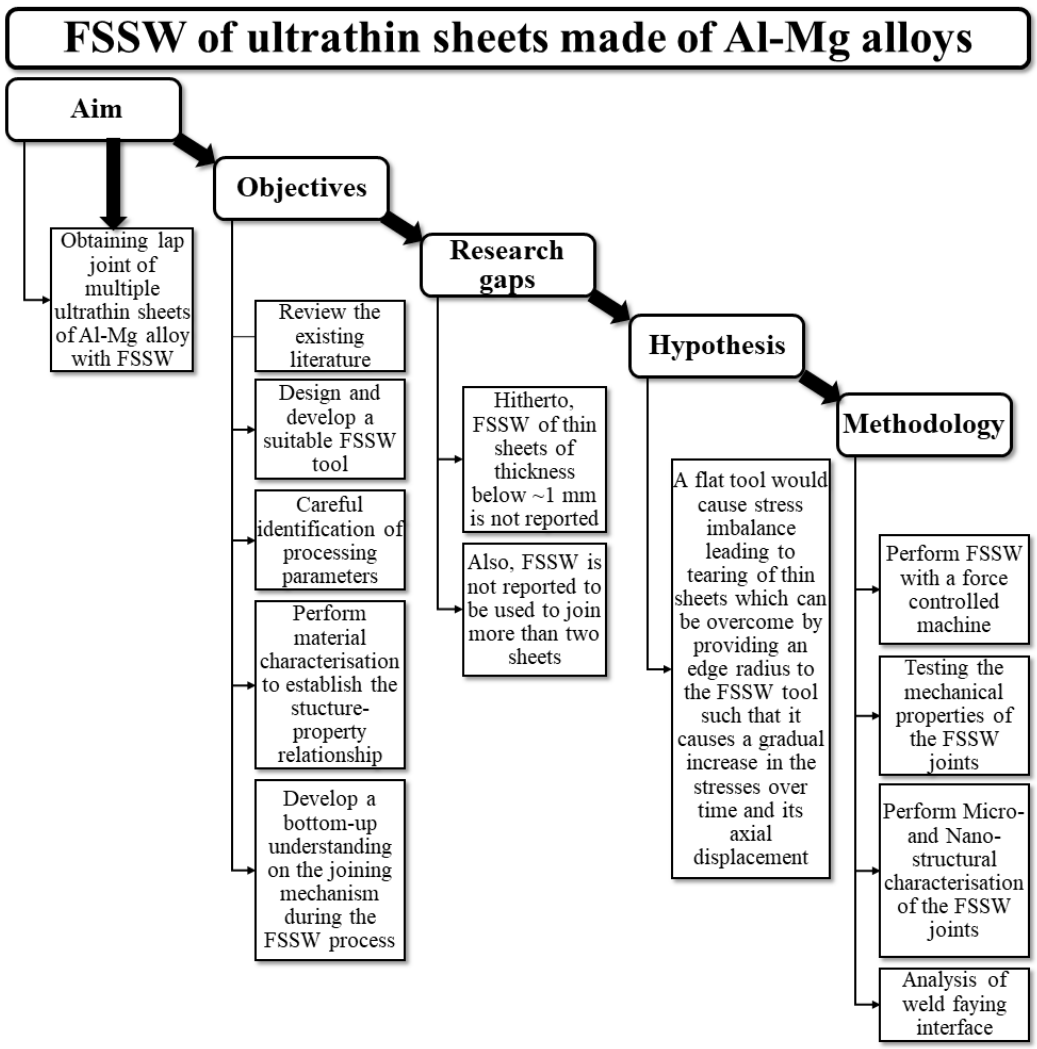

Fig. 1.1 *Research flow chart showing the direction of steps taken in this thesis*

2. LITERATURE REVIEW

2.1 Aluminium alloys

With an annual consumption of 35 million tons, aluminium has become one of the world's most commonly used metals [23]. It's strength, barrier properties, conductivity, excellent corrosion resistance along and low density are the main reasons for its continuously growing demand in production. Aluminium's lightweight properties are highly favourable in electronic, automotive and aerospace industries [23,24].

Aluminium alloys are divided into two major groups [23]:

(i) Work hardening, non-heat-treatable alloys (Al99.95%, Al-Mg, Al-Mn, etc.) and
(ii) Age-hardening or precipitation hardening alloys (Al-Cu-Mg, Al-Mg-Si, and Al-Zn-Mg-Cu).

With heat-treatable alloys, strain-hardening can supplement the strength achieved by precipitation-hardening.

In **Table 2.1** examples of wrought and cast aluminium alloys series are given. Since high-purity aluminium in the annealed condition retains a low yield strength (7-11 MPa), several aluminium alloys were developed over the past few years. Although aluminium can be alloyed with most metals, only a few have enough solid solubility to serve as major alloying elements (more than 10 atomic %). Zn, Mg, Cu and Si have significant solubilities in aluminium. However, a few other elements with solubilities below 1 atomic % confer significant improvements to alloy properties, such as Cr, Mn, and Zr, which are primarily used to form compounds that can control grain structure. This way, solid solution hardening was introduced to improve the mechanical properties of annealed material. To achieve that, the solute must have a high solid solubility at the annealing temperature and to remain disolved after a slow cooling. Also, it is important not to allow any reaction with other elements that may create undesirable insoluble phases [24].

The increase of yield strength that occurs when solutes are added to pure aluminium is shown in **Fig. 2.1a** and **b**. At an atomic level, Mg and Cu are the most effective strengtheners (at 0.5 % or less). In non-heat-treatable alloy, Cu additions are held at a maximum of 0.3 % to avoid the possible formation of insoluble Al-Cu-Fe constituents. Magnesium turned out to be the most effective strengthener because of its relatively high solid solubility. It is interesting that Zn also has high solubility but causes slight hardening. However, during ingot preheating and hot processing, Mn usually precipitates as dispersoid Al_6Mn; only 0.2-0.3 % of Mn tends to remain in the solution [23–25].

Table 2.1 The Aluminium Association alloy designation system [25]

Wrought alloys		
Series	Major alloying elements	Heat treatable
1xxx	Al ≥ 99%	No
2xxx	Al-Cu-(Mg)	Yes
3xxx	Al-Mn	No
4xxx	Al-Si	No/Yes
5xxx	Al-Mg	No
6xxx	Al-Mg-Si	Yes
7xxx	Al-Zn-(Mg)-(Cu)	Yes
8xxx	Al-(other elements)	No/Yes
9xxx	Unused series	
Cast alloys		
Series	Major alloying elements	Heat treatable (not many are used as cast)
1xx.x	Al ≥ 99%	No
2xx.x	Al-Cu	Yes
3xx.x	Al-Si (Cu or Mg)	Yes
4xx.x	Al-Si	No
5xx.x	Al-Mg	No
6xx.x	Unused series	
7xx.x	Al-Zn-(Mg)-(Cu)	Yes
8xx.x	Al-Sn	No
9xx.x	Al-(other elements)	

Note: *While the Aluminum Association wrought alloy designations are very widely used, there are no universal casting alloy designations in wide use. However, for any casting alloy, there are usually equivalent alloy designations from each different region.

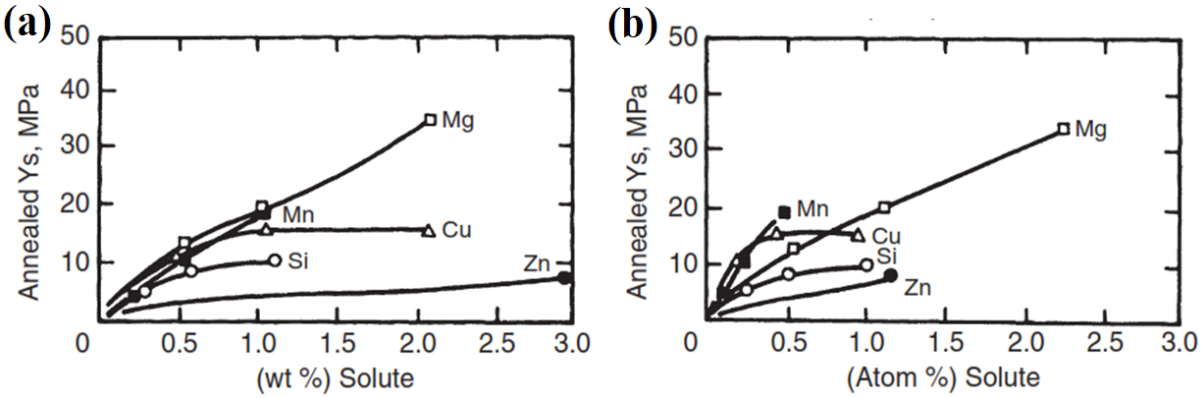

Fig. 2.1 *Solid solution strengthening of high-purity binary aluminium alloys: (a) mass weight; (b) atomic weight* [24]

Aluminium possesses high stacking fault energy (~170 $mJ \cdot m^{-2}$). During deformation, the cellular substructure can form inside of the grains rather than stacking faults or twins. Cellular substructure causes strengthening [24,26]. This can be explained with the Hall-Petch equation [24,27]:

$$\sigma = \sigma_0 + k_1 \cdot d^{-m} \tag{2.1}$$

σ-yield strength;
σ_0-frictional or Peierls stress;
k_1-strength of the cell boundaries;
d-grain diameter;
m-exponent that varies from 1 to 0.5.

At relatively low temperatures, the substructure produced by work hardening is usually referred to as cells-structure. The difference in orientation of these cells is only about 1° and they have walls comprising of tangled dislocations. However, deformation at higher temperatures produces subgrains bounded by well-defined, narrow walls. Misorientation of those subgrains is higher compared with that of the cells and goes up to 15°. If the alloy undergoes the process of recovery the value of *m* changes from 1 to 0.5. It causes the substructure to change from cells to subgrains. The formation of subgrains causes an increase in mechanical properties.

For an alloy to be susceptible to age-hardening there must be a decrease in the solid solubility of one or more of the alloying elements and decreasing temperature. Most alloys that respond to the ageing will undergo some hardening at room temperature, so-called *natural ageing,* and can last indefinitely with a drop of the ageing rate over time. Ageing at elevated temperature, so-called *artificial ageing,* is distinguished by a different behavior. In this case, hardness usually increases to the maximum value and then decreases. The softening mechanism that occurs on prolonged artificial ageing is known as "*overageing*". The maximal hardness is obtained when there is a presence of critical dispersion of intermediate precipitates. In some alloys, more than one type of intermediate precipitates can be formed. Some aluminum alloys are cold worked after quenching and before ageing. This treatment increases the dislocation density and also provides more initial sites where heterogeneous nucleation of intermediate precipitates can occur during ageing [24,27].

The interaction between dislocation and solute elements has been studied for many years. However, in present literature, the solid solution which is unstable with respect to a precipitation reaction during deformation was not studied in detail. In other words, the influence of moving dislocations on the precipitation process (*so-called dynamic precipitation*) is less documented [28]. Dynamic precipitation was studied during low-temperature-high-deformation processes like equal-channel angular pressing (ECAP) of alloys Al-Mg-Si [29] and Mg-Al [30] or hot extrusion of the alloys Al-Mg-Si [31] and Al-Zn-Mg [28]. In all cases, a nucleation of new precipitates caused by dislocation interaction with solute atoms was observed.

2.1.1 Al-Mg alloys

Aluminium and magnesium tend to form a solid solution. The most widely used wrought aluminium alloys contain 0.8 to 5 % magnesium. Mechanical properties in annealed conditions vary significantly. Alloy 5005 has a tensile strength of 125 MPa whereas the alloy AA 5456 which has a strength of 310 MPa, which is the highest tensile strength among 5xxx alloys. Elongation usually exceeds 25 %. The alloys work harden easily and with a higher content of magnesium the rate of work hardening increases [23,24].

Some Al-Mg alloys may exhibit some instability of properties. If aluminium contains 3-4 % magnesium there is a tendency to develop the β-phase. Also, Mg_5Al_8 phase precipitates to slip bands and grain boundaries which may lead to intergranular and stress corrosion cracking. Work hardening alloys can undergo what is known as age softening at ambient temperature. During age softening the mechanical properties drop due to a localized recovery within the recovered grains [23–25,32].

Fig. 2.2 depicts the stable Al-Mg phase diagram and indicates the following phases: two-terminal solid solutions Al (Mg) and Mg (Al) and three intermetallic compounds Al_3Mg_2, R and $Al_{12}Mg_{17}$. During welding processes like FSSW, the presence of intermetallic compounds can significantly influence the weld quality. If there is high deformation and low process temperature, dynamic precipitation can cause the formation of new precipitates. Also, already present precipitate in the alloy can be grounded to the smaller pieces and distributed along the grain boundary. To overcome these problems, appropriate welding parameters needs to be chosen.

The 5xxx alloys have high strength, weldability, good formability and a high level of corrosion resistance. Because of their good mechanical properties in the annealed condition, Al-Mg alloys with a higher amount of magnesium are candidates for the rapidly growing automotive industry. They are widely used for welding applications [24,32].

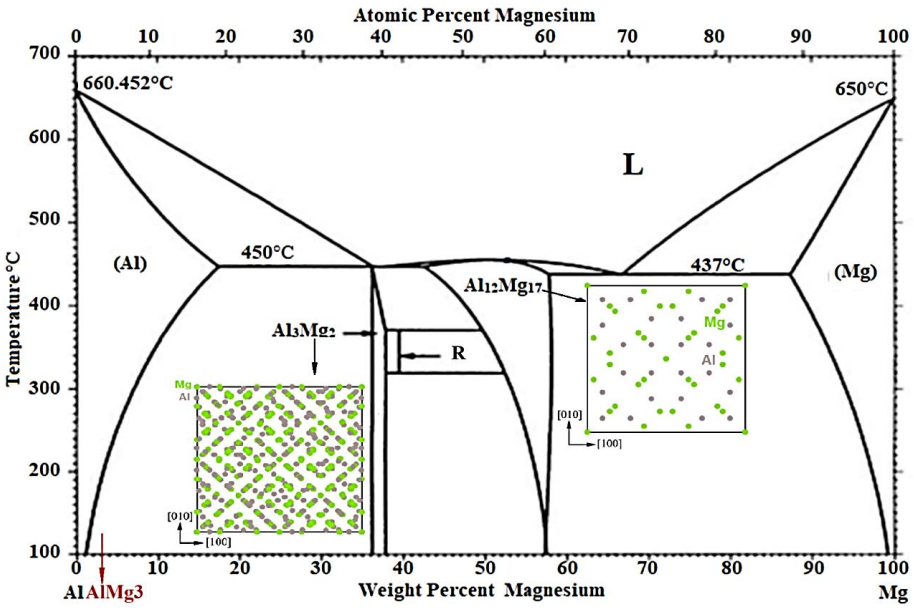

Fig. 2.2 *Al-Mg phase diagram* [32,33]

2.2 Review of friction stir spot welding (FSSW)

FSW was invented and patented in 1991 at TWI as a solid-state joining technique. It was initially applied on aluminium alloys [34] and developed for butt joints. Afterwards, Mishra *et al.* [35] developed friction stir processing (FSP), which was inspired by FSW but, instead of joining, was used for grain refinement of AA 7075 aluminium alloy. Thereafter, the basic principle of FSW was implemented in the development of different kinds of friction-stir assisted manufacturing processes (FSAMP). As a part of this research, an attempt was made to classify and summarise FSAMP processes as shown in **Fig. 2.3**.

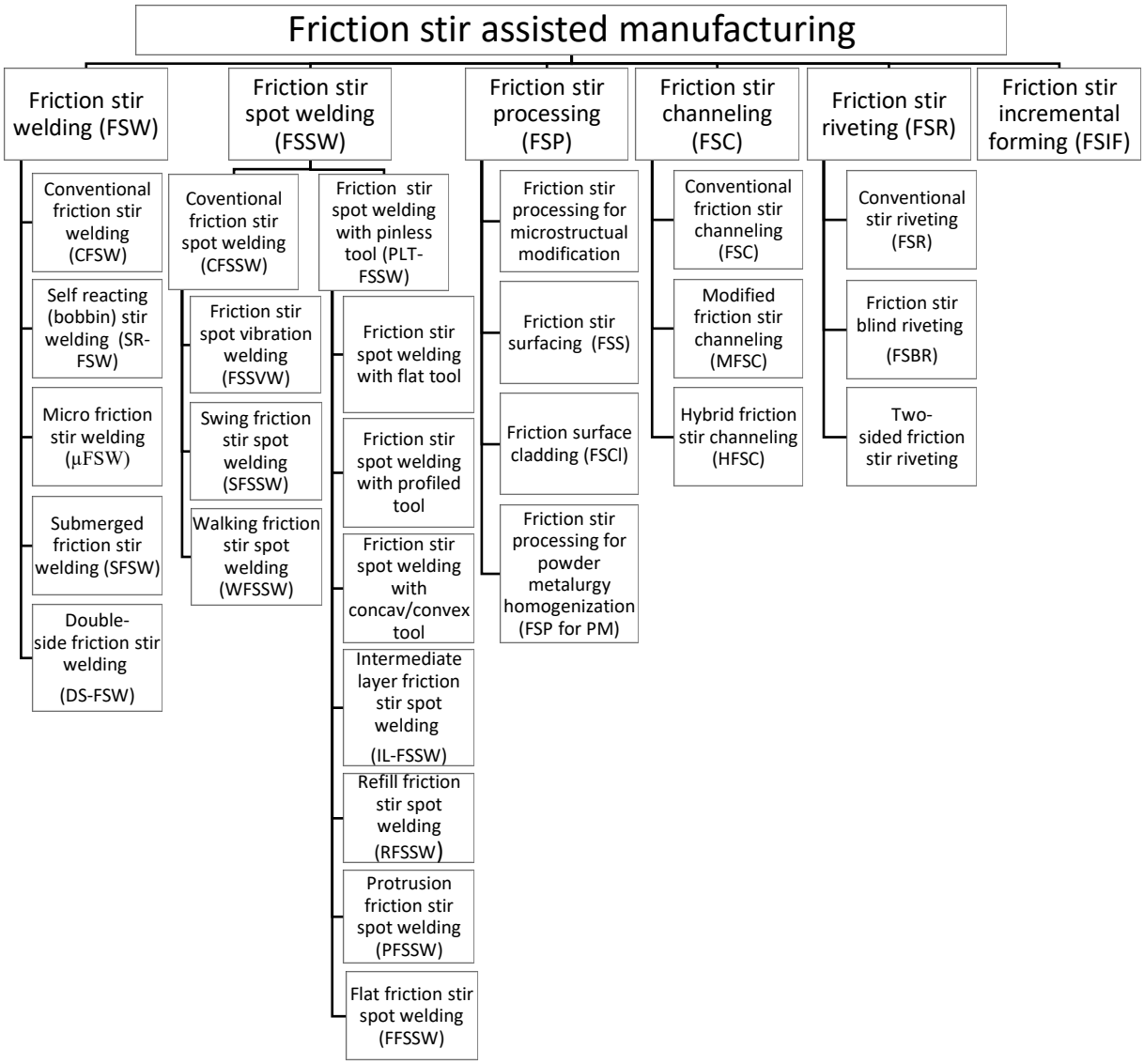

Fig. 2.3 *Classification of the friction stir assisted manufacturing processes*

FSSW is solid-state joining technology which has a high energy efficiency due to the low heat input required in the process. The most pronounced advantage of FSSW is the capability to weld materials that are classified as non-weldable due to a poor solidification microstructure and porosity in the fusion zone (such as highly alloyed heat-treated aluminium alloys from series 2xxx and 7xxx). In addition, FSSW has no impact on human health and safety as it has no residual radiation and has low operations hazards. Moreover, minimal distortion, small thermal deformation, minimal joint preparation, low residual stresses, no welding consumables (shielding gases, cooling agents, vacuum chambers, etc.), high welding efficiency, sound mechanical properties, refined microstructure, and suitability for automation significantly increase the use of FSSW in the industry [3,10,25,36–40]. Although FSSW was first developed for joining aluminium alloys, throughout the years this technique was used for joining other metals and its alloys such as magnesium [41], titanium [42], steel [43] and copper [44]. It also proved to be an adequate technique for welding dissimilar metals like aluminium-to-copper [45], aluminium-to-steel [46], and aluminium-to-titanium [47]. Finally, FSSW of multi-material, metal-to-metal, polymer-to-polymer, and metal-to-polymer hybrid structures was developed recently [48].

As discussed in the following sections in detail, FSSW is a welding technique which derives from FSW but without translating the tool. The process uses a non-consumable rotating tool that can be with pin or pin-less. The basic principle is the same: the tool is plunged into the upper sheet of a lap joint while the anvil supports the downforce. In both cases, the tool has two primary functions: to heat the workpiece above the recrystallization temperature and to cause plasticity-induced material flow. The friction induces the heat between the tool and the workpiece. Consequently, the softened material underneath the tool is pressed by the applied axial load and tool rotation facilitates material flow. The material flow is highly dependent on the tool geometry and this is where two different research directions have now developed:

(i) Conventional FSSW (CFSSW)
(ii) FSSW with a pin-less tool (PLT-FSSW).

2.2.1 Conventional friction stir spot welding

In CFSSW. The rotational tool consists of a shoulder and a pin (probe). Even though it is a continuous process, it can be divided into three stages as shown in **Fig. 2.4a**. The friction at the contact interface between the tool and the workpiece creates the heating which softens the surrounding material. The heat is generated in the plunging and stirring stages. The rotational action and normal downward axial load of the tool facilitate plastic flow and mix the material of the upper and lower sheets together [3,49,50]. The tool reaches a predetermined plunge depth in the material and it is held in that position for a certain time (so-called dwell time). Afterwards, the tool is retracted from the workpiece leaving the FSSW joint with a keyhole depending on the shape of the non-consumable tool used in the process (**Fig. 2.4b**). The rotational tool is subjected only to torsion. By contrast, FSW exerts torsion as well as bending movement as a result of rotational and translation motions, respectively [51].

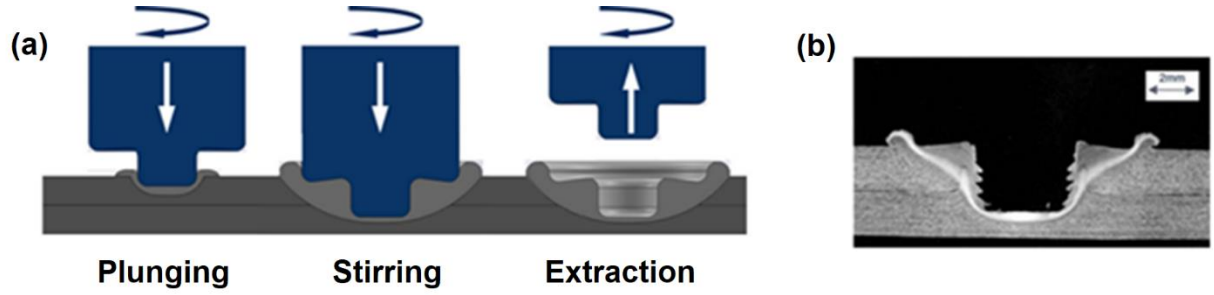

Fig. 2.4 *(a) Scheme of the conventional FSSW process; (b) corresponding cross-section [49]*

The axial load provides contact between the two metal surfaces. The pressure of the tool creates frictional heat and the formation of a metallurgical bond [52]. Due to severe movement of the welded material, the stir zone withstands a high strain rate, thereby, original grains are transformed into much finer and equiaxed ones, leading to the improvement of mechanical properties of the FSSW joints. The most influencial parameters on heat generation and material flow are plunge depth, rotational speed and dwell time. However, the CFSSW process has several disadvantages, such as the creation of a keyhole after welding, which can lead to a corrosion attack [53]. FSSW is not as flexible of a technique as, for example, arc welding; it requires rigid assembly between the tool and backing anvil as well as a rigid clamping system [36]. It is restricted to welding sheets of approximately 1 to 5 mm thickness and the welding time is relatively long compared the time required for resistance spot welding. Efforts are underway to overcome some of these disadvantages and improvements are mostly focused on tool geometry and joint formation approaches. The key parts of the FSSW tool are the pin and shoulder. The pin facilitates material flow between the workpieces and mix materials in the stir zone while the shoulder establishes the bulk of the frictional or deformational heat so softening of material can occur. Developing these parts by incorporating new features or removing geometrical characteristics is the main goal of recent research [3,54].

2.2.2 Friction stir spot welding with a pin-less tool (PLT-FSSW)

Friction stir spot welding with a pin-less tool (PLT-FSSW) makes use of a tool without a pin and with or without modification of the tool shoulder. Tozaki *et al*. [55] did the pioneering work in developing the pin-less tool but with a scroll groove on its shoulder surface. Thereafter, a number of research on different geometries of the pin-less tool was done [1,19,20,41,56,57]. High strength welds with no keyhole or with a shallow surface can be created with PLT-FSSW. The pin-less shoulder provides better penetration of the upper sheet into the bottom sheet and establishes uniformed contact of the tool surface across the welding region [3,58].

According to the tool geometry and complexity of the tool movement, PLT-FSSW can be classified into the following:

1. Friction stir spot welding with a flat tool
2. Friction stir spot welding with a profiled tool
3. Intermediate layer friction stir spot welding (IL-FSSW)
4. Refill friction stir spot welding (RFSSW)
5. Friction stir spot welding with concave/convex tool
6. Protrusion friction stir spot welding (PFSSW)
7. Flat friction stir spot welding (FFSSW)

2.2.2.1 Friction stir spot welding with a flat tool

The basic concept of the FSSW with a flat tool [20,59,60] is shown in **Fig. 2.5**. With CFSSW, the tool is plunged into all sheets. The movement of the tool can be either displacement-controlled [61] or force-controlled [22]. With PLT-FSSW the tool is plunged only into the upper sheet. The stir zone and bond between sheets are the result of continuous dynamic recrystallisation (CDRX) [62] and diffusion bonding between the sheets [13], respectively.

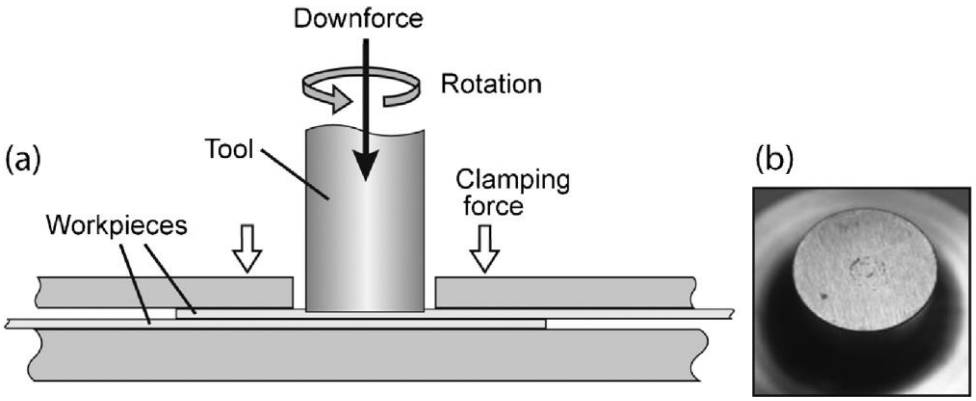

Fig. 2.5 *(a) S Scheme of FSSW with a pin-less tool design; (b) FSSW with a flat tool design [55]*

Bakavos *et al.* [20] and Reilly *et al.* [56] reported that a flat tool, when compared with a profiled tool, exhibits less friction between the tool and sheet. As a consequence, a shallower deformation zone during a longer welding time were observed (see **Fig. 2.6a** and **Fig. 2.6b**) The main disadvantage of the profiled tool compared with the flat tool is the formation of so-called hook defects, especially when dwell time is increased. As a result, the upper sheet is thinned and resultant shear strength decreases.

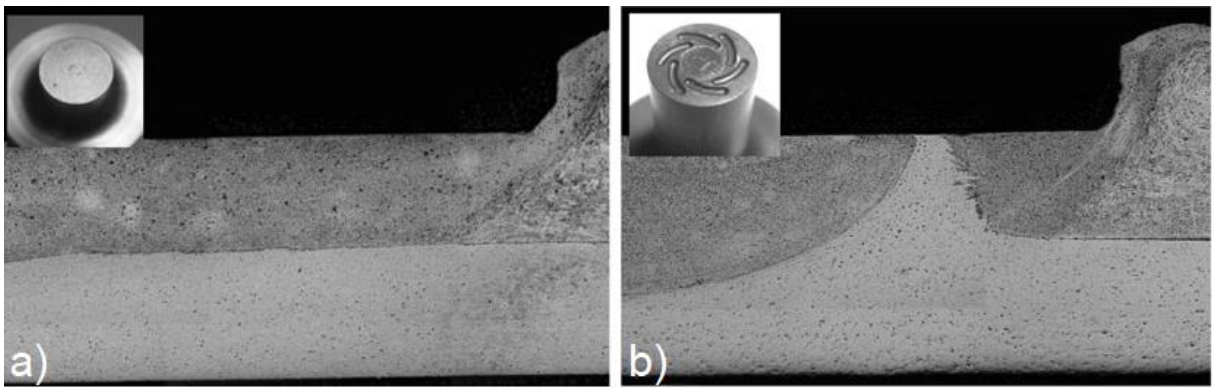

Fig. 2.6 *Cross-section views showing the influence of tool features on the "hooking" behaviour and penetration depth: (a) flat tool; (b) the short flute wiper tool* [20]

2.2.2.2 Friction stir spot welding with a profiled tool

The basic principle of FSSW with the profiled tool is the same as with flat tools. However, the profiled pin-less tool design proved to be the most effective for thin sheets [19,20,56,57]. In **Fig. 2.7** a few examples of profiled tools are shown [19,20,57,59] . Except for the tool shown in **Fig. 2.7g**, all the tools shown in **Fig. 2.7** allow for a higher penetration depth to be achieved but create the formation of hook defects in the stir zone and increase of dwell time. The cylindric tool with projection behaves like a flat tool in regards to deformation and HD.

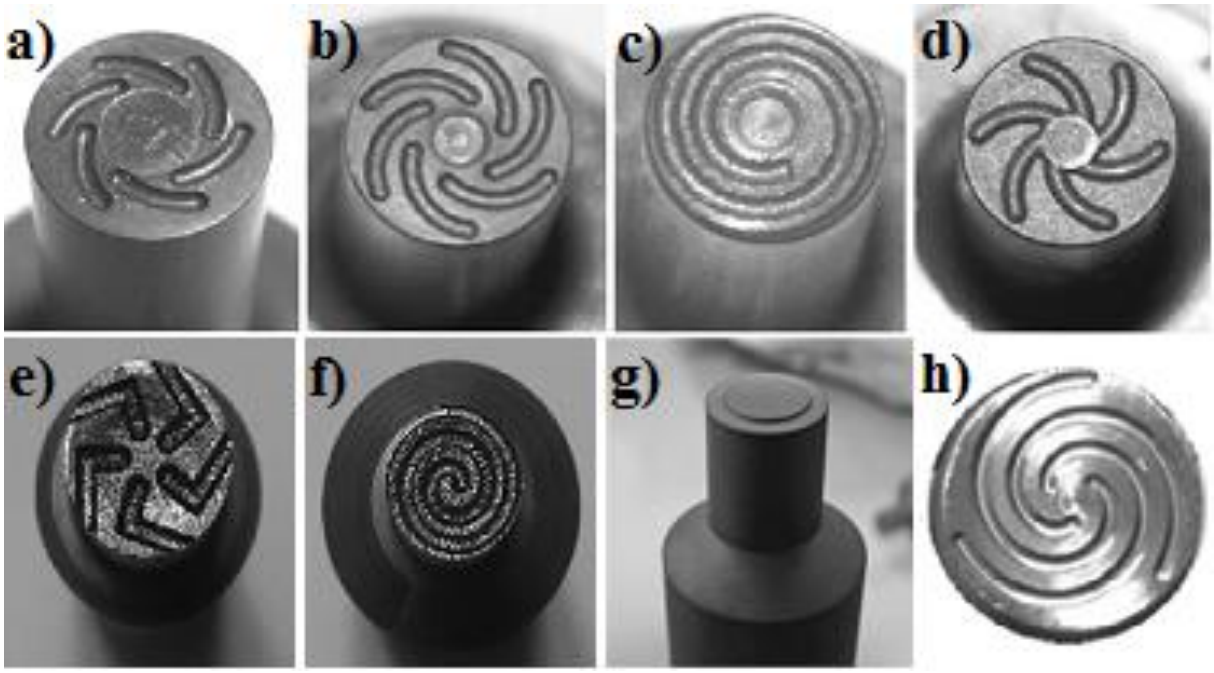

Fig. 2.7 *The different pin-less tool designs compared: (a) the short flute wiper tool* [20]*; (b) the long flute wiper tool* [20]*; (c) the fluted scroll tool* [20]*; (d) the proud wiper tool* [20]*; (e) the tool with scrolled grove* [57]*; (f) the tool with L-shaped grooves* [57]*; g) cylindric tool with projection* [59]*; h) tool with involute groves* [19]

Li *et al*. [19] used the tool shown in **Fig. 2.7h** to eliminate the hook defects caused by FSSW. Their premise was based on the innovative method of combining FSSW and subsequent friction stir welding (FSSW-FSW), as shown in **Fig. 2.8**. The results they obtained show that the HD in pin-less friction stir spot welded AA2024 joints can be eliminated by using FSSW-FSW.

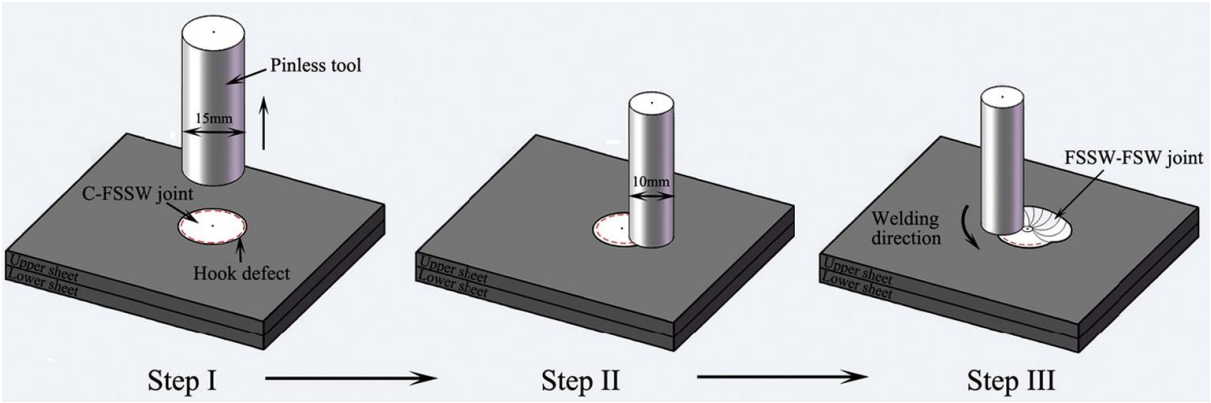

Fig. 2.8 *Scheme of the FSSW plus subsequent FSW process* [19]

2.2.2.3 Intermediate layer friction stir spot welding (IL-FSSW)

IL-FSSW is a spot-welding technique which was developed to eliminate the keyhole associated with CFSSW. The process is based on preventing the keyhole defect by using the intermediate layer (IL), rendering additional post-treatments unnecessary [63,64].

Four stages of IL-FSSW process are shown in **Fig. 2.9**. In the first step (shown in **Fig. 2.9a**) it can be seen that, with the virtue of this layer, the upper sheet is elevated. The shoulder presses the upper sheet to connect it with the IL and the lower sheet, leading to a convex protrusion that encloses the IL. The stationary shoulder clamps the sheets and prevents movement during the welding process as shown in **Fig. 2.9b**. Thereafter, the rotational tool is plunged into the upper sheet, causing frictional heat to occur at the top of the protrusion, as seen in **Fig. 2.9c**. Temperature increases and the tool continues plunging, resulting in stirring and plastic deformation of the upper and lower sheets with the IL. A flat welding spot is created at the original surface level of the upper sheet after the tool is retracted, as shown in **Fig. 2.9d**. The absence of a keyhole means there is no need for post-welding processing.

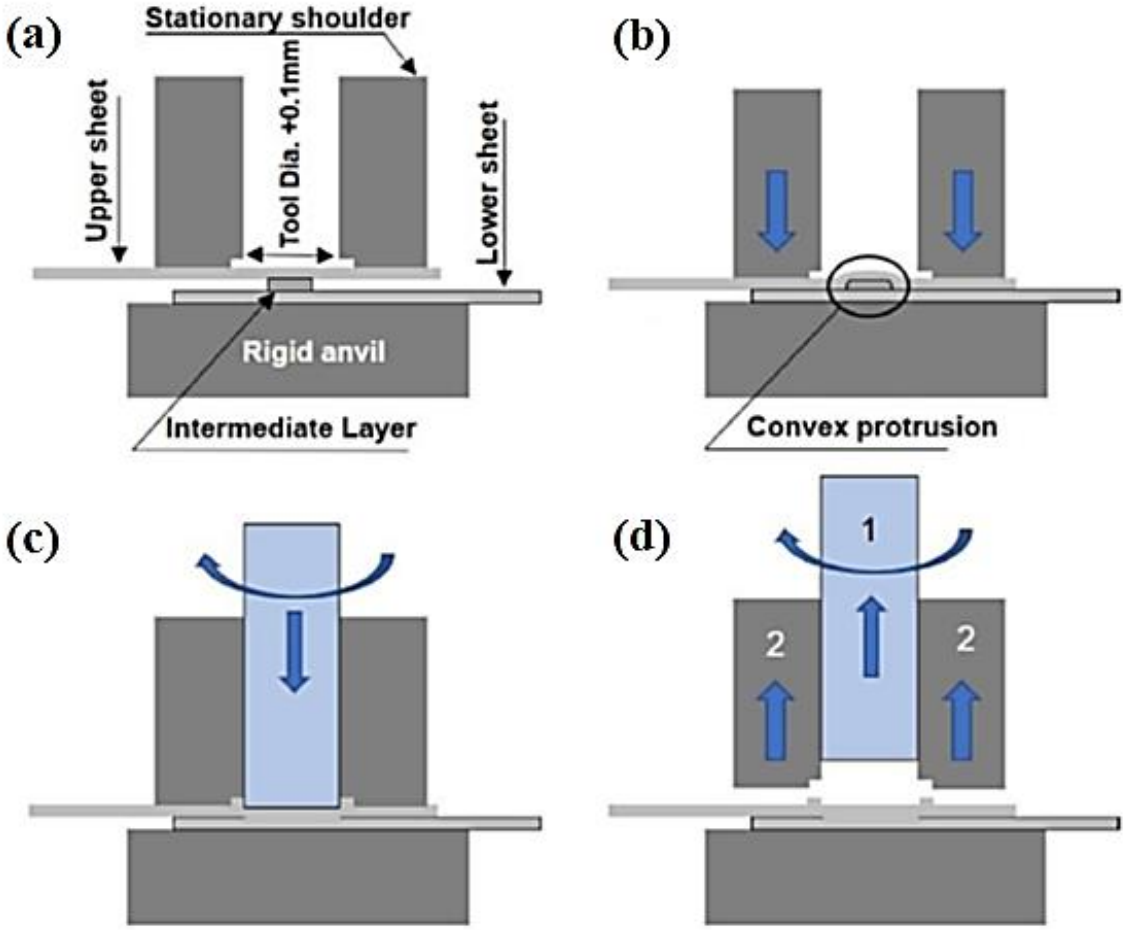

Fig. 2.9 *Scheme of the IL-FSSW process: (a) welding fixture; (b) part clamping; (c) tool plunge; (d) tool retraction* [63]

2.2.2.4 Refill friction stir spot welding (RFSSW)

Refill FSSW (also known as FSpW [65,66]) was developed and patented by the Helmholtz-Zentrum Geesthacht in Germany [67]. It was developed to eliminate or to reduce the formation of the keyhole and improve the mechanical properties of weld joints. RFSSW uses a non-consumable welding tool consisting of three parts shown in **Fig. 2.10a**: clamp, sleeve and pin [68–71]. Two separate actuators independently move the sleeve up and down. The third actuator is used for clamping the sheets.

The process consists of four stages **Fig. 2.10**:

(i) Initial rotation of the sleeve and pin; the welding head moves downwards with all the tool faces aligned. Thus, all sheets are clamped between the welding head and a backing anvil to keep them tightly secured during the process.

(ii) In this stage, both the sleeve and the pin start moving in opposite directions to each other. Two combinations of pin-sleeve moving can be performed shown in **Fig. 2.10**. The first is *Pin plunging and sleeve retraction* (**Fig. 2.10a**) [72] and second is *Sleeve plunging and pin retraction* (**Fig. 2.10b**) [65,71,73,74].

(iii) When the plunge sleeve reaches a predetermined depth, the motion of the sleeve and pin is reversed. The plunged sleeve is left rotating for a predetermined time (dwell time) in the lowest position to help increase material intermixing. The downward movement of the pin will force plasticized material from the cylindrical cavity back into the keyhole left by the sleeve and refill it.

(iv) Finally, the tool is retracted. The result is completely refilled hole with minimum material loss and a flat surface.

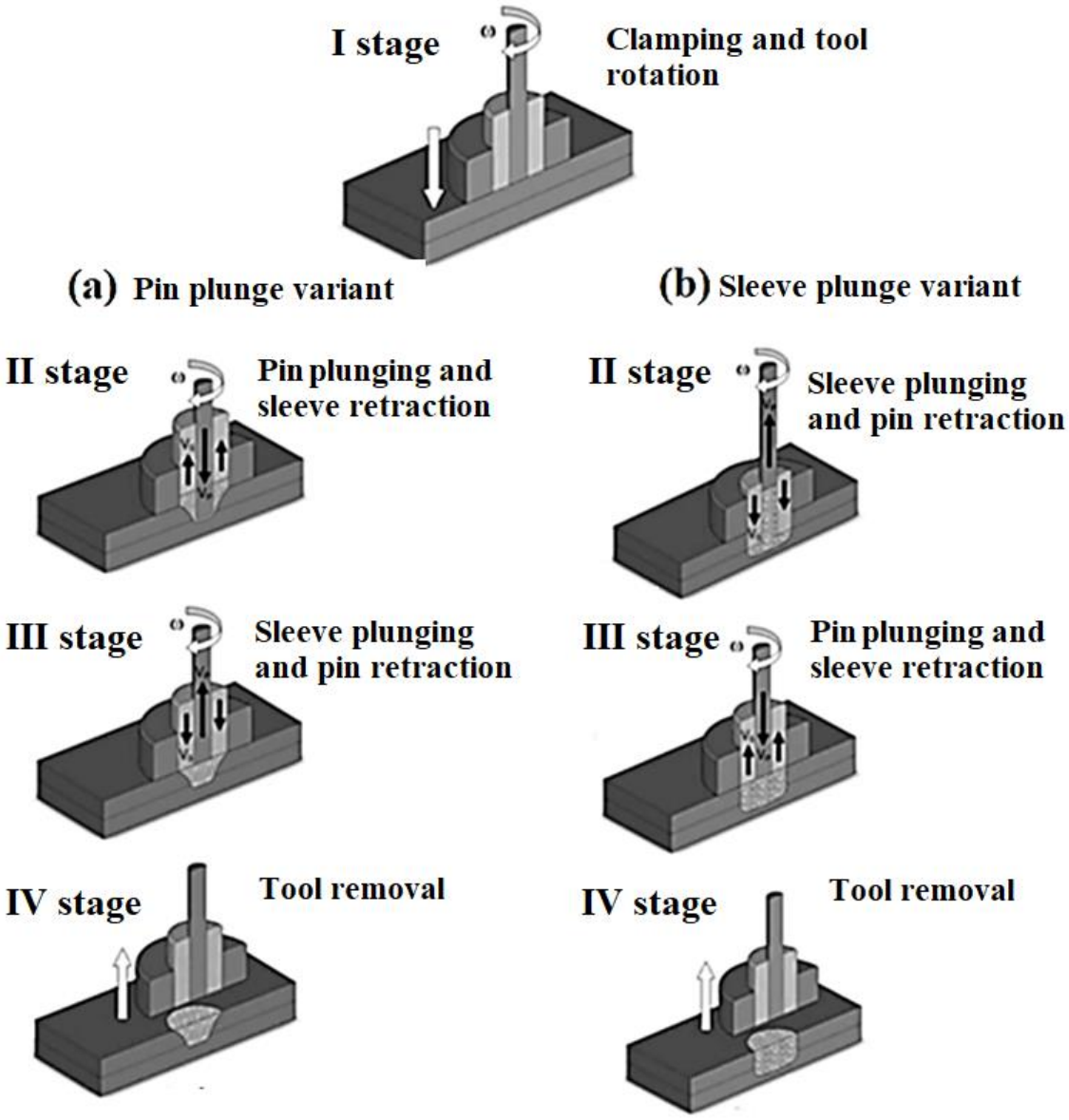

Fig. 2.10 *Schematic of the two RFSSW process variants: (a) pin plunging and sleeve retraction; (b) sleeve plunging and pin retraction* [74]

2.2.2.5 Friction stir spot welding with concave/convex tool

In FSSW, the different types of shoulders highly affect the material flow [75]. The flat tool has a simple design, but it is not effective for trapping the flowing material directly below the tool. The softened material flows upward and outward, leading to the obvious plastic deformation on the periphery of the stir zone, which results in significant heat loss. Therefore, the flat tool is impractical for the accumulation of heat and maintaining of pressure, leading to a difference in the extent of reaction at the centre and the periphery of the joint.

Xu *et al.* [41] studied FSSW of Mg-3Al-1Zn magnesium alloy with a Zn interlayer by concave and convex tools, as shown in **Fig. 2.11**. For the convex tool, the protruded part of the tool increases the plunge depth. In addition, the softened material with a high temperature below the central zone of the tool is easier to push away from the centre to the periphery of the convex tool. The convex shoulder can keep contact with a workpiece at any location along the tool Briefly, the convex tool can supply a higher welding pressure than the flat tool, thus providing better bonding conditions [41,76].

For the concave tool, the cavity could serve for escaping volume (material escape, base metal escape, the escape of some amount of the material/base metal) for the heated material and produce a compressive forging force on the stir zone. This way, the plastic deformation zone below the concave tool is more concentrated than that with a flat tool. Thus, the concave tool produces a higher temperature and pressure assisting the stirring of material. However, it leaves a complex surface morphology after welding [41,57].

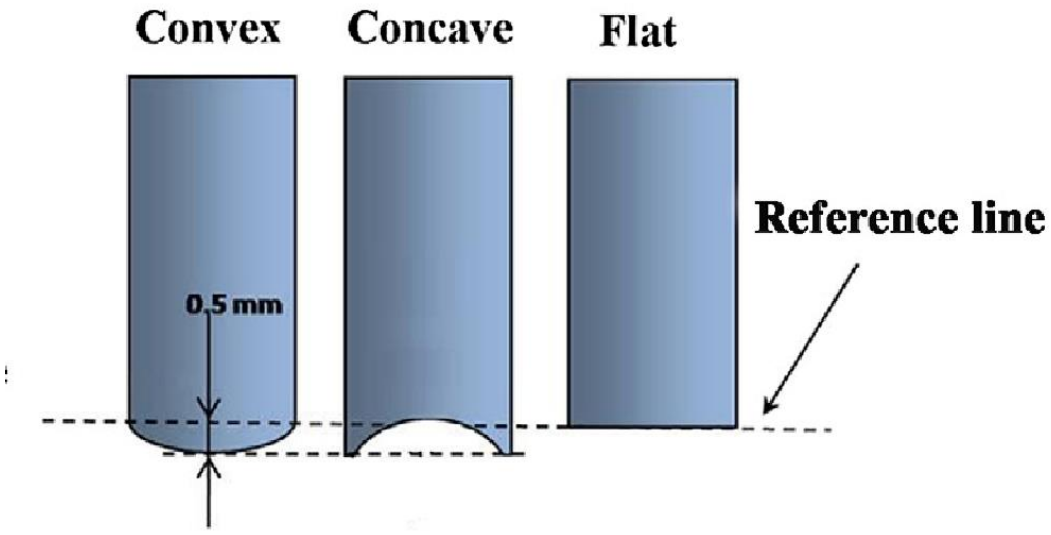

Fig. 2.11 *Schematic of FSSW with convex/concave/flat tool* [41]

2.3 Heat generation during FSSW

During FSSW, heat is generated from two sources: (i) the friction between the rotating tool and the workpiece and (ii) the plastic deformation in the region below the tool [77,78]. Most authors [79–81] claim that the largest portion of generated heat comes from the friction between the tool and workpiece. Several process variables shown in **Fig. 2.12**, such as axial load (1), rotational speed (2), the initial contact surface between the tool and workpiece and profile of the tool (3) and penetration (plunge) depth (4), can influence the heat generation. According to Su *et al.* [82], the generation of heat is mostly influenced by the rotation of the tool.

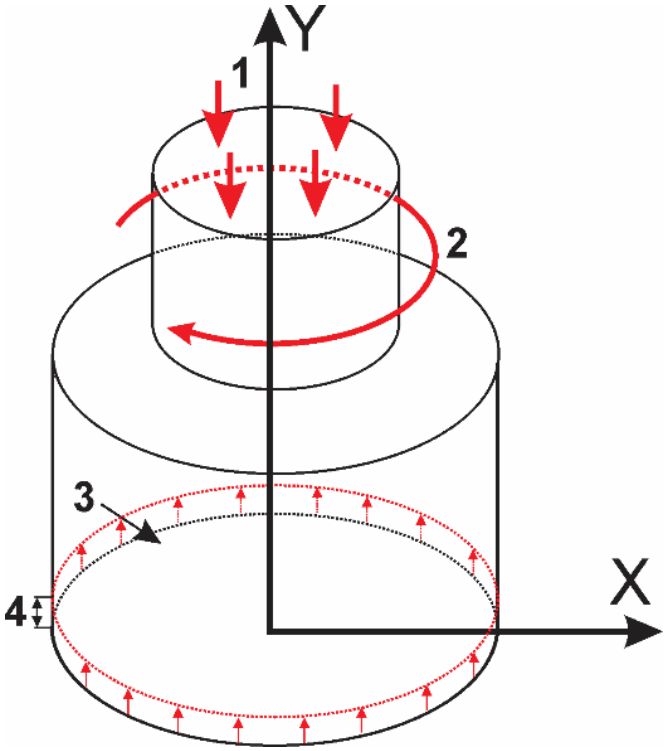

Fig. 2.12 *Schematic of FSSW process: 1-axial force; 2-rotational speed; 3- initial contact surface between the tool and workpiece; and 4 penetration depth*

One of the analytical models explaining FSSW was described by Roos *et al.* [83]. He assumed that the tool surface is built up from infinitesimal small rings with the thickness *dr*. The frictional resistance then becomes:

$$dF_r = \mu \cdot F_N \cdot dA = 2 \cdot \pi \cdot \mu \cdot p(r) \cdot r \cdot dr \quad (2.2)$$

dF_r - resistance force for element *dr* [N]
μ - coefficient of friction (CoF)
r – tool contact radius [mm]

$$p(r) = \sigma_n = \frac{F_N}{\pi \cdot R^2} \text{ - axial stress [MPa]} \quad (2.3)$$

F_N - axial load [N]
σ_n-normal stress [MPa]

$$q_0 = \dot{Q} = \int_{R_i}^{R_0} v \cdot dF_r = 2 \cdot \omega \cdot \pi \cdot \mu \cdot \sigma_n \int_{R_i}^{R_0} r^2 \cdot dr \quad (2.4)$$

ω - angular velocity [Rad/min]

Since the influence of the axial movement of the tool can be neglected, the present equation can be simplified. By neglecting the influence of the axial movement of the pin and setting R_i=0 the heat flow becomes:

$$\dot{Q} = \frac{4}{3} \cdot \pi^2 \cdot \mu \cdot \sigma_n \cdot n \cdot R^3 \quad (2.4)$$

n - rotational speed [rpm]
R -the outer radius [mm]
Kinetic coefficient of friction can be calculated in two ways [84] and [85]:

$$\mu(t) = \frac{3 \cdot T(t)}{2 \cdot F_N \cdot r(t)} \quad (2.5)$$

$$\mu(t) = \frac{\tau}{\sigma_n} = \frac{2 \cdot T(t)}{F_N(t) \cdot r(t)} \quad (2.6)$$

$$\sigma_n = \frac{F_N(t)}{r(t)^2 . \pi} \quad (2.7)$$

$$\tau = \frac{2 \cdot T(t)}{\pi \cdot r(t)^3} \quad (2.8)$$

T- torque [N·mm]
τ- shear stress [MPa]

During CFSSW, a higher amount of the energy is generated by the pin (more than 70%). The tool shoulder only comes in contact with the workpiece near the end of the process [82]. About 80 to 99% of energy during PLT-FSSW is generated from the shoulder if the friction is assumed to be the main source of heating, thus making it a more appealing process for the welding of thin sheets [20,61].

In FSSW, temperature profiles and cooling rates are directly influenced by material properties and welding parameters. The maximum temperature in the stir zone should be high enough to provide unobstructed material flow but, also low enough to prevent abnormal grain growth during dynamic recrystallization [68,86]. The generation and dissipation of the heat during the FSSW process is shown in **Fig. 2.13**. The heat energy is induced directly into the tool and the workpiece. Through heat radiation, the heat is emitted from the tool, workpiece and clamping surface. These heat conventions occur because of unequal heat conduction coefficients and different material thicknesses. Awang *et al.* [87] have shown that only a small amount of the energy generated during the FSSW process is expended for the formation of the stir zone. Su *et al.* [88] reported only 4.03% of the total energy to be involved in joint formation in Al 6061-T6 alloy. The rest of the energy was dissipated into the tool, clamping system, anvil support and workpiece.

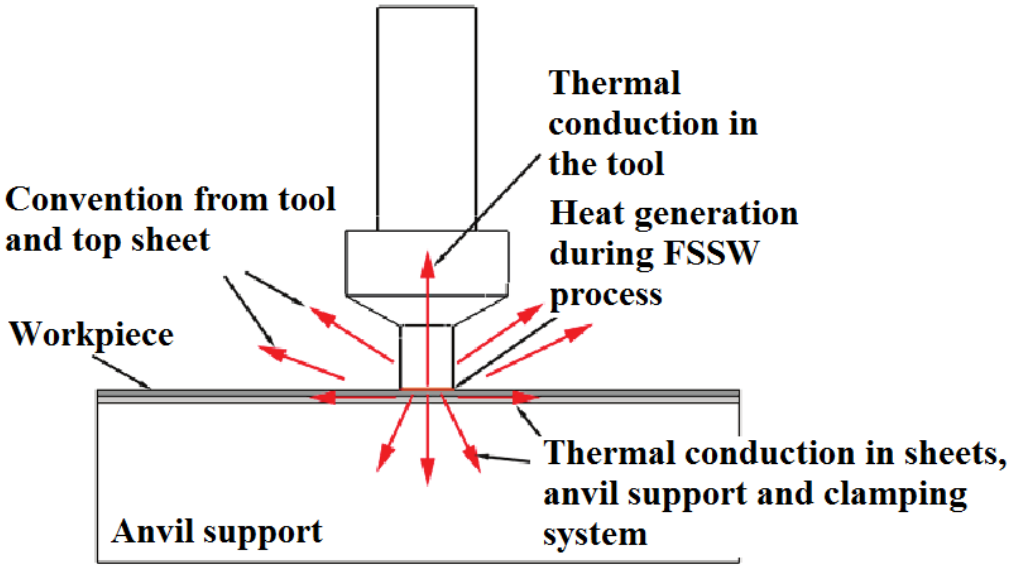

Fig. 2.13 *Generation and dissipation of the heat during the FSSW process (adapted from* [83]*)*

The cooling rate after the FSSW process plays an important role in the size of grains formed, workpiece distortions, residual stresses and precipitation formation in age hardening alloys [68,89]. The four weld features that have the most influence on cooling rate are: (i) the size of the stir zone; (ii) the mass of the workpiece and clamping system; (iii) rotational speed of the tool; (iv) material thermal conductivity.

The temperature during FSSW can be monitored by several different methods. The most popular method is with thermocouples. Lately, infrared cameras (IR) also gain popularity. They are mainly used for showing the temperature distribution of the surface of interest. The main disadvantage of the IR camera lies in establishing the emissivity of the plastically deforming metastable phase of the material, which represents a crucial parameter for precise measurement. Therefore, most authors use thermocouples in combination with an IR camera for calibration. Lanc *et al.* [90,91] explained the influence of surface roughness on the increase of the emissivity at high temperatures in Al 6082 alloy. Roos *et al.* [83] used a combination of thermocouples and an IR camera. Additional measurements with an IR camera led to an extended understanding of the temperature development during the hybrid friction diffusion bonding (HFDB) process (friction stir welding with pin-less tool).

Bakavos *et al.* [20] obtained temperature profiles of the FSSW samples with thermocouples at different welding times. **Fig. 2.14a,** the influence of welding time on the maximal temperature of Al 6111-T4 alloy is shown. The thermal profile shows a very rapid increase in temperature. In **Fig. 2.14b**, the IR image of the FSW sample can be seen. The temperature of the tool used for FSW during process was measured to evaluate how the temperature affects microstructure and whether the temperature is correlated to the properties of the welds.

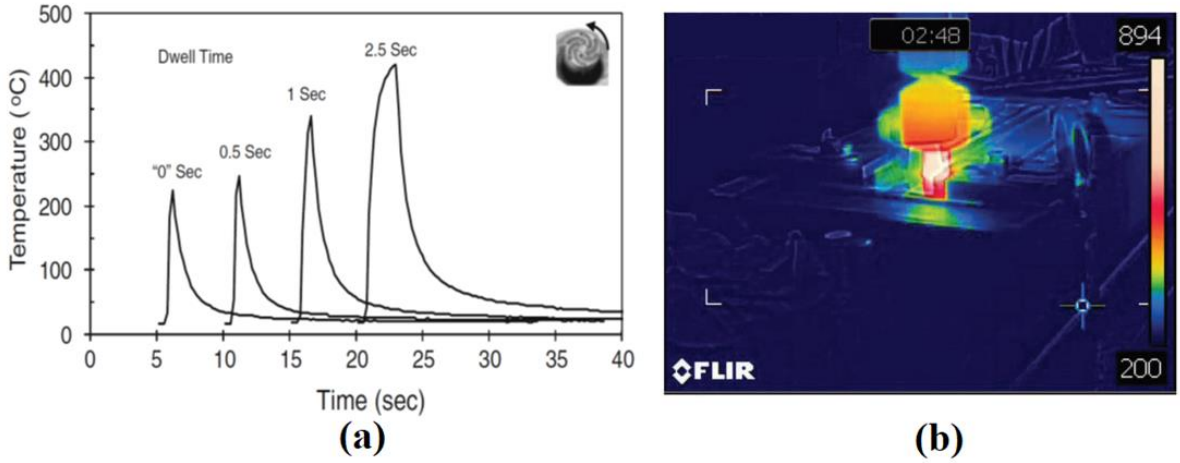

Fig. 2.14 *(a) Thermocouple measurements from the base of the weld obtained with a pin-less long flute wiper tool for different welding times* [20]*; (b) the temperature of the tool workpiece set-up during FSW (°C)* [92]

Modelling and simulations have been popular approaches for determining the temperature distribution during the FSSW process. They help gain a better understanding of temperature influence on material flow in order to optimise the tool geometry and process parameters. A number of authors have studied thermomechanical coupled models of the FSSW by using computational fluid dynamics [93–95], a meshless particle method [54] and a finite element method [78,96–98].

Jedrasiak *et al.* [98] studied a thermal-only implicit FE model of pin-less FSSW. Predicted temperature distributions during the FSSW process with flat and fluted tools are shown in **Fig. 2.15**. It shows the influence of tool geometry on temperature distribution. It should be noted that in all cases the predicted temperature at the centre was higher for the fluted tool than that of the flat tool, while a heat generation was similar or even lower. The concentration of higher temperatures in the centre reflects the relative positions of the peak in the heat input.

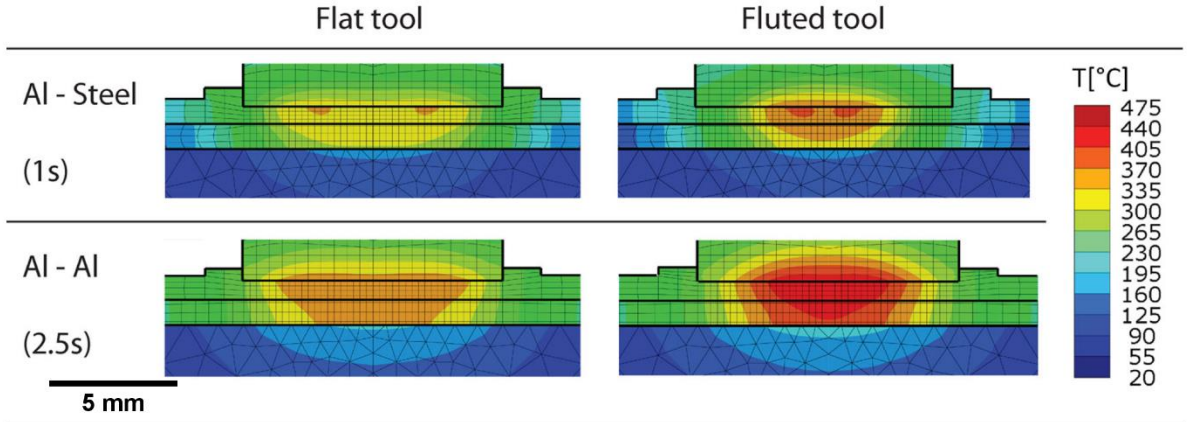

Fig. 2.15 *Predicted temperature distribution after 1 and 2.5 s dwell time at the weld plane of symmetry for Al 6111-Al 6111and Al 6111- DC04 welds, with a flat and fluted tool* [98]

2.4 Effect of welding parameters on the FSSW process

The microstructure and mechanical properties of the welds are highly dependent on the welding parameters. The tool geometry, process parameters and joint configuration influence heat generation, material flow and mechanical properties of the weld. Therefore, careful selection of welding parameters is essential in order to prevent the formation of defects such as hook defects, partial bond or voids in the FSSW welds. The defects influence the fracture mechanism and reduce mechanical properties of the welds [3,99]. The most influential parameters during FSSW are: (i) rotational speed; (ii) penetration (plunge) depth; (iii) axial load and (iv) dwell (welding) time.

2.4.1 Tool rotational speed

Tool rotational speed is the most influential parameter on material flow, heat generation and weld quality. Until now authors have obtained welds with rotational speeds ranging from 20 RPM (so-called low-temperature friction stir spot welding LT-FSSW) [100] to ultra-high rotational speeds of 30,000 RPM (so-called micro friction stir welding μFSW) [101]. Higher rotational speeds create excessive frictional heat input, high plastic flow and significant flash between the interface of welded sheets. However, when tool rotational speed is low, a higher density of dislocation is present, which causes strain hardening to occur.

Sun *el at.* [100] studied the FSSW of 6061-T6 alloy at low rotational speeds (30, 40 and 50 RPM). The result was an ultrafine grain structure with a high dislocation density and without obvious dynamic recovery and recrystallization of the stir zone. Kumar *el at.* [102] observed strain hardening in samples welded at rotational speeds ranging from 200 to 1400 RPM. However, if the rotational speed is too low below some critical value, defects including insufficient mixing, fracture modes (such as eyelet fracture patterns) and week weld strength can occur [103]. On the other hand, if the rotational speed is too high, the material below the tool softens to fast and, instead of deformation transferring to lower sheets, it flows up around the tool and the shear stress cannot be properly transferred to the lower sheets. The result is partially bonded area or no bond at all. The optimal rotational speed depends on material properties, thickness, tool geometry, axial load and plunge depth [3,37,104].

Bozzi *et al.* [104] reported that weld strength increased when the rotational speed was increased up to 1300 RPM while maintaining an constant axial load. After 1300 RPM strength starts to decrease as shown in **Fig. 2.16a**. Welds were formed from 1.2 mm thick upper sheets and 2 mm thick bottom sheets both from Al 5182-O. Bozkurt *el at.* [105] with help of the Taguchi method has studied FSSW joints AA2024-T3/AA 5754-H22 1.6 and 1.5 mm thick, respectively. Dissimilar FSSW lap joints were produced with different welding parameters. Rotational speed had the highest influence on strength (53.66%) followed by tilt angle (23.75%), tool plunge depth (12.54%) and dwell time (5.45%).

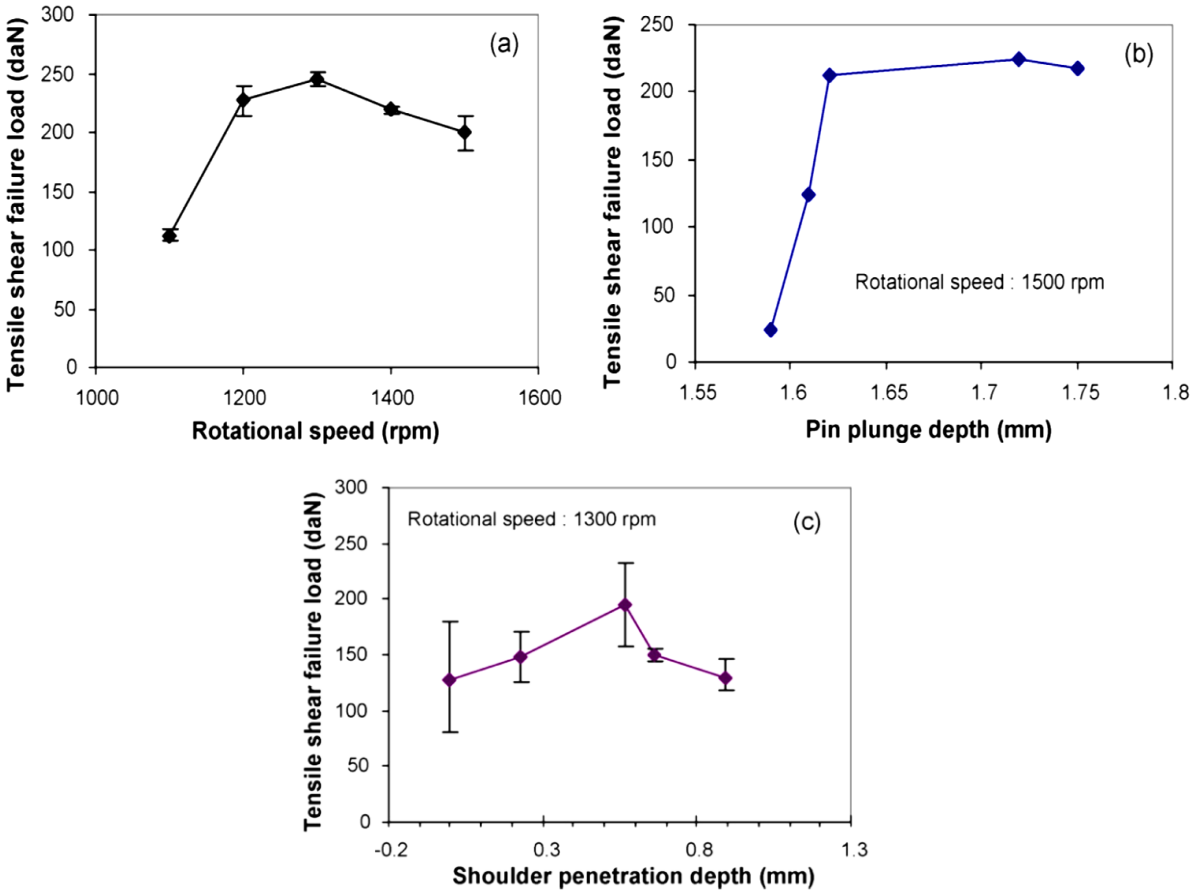

Fig. 2.16 *Influence of (a) tool rotational speed; (b) pin plunge depth; (c) shoulder penetration depth on weld strength in friction stir spot welded AA5182-O alloy* [104]

2.4.2 Penetration (plunge) depth

Penetration during FSSW depends on the thickness of the workpiece. The axial pressure on the tool increases with an increase in the penetration depth of the tool. Bozzi *et al.* [104] reported the influence of penetration depth of the pin (**Fig. 2.16b**) and shoulder (**Fig. 2.16c**) separately. Pin penetration depth was modified by using a constant pin length but with different axial loads. Shoulder penetration depth was changed by using different pin lengths but with sheets of a constant thickness. **Fig. 2.17a** shows that, with an increase of penetration depth up to a certain level (0.6 mm), strength increases as well. Choi *et al.* [59] reported the influence of penetration depth on weld strength with three different tools: (i) threaded pin tool, (ii) cylindrical flat tool and (iii) cylindrical tool with projection. Contrary to the results reported by Bozzi *et al.* [104], Choi *et al.* [59] reported a decrease in strength obtained with a tool with a pin after 1.55 mm penetration depth (**Fig. 2.17a**). Both pin-less tools achieved an increase of strength when penetration depth was increased, as shown in **Fig. 2.17b** and **c**.

According to them, the plastically deformed structure was dominant in influencing strength. During welding with a pin-less tool, penetration depth is a crucial parameter. If the penetration depth is too low, low-pressure conditions occur and cause a weakly bonded region to form.

However, in the high-pressure condition, sheets are fully bonded, which suggests that the increase in penetration depth affects the strength of the joints.

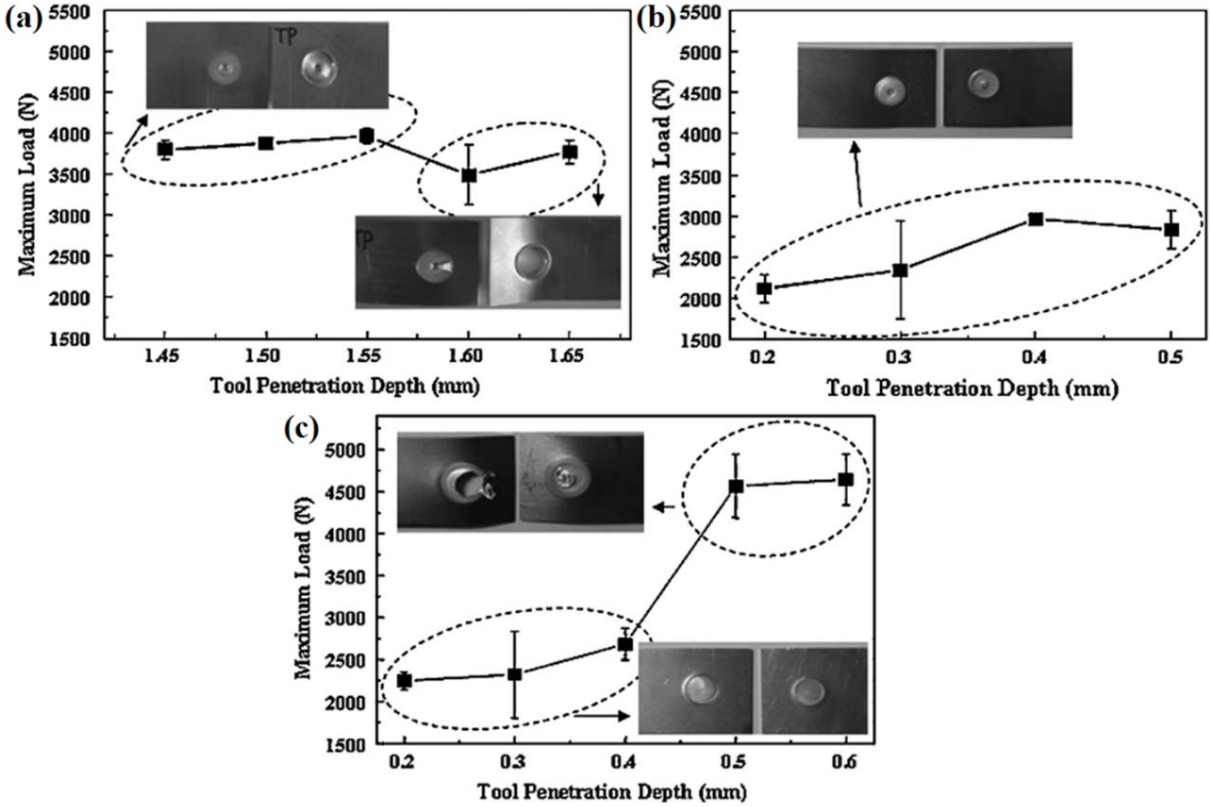

Fig. 2.17 *The influence of penetration depth and tool geometry on maximum tensile shear load: (a) threaded pin tool; (b) cylindrical flat tool; (c) cylindrical tool with projection* [59]

2.4.3 Dwell (cycle) time

Dwell time or welding time is the time that a non-consumable rotational tool spends penetrated in the workpiece before its retraction. It is one of the most important parameters that provides the energy input required for producing a strong bond between sheets. Dwell time also influences the mixing rate and material flow during FSSW and, for this reason, in the automotive industry dwell time critically influences productivity. Even though FSSW in most cases gives higher mechanical properties of aluminium joints than resistance spot welding does, FSSW is still not widely accepted in the automotive industry due to several disadvantages. The most important disadvantage of the FSSW process includes the welding (dwell) time which is relatively long (2-5 s) compared with that of RSW (0.01-0.63 s). For FSSW to compete with RSW, especially in automotive industry, reduction of dwell time (at least below 1 s) is an utmost requirement [5,50,106–108].

Depending on the type of machine used for FSSW, two different approaches for defining dwell time exist:

(i) displacement-controlled machines and
(ii) force-controlled machines.

In the case of displacement -controlled machines, dwell time can be given as an input parameter. This is also the case when a milling machine is used for FSSW. The tool penetrates until it reaches penetration depth. Afterwards, it is kept in that position for a certain time until the tool retracts. The force value cannot be pre-entered; it depends on the ratio between penetration speed and workpiece material properties.

In the case of force-controlled FSSW machines, the process is led by force and penetration depth. When penetration depth and force are set, dwell time will be defined by the time needed for a tool with certain force to penetrate to a certain depth before retracting. In this case, dwell time value cannot be pre-entered; it depends on workpiece material properties, pre-defined force and penetration depth.

Bakavos *et al.* [20] has used a position-controlled machine with a novel pin-less tool design to achieve good welds with a welding time of less than 1 s during FSSW of 0.93 mm thick 6111-T4 aluminium alloy. The optimal combination of the tool geometry and welding parameters produced welds with high mechanical properties and without or with a small number of defects while still achieving a dwell time of less than 1 s (0.3, 0.5 and 1 s).

According to Shen *et al.*[108] and Rostamiyan *et al.*[103], an increase of the dwell time increases the heat input during the FSSW process. When the dwell time is too long (usually more than few seconds), the weld strength will be drastically affected due to grain coarsening. When weld time is far below the expected value, low heat input will cause poor mixing which eventually will affect weld strength. Rosendo *et al.* [99] studied the influence of rotational speed and dwell time on the microstructure and mechanical properties of AA 6181-T4 aluminium welds obtained with RFSSW. The optimal dwell time which provided the highest mechanical properties was observed in range from 2.6 to 3 s.

2.5 Material flow in FSSW

During FSSW, the material flow is very complex, and it is dependent on the wide range of parameters such as tool geometry, process parameters and material properties. Therefore, it is necessary to understand material flow to be able to design the right tool and to choose proper welding parameters. This has motivated numerous studies of material flow during FSSW. For tracing the material flow during FSSW, different approaches have been used, such as the tracer technique by marker or a flow visualisation by FSSW of dissimilar materials. In addition, some different flow models were proposed [56,93].

The tracer technique by marker is based on using a marker material that is different from the material being welded. Yang *et al.* [109] has used copper foil as tracer material. Prior to

welding, the copper foil is placed on three different configurations: (i) on the entire top surface of the upper sheet; (ii) at the interface between the sheets from the left side (half of the weld zone is covered up) and (iii) at the entire interface between sheets.

Bakavos *et al.* [20] has used aluminium alloys with dissimilar copper content, 6xxx alloys, X-ray tomography with a sputtered gold film marker to trace material flow. Tozaki *et al.* [38] has used copper powder to track the material flow during FSSW with scroll and flat tools. It was carried out by drilling a hole 1 mm in diameter and 0.7 mm in depth in the upper sheet under the shoulder and filling the hole with copper powder. During the welding, the powder was dispersed within the material. After revealing the microstructure, the dispersed powder showed the material flow in the cross-section of the sample. However, material flow is highly influenced by the tool design. Therefore, it should not be generalised. In FSSW, the difference influenced by the tool geometry on material flow is most pronounced between tools with a pin (CFSSW) and without pin (PLT-FSSW).

During CFSSW, the material flow is divided into two sequential stages: At the first stage only, the pin penetrates the workpiece; frictional heating is far below peak one. At the second stage, the shoulder is touching the upper sheet; deformation is performed simultaneously by the shearing of both (the shoulder and the pin). **Fig. 2.18** illustrates flow of plasticized material during the CFSSW [82,109,110]. The material underneath the shoulder first moves towards the pin root (Motion 1) and then, as a result of the dragging force of threads, spirals along the pin surface downwards (Motion 2). When the material reaches under the pin it is forced upwards and outwards and then moves back towards the pin, following a helical rotational path (Motion 3). Thereafter, the process is repeated at increasing distances from the pin periphery to develop a stirred zone.

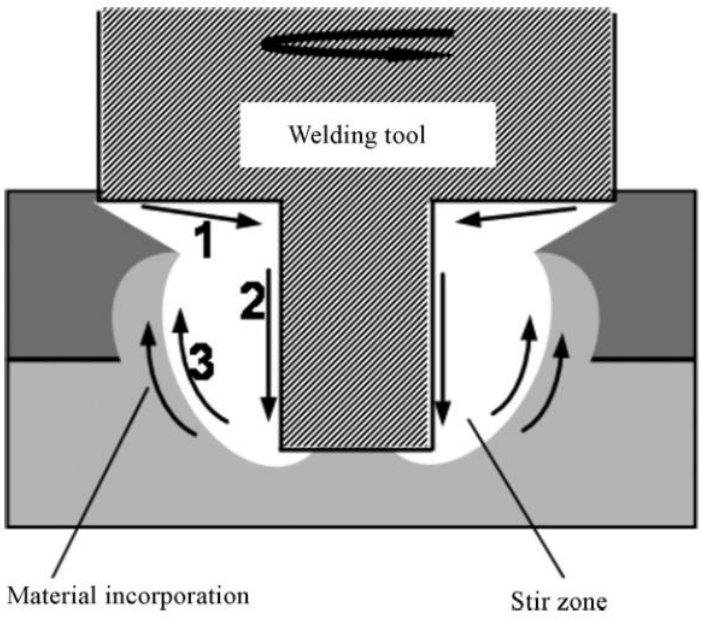

Fig. 2.18 *Schematic illustration of a model of material flow during CFSSW* [109]

To understand the material flow during the PLT-FSSW, Reilly *et al.* [56] developed a novel kinematic flow model (see **Fig. 2.19**) which successfully predicts the material flow in dissimilar aluminium alloys under a range of process conditions.

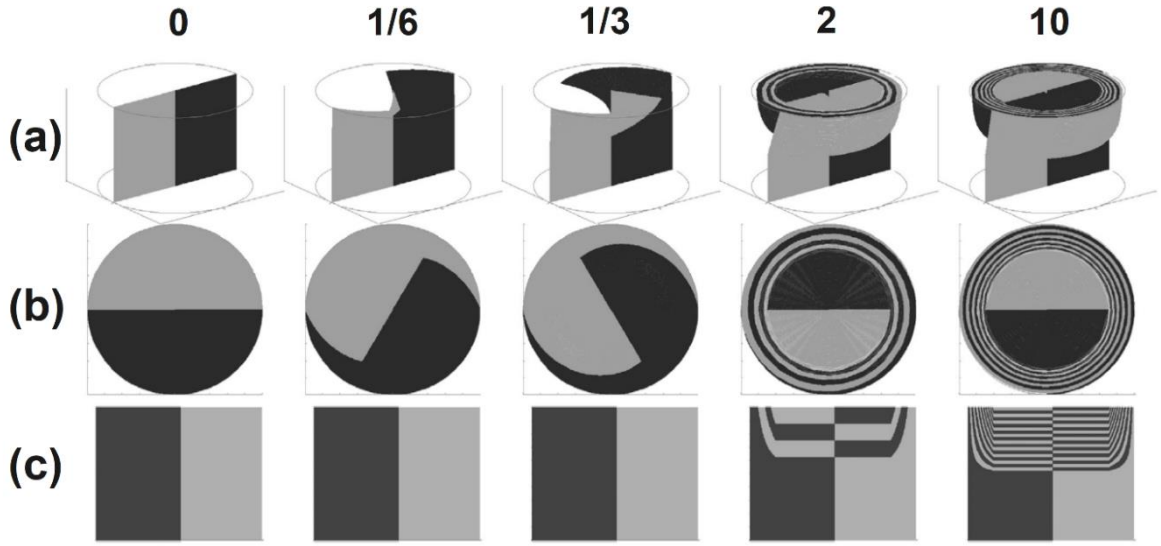

Fig. 2.19 *Kinematic model output using velocity profile 2: (a) isometric; (b) top-down; (c)section view* [56]

This model was compared with experimental observations and together they provide an interpretation of the stick-slip conditions at the tool-workpiece interface. A close inspection of this prediction model and experiments presented in the same paper indicated that, during the early stage of contact, the centripetal velocity drags the material inwards underneath the tool. This portion of material trapped between the tool and workpiece continues to be churned under the combination of axial and shear load presented by the tool. At some point, the base material under the tool becomes attached to the tool and detached from the surrounding base material. Once the FSSW process stabilizes and steady-state welding conditions are achieved, the material begins to flow.

2.6 Microstructure formation in weld joints

During FSSW, the contribution of intense plastic deformation triggered by shear stress and frictional heating within the workpiece results in microstructural changes and the formation of a few distinctive zones. Microstructural properties of the workpiece such as grain size and distribution highly influence the quality of the welds. Finer and uniform grain distribution increase the mechanical properties such as weld strength and hardness while large, coarse grains will lead to poor mechanical properties. Microstructural and mechanical properties vary significantly with tool geometry and process parameters. Thus, the microstructure of the FSSW joints tends to become coarser with increasing tool rotational speed due to more frictional heat and strain energy induced [111].

Microstructural analysis of the weld zones was performed on a light microscope (LM), Scanning Electron Microscope (SEM), Energy-Dispersive X-ray spectroscopy (EDX), Electron Backscatter Diffraction (EBSD) and Transmission Electron Microscope (TEM) to examine the size, orientation and boundaries, and intermetallic phase evolution of grains and for identification of chemical composition and fracture mode mechanism.

Based on the microstructural characterization of grains and precipitates, three different zones can be found in FSSW samples (**Fig. 2.20)**: (i) stirred zone (SZ); (ii) thermo-mechanically affected zone (TMAZ) and (iii) heat-affected zone (HAZ). The microstructural changes in different zones have a high influence on post-weld mechanical properties. Therefore, the microstructural evolution has been studied by various researchers [3,16,33,37,50,52,60,69,96,112].

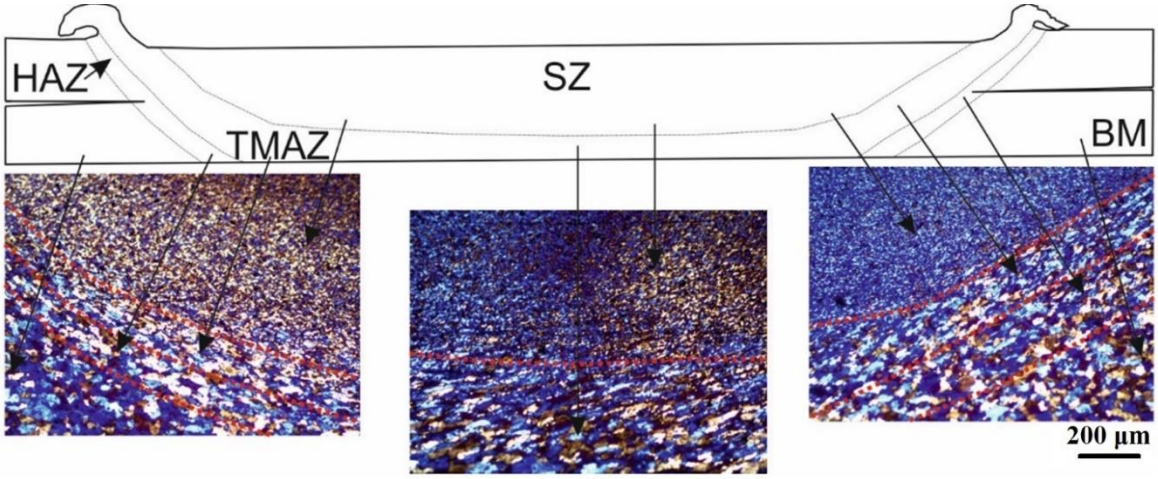

Fig. 2.20 *Schematic illustration followed by micrographs from transition zones in FSSW AA 5754 (flat tool, 2000 RPM, 4 kN) obtained with LM*

2.6.1 Stir zone (SZ)

Intense plastic deformation and heating during FSSW result in the formation of the so-called stir zone formed of dynamically recrystallized fine-grain microstructure. Inside the recrystallized grains, an increasing dislocation density compared with that of the base material was observed. Gao *et al.* [113] studied three kinds of dislocation densities in AA 6082 during FSSW with a cylindrical shaped tool with a shoulder and pin of 11 mm and 5.5 mm in diameter, respectively. The pin length was set to be 2 mm. After calculating dislocation density as a function of strain, strain rate and temperature in the material, *mobile dislocation density* did not increase very much in the stir zone as a result of its mobility under-evaluated temperature, which reminded almost unchanged, and maximum *mobile dislocation density* was 1.5×10^{12} m/m^3. However, *dislocation density in cell walls* significantly increased (around the keyhole average value reached 3.40×10^{13} m/m^3). The value of *immobile dislocation* was between those of *dislocation density in the cell wall* and *mobile dislocation density*. Therefore, a higher

density was mainly located at the interface between tool pin and stirred material, while the rest of the workpiece stayed almost unchanged, following the strain rate distribution in the material.

However, some previous research has reported small recrystallized grains in the stir zone to have a high density of sub-boundaries or subgrains. Bagheri *et al.* [27] compared CFSSW and friction stir spot vibration welding (FSSVW), with and without coolant, using Al 5083 alloy. In this study, during CFSSW and FSSVW, a high density of low angle grain boundaries (LAGBs) compared with the density of high angle grain boundaries (HAGBs) was observed. The densities in CFSSW were f_{HAGBs}=44.5% and f_{LAGBs} =37.9%. In FSSVW, the densities were f_{HAGBs}=49.3% and f_{LAGBs} =28.2%.

However, in both cases, inducting cooling produced finer grain microstructure with a lower amount of LAGBs (f_{HAGBs}=57.6% and f_{LAGBs} =24.7%), and (f_{HAGBs}=78.4% and f_{LAGBs} =14.1%) respectively, due to decreasing the temperature and impending the grain growth by the presence of coolant.

During FSSW, dynamic recrystallization results in the generation of fine and equiaxed grains in the stir zone [26,33,86,109,114]. Tool geometry, material properties of the workpiece, process temperature, rotational speed, axial load, dwell time and active cooling exert significant influence on the size of the recrystallized grains in the FSSW materials.

Andalib *et al.* [115] studied the influence of tool geometry on dynamic recrystallization phenomena in the stir zone of AA 5754 - H111 aluminium alloy. Three different shapes of tool geometry were used: (i) with a concave shoulder and a pin length 1.6 mm and 5 mm in diameter; (ii) with a flat shoulder and (iii) with a pin-less tool. In all three cases, dynamic recrystallization as a refining grain mechanism and dynamic recovery in stir zone formed highly refined and equiaxed grains. The average grain size of the AA 5754-H111 base material was 24.6 μm while the FSSW sample with a concave tool reduced a grain size up to 6.1 μm. The concave tool showed the highest reduction in grain size compared with the use of other tools.

Gerlich *et al.* [50] studied the effect of welding parameters on the strain rate and microstructure of CFSSW 2024-T351 aluminium alloy 6.3 mm thick. By varying the rotational speed from 750 to 3000 RPM, the stir zone microstructure, temperature and strain rate in the stir zone were studied. The stir zone microstructure was examined with a combination of EBSD and TEM microscopy while the strain rate during the CFSSW was calculated by incorporating measured temperatures and the average subgrain in the Zener-Hollomon equation. The average temperature and heating rate increase with increased rotational speed during CFSSW with a dwell time of 4 s, as shown in **Fig. 2.21**.

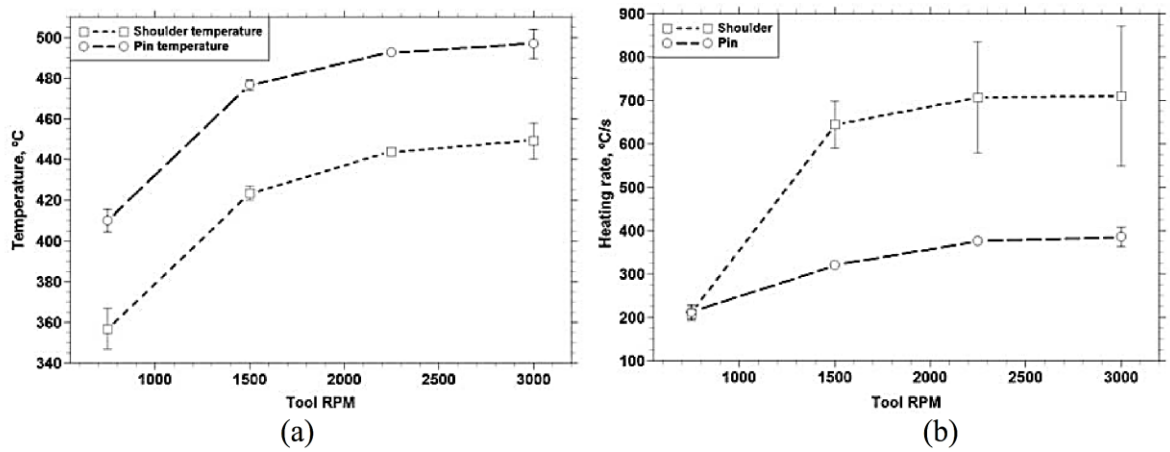

Fig. 2.21 *(a) Relationship between tool rotation speed and average temperature during CFSSW when dwell time is 4 s; (b) the heating rate during spot welding when different tool rotational speeds are applied. The error bars indicate standard deviations of temperature* [50]

Table 2.2 shows average subgrains vary from 0.57 μm for a rotational speed of 750 RPM to 1.23 μm for 3000 RPM. It was suggested that it is implausible that the fine-grade microstructure found in the Al 2024 stir zone is associated with particle stimulated nucleation since the formation and the growth of the nuclei are limited when the Zener-Hollomon parameter is in the range from 10^9 to 10^{14} s^{-1}.

Table 2.2 Average subgrain dimensions and grain boundaries misorientation statistic determined from EBSD and TEM during FSSW process [114].

RPM	EBSD average subgrains dimensions (μm)	EBSD 2º to 15º boundaries	EBSD >15º Boundaries	TEM Average subgrain dimensions (μm)
750	0.57 ± 0.02	1.6	98.4	0.62 ±0.09
1500	0.80 ± 0.06	2.2	97.8	-
2250	0.87 ± 0.09	2.8	97.2	-
3000	1.23 ± 0.21	3.1	96.9	1.57 ±0.44

During FSSW operation, validity of the calculated strain values in [50] depends significantly on the accuracy with which temperature and grain size are measured. Strain rate during FSSW of AA 5754 and Al 6061 alloys was calculated by using the Zener-Holloman parameter, Z, which is related to deformation flow stress, strain rate, and temperature and they are plotted in **Fig. 2.22a** and **b**. It can be observed that strain rate increases in both cases with an increase of rotational speed from 750 to 3000 RPM. However, during FSSW of Al 7075 and Al 2024, an opposite strain rate vs RPM relationship was found. The estimated strain rate of these spot welds decreased significantly with an increase of rotational speed from 1000 to 3000 RPM. It was suggested that spontaneous melting of second phase particles caused tool slippage to facilitate at the contact interface.

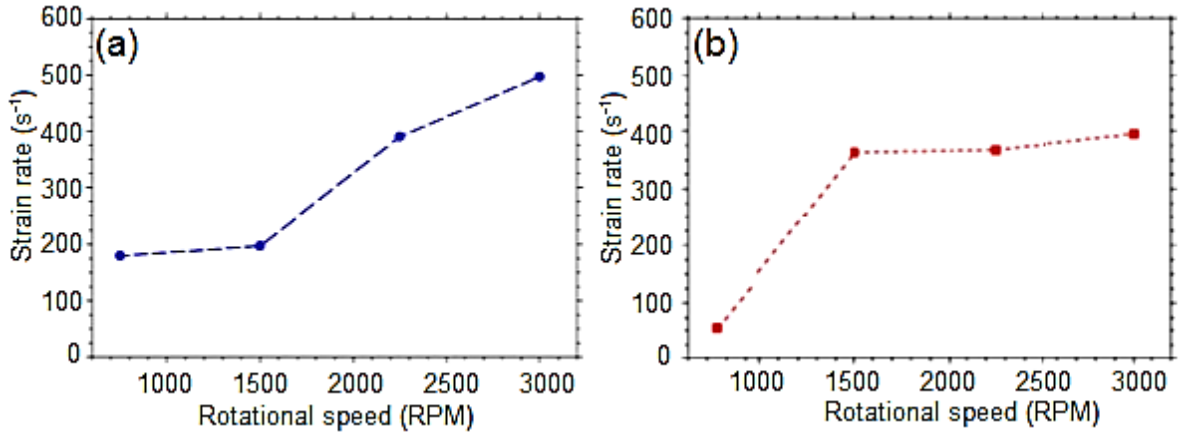

Fig. 2.22 *Relation between the calculated strain rate and the tool rotation speed in (a) AA 5754 FSSW welds and (b) Al6061 FSSW welds* [116]

Sun *et al.* [100,117] reported the formation of ultrafine grains during FSSW with no heat-affected zone in 2 mm low carbon steel plates and in 1 mm thick 6061-T6 aluminium alloy, respectively. In both papers, FSSW at low rotational speeds (up to 50 RPM) was performed, aiming to prevent hardness reduction in the HAZ. The highest measured temperatures were below 200 ^{o}C. As a result, no HAZ was detected and an ultrafine grain microstructure with a high density of dislocations formed in the stir zone with the average grain size of 500 nm for 6061 alloy and 410 nm for SPCC.

In **Fig. 2.23a** light optical micrograph of the macrostructure was shown with the marked area (red square) where the EBSD method was applied, while **Fig. 2.23b** shows the overall EBSD map of the microstructure from the BM to SZ [100]. The microstructure changes from a coarse equiaxial grain structure in the base metal to a deformed grain structure in the TMAZ and finally to a fine equiaxial grain structure in the SZ.

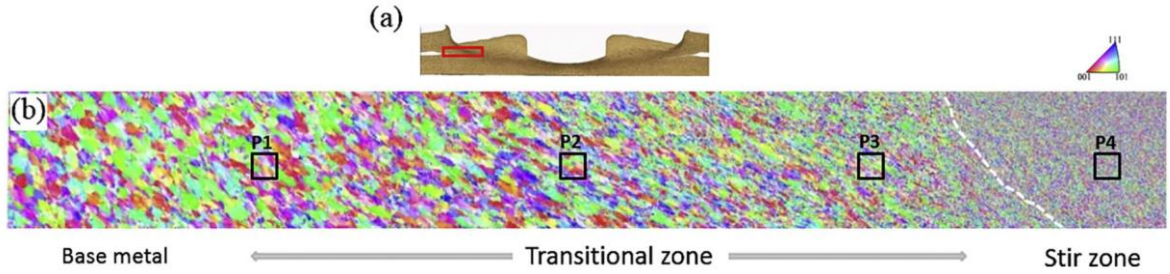

Fig. 2.23 *(a) Location in the joint for the EBSD measurement; (b) EBSD maps showing macrostructural evolution from the BM to the SZ* [100]

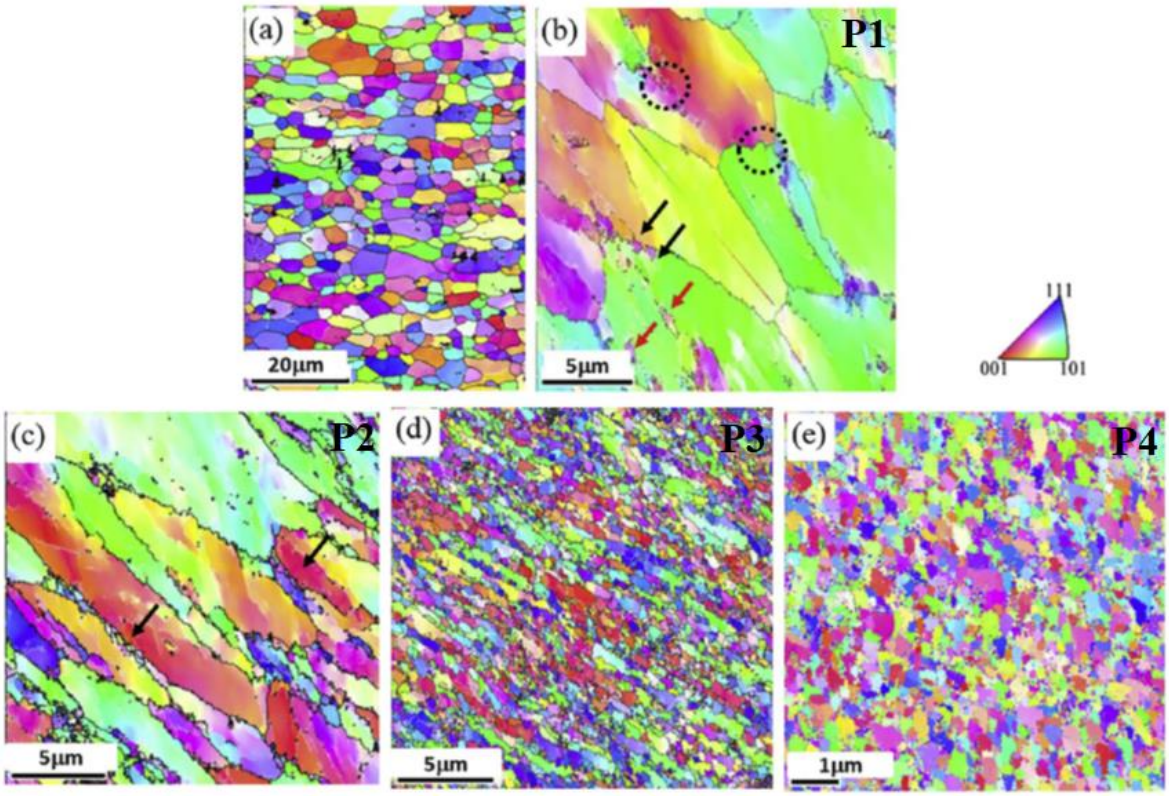

Fig. 2.24 *(a) EBSD of 6061-T6 base metal; (b-e) EBSD maps showing the microstructure of the area marked as P1 to P4 in* **Fig. 2.23** [100]

In **Fig. 2.24e,** the microstructure of stir zone had a homogeneous equiaxial grain structure with a smaller grain (480 nm) compared with that of the base material (14.7 μm) and, in **Fig. 2.24a,** elongated grains can be hardly seen anymore. It may be postulated that, due to an increase of equivalent strain, more and more dislocation cells will be transformed into a low angle grain boundary (LAGB) and finally to a high angle grain boundary (HAGB) due to the generation of more dislocation and rearrangement of the cell body structure. As a result, a high level of HAGB was observed in the stir zone. The microstructure will become finally stabile after deformation reaches a critical accumulative strain, at which the formation of new dislocation was balanced with the annihilation of the dislocation in the grain boundaries due to plastic deformation. This phenomenon occurs during the formation of ultrafine-grained materials by severe plastic deformation [100,118].

2.6.2 Thermo-mechanically affected zone (TMAZ)

Unique to the FSW process compared with conventional welding processes is a formation of a transit zone, the so-called *thermo-mechanically affected zone*. It is located between the stir zone and heat-affected zone or base material as shown earlier in **Fig. 2.20**. The TMAZ is exposed to both temperature and deformation during the FSSW process. Highly deformed structure is present in the TMAZ. The grains of the base material are deformed in an upward following

pattern around the nugget zone. Although the TMAZ undergoes plastic deformation, recrystallization does not occur due to an insufficient strain rate [16]. However, some research has confirmed that grains in the TMAZ contain a high density of sub-boundaries [16,119].

Garg and Bhattacharya *et al*. [120] have studied FSSW of AA 6061-T6 sheets with three tools with different pin geometries (circular with a plunge depth of 0.4 and 0.6 mm and square and triangular tools with a plunge depth of 0.4 mm) to characterize various zones of welds. The size of the grains in the TMAZ (7-10 μm) varied between the SZ (2.54 μm and 3.69 μm) and base material (20 μm). The microhardness of the TMAZ was found to be lower compared with that of the SZ, (81 vs. 112 HV).

Sato *et al.* [121] studied heat and deformation influence during FSW on precipitation-hardened Al 6063-T4 and T5 alloys. 6063-T4 alloy contained a high density of fine *needle-shaped precipitates* and a low density of *rod-shaped β′ precipitates* but, during the stirring, all precipitates dissolved in the SZ due to a high temperature and strain rate. However, in the TMAZ, a low density of needle-shaped precipitates and a high density of rod-shaped β′ precipitates were found. The density of the needle-shaped precipitates decreases from the base material region toward the SZ. Due to that phenomenon, the hardness is expected to be higher in the TMAZ depending on the density of precipitates around the SZ.

Sun *et al.* [100] observed that the TMAZ has bigger grains in the area near to the base material (**Fig. 2.24b**) in comparison with an area near to stir zone (**Fig. 2.24d)**. The area near base material experienced a lower strain rate. The grains are elongated with the aspect ratio 2-3 in the material flow direction. So, in this region, only a few small grains with a HAGB will be formed within the grains as shown by the arrows in **Fig. 2.24b** and **c**. In the region shown in **Fig. 2.24c**, plastic deformation is higher and accumulative strain becomes higher. The arrows point to small equiaxial grains with HAGBs distributed along the original grain boundary. The closest region to the stir zone experiences more plastic deformation. Grains in this region are still elongated but with decreased size. The final result is the formation of the equiaxial grain structure due to the fragmentation of the original grains. This shows that the TMAZ is a transition zone which has no uniform structure and mechanical properties.

2.6.3 The heat-affected zone (HAZ)

Beyond the TMAZ, a heat-affected zone can be found. This zone does not undergo any plastic deformation but experiences a heating cycle. The heat generation affects weld performance, influencing the material flow and improving stirring of material during the process. However, when the heat input goes beyond the critical value, it decreases the quality of the weld. Heating during the FSSW is triggered by the deformation process of material and by friction between the tool and workpiece. During that process, the temperature rises, creating a precipitate dissolution in the matrix and causing coarser strengthening precipitates than those in the base material. The most influential welding parameters on heat generation during the FSSW are tool rotational speed and dwell time. If the rotational speed and dwell time are not too high, grain

growth can be negligible. Also, the precipitates become finer and uniformly distributed [3,69,103,111].

Su *et al.* [122] defined the HAZ as a zone experiencing temperatures above 250 ^{o}C for heat treatable aluminium alloys. In **Fig. 2.25,** the FSW can be seen to have little effect on grain structure in the HAZ. However, thermal exposure above 250 ^{o}C exerts significant effect on the precipitate structure.

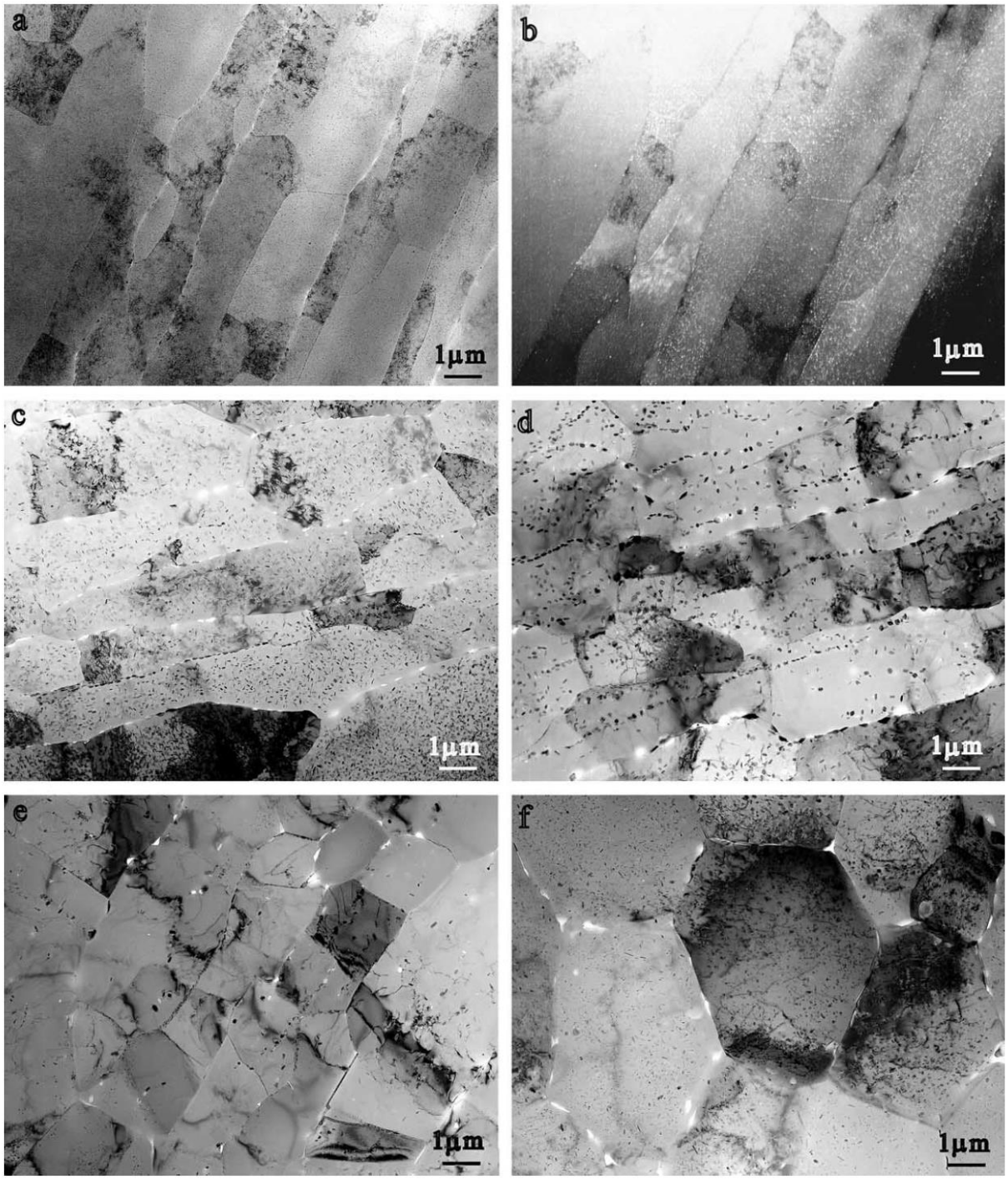

Fig. 2.25 *TEM images of grain structure in different weld regions: (a) base material; (b) dark-field image base material; (c) HAZ, (d) TMAZ I; (e) TMAZ II; (f) SZ* [122]

2.7 Mechanical properties

Due to the significant microstructural variation within and around the SZ, TMAZ and HAZ, FSSW shows huge variations in the mechanical properties of welds.

The difference in mechanical properties of aluminium welds obtained with the FSSW are triggered by following mechanisms in the welded zone:

(i) grain size reduction
(ii) re-precipitation accompanied by ageing
(iii) strain hardening.

In the following sections, strength, hardness and fatigue are briefly reviewed as the most important and influential mechanical properties.

2.7.1 Tensile shear strength of the FSSW joints

The strength of the FSSW weld joints mostly depends on process parameters and the defects that may occur inside the welds. To obtain suitable strength from the FSSW joined samples, a tensile shear test or a cross tension test are usually used. Numerous studies have reported the influence of welding parameters on lap-shear loads, such as tool geometry [57], rotational speed [123], penetration depth [115], axial load [100], dwell time [20] and cooling rate [27].

In CFSSW processes, the presence of a keyhole is a limiting factor in achieving high strength. Yazdi *et al.* [57] proposed using a pin-less tool to improve joint strength. For the lap FSSW of 2 mm tick Al 6061-T6 sheets, two tools with pin lengths 2 and 3 mm and two pin-less tools with a scroll groove (**Fig. 2.7e**) and L-shaped grooves (**Fig. 2.7f**) were used. From **Fig. 2.26**, it can be seen that the tensile strength of the welds obtained with a tool having a 3 mm long pin was about three times larger in comparison to the weld obtained with a 2 mm long pin. This difference was the result of the higher penetration depth in welds produced with a longer tool pin, which caused a higher volume of displaced metal and bigger stir zone. Both keyhole-less welds were stronger due to a larger effective cross-section area and the absence of a keyhole. The slightly higher strength in welds obtained with an L-shaped pin-less tool compared with that of a pin-less tool with a scroll groove was the result of the larger stir zone and more severe stirring caused by the grooves with sharp corners.

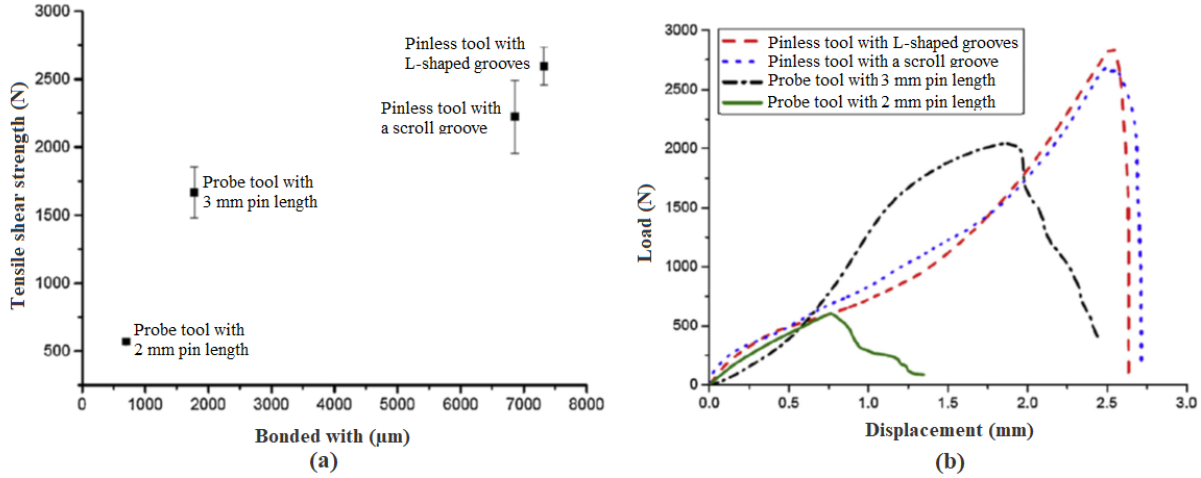

Fig. 2.26 *The influence of tool geometry at tensile shear strength* [57]

In **Fig. 2.27**, the maximum and minimum peak load reported by different authors were compared for different types of FSSW. Results in this comparison indicate that PLT-FSSW provides highest shear tensile strength followed by the RFSSW and FFSSW. The lowest strength was obtained from CFSSW.

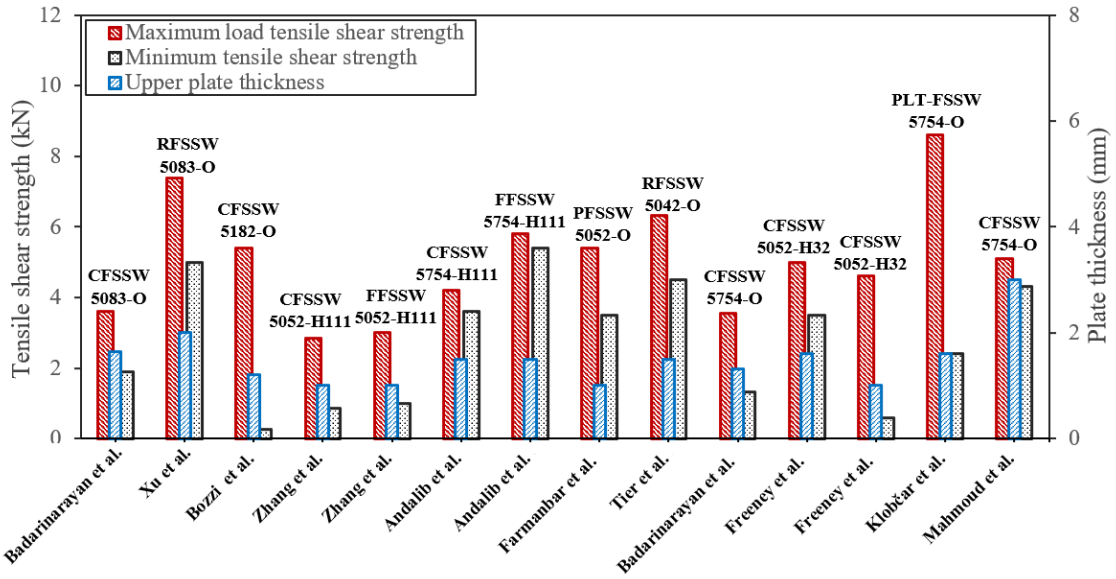

Fig. 2.27 *Comparative plots of maximum and minimum failure load of welding samples by different types of FSSW and different aluminium alloys from 5xxx series* [18,70,129,104,111,115,124–128]

Rotational speed is one of the welding parameters that influences the mechanical properties of the weld the most. Li *et al.* [123] studied the impact of rotational speed on mechanical properties and microstructural evolution during the RFSSW of 2A12-T4 aluminium alloy. It was observed that the tensile-shear properties of RFSSW welds depend on hook geometry, distribution of the bonding ligament and hardness in the stir zone. With an increase of the rotational speed from 900 to 1300 RPM, the tensile shear failure load (TSFL) increases from 7.95 kN to the maximum value of 10.03 kN and then decreases again to 9.3 kN for the rotational

speed of 1700 RPM. In samples welded with higher rotational speeds of 1300 RPM, formation of liquation cracks during the subsequent cooling process was found, which resulted in the decreasing of the TSFL. An increase of the rotational speed up to 1300 RPM causes hook height to increase. Consequently, the bonding ligament is more dispersed at the weld periphery and the hardness of the stir zone decreases.

Sun *et al.* [100] studied the influence of low rotational speeds (from 30 to 50 RPM) and different axial loads (from 3.5 to 8 t) with a flat tool and a tool with a pin with length of 1 mm on shear tensile load. Shear tensile load significantly varied depending on the parameters. In all samples, higher strength was obtained by using a higher applied load or rotational speed. The maximal shear tensile strength of the friction spot welds obtained with a flat tool reached about 5.4 kN, while by using a tool with a pin, the highest obtained shear tensile strength reached 4.5 kN. When rotational speed drops, shear strength also drops. This is especially evident in samples welded with 30 RPM where the shear strength was between 1 and 1.5 kN depending on axial load used. The samples welded with a flat tool and tool with a pin showed the same trend when it comes to influencing of the axial load on shear tensile strength. In all samples with increasing of the axial load the shear tensile strength increases as well.

Sun *et al.* [117] compared shear tensile load obtained in samples welded with LT-FSSW at 5, 10 and 20 RPM with the load of samples welded with CFSSW at 800, 1000 and 1200 RPM, as shown in **Fig. 2.28**. The tensile shear strength varied under different rotational speeds. Higher rotational speed provided higher tensile shear strength. When using a flat tool, the maximum shear loads of the welds reached 10, 8 and 5.5 kN for rotational speeds 20, 10 and 5 RPM, respectively, while the maximum shear loads of the CFSSW samples were 3.74, 4.62 and 6.95 kN for 1200, 1000 and 800 RPM, respectively.

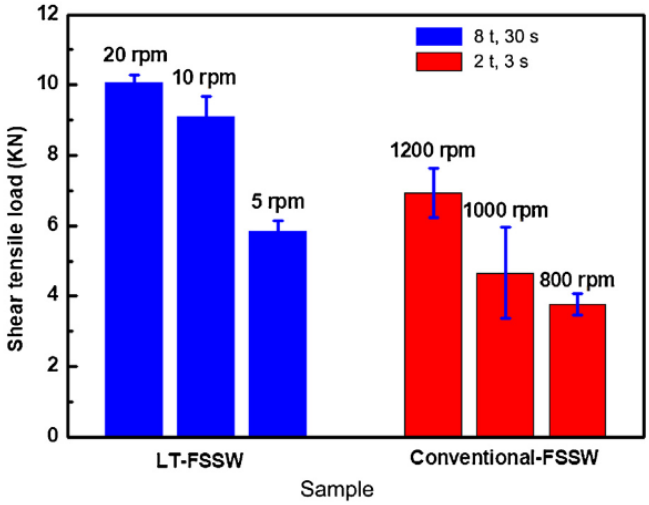

Fig. 2.28 *Shear tensile load of LT-FSSW samples and CFSSW samples welded at different rotational speeds* [117]

Bageri *et al.* [27] compared tensile shear strength of the samples welded by CFSSW and Friction stir spot vibration welding (FSSVW) with and without coolant. Shear strength of the FSSVW samples was higher than the strength of CFSSW samples and the presence of coolant

during both welding processes (FSSVW and CFSSW) increased strength. For the CFSSW and the FSSVW samples, shear tensile strength was approximately 2.25 kN and 2.7 kN respectively. With the same welding conditions but with the use of coolant tensile, strength was about 3.2 kN and 3.5 kN for CFSSW and FSSVW, respectively. That can be correlated with the effect of grain size. The FSSVW samples in stir zone obtained an average grain size of 27 μm, while in samples welded with the CFSSW the average grain size was 39 μm. However, FSSVW and CFSSW with coolant produced welds with the average grain size 9 and 15 μm, respectively, which is 64% smaller than in samples welded with the same conditions without coolant. With the drop of the grain size, the volume content of grain boundaries increases. The grain boundaries represent obstacles to the movement of dislocation and increase weld strength [130].

Andalib *et al.* [115] studied the effect of plunge depth on joint strength. For studying the influence of penetration depth, rotational speed and plunge rates were set to be 750 RPM and 20 mm/min, respectively, for both processes (CFSSW and FSSW with pin-less tool). The strength of the CFSSW sample was found to be interlinked with the sheet thickness. Increasing the penetration depth to a certain level improves the stirring process and material flow. However, higher penetration depth affects joint strength due to sheet thinning under the tool shoulder. This waydeeper keyhole is created, which causesstress concentration around the weld keyhole. In the case of FSSW with a pin-less tool, penetration depth was higher compared with that of CFSSW due to a cavity on the backplate. Also, shear strength of the samples welded with a pin-less tool (average shear strength was 5.1 kN for a pin-less tool with concave shoulder and 4.1 kN for a pin-less tool with flat shoulder) was higher than that of CFSSW samples (average 3.8 kN). A penetration depth to sheet thickness ratio ranges from 1.95 to 2 provides the highest shear strength. Beyond these values, shear strength significantly drops by about 45 %.

Li *et al.* [19] studied the influence of dwell time on failure load during the tensile shear test. From **Fig. 2.29**, it can be seen that the strength of the weld increases from 1.5 kN for samples welded with a dwell time of 6 s up to 6.5 kN for samples welded with a dwell time of 12 s or more. Value of the failure load is steady after 12 s. Dwell time can be seen to have a significant effect on the failure load up to some point (when dwell time reaches 12 s). No effect on failure load above dwell time of 12 s can be expected.

Welding parameters influence heat input of the FSSW welds, and this affects the weldability, structure and performance of the weld joints. In most cases, hook defects play a significant role in strength reduction of FSSW joints.

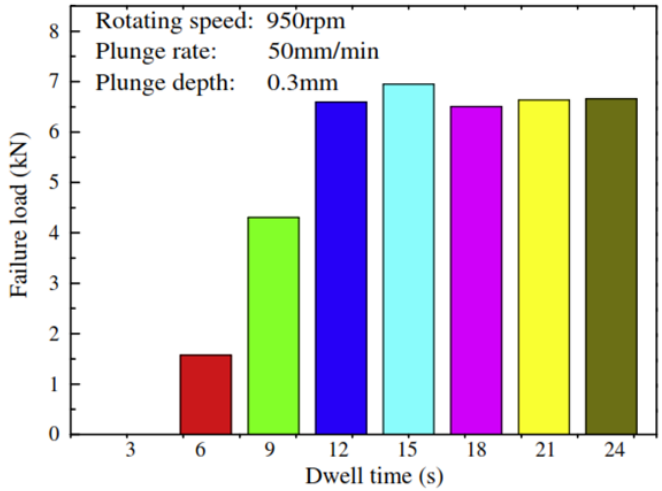

Fig. 2.29 *Effect of dwell time on the tensile-shear load of CFSSW joints [17]*

.

2.7.2 Microhardness of FSSW joints

The microhardness values in welds of aluminium alloys obtained with FSSW are affected by the disparity in grain size and strengthening precipitates. According to the Hall-Petch equation (2.1) hardness is dependent on grain size in the same way as strength. In non-heat treatable aluminium alloys, higher hardness in the stir zone compared with that of the base material can be observed due to a low thermal cycle, reduced grain size and high deformation level which causes strain hardening [27,104]. However, in some heat-treatable alloys due to a high frictional thermal cycle and shear stress caused by deformation, coarsening of the grains and precipitates can occur. The frictional heating induces grain growth, producing coarser grains and causing lower dislocation density in the HAZ. Thus, the hardness of the weld will be lower in comparison to the base material [3,111,125].

Different microstructural evolution over the cross-section of the FSSW sample leads to inhomogeneous mechanical properties inside of the welds. Because of that, microhardness is usually measured over the cross-section in order to follow the change of mechanical properties inside of workpiece from the base material to the stir zone. Microhardness of FSSW samples is measured using the Vickers hardness test. Considering that the hardness values in the weld zone (SZ, TMAZ and HAZ) of aluminium alloys are fundamentally affected by the disparity in grain size and precipitation mechanisms, it is required that tested area always covers all associated weld zones, including the base metal, and to be symmetric to the tool axis or the weld centre. Several different hardness profiles can be obtained in the FSSW depending on the welding parameters, tool geometry and processed material. Depending on geometry of the tool, two different types of profiles can be obtained. These can be seen in **Fig. 2.30a** (CFSSW samples) [103,111,123,131,132] and in **Fig. 2.30b** (FSSW with flat tool samples) [27,99,100,108,120,125,133].

In **Fig. 2.30a,** microhardness profile of the FSSW of AA 5182-O aluminum alloy was obtained in order to understand the relationship between microstructural evolution and local mechanical

properties. Indentations were performed with a load of 50 gf (0.49 N) and the space between indentations of 0.25 mm along the line. The microhardness increases significantly approaching the keyhole left by the tool pin. The microhardness increases as grain size drops. However, in **Fig. 2.30b,** the hardness in the stir zone in alloy 2A12-T4 FSSW dropped with the flat tool. The microhardness profiles are either U-shaped or W-shaped, depending on the rotational speed. W-shaped microhardness profile is discerned in samples welded with lower rotational speeds (900, 1100 and 1300 RPM), i.e. microhardness drops significantly in the TMAZ and then rises in the SZ, although it is lower than in the base material. In samples welded with 1500 and 1700 RPM, the microhardness only recovers slightly within the SZ after reaching the minimum in the TMAZ, indicating the formation of the U-shaped microhardness profile. This thermal softening effect in the weld zone of heat-treatable aluminium alloys is related to the dissolution and coarsening of the strengthening precipitates [98,119,134].

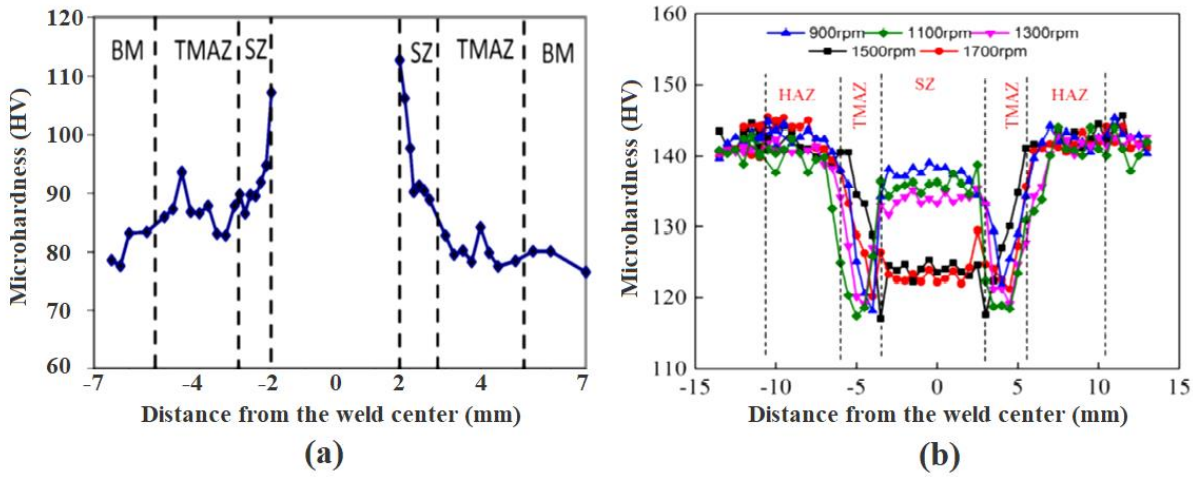

Fig. 2.30 *Microhardness profiles from base material to stir zone for: (a) CFSSW of AA 5182-O aluminium alloy [99]; (b) FSS welds welded with flat tool of 2A12-T4 alloy welded with different rotational speeds* [123]

Bakavos *et al.* [20] studied microhardness variations in heat-treatable AA 6111-T4 aluminium alloy. **Fig. 2.31** shows microhardness profiles measured in the top sheet, 0.2 mm below the shoulder for the welds produced with the long flute wiper tool, for different dwell times. In **Fig. 2.31a** and **b** hardness measurements immediately after welding (within 1 hour) and after natural ageing after 3 months were compared, respectively.

After welding (**Fig. 2.31a**), microhardness reaches 60-80 HV in the SZ, TMAZ and HAZ, compared with 80 HV for the base material. The microhardness profile for a longer dwell time of 2.5 s is W-shaped with lower microhardness values inside of the TMAZ. However, the samples welded with the shortest 0.5 s dwell time have U-shaped microhardness profiles. It is suggested that softening is caused by the dissolution of solute clusters and the fine β" phase present in the T4. However, in **Fig. 2.31b**, it can be seen that after three months of natural ageing the weld zone was found to be harder than the base material by ~15 HV and harder than the weld zone before natural ageing by ~31 HV.

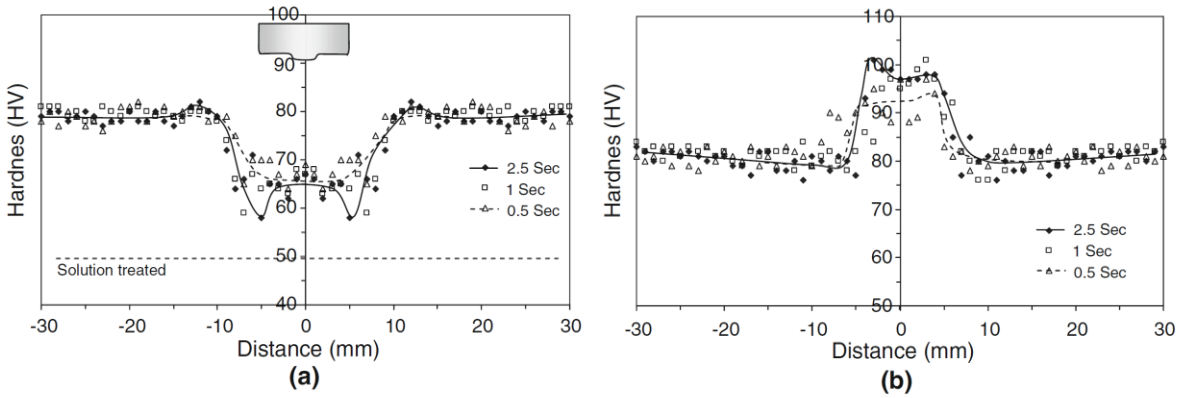

Fig. 2.31 *Microhardness profile of AA 6111-T4 FSSW samples obtained: (a) immediately after welding and (b) after natural ageing of 3 months* [20]

Although hardness is often observed to be recoverable by natural ageing in friction stir welds, in this case microhardness has increased by ~15 HV compared with the those of the base material, which is more than the natural ageing response of base material. This can be attributed to the high level of deformation which results in a grain size of only 2-5 μm in the stir zone.

Microhardness variation in the welds during the FSSW can also be presented with microhardness maps as shown in **Fig. 2.32** [27,135]. Microhardness maps give a better insight into the entire welding cross-section when compared with insight gained from the microhardness profiles, which describe microhardness only in one line.

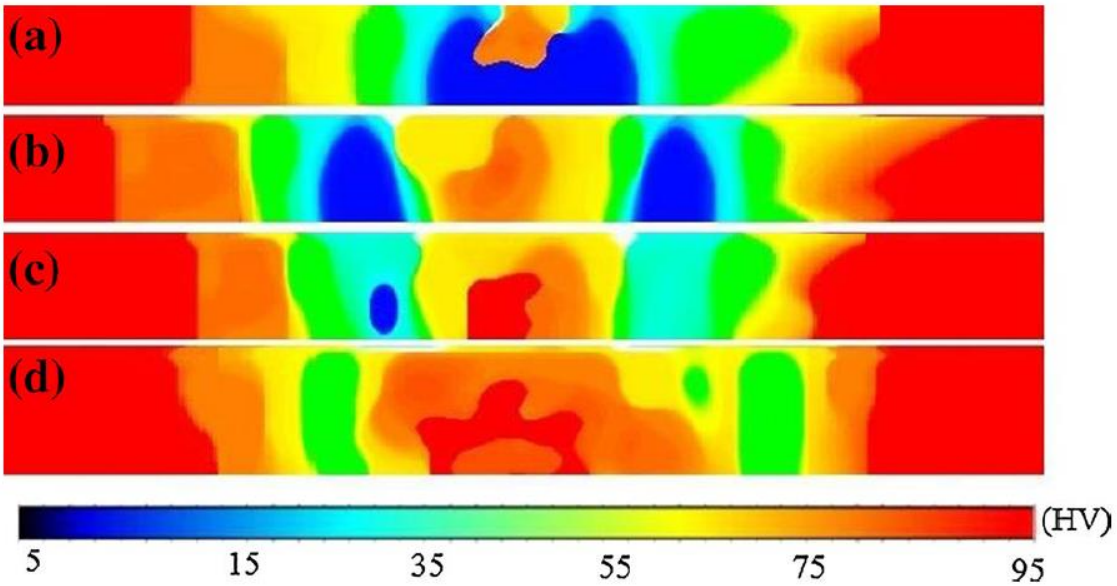

Fig. 2.32 *Weld cross-section hardness maps of the samples: (a) FSSW; (b) FSSVW; (c) FSSW+coolant; (d) FSSVW+coolant* [27]

2.7.3 Fatigue properties of FSSW joints

Fatigue properties are critical for many applications such as transport vehicles, aerospace structures, platforms, etc. Therefore, due to a potentially wide range of engineering applications of the FSSW technique, it is important to understand fatigue characteristics [16].

Fatigue failure is frequently seen in many engineering components. Even though most FSSW workpieces are subjected to uni-axial loads, multi-axial states are often present at the critical area around the welded zone. This is due to the nature of FSSW joints. Researchers propose different methods to predict the real-life services of mechanical components with uni-axial and multi-axial states. Consequently, many well-known critical plane fatigue criteria have been employed to predict the fatigue life of welded structures. Multi-axial fatigue theories can be categorized into: (i) stress; (ii) strain and (iii) energy-based approaches [3,39,136–139].

Lin *et al.* [107], Uematsu *et al.* [72], Tran *et al.* [140] and Su *et al.* [141] developed fatigue crack growth models to estimate the fatigue life of the FSSW samples of AA 6111-T4, AA 6061-T4, AA 5754-O and alclad 2024-T3 aluminium alloys, respectively.

Lin *et al.* [107] studied failure modes in welds produced by FSSW in lap-shear 0.94 mm thick samples of AA 6111-T4 aluminium alloy by using a load ratio of R=0.2 and a test frequency of 10 Hz. The failure modes under low-cycle fatigue (10^3-10^4) and high-cycle fatigue (10^4-10^5) were different. The *kinked fatigue crack* growing in the lower sheet outside of the stir zone is the dominant fatigue crack in welds.

In **Fig. 2.33**, a comparison of experimental fatigue life for FSS welds made with concave and flat tools in a lap-shear sample are shown. In terms of fatigue life, the performances of the welds produced with a concave tool are better. Nevertheless, at large load ranges, the fatigue life of the FSS welds made with a flat tool is significantly shorter than those produced with the concave tool. However, at small load ranges, values of fatigue life for welds produced with the concave and flat tools are almost the same. Therefore, the failure strength of FSS welds under quasi-static loading conditions should be used cautiously [3,107].

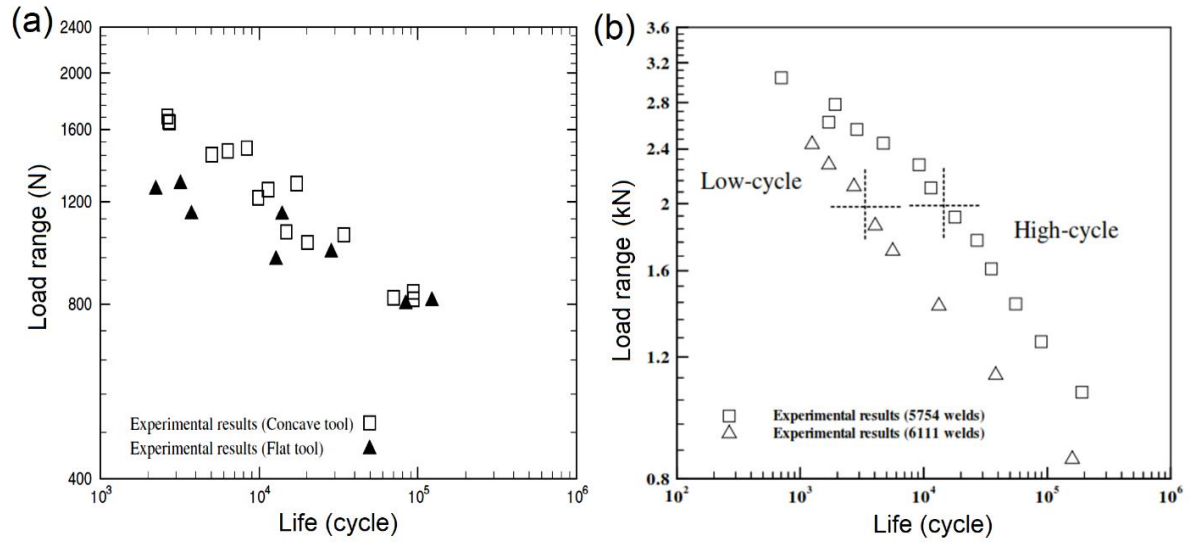

Fig. 2.33 *(a) Fatigue life of spot friction welds obtained with the concave and flat tools in lap-shear samples* [107]*; (b) Fatigue life of FSS welds of AA 5754 aluminium alloy produced with the concave tool and AA 6111 aluminium alloy produced with a flat tool in lap-shear samples under cyclic loading conditions* [140]

Uematsu *et al.* [72] compared fatigue properties of welds of 2 mm thick 6061-T4 aluminium alloy produced with RFSSW and CFSSW, using the stress ratio R=0.1 with a test frequency of 10 Hz. Under fatigue cyclic loading conditions, *plug or pull-out fracture type* was found in the RFSSW joints (**Fig. 2.34a)** while in the CFSS welds *shear fracture modes* through the stir zone were observed (**Fig. 2.34b)**. Lower fatigue strength was obtained in the RFSS welds due to the fracture mode.

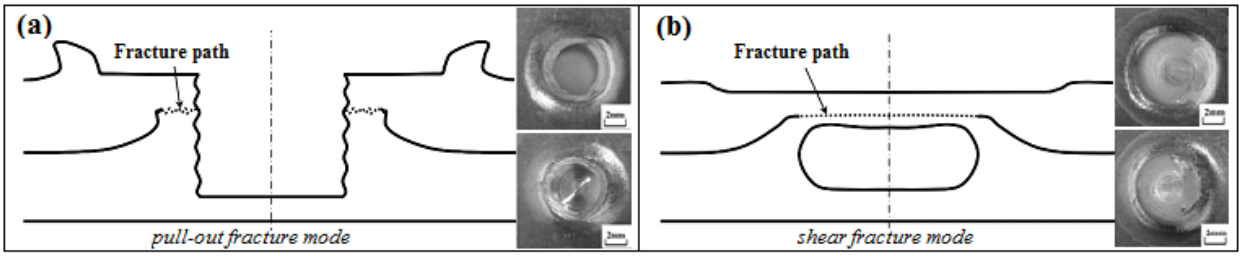

Fig. 2.34 *Schematic illustration of fracture path (the loading direction is horizontal direction): (a) in CFSS welded sample; (b) in RFSSW sample* [72]

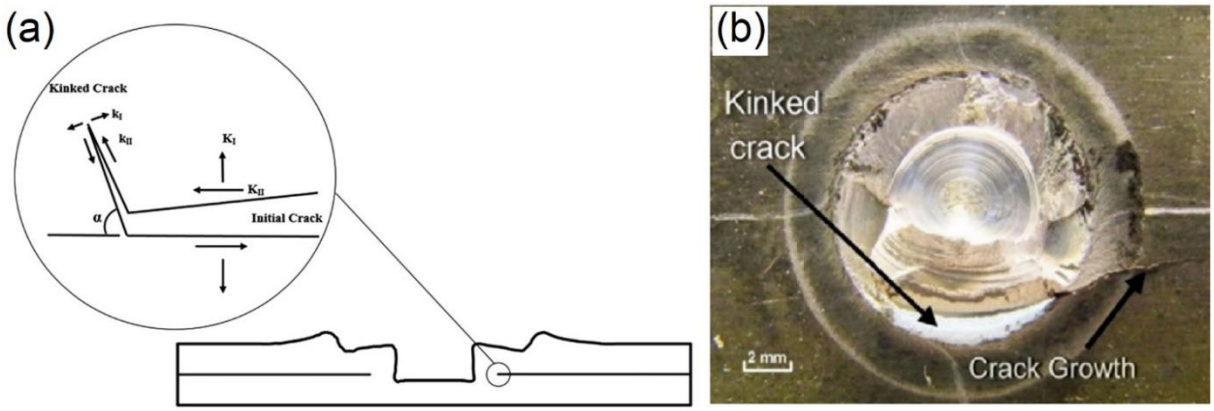

Fig. 2.35 *(a) Schematic view of the FSSW cross-section with a magnified view of initial crack, kinked crack and the global and local stress intensity factors (SIF)* [142]*; (b) macrograph of the crack growth in the sheet and the final fracture surface at the mid-load level* [143]

Tran *et al.* [140] studied fatigue properties of FSSW AA5754-O and AA 6111-T4 aluminium alloy welds at the load ratio R=0.2 and a test frequency of 10 Hz. Experimental results of the AA 5754 and AA 6111 FSS welds produced with the concave tool and flat tools, respectively are shown in **Fig. 2.33b**.

Both welds (AA 5754 and AA 6111) failed to form the *kinked crack* through the thickness of the upper sheets and fracture occurred through the stir zone, under low cyclic loading. However, under high cyclic loading, both welds failed to form the *kinked crack* through the upper and lower sheet thickness.

According to Su *et al.* [141], the failure in FSSSW alclad AA 2024-T3 aluminium sheets 1.6 mm thick initiated from the crack tips and grew in a zig-zag pattern through the upper sheet when the sample was subjected to low cycle loading conditions. However, under high cyclic load conditions, failure began in the surface of the curved interface and propagated directly through the lower sheets.

Recently, Shahani *et al.* [142] studied fatigue behaviour of the FSSW lap-shear samples of AA 6061-T6. Two distinct failure modes were observed depending on the load levels: (i) the shear fracture at high loads levels and (ii) transverse crack propagation in the sheets (at low load levels). At the mid-level load, a combination of those two failure modes was observed. However, in all samples, kinked crack from the interface of the joint was the main factor affecting the failure.

In the field of FSSW, the available literature on fatigue properties of welds is still scarce. Most of the studies made in this field are focused on the CFSSW of aluminium alloys. However, aluminium tends to absorb a significant amount of impact energy by crumpling. In the automobile and train industries, the credibility of FSSW joints must be very high. The unexpected failure of these joints can have big consequences.

2.8 Defects in FSSW joints

Due to the complexity of material flow during FSSW of aluminium, defects in the joints are likely and they tend to influence the integrity of welds. Many defects act as initiation sites for cracking [3,69,108]. In the defect region of the weld, high-stress concentration is present, which triggers the crack to propagate if the weld is subjected to monotonic loading or cyclic loading conditions.

Depending on the type of FSSW method, tool geometry and process parameters, several kinds of defects can form such as: (i) keyhole; (ii) hook defects; (iii) voids; (iv) bonding ligaments; (v) partial metallurgical bond (PMB); (vi) trapped oxide at the interface, or (vii) dynamic precipitation at the interface. These are explained hereunder.

2.8.1 Keyhole and hook defects

The CFSSW process has shown great potential in substituting conventional welding methods such as the RSW. However, lots of studies proved that keyhole [57] and hook defects [19] presented in the FSSW joints **Fig. 2.36a** reduce mechanical properties such as tensile shear and fatigue strength. Keyhole is an inherent defect found in CFSSW which serves as a notch for initiating crack propagation and as a favourable corrosion site in a corrosive environment. Hook defect is a partially bonded or an unbonded metallurgical region inside the friction stir spot welded joint and it is caused by plastic deformation of the lower sheet.

To eliminate keyhole and hook defects, many studies were published [18,19,38,124,144,145] and some of, modified FSSW processes were developed, such as RFSSW [72], PFSSW [125], FSSW plus subsequent friction stir welding (FSSW-FSW) [19] and PLT-FSSW [57].
Fig. 2.36a-c presents schematic illustration of CFSSW; RFSSW and PLT-FSSW, respectively.

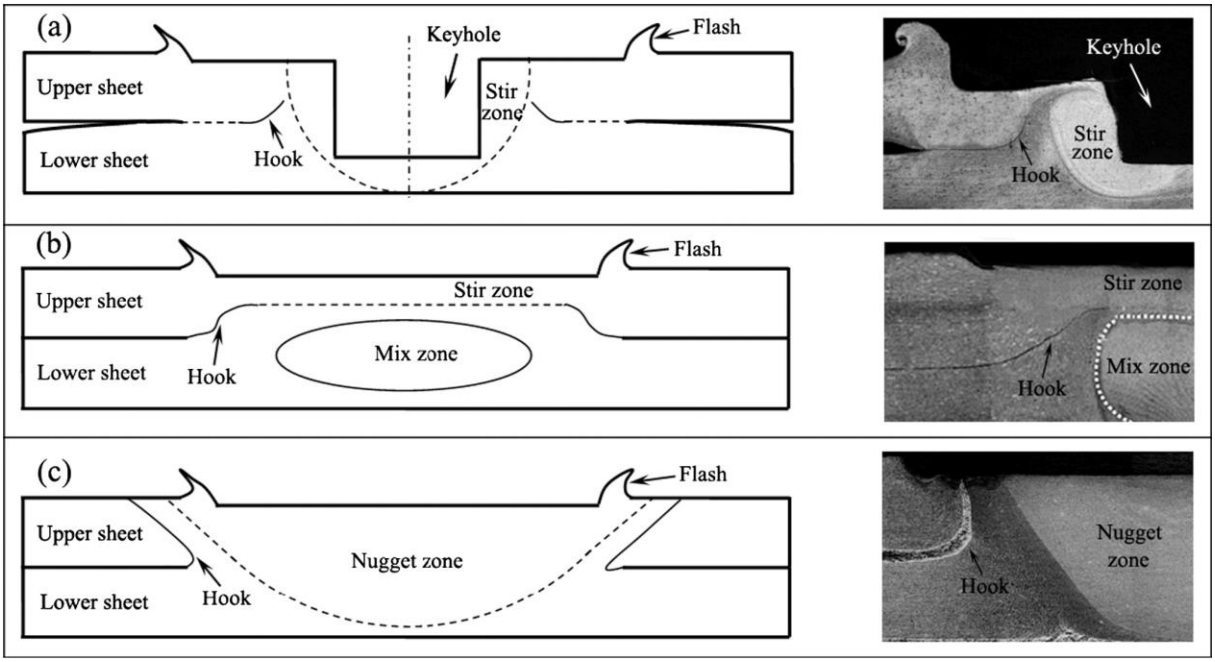

Fig. 2.36 *Schematic illustration and macrographs of the hook defects inside of welds produced by: (a) CFSSW* [124]*; (b) RFSSW* [72]*; (c) PLT-FSSW [17]*

Xu *et al.* [70] studied the influence of RFSSW of AA 5083-O tempered aluminium alloy at the mechanical properties of the weld joint by eliminating keyhole defects. High shear tensile strength was obtained (7.72 kN) by virtue of refilling the keyhole. However, three fracture modes (shear fracture mode, shear-plug fracture mode and plug fracture mode) affected by the hook defects were obtained during the lap shear test. This indicated that RFSSW is a good technique for refilling the keyhole. However, hook defects remained present, which can cause fatigue crack propagations during exploitation.

Farmanbar *et al.* [125] successfully welded 1 mm thick AA 5052 sheets with PFSSW. It is a low-cost, high-quality method with a simple design that produces no-keyhole joints. Shear tensile strength obtained during PFSSW was 5.5 kN at a lower rotational speed. However, hook defects were present in post-welds and its geometry significantly affects failure mechanism.

Li *et al.* [19] introduced a novel method designated as FSSW-FSW for improving the mechanical properties of AA 2024 aluminium welds by eliminating hook defects. The joint between 1.5 mm thick sheets without HD exhibited a tensile shear load of 12 kN, which was significantly higher in comparison to the welds with HD (6.9 kN).

Various researchers studied pin-less FSSW it in recent years. Bakavos *et al.* [20] was the first to prove that PLT-FSSW can produce welds without a keyhole. Moreover, Tozaki *et al.* [38] and Yazdi *et al.* [57] found tensile shear strength of the PLT-FSSW joints to be higher than those of CFSSW. Although some efforts on PLT-FSSW were done, the problem of HD still remains the main obstacle in improving the mechanical properties of the welds.

2.8.2 Bonding ligaments and voids

The banded structure in the stir zone as shown in **Fig. 2.37a**, **b** and **c** lies at the interface between welded sheets and is referred to as bonding ligament. According to Shen *et al.* [108], bonding ligament is an area of good adhesion with strong resistance between sheets. From **Fig. 2.37b** and **c**, different appearances of bonding ligament between the edge and the centre can be seen. On the edge, inclined zig-zag ligaments can be found. Their orientation is correlated with the material flow. The characteristic shape on the edges is a result of plasticized material being pushed back to its original position.

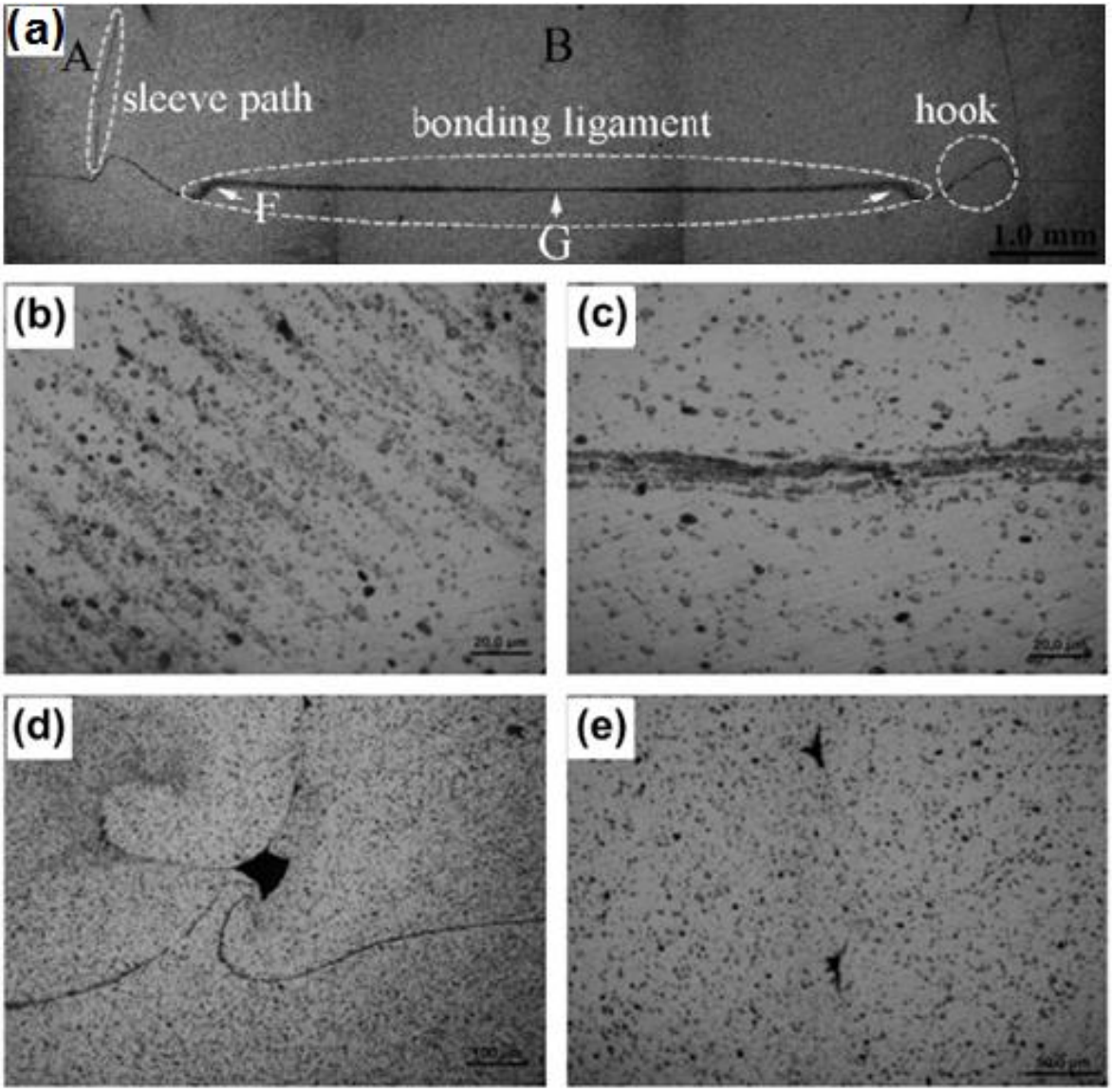

Fig. 2.37 *Characteristics of the defects of the joint: (a) cross section of weld zone; (b) magnified view of region F from (a); (c) bonding ligament (magnified view of region G in (a); (d) void on the hook; (e) voids on retractable line* [108]

Ji *et al.* [146] and Wang *et al*. [147] both studied the joint quality of RFSSW of LY12 and Al-Cu-Mg aluminium alloy, respectively. In both cases, it was found that the fracture path was along bonding ligaments, resulting in a shear fracture mode.

The void formation is attributed to the material flow and it is highly influenced by processing parameters shown in **Fig. 2.37e** and **f**. Also, voids can be the product of inadequate consolidation of plasticized material due to a reduced pressure combined with inadequate material clamping [3]. The voids are frequently formed on the hook (**Fig. 2.37e**) or on the path through which the sleeve plunge into the sheet (**Fig. 2.37f**) during the RFSSW. Oliveira *et al.* [148] associated void formation with thermal shrinkage, entrapped air or/and physical-chemical structural change.

2.8.3 Partial metallurgical bond (PMB)

The partial metallurgical bond (PMB) is a transition region where the bonding between sheets is not so strong [71,99,124,127]. It is also known as partial bonding (PB) [99] or kissing bonds (KB) [71] and surface oxides and voids can be present. There is also the term "near full metallurgical bonding" which refers to situations where oxide remains broken up due to metal flow and few voids remain. It typically appears like a short and uneven line on the joining interface.

Bakavos *et al.* [149] studied the influence of tool pin length and the application of the insulating back face anvil to improve the temperature distribution and strength of the FSS weld of 6111-T4 aluminium alloy. The estimated lengths of each bond type are compared at different conditions. It was concluded that poorer interface bond is formed under the shoulder region where a partial metallurgical bond was found. The samples with a higher percentage of the partial metallurgical bond length had reduced strength.

In **Fig. 2.38a**, the interface between the two sheets underneath the tool shoulder is presented. According to Mitlin *et al.* [106], the joint interface underneath the tool shoulder can be subdivided into two main zones. The first is the *kissing bond (KB)* which begins past the non-contacting interface (**Fig. 2.38a**). It is transferred towards to the second zone located near the weld center, the *partial metallurgical bond (PMB),* which is shown in **Fig. 2.38b**. In **Fig. 2.38c**, a high magnification image of the PMB containing large elongated pores can be seen. The gradual transition from a PMB to the nearly full metallurgical bond is shown in **Fig. 2.38d**.

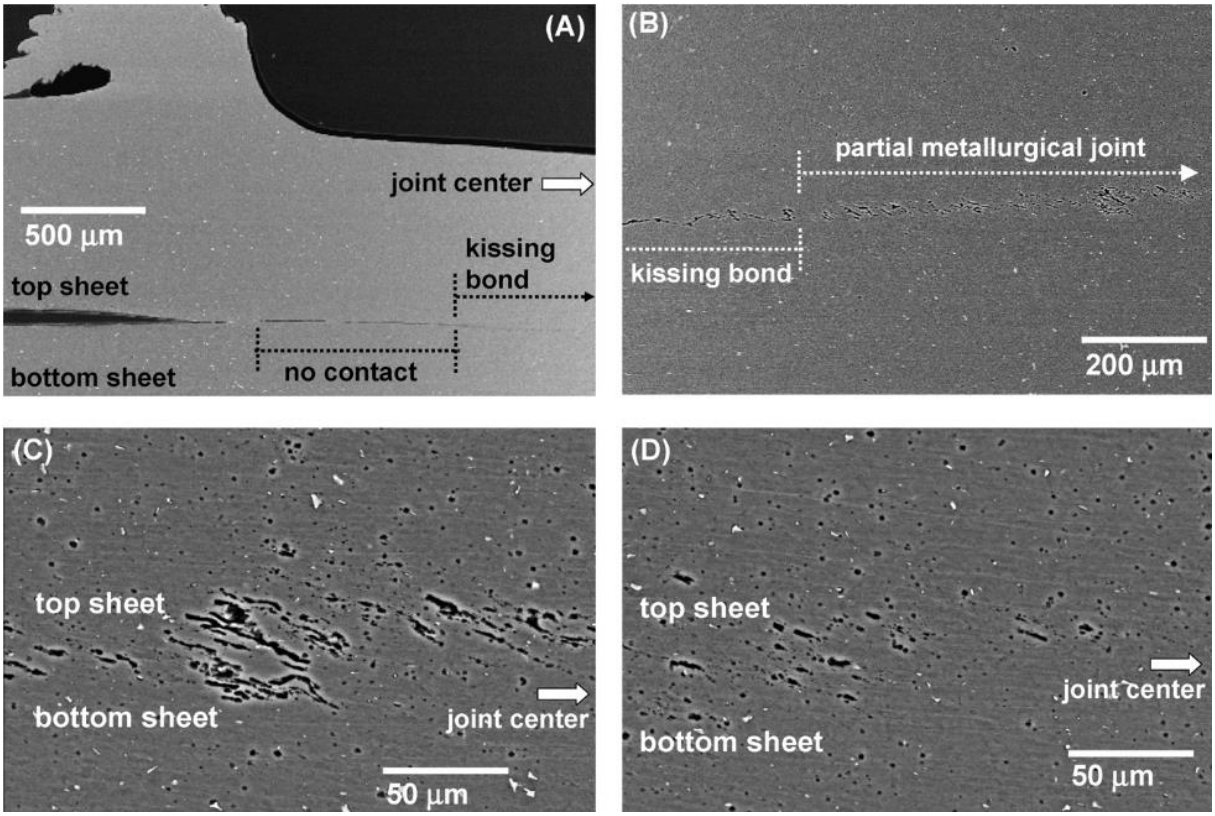

Fig. 2.38 *(a) Wide non-contacting and kissing bond region under the shoulder; (b) transition from kissing bond to the partially metallurgically bonded area; (c) partially metallurgically bonded region; (d) transition from partially metallurgically bonded region to the full metallurgical bond* [106]

2.8.4 Trapped oxide at the interface

Welding of aluminium, particularly with solid-state welding techniques, is difficult due to a tenacious and chemically stabile aluminium oxide layer. The layer developes on sheets before the welding process as a result of a reaction of aluminium with oxygen. After welding, the layer may remain trapped on the interface between sheets [12,13,150]. The oxide layer acts as an effective barrier preventing atoms from inter diffusing across the bonding interface and, consequently, yields a poor metallurgical bond [8,151]. This phenomenon was first observed during the diffusion bonding of aluminium alloys [8,14,151,152]. During solid-state welding, all alloys with stable oxide layer suffer from poor bonding due to the presence of a stabile oxide film at the bonding interface. In most cases, this Al_2O_3 oxide layer is 5-10 nm thick. However, depending on alloying elements of the base material, mixed oxides can also be present at the interface.

Fishkis *et al.* [153] observed that the hot rolling of a not-heat treatable aluminium alloy containing magnesium resulted in the formation of a subsurface layer 1.5-8 μm thick composed of magnesium and aluminium oxides which mixed with the metal (after the first pass MgO, γ-Al_2O_3, and $MgAl_2O_4$ spinel, the second pass of MgO and γ- Al_2O_3 and after the last pass only

of MgO). This oxide is not uniform in thickness and composition. The subsurface mixed layer was covered with a continuous surface oxide layer 25-160 nm thick containing MgO and Al_2O_3. All these oxides are stable, and their melting point is high above the process temperature during any solid-state welding process.

Two theories were proposed to explain the characteristics of the solid-state welding process: the film theory and energy barrier theory. In the film theory, the bond during solid-state welding occurs when two atoms are brought to less than 10 atomic spacings (the metallic radius of aluminium atoms is 0.143 nm). The attractive inter-atomic forces will form a joint, causing the crystal to mismatch with a non-cohesive grain boundary. This process, therefore, requires a clear interface between two sheets without any oxides or other contaminants [13]. The energy barrier theory has been branched in two theories: the mismatch of the crystal lattice [154] and recrystallization theory [86]. Semenov *et al*. [154] stated that some distortion of the crystal lattice between two surfaces must be achieved in order to obtain the bond, representing an energy barrier that must be overcome. However, Conrad and Rice *el at.* [62] observed bonding without deformation if contact is made between clean surfaces. However, Shirzadi *el at.* [14] implied that deformation during solid-state welding is needed to break up the brittle and continuous oxide layer; metal-to-metal contact is thus promoted because of local disruption of the oxide film on both faying surfaces.

Hence, significant improvement in bond integrity would be achieved by developing a method to disrupt the oxide layer. Currently, there are three major approaches used to disrupt the oxide layer during diffusion bonding [155]:

(i) Imposing substantial plastic deformation;
(ii) Enhancing microplastic deformation of the surface asperities and
(iii) Presence of active alloying elements.

Imposing substantial plastic deformation will lead to the fracture of the brittle continuous oxide layer. The oxide film has lower ductility (only a few percentages) compared with that of the base material. Hence it ruptures when the workpiece is subjected to a high degree of plastic deformation. Metal-to-metal contact has arisen as a consequence of local disruption of the oxide film on both faying surfaces, **Fig. 2.39a** [13,152,155].

Enhancing microplastic deformation of the surface asperities is an alternative approach which uses a rough surface finish to overcome the oxide problem in solid-state diffusion bonding. This may lead to microplastic deformation and disturbance of the oxide layer and exposure ot the metal contact between base metals as shown in **Fig. 2.39b** [14,155].

Presence of active alloying elements: the active alloying elements such as magnesium and/or lithium chemically interact with and break up the continuous and amorphous aluminium oxide layer at the interface and form an array of discrete particles [12,155].

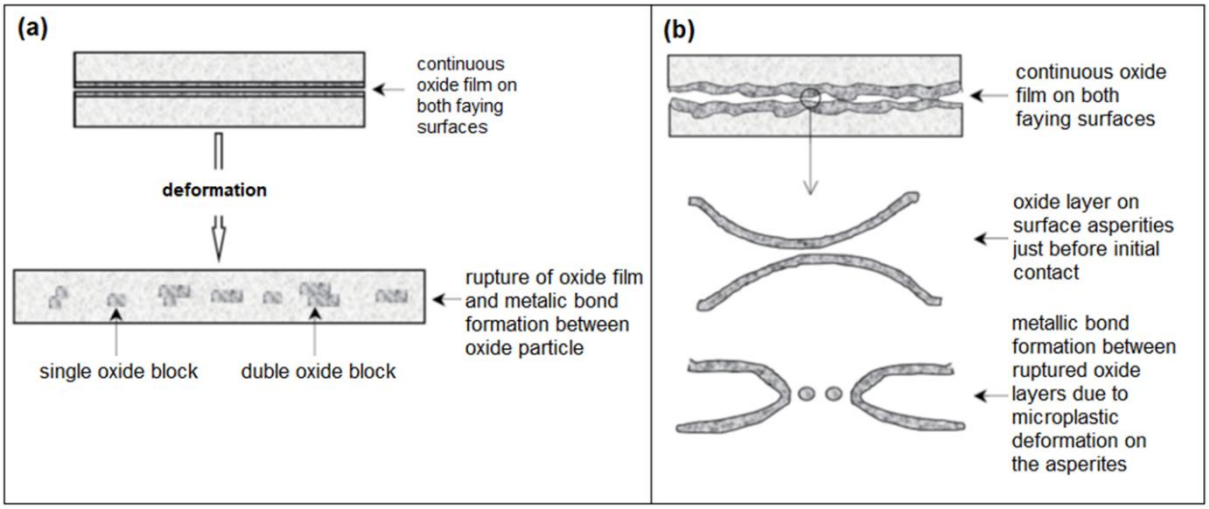

Fig. 2.39 *Schematic illustration of solid-state diffusion bonding of material with stabile oxide layer by: (a) Imposing substantial plastic deformation (b) Enhancing microplastic deformation of the surface asperities (adapted from* [155]*)*

The approach "*Presence of active alloying elements"* is presented in **Fig. 2.40**. Shirzadi *et al.* [155] has schematically presented the role of active magnesium in the formation of a bond line of aluminium-magnesium samples. **Fig. 2.40** indicates that amorphous Al_2O_3 reacts with magnesium and creates crystalline MgO.

$$Al_2O_3 + 3Mg \rightarrow 3MgO + 2Al$$

The nature of the aluminium oxide at the interface changes from amorphous to crystalline during the bonding cycle. Also, a good correlation between bond strength and the broken oxides was reported. This implies that the higher content of active elements is, the greater disruption of the oxide layer and therefore achieving a higher bond strength. Also, it was implied that magnesium is more effective than lithium in increasing bond strength.

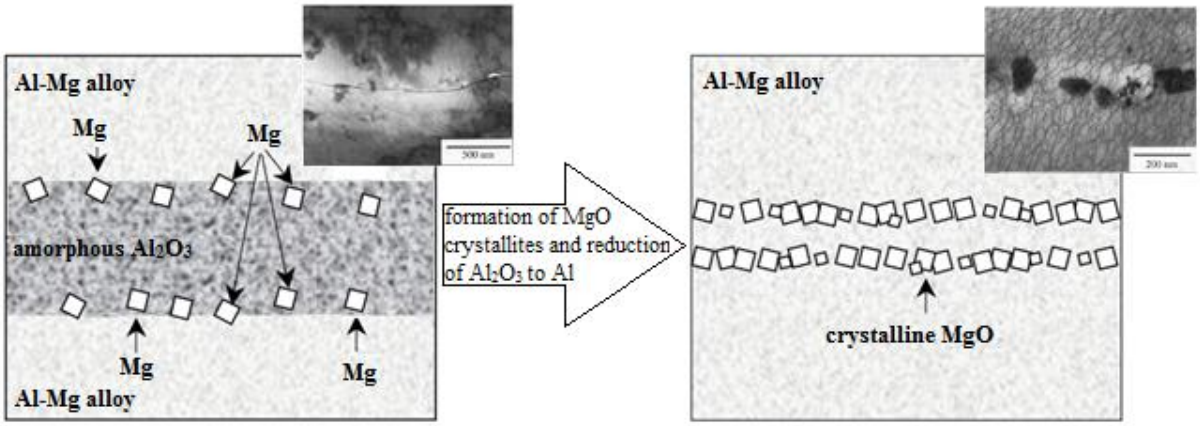

Fig. 2.40 *Schematic presentation of the role of active magnesium in the formation of the bond line of AA 8090 aluminium diffusion bonded joint (adapted from* [155]*)*

During FSSW, the influence of the stable oxide layer is not so pronounced as in diffusion bonding due to a high level of deformation which leads to the oxide layer easily being disrupted.

The new clean surface between the disrupted oxides will be exposed to diffusion and bonding will occur [56].

However, Shen *et al.* [156] found that the welding interface of AA 6061-T4 CFSSW joints contained an array of discontinuous oxide particles. It was postulated that the lower deformation prevented metal-to-metal contact and leads to the formation of partial metallurgical bonding. It was also observed that the degree to which the oxide layer breaks up depends on the distance from the pin.

Other authors [10,18,56,57,95,115,127,142,145,149] have also mentioned oxide as a defect that leads to the partial bonding or kissing bond defect. However, in open literature dealing with FSSW, a detailed analysis of these oxides and their influence on weld strength was not found.

3. EXPERIMENTAL METHODS

3.1 Base material

The material samples used for the FSSW were cut to dimensions 44 × 50 × 0.3 mm from thin sheets of rolled commercial aluminum alloy AA 5754-H111. In **Table 3.1**, the chemical composition of the base material (AA 5754-H111) is given. The chemical composition was determined using an optical emission spectrometer (ARL 3580). Prior to the welding expeirments, the uniaxial stress-strain properties of the base metal were tested by using a Hegewald & Peschke, Inspect Retrofit universal testing machine with testing range up to 20 kN. The tensile test was performed according the standard DIN EN ISO 6892-1 on samples with cross section of 12 × 1.2 mm and gauge length of 80 mm. The test was repeated three times. The tensile stress-strain curves obtained from the test are shown in **Fig. 3.1**.

Table 3.1 Chemical composition of commercial AA 5754 - H111 aluminum alloy

Element	Si	Fe	Cu	Mn	Mg	Cr	Zn	Ti	Al
wt. (%)	0.19	0.24	0.03	0.30	3.10	0.03	0.005	0.014	bal.

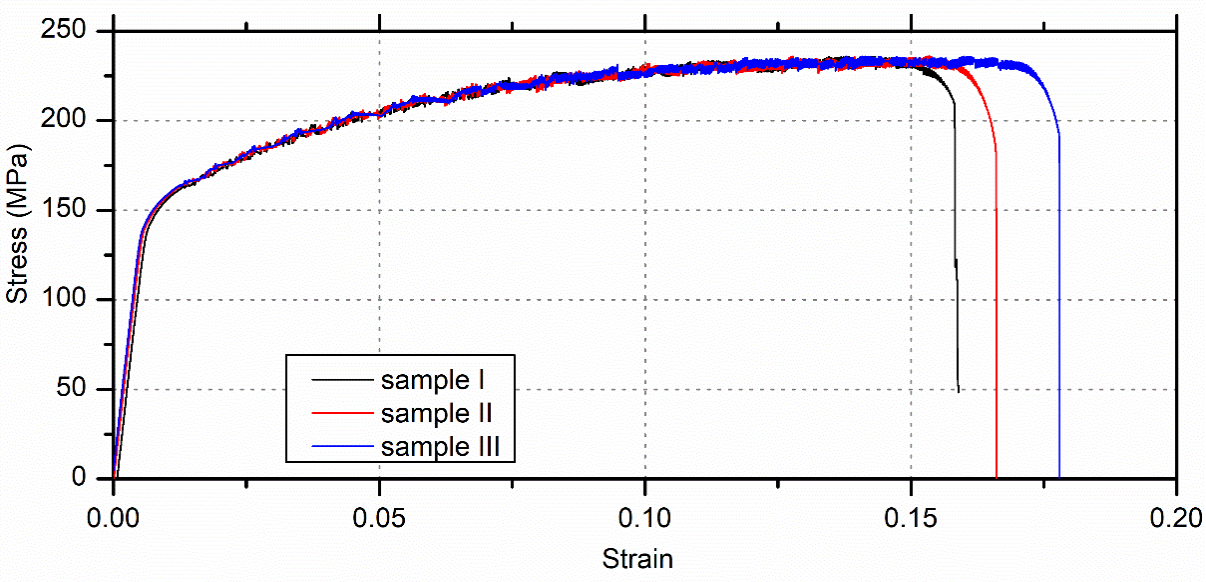

Fig. 3.1 *Stress-strain curve of base material AA5754 alloy*

3.2 Welding process

3.2.1 Welding machine

All experiments in this work were carried out on an adapted force controlled EJOWELD C50R FSSW machine. The machine specifications were that it can achieve a maximum rotational speed of 9000 RPM, a peak axial load of 8 kN and dwell time of up to 5 s. The welding experiments were performed in the Laboratory for Pressure Welding at the Department of Production Technology, Ilmenau University of Technology, Ilmenau, Germany.

As shown in **Fig. 3.2**, the welding system comprises of a clamping system movable in a vertical direction, together with an anvil, causing the sheets to be fixed between each other. The functioning of this machine is relatively simple; the sample is first pressed by the clamping system and thereafter, the tool starts to move vertically downwards to the substrate at a predetermined axial load *F*. After reaching the surface of the upper sheet, it is plunged into the upper sheet at a fixed load and rotational speed. After achieving desirable penetration depth, the tool retracts. The dwell time is a function of the applied load, rotational speed and material properties.

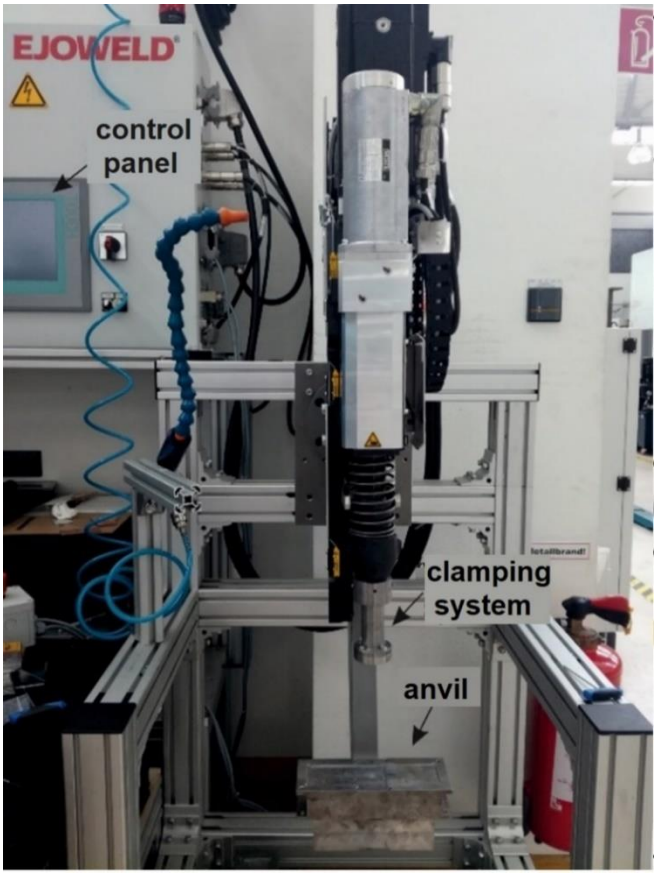

Fig. 3.2 *Adapted force controlled EJOWELD C50R FSSW machine*

The axial load was maintained at 2 kN for batch I and 4 kN for batch II for various experiments reported in this work. The axial displacement (*h*) (penetration depth) made by the rotating tool was maintained at 0.25 mm. The tool geometry, axial load (*F*) and rotational speed (*n*) were varied as shown in **Table 3.2**. Each experiment was repeated three times and an average value with the standard deviation was used for the analysis.

Fig. 3.3 shows a schematic illustration of the FSSW process wherein a K-type thermocouple was placed at the bottom between the last sheet and the anvil to study variation in the temperature during the experiments. The experimental trials performed were exploratory i.e. a major variable explored here was the rotational speed which governs the applied strain rate crucial for the quality of weld-joint and no Design of Experimental approach was used.

Table 3.2 FSSW parameters for batches I and II

Batch I (T1) *	**F (kN)**	**n (RPM)**	**h (mm)**	**Batch II (T2) ***	**F (kN)**	**n (RPM)**	**h (mm)**
RW1	2	1500	0.25	RWA1	4	1000	0.25
RW2	2	2000	0.25	RWA2	4	1500	0.25
RW3	2	2500	0.25	RWA3	4	2000	0.25
RW4	2	3000	0.25	RWA4	4	2500	0.25
RW5	2	3500	0.25	RWA5	4	3000	0.25
				RWA6	4	3500	0.25
				RWA7	4	4000	0.25
				RWA8	4	4500	0.25

T1 and T2 are the tool geometries shown in **Fig. 3.5*

3.2.2 Tools

3.2.2.1 Tool material-H13 tool steel (X40CrMoV51)

The tools were fabricated in the lab using H13 (X40CrMoV51) hot-work tool steel; the material's chemical composition is shown in **Table 3.3**. An experimental scheme used for lap joining of the four thin sheets during FSSW is illustrated in **Fig. 3.3**.

Table 3.3 Chemical composition of H13 tool steel (X40CrMoV51) from the supplier's datasheet

Element	C	Cr	Mo	V	Fe
Wt.%	0.4	5.1	1.35	1.1	bal.

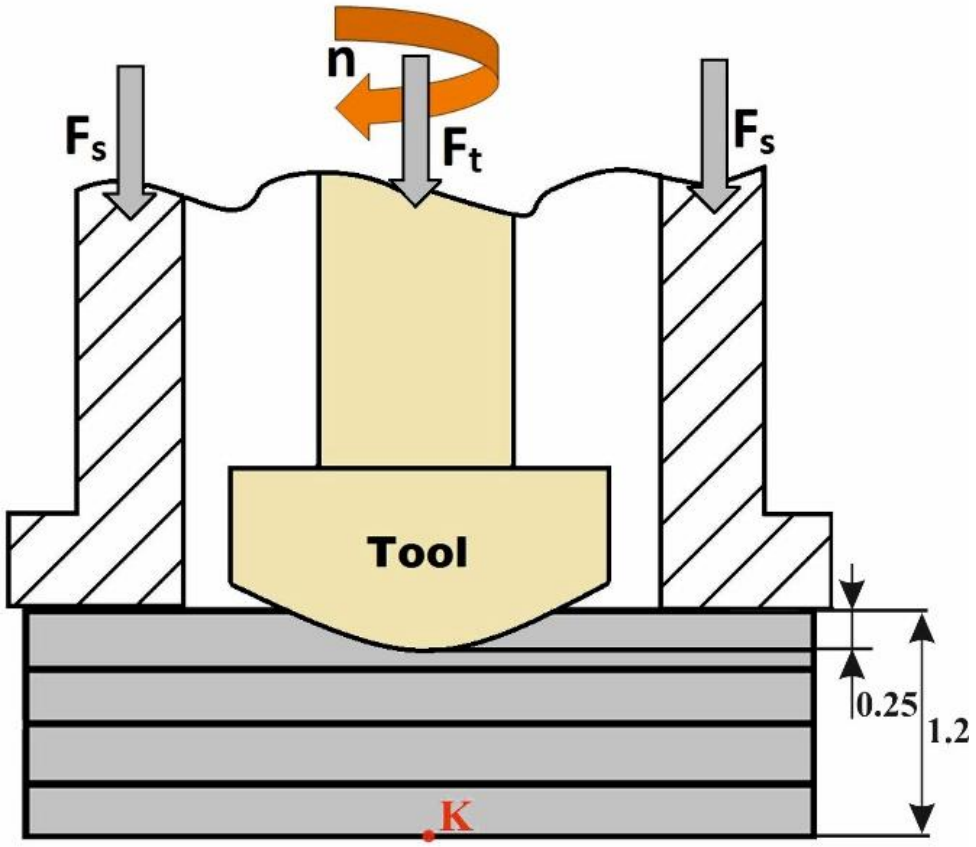

Fig. 3.3 *FSSW tool setup F_t-force on the tool, F_s-clamping force (all dimensions are in mm)*

After a batch of dummy trials, it was found that a pin-less tool does not work for joining multiple thin sheets. To produce a multilayer weld joint with high-strength, it is necessary to produce a certain level of temperature and stress to induce material flow. This way conditions for dynamic recrystallisation as well as diffusion between layers are created [16]. During PLT-FSSW, the material flow is most pronounced at the maximal contact radius of the tool where the angular velocity of the tool is the highest. According to the model of Reilly *et al.* [56], during PLT-FSSW, a small central region of the sample gets stuck to the tool. The material flows in spirals in the outer slip region, with the number of layers increasing with the number of rotations. In other words, during PLT-FSSW, material rotates with the tool in the centre of the weld below the tool. It is sheared as well as compressed due to the axial pressure present in the contact zone. At the centre, the tool rotation has no influence. This can cause no bond or partial bond in this region. Furthermore, the flat tool can cause tearing of thin sheets due to a uniform pressure along the entire radius of the tool, which makes it unsuitable for welding multiple thin sheets. In **Fig. 3.4**, an example from pre-experimental work done with flat tool is presented. The upper sheet was noticeably torn, especially at the periphery of the weld. Contrary to this, a convex tool presented a gradually-increasing contact radius as a function of the depth of tool engagement and provided for better contact conditions between the tool and the sheets. The convex tool with the gradually-changing tool contact radius caused the shear stress to grow gradually as a function of contact depth, which is a function of the contact radius magnitude from *0* to *r*.

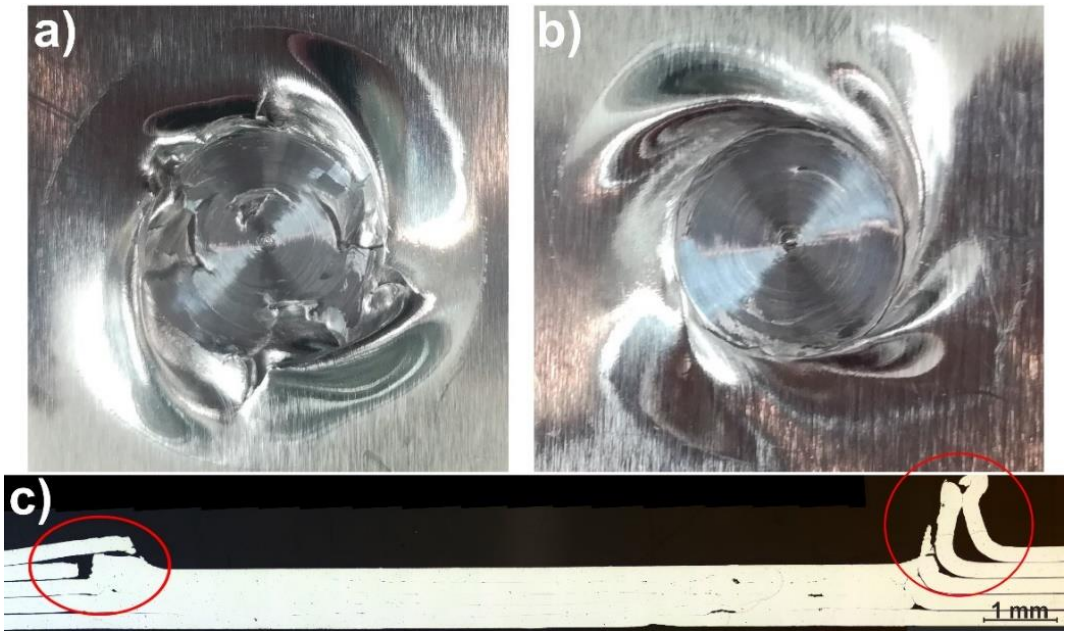

Fig. 3.4 *Macrographs obtained from pre-experimental work of two samples and a cross-section view of the samples welded with a flat tool of diameter 10 mm (Al 99.5, five sheets of 0.2 mm thickness) welded with (i) 2000 RPM, 0.2 mm penetration depth and 5 kN axial load and (ii) with 2000 RPM, 0.2 mm penetration depth and 2 kN axial force; red circles show tarred edges of the first two sheets after welding with flat tool sample*

The two tool shapes (T1 and T2) with different radius used are shown in **Fig. 3.5**. It is believed that the radius of the convex tool has significant influence on the welding performance and this is an area worthy of future investigation.

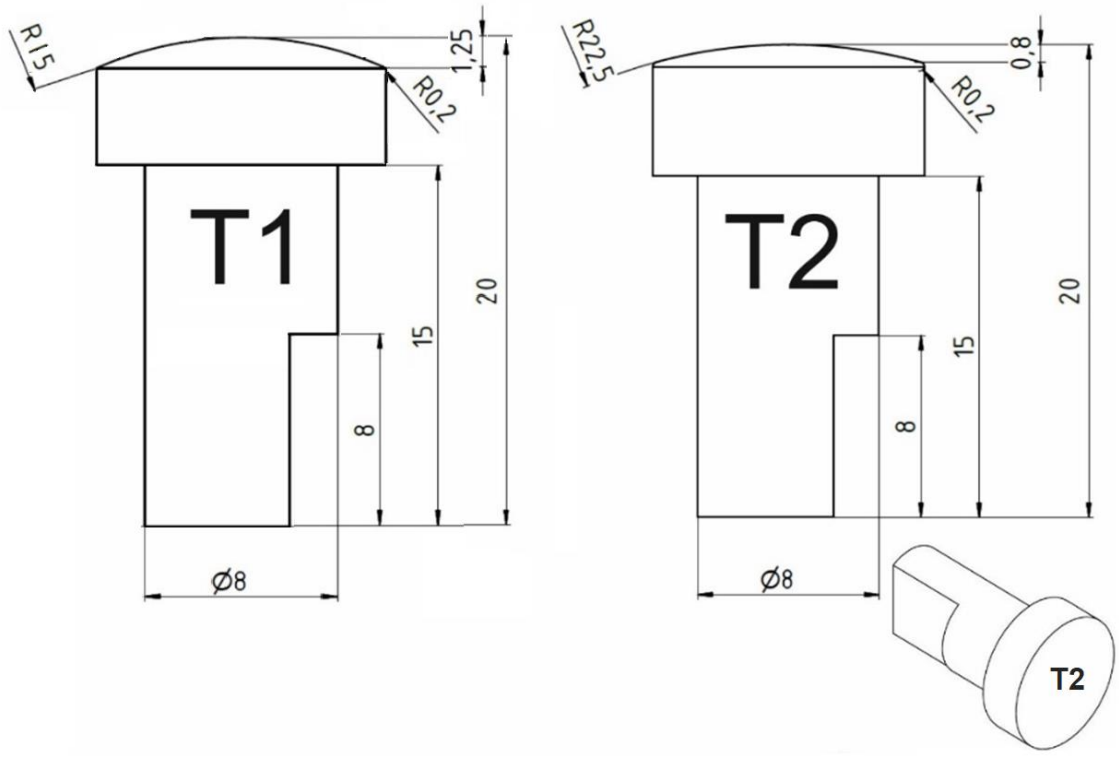

Fig. 3.5 *Details of tool geometries (all dimensions shown are in mm)*

3.3 Surface topography assessment

During FSSW, a rough surface is desirable because the process relies on maintaining considerable friction between the rotating punch and the sheets (workpiece). It was therefore considered relevant to characterise the surface roughness of the punch and to later link it with the surface topography of the welded surface and analyse the correlation. Accordingly, surface topography measurements were performed at the School of Aerospace, Transport and Manufacturing, Cranfield University, UK. A contact mode surface profilometer (Taylor Hobson Form Talysurf Series 2) having a semispherical tip of a 2 μm radius (see **Fig. 3.6**) was used to obtain the primary profile of the tool surface. The primary profile was filtered to look into the planar undulations on the surface (roughness profile). This was done by removing a circular form with a radius of 16.83 mm and by applying a roughness filter of 0.8 mm (ISO 3274), as is suggested in the Good Practice Guide by National Physical Laboratory, UK [157].

Fig. 3.6 *Contact mode surface profilometer (Taylor Hobson Form Talysurf Series 2)*

3.4 Scanning Acoustic Microscope (SAM)

The non-destructive assessment of weld interiors to examine various defects in the weld zone was tested using a Scanning Acoustic Microscope (SAM) (PVA TePla made, Westhausen, Germany) available at London South Bank University, UK (see **Fig. 3.7a**). A transducer is a very important component in governing the sensitivity, repeatability and accuracy of the instrument. In this case, an SAM having a H2 PreAmplifier was used to measure the amplitude of FSSW joints. The half-cross section of the FSSW joint was immersed in a water tank (deionised water). To obtain images from acoustic waves, a transducer PT30-6-12.7 with 20 dB gain was used, as shown in **Fig. 3.7b**. A transducer with a frequency of 30 MHz, diameter of 6 mm and a focus distance of 12.7 mm was used and found appropriate here. Images of samples obtained from the SAM were used to analyse the extent of delamination, voids and the oxide layer trapped at the interface between the sheets. For this purpose, samples were scanned with A-scan, C-scan and B-scan modes. Tested wavelength was set to be 20000 ns for all samples. For C-scan, the gate length was held for 50 ns.

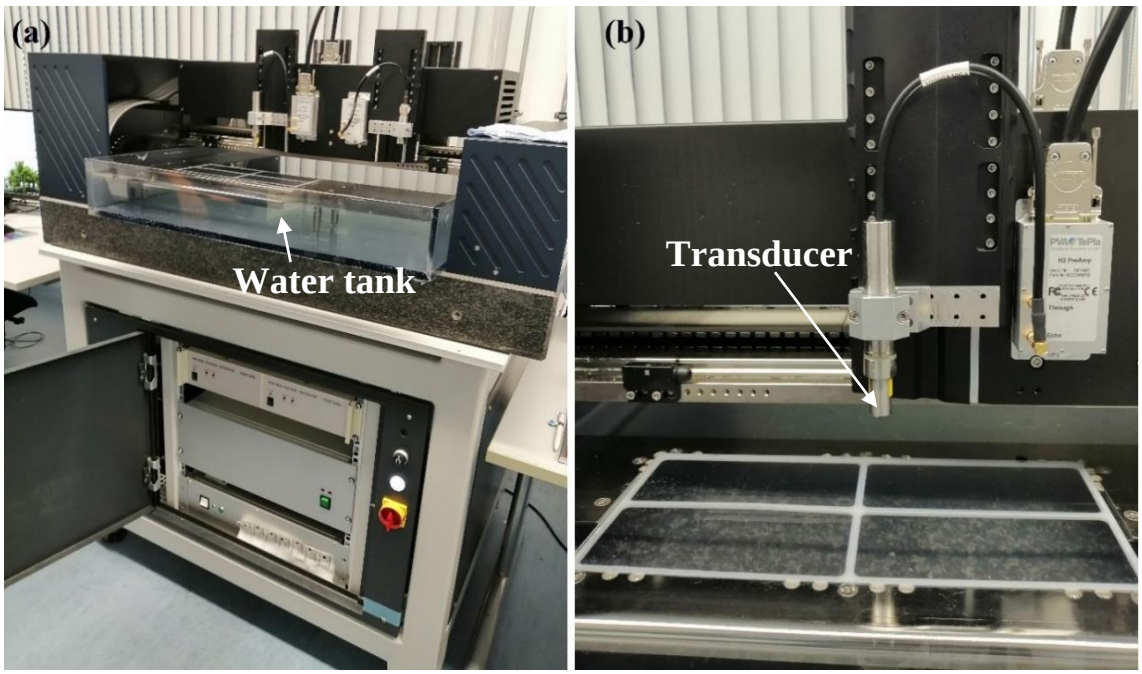

Fig. 3.7 *(a) PVA TePla Scanning Acoustic Microscope (SAM) with H2 PreAmp; (b) PT30-6-12.7 transducer*

3.5 Metallographic examination of the welds

Sample preparation is an essential step post-joining to analyse various metallurgical processes. This part of the work on sample preparation was done at the Department of Production Technology, Ilmenau University of Technology, Ilmenau in Germany.

For metallographic analysis, the welded joints were sectioned across the central line and then cold-mounted in a Buehler Cast N' Vac 1000 vacuum chamber, as shown in **Fig. 3.8a**. Thereafter, fine grinding and polishing was done with the Buehler Phoenix 4000 as part of sample preparation as shown in **Fig. 3.8b**. To accomplish the task, sandpaper (360, 600, 1200 and 2500 grit sizes) and water lubricant were used for grinding the sample for up to 2 minutes for each step. The samples were finally treated with diamond suspensions (6 and 3 μm) for up to 1 minute at each step. A final step of polishing involved treating the sample with colloidal silica with average particle size of 0.05 μm (OP-S) for 3 minutes on all samples. Between each stage, the samples were carefully cleaned in an ultrasonic bath for 1 minute and thereafter cleaned with isopropanol and dried by a dryer.

After polishing, electrolytical etching with Barker's etching agent (5ml HBF_4 + 200ml. H_2O) was done for light microscopy on Struers LectroPol-5 equipment ,as shown in **Fig. 3.8c**, (40 V, 2 min). The preparation of the samples was done at the Department of Production Technology, Ilmenau University of Technology, Ilmenau, Germany.

Fig. 3.8 *(a) Buehler Cast N' Vac 1000 vacuum chamber; (b) Buehler Phoenix 4000 sample preparation systems; (c) Struers LectroPol 5 electropolisher*

3.5.1 Light microscopy (LM)

The cross-section morphology of the joints, grain size and the failure behavior of the samples were analysed by Zeiss, AxioScope A1 light microscope with AxioCam ICc3 for the etched samples shown in **Fig. 3.9a** and Zeiss Axio Vert.A1 MAT with AxioCam 105 for the polished samples shown in **Fig. 3.9b**. The etched samples were analysed with crossed polarized light under sensitive tint (etching procedure was described previously). The microstructure evaluation was done at the Department of Production Technology, Ilmenau University of Technology, Ilmenau, Germany.

The grain size was estimated from etched micrographs with the help of Image J software [158] by measuring the surface area of the grain and thereafter calculating the average diameter from an area of interest.

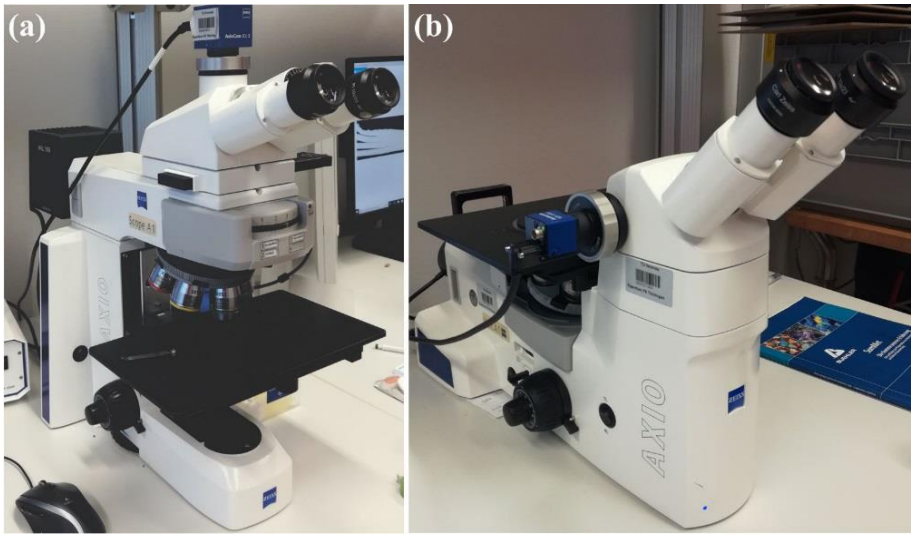

Fig. 3.9 *Light microscopes: (a) Zeiss AxioScope.A1 with AxioCam ICc3; (b) Zeiss Axio Vert.A1 MAT with AxioCam 105*

3.5.2 Scanning Electron Microscopy (SEM)

In this study, JEOL JSM-6460LV scanning electron microscope was used and is shown in **Fig. 3.10**. The reaserch was done at the University Centre for Electron Microscopy, University of Novi Sad, Novi Sad, Serbia. SEM was used to study samples after small punch test to investigate failure morphology.

Fig. 3.10 *Scanning Electron Microscope SEM JEOL JSM-6460LV, Novi Sad*

3.5.3 Focused Ion Beam (FIB) Milling

FIB milling was performed at the Department of Material Science & Technology, University of Cambridge, Cambridge, UK. This unique access became possible via the Henry Royce PhD Equipment Access Scheme which enables access to TEM facilities at Royce@Cambridge. In this study, Zeiss Crossbeam 550 FIB-SEM (**Fig. 3.11a**) and FEI Helios FIB (**Fig. 3.11b**) were used to cut and prepare the lamella sample for TEM. They both combine imaging, milling and analytical performance for nanoscale tomography and sample preparation.

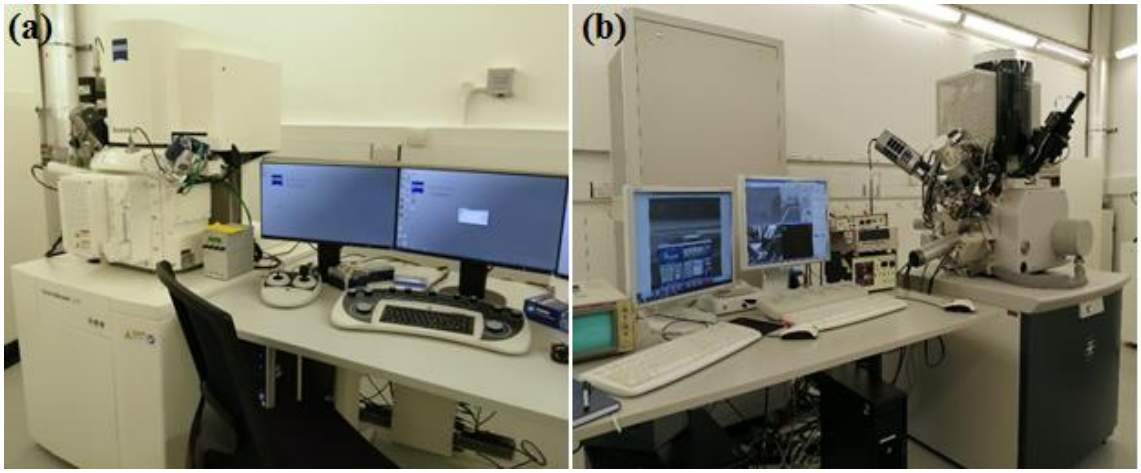

Fig. 3.11 *(a) ZEISS Crossbeam 550 FIB-SEM; (b) FEI Helios FIB*

Fig. 3.12 shows an SEM image indicating the area where the TEM lamella was cut (white square) from the sample welded with 1000 RPM from batch II. The sample and the area for the analysis were chosen due to the highest level of delamination observed during the SPT between both batches. The area chosen was between the full bonded and unbonded region.

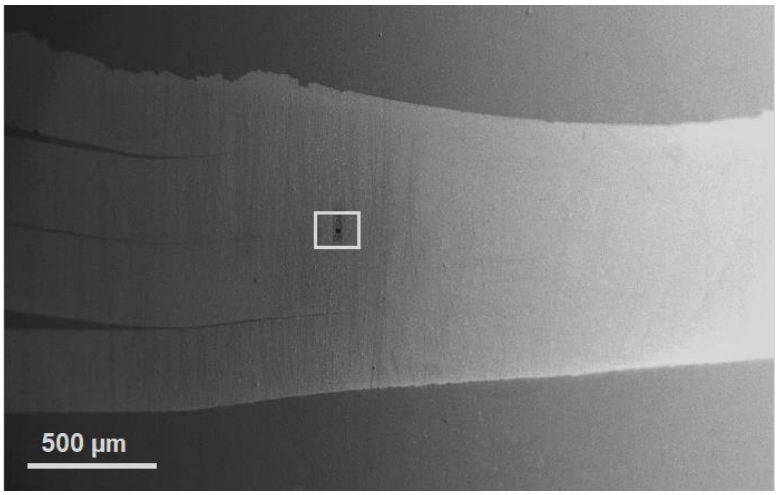

Fig. 3.12 *SEM image indicating the area where the TEM lamella was cut from the sample welded with 1000 RPM from batch II*

In **Fig. 3.13**, various steps for preparing the TEM lamella using the FIB technique are shown and they are discussed below:

Step I: involves the deposition of the Pt in the area of the interest in order to protect it.
Step II: concerns milling the trenches with the help of an ion beam. The milling was done from both sides of the deposed Pt.
Step III: concerns cutting the sample in a U shape, leaving a small bridge between the lamella and sample, to provide enough stiffness for the lamella.
Step IV: involves positioning the needle micromanipulator to attach it to the lamella. The needle of the micromanipulator is attached to the TEM lamella by depositing platinum to the contact area between the needle and the TEM lamella.
Step V: The lamella is released with the help of the ion beam and lifted from the bulk.
Step VI: The lamella is attached to the TEM grid and released from the needle with the help of the ion beam. Afterwards, lamella is ready for further study in transmission mode.
These steps were followed by several thinning steps, which were done by finely milling the surface. As a result, a thickness of less than 300 nm can be cut. Finally, the surface was cleaned to remove impurities from the TEM sample deposited during the process [159].

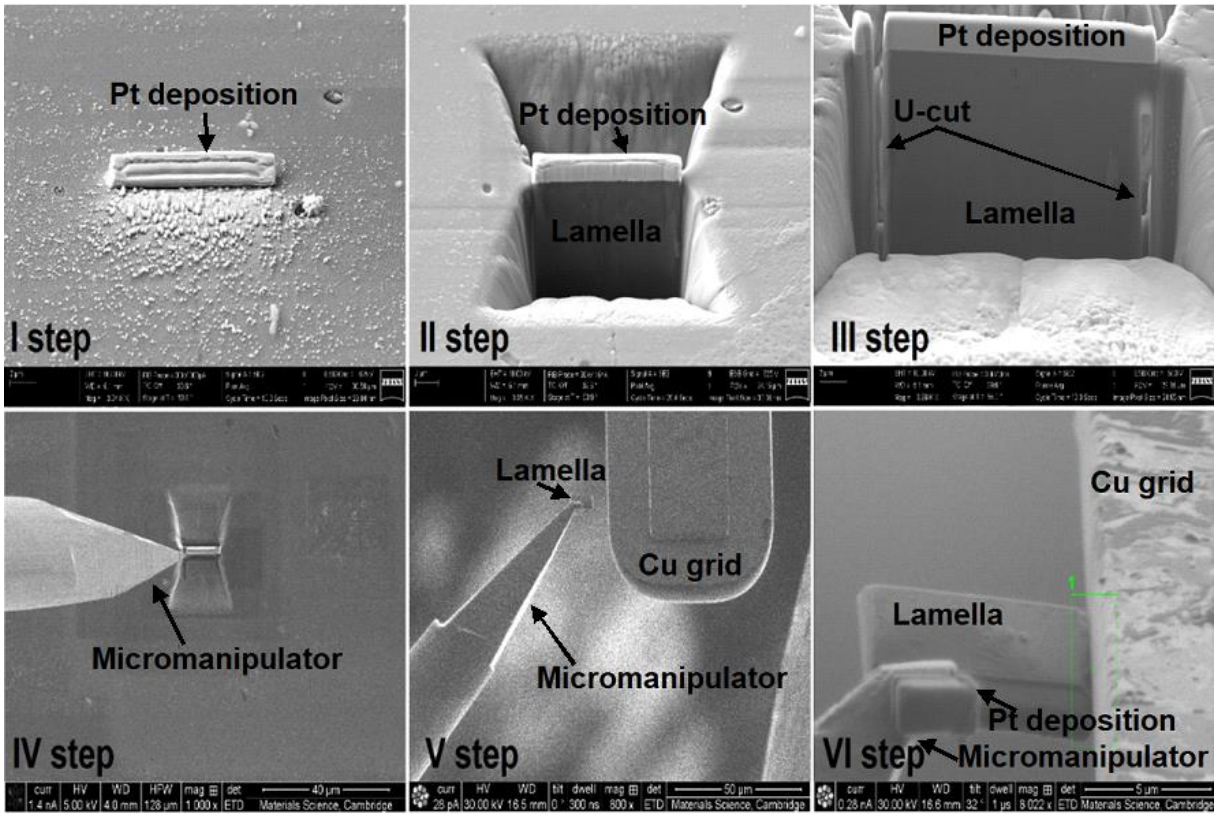

Fig. 3.13 *The FIB procedure of TEM sample preparation*

3.5.4 High resolution Transmission Electron Microscopy (HR-TEM) and EDX

In this study, a FEI Tecnai G2 (T20) high-resolution transmission electron microscope (HR-TEM) with a range of accelerating voltages from 80 to 200 kV was used, (**Fig. 3.14a)**. The samples were analysed in two modes: (i) conventional imaging mode to analyse microstructure at the interface between the sheets and to understand different behaviour between samples welded at different rotational speeds and (ii) diffraction mode to identify the existing phases. The second TEM used in this study was a fully-digital FEI Tecnai Osiris S/TEM at 200 kV with a STEM system including a high-angle annular dark-field (HAADF) detector, as shown in **Fig. 3.14b**.

The TEM analysis was performed at the Department of Material Science & Technology, University of Cambridge, Cambridge, UK. Both TEMs were equipped with EDX spectroscopy. The Tecnai G2 is equipped with Peltier-cooled Ametek silicone drift detector, Genesis. EDX was used to analyse chemical composition and distribution of the oxides and precipitates within the welds. Two different modes were used: (i) EDX surface mapping and (ii) EDX spectrum analysis.

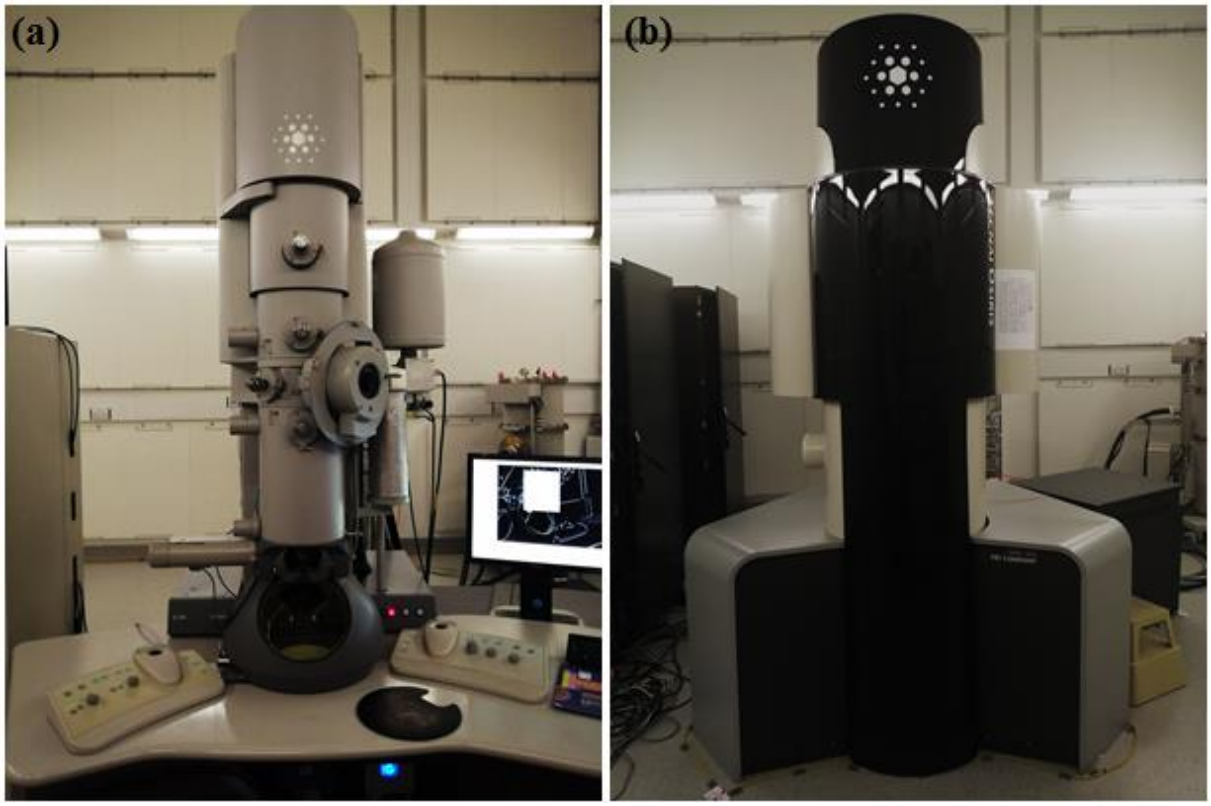

Fig. 3.14 *(a) FEI Tecnai G2 (T20) HR TEM; (b) FEI Tecnai Osiris S/TEM*

3.5.5 Frequency-Modulated Kelvin Probe Force Microscopy (FM - KPFM)

Surface potential (SP) mapping was carried out using Frequency-Modulated Kelvin Probe Force Microscopy (FM-KPFM). The sample prepared for TEM analysis (TEM lamella) was also tested with FM-KPFM. It was selected from batch II (joint welded at a low rotation speed of 1000 RPM). The FM-KPFM testing was performed in the same area as TEM testing in order to get a detailed analysis of the weld faying interface. This study was done on a Bruker Dimension Icon XR scanning probe microscope with the newly developed Bruker Peak Force KPFM probe (PFQNE-AL), as shown in **Fig. 3.15a**. The experiments were carried out at the Industrial laboratory of Bruker in Coventry, UK

The geometric characteristics of the silicon tip used for FM-KPFM are shown in **Fig. 3.15b.**

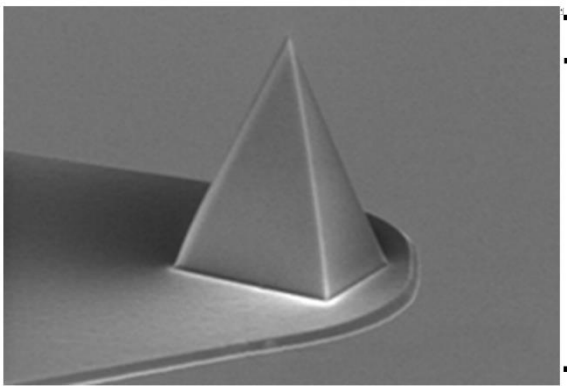

(a)

Geometry:	Rotated (Symmetric)
Tip height (μm)	2.5-8
Back angle (°)	25±2
Side angle (°)	17.5±2.5
Tip radius-Nom (nm)	5
Tip radius-Max. (nm)	12
Tip Set Back- Nom (μm)	5
Tip Set Back-RNG (μm)	0 – 7

(b)

Fig. 3.15 *(a) Silicon tip on silicon nitride cantilever (PFQNE-AL); (b) geometric characteristic of the tip* [160]

The topography of the surface was determined using the tapping mode at a cantilever resonance of 300 kHz. For the tests, the peak force was set at 2 nN while peak force amplitude was 30 nm. FM-KPFM is a single-pass high spatial resolution surface potential imaging technique which uses a small probe with a sharp tip (~ 5 nm) for scanning the sample in the predefined area to measure the surface potential, as shown in **Fig. 3.16a**. During FM-KPFM, a force gradient rather than the force is measured. [161].

The force gradient (dF_{es}/dz) technique is used to provide accurate measurements of work function. The work function is the minimum energy (or work, measured in eV) needed to remove an electron from a solid to a point immediately outside the solid surface. When two different conductors are brought in electrical contact, the electron will flow from the conductor with a lower work function to the conductor with a higher work function. This way the Femi energies equalize. If the conductors are made into a parallel plate capacitor, equal and opposite charges will be induced onto the surface. The surface (contact) potential established between those two surface equals the work function difference between the two materials [161,162].

Regarding FM-KPFM, if the work function of the probe is familiar, then the work function of the sample can be estimated as [161]:

$$\Phi_{sample} = \Phi_{probe} - e\Delta V_{CPD} \tag{3.1}$$

where Φ_{sample} is a work function of the sample (eV); Φ_{probe} is a work function of the probe (4.09 eV); ΔV_{CPD} is the contact potential difference between the probe (mV) and the sample extracted from the FM-KPFM results; e- is the charge of an electron.

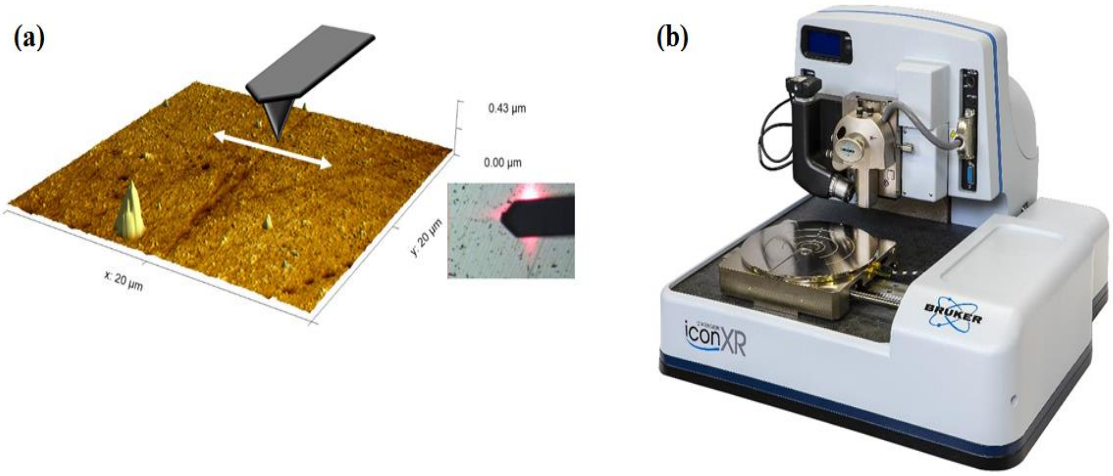

Fig. 3.16 *(a) Working principle of KPFM; (b) Bruker Dimension IconXR scanning probe microscope*

However, it is important to note that the values obtained are not by any means the fundamental parameters of the material phases and are strongly depended on surface state. The work function is extremely sensitive to the substrate (intrinsic) and environmental (extrinsic) gating due to its two-dimensional nature: Being representative of the surface state, work hardening can be strongly affected by such factors as traces of gas contamination, temperature, and humidity.

3.6 Mechanical properties

3.6.1 Microhardness

For evaluating the local variation in the mechanical properties, microhardness maps of the weld joints were obtained by using standard Vickers microhardness tests (DIN EN ISO 6507 1–2018) with a load of 0.1 kgf (0.98 N) using the Struers DuraScan 70 device illustrated in **Fig. 3.17**. A schematic diagram showing the microhardness mapping scheme on the FSSW sample cross-section is shown in **Fig. 3.18**. The distance between the two sequential indentation points was maintained at 0.33 mm to avoid interference of the stress waves between the two indent points.

The measurements were made in the form of four parallel lines. However, to avoid measuring hardness in the space between sheets and to avoid the influence of sheet edges on hardness values, some measurement points in the base material were adjusted around the sheet edge.

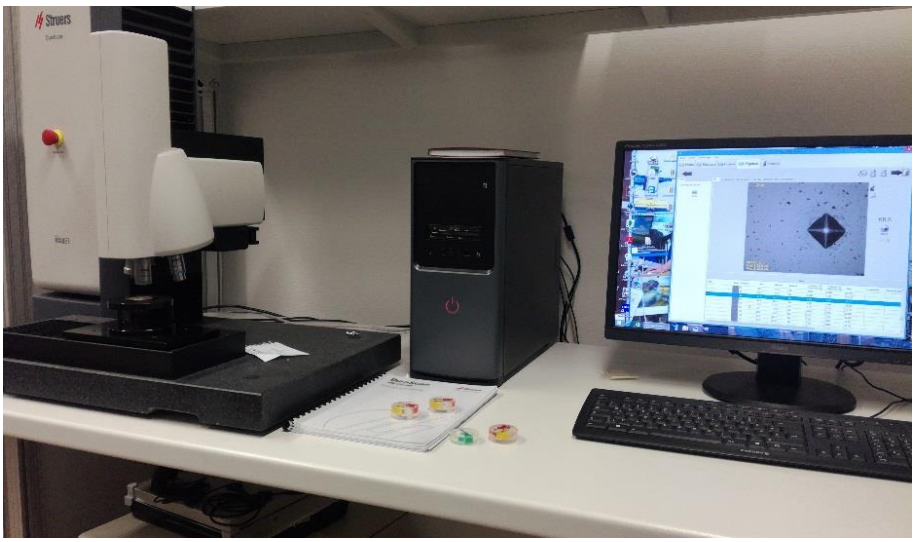

Fig. 3.17 *Vickers microhardness machine Struers DuraScan 70*

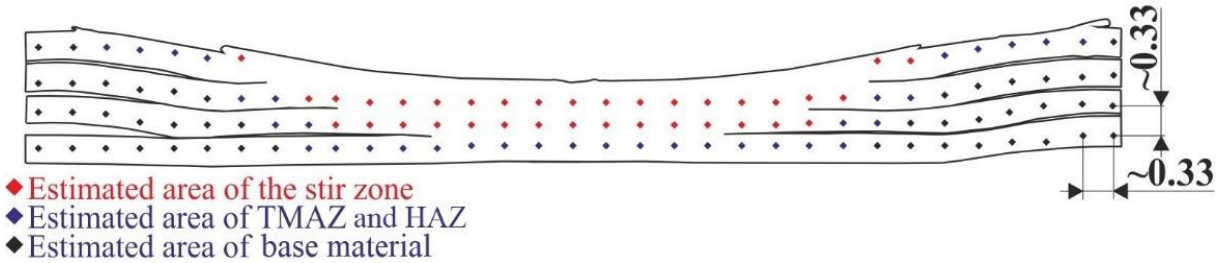

Fig. 3.18 *Schematic of the location of the microhardness measurement (all dimensions are in mm)*

3.6.2 In-situ Scanning Probe Microscope (in-situ SPM)

In this study, high-speed property mapping was performed to analyse the welding interface, as shown in **Fig. 3.19a** (red square), using the advanced nanomechanical test instrument Bruker Hysitron TI 980 Nanoindenter, which is shown in **Fig. 3.20**. The experiments were carried out at the Industrial laboratory of Bruker in Coventry, UK. High-speed X-Y actuation (up to 6 indents per second) can be achieved by using Hysitron tip-scanning piezo. The instrument was equipped with a Berkovich nanoindenter, which is a three-sided diamond pyramid with the same projected area-to-depth ratio as a Vickers indenter.

The Nanoindentation hardness calculations were made in accordance with the popular Oliver-Pharr Method [163,164]:

$$H_{IT} = \frac{P_{max}}{A_C} \tag{3.2}$$

where: P_{max} -peak force (N) and Ac -projected contact area (mm)

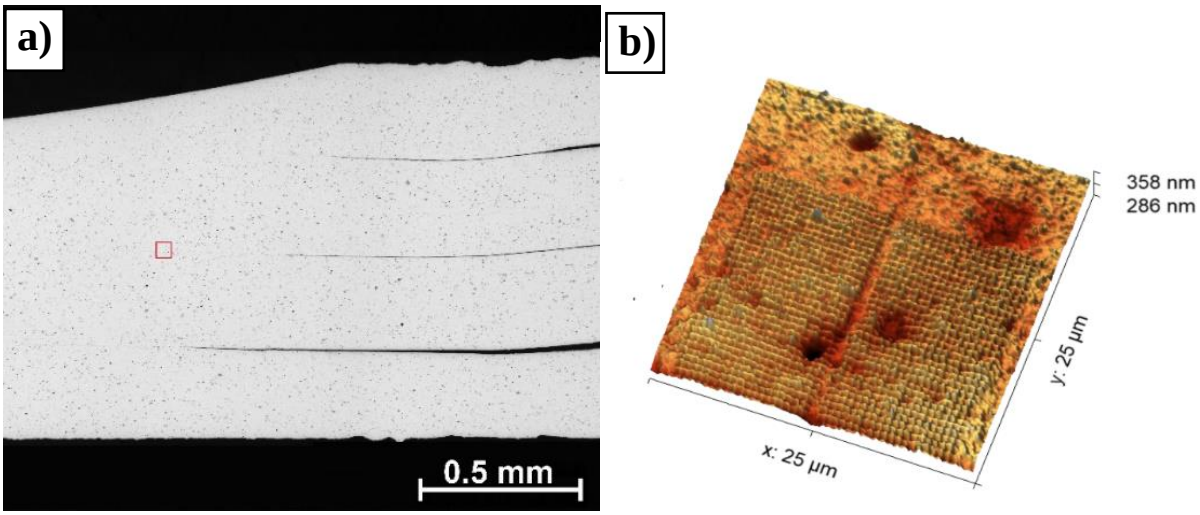

Fig. 3.19 *(a) Sample welded with 1500 RPM with an area where nanoindentation maps were made; (b) property map*

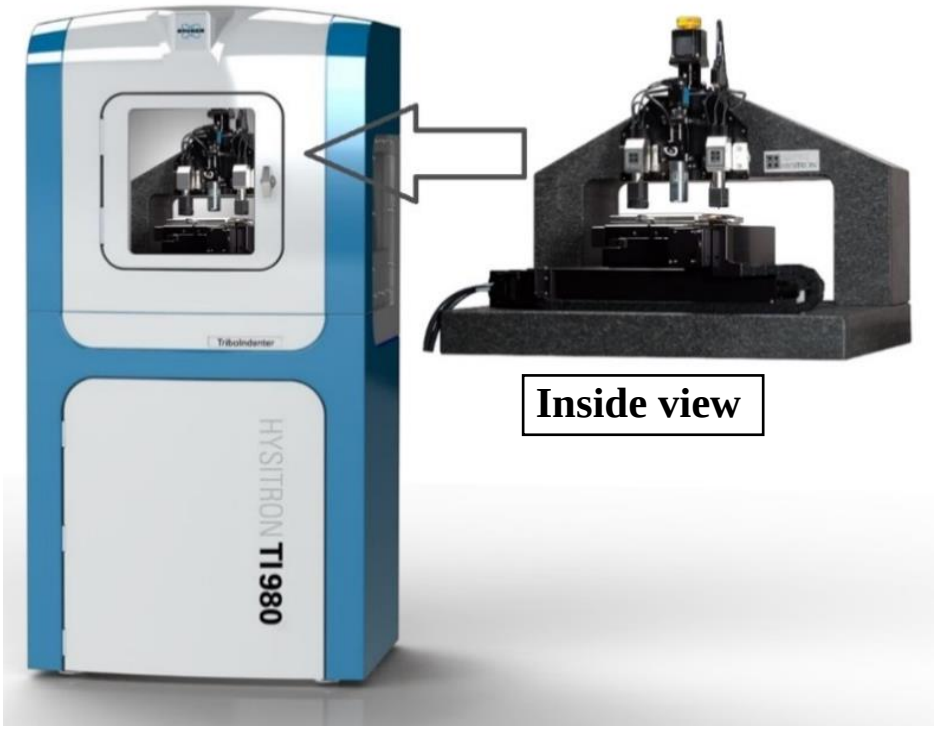

Fig. 3.20 *Bruker Hysitron TI 980 Nanoindenter*

Load is an important parameter during a nanoindentation hardness test. Pressing an unknown sample by the indenter while it achieves the present peak load in a given span of time governs

the loading rate whereas the retraction of the indenter in a given time governs the unloading rate. The representative load function used in this work is shown in **Fig. 3.21**. This load function was used to create an indentation map such that it contained 20 × 20 indents, each separated by 500 nm, created with a force-controlled method using a peak load of 150μN. Thus, 400 indents were created in a span of about 3 minutes.

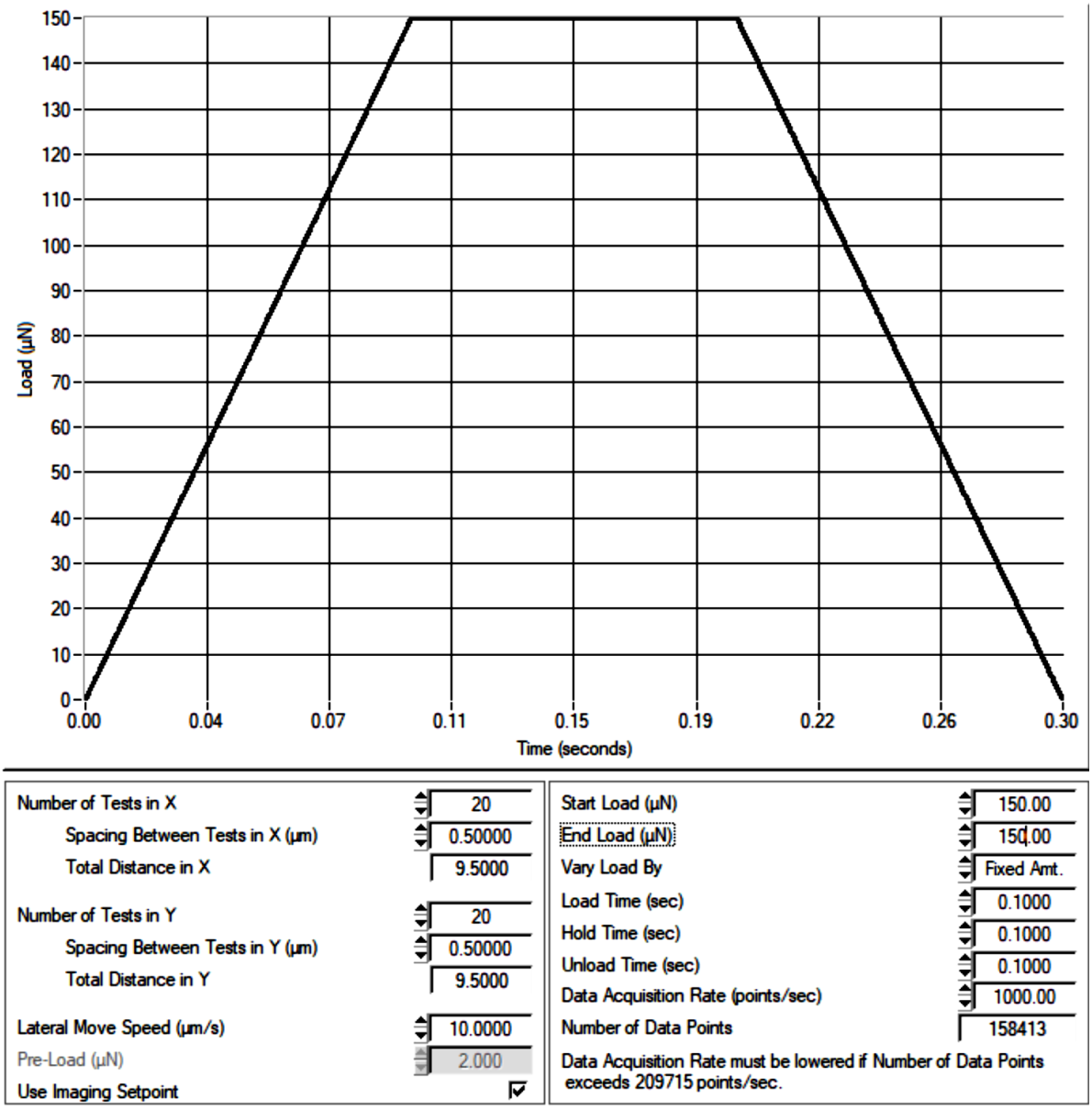

Fig. 3.21 *Nanoindentation parameters*

3.6.3 Small Punch Test (SPT)

To understand the mechanical properties of weld zone, a small punch test was performed. During the standard shear tensile test, which is usually used for obtaining information from spot welds, the fracture path is either observed at the periphery of the weld zone or along the

path of the weld interface. Therefore, no clear information from the mechanical properties of the weld zone can be provided. A SPT is a relative test which assesses load carrying capacity of fixed size specimens prior to failure. Thus, a SPT allows for a strength assessment of a material by assuming the load to be directly related to the strength of material, considering the geometry of test specimens remains the same in all specimens.
Welded samples from both batches (Batch I and Batch II) post-FSSW were tested by a small punch test, as shown in **Fig. 3.22**. The samples were cut in circles of 8 -0.005 mm in diameter. Thereafter, they were fine-grinded with 600, 1200 and 2500 grit abrasive papers to the target thickness of 0.8 ± 0.01 mm, as shown in **Fig. 3.22**. Also, the three samples from the base material AA 5754 – H111 were prepared for a SPT in order to estimate weld efficiency. The plates used for preparation of the specimens were 1.2 mm thick, obtained from the same supplier, in order to provide 0.8 mm thick specimens for the SPT.

The European "Code of Practice" [165] suggest using a standard geometry of 0.5 mm thick sample. However, in this study, it was important to take all three weld interfaces (between the four sheets), so a sample thickness of 0.8 mm was considered judiciously. The emphasis was on comparing the mechanical properties of samples welded with different parameters and to compare them with base material in order to determine weld efficiency. Fracture path after the SPT was also examined.

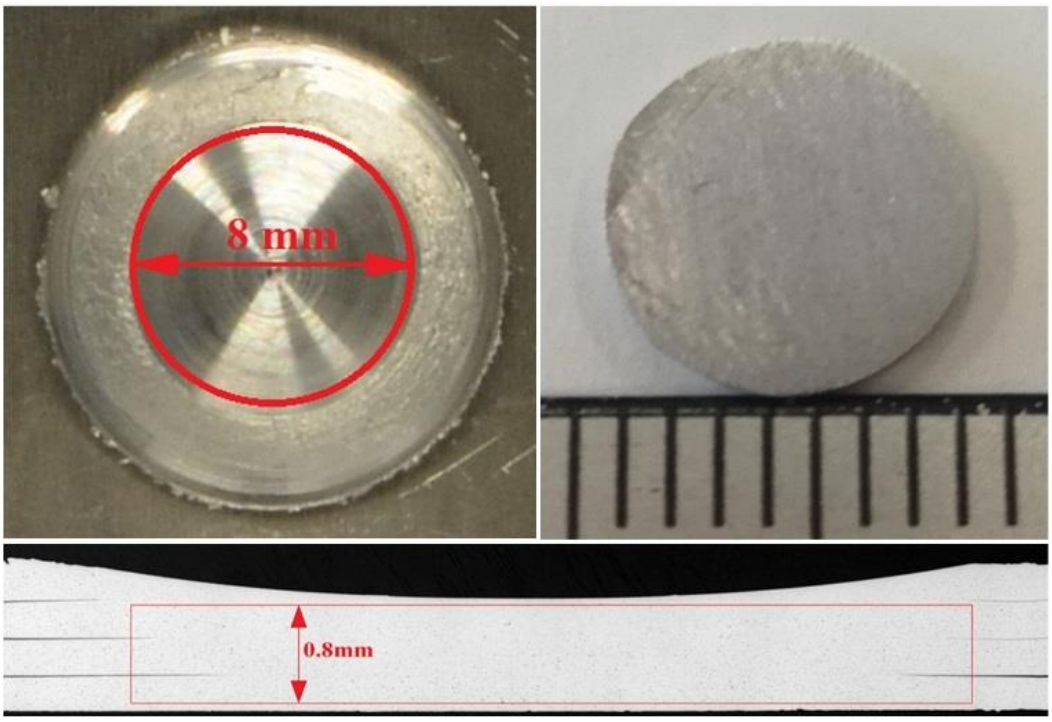

Fig. 3.22 *Preparation of the SPT sample; the top figure shows the 8 mm diameter of the sample (width measurement in the bottom figure) such that the thickness of the sheet was 0.8 mm*

The small punch test (SPT) was carried out on a Hagewald and Reshke Inspect Retrofit universal testing machine with a maximum load of 20 kN, as shown in **Fig. 3.23a**. The SPT helped in evaluating the mechanical properties of weld joints according to the procedure described by Rasche *et al.* [166]. A test speed of 2 mm/min was chosen to ensure the quasi-

static loading state. Three SPT samples were tested from each weld obtained with different rotational speed and from base material. The preparation of the samples and the SPT were performed at the Department of Production Technology, Ilmenau University of Technology, Ilmenau, Germany.

The SPT equipment setup is shown in **Fig. 3.23b**. A disc-shaped sample of 8 mm diameter and 0.8 mm thickness was centrally positioned in a receiving die and then deformed with a spherically tipped punch until failure. In comparison to the geometry recommended by European "Code of Practice" CWA 15627:2006, the SPT setup geometry was modified as to use smaller samples (diameter 3 mm and 0.25 mm thickness). In a standard SPT setup, the outer part of the disc is clamped rigidly between the receiving and counter dies (Small Punch Bulge Test) or only positioned loosely between them (Small Punch Drawing Test) to prevent vertical deformation. The screwed counter die is named the *downholder*. In this study, an improved experimental setup is used without the downhoader, so this technique can be considered to be a *Small Punch Bending Test* [166,167]. The SPT Parameters used for the testing are shown in **Table 3.4** and **Table 3.5**.

.

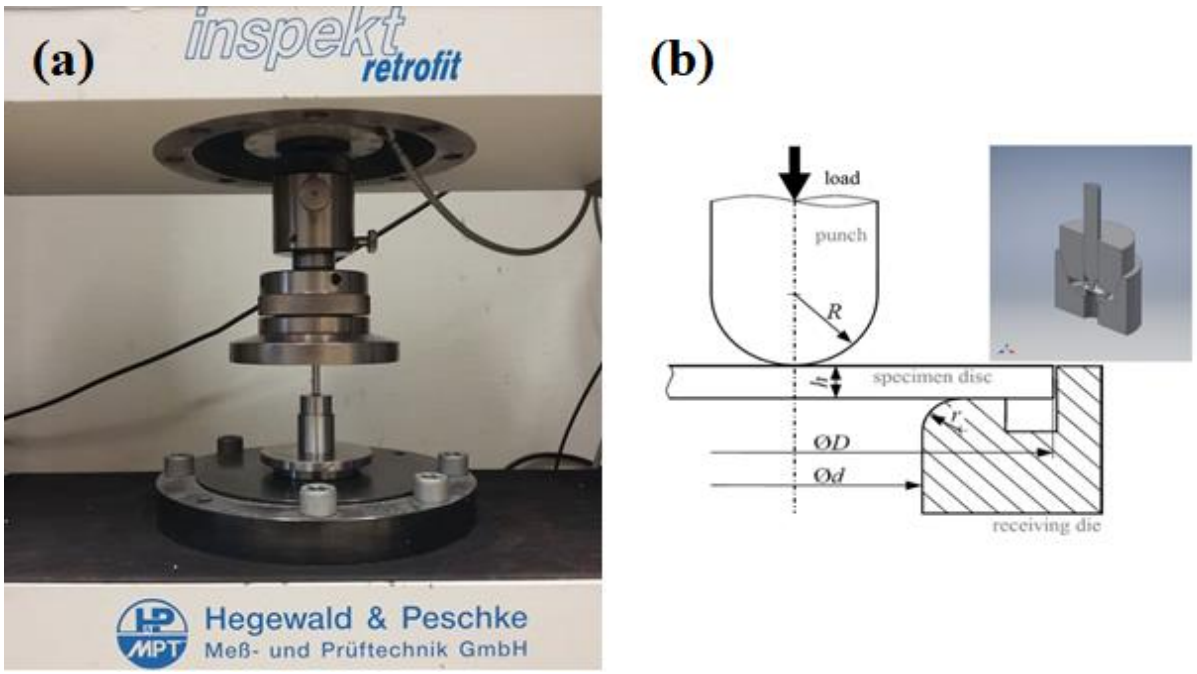

Fig. 3.23 *The SPT setup: (a) SPT setup placed on the tensile test machine; (b) SPT setup designed by Rasche et al.* [166]

Table 3.4 SPT parameters for batch I welded with tool T1

Sample	Welding parameters				SPT sample	
	Axial force F (kN)	Rotational speed n (RPM)	Plunge depth h (mm)	Time t (s)	mass m (mg)	thickness a (mm)
Batch I (T1)						
SPT-RW1-1	2	1500	0.25	5	90	0.795
SPT-RW1-2				4,67	93	0.795
SPT-RW1-3				4,70	93	0.8
SPT-RW2-1	2	2000	0.25	3,60	93	0.8
SPT-RW2-2				3,65	98	0.795
SPT-RW2-3				3,12	97	0.795
SPT-RW3-1	2	2500	0.25	2,39	91	0.795
SPT-RW3-2				2,43	88	0.795
SPT-RW3-3				2,26	92	0.790
SPT-RW4-1	2	3000	0.25	2,57	91	0.8
SPT-RW4-2				2,28	96	0.8
SPT-RW4-3				2,07	97	0.8
SPT-RW5-1	2	3500	0.25	1,32	96	0.790
SPT-RW5-2				1,53	90	0.795
SPT-RW5-3				1,48	93	0.8

Table 3.5 SPT parameters for batch II welded with tool T2

Sample	Welding parameters				SPT sample	
	Axial force F (kN)	Rotational speed n (RPM)	Plunge depth h (mm)	Time t (s)	mass m (mg)	thickness a (mm)
Batch II (T2)						
SPT- RWA1-1	4	1000	0.25	1.81	92	0.795
SPT- RWA1-2				1.67	90	0.795
SPT- RWA1-3				1.75	92	0.8
SPT- RWA2-1	4	1500	0.25	1.46	94	0.795
SPT- RWA2-2				1.39	96	0.795
SPT- RWA2-3				1.31	93	0.795
SPT- RWA3-1	4	2000	0.25	1.02	90	0.795
SPT- RWA3-2				0.99	95	0.79
SPT- RWA3-3				1.15	91	0.795
SPT- RWA4-1	4	2500	0.25	1.14	98	0.8
SPT- RWA4-2				0.99	95	0.8
SPT- RWA4-3				0.96	92	0.79
SPT- RWA5-1	4	3000	0.25	0.98	95	0.795
SPT- RWA5-2				0.93	96	0.795
SPT- RWA5-3				1.01	93	0.8
SPT- RWA6-1	4	3500	0.25	0.96	94	0.8
SPT- RWA6-4				1.03	94	0.795
SPT- RWA6-5				1.04	94	0.8
SPT- RWA7-2	4	4000	0.25	0.95	97	0.8
SPT- RWA7-3				0.97	93	0.8
SPT- RWA7-4				0.76	91	0.79
SPT- RWA8-1	4	4500	0.25	0.92	91	0.8
SPT- RWA8-2				0.89	93	0.795
SPT- RWA8-3				0.94	91	0.795

4. EXPERIMENTAL RESULTS

In this chapter, the results of the experimental research of FSSW aluminium alloy AA 5754-H111 joints produced by using two tool geometries, T1 and T2 (see **Fig. 3.5**), are presented. The aim was to develop and understand the FSSW process of multiple sheets and to optimise the process for rapid welding with a dwell time of less than 1 second.

To understand the welding process and bonding mechanisms, several experimental studies were analysed, including:

(i) analysis of the welds at the micro-level in order to understand the mechanisms leading to inconsistent mechanical properties, the differences in grain size in different weld zones (SZ, TMAZ, HAZ), variations in grain size between welds obtained with different tools and parameters, and the difference in shape and size of welded zones between samples welded with different welding parameters.

(ii) analysis of the mechanical properties of the welds obtained with different welding parameters and tool geometries in order to understand their influence on weld strength.

(iii) analysis of the welding interface at a nano level in order to understand bonding mechanism, the size and type of defect, and their influence on fracture mechanism.

To understand weld formation, a series of tests such as thermal measurements, dimensional quantification, microstructural characterization and mechanical testing (at the micro and nano level) were performed.

4.1 Analysis of welding variables

The most influential parameters on the welding process are rotational speed, axial load, penetration depth, dwell time and tool geometry. The penetration depth was selected to be 0.25 mm in all experiments. This depth was optimum as it was found to be the minimum depth from trial experiments that allowed bonding between four sheets to occur. Axial loads of 2 kN for batch I and 4 kN for batch II were found to be the maximum loads that could provide welding conditions between four sheets. If the axial loads are set to be less than 2 kN with tool T1 or 4 kN with tool T2, dwell time increases significantly. Thereafter, rotational speed was varied from 500 RPM to 5000 RPM. It was found that the bonding between all four sheets can be accomplished with rotational speeds of 1500 to 3500 RPM for batch I and 1000 to 4500 RPM for batch II. Outside of these ranges, the last two sheets were not successfully bonded, as shown in **Fig. 4.1**, or dwell time exceeded 5 seconds, which is the maximum time possible with the machine used for the experiments.

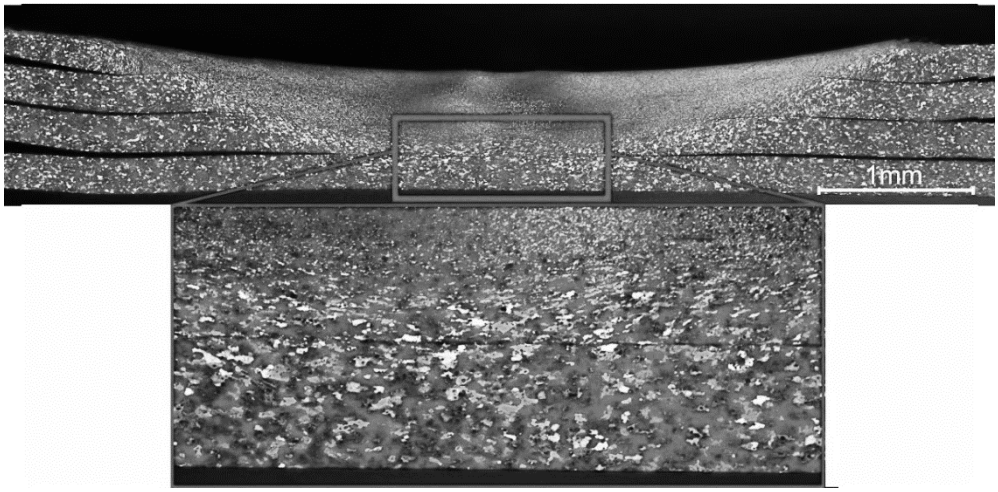

Fig. 4.1 *Sample welded with tool T1; rotational speed 4000 RPM, axial load 2 kN and penetration depth 0.25 mm (the last two sheets were not bonded)*

4.1.1 Stress analysis

The evolution of two major stresses present in the stir zone, namely applied axial stress and shear stress, over the dwell time and contact radius are presented in **Fig. 4.2** (from **a** to **e**) for batch I and in **Fig. 4.3** and **Fig. 4.4** (from **a** to **d**) for batch II. In all these figures, shear and axial stresses are presented in black and red lines, respectively. The purple dashed lines correspond to incipient strain hardening of the base material and blue dashed lines correspond to the tensile strength of base material, both obtained from stress-strain curves of the base material provided in **Fig. 3.1**. It is important to consider that, during welding, a frequent alteration of the strain hardening and thermal softening is likely. The axial stress and shear stress were calculated from equations (2.8) and (2.9).

In both batches at low rotational speeds (1500 and 2000 RPM in batch I and 1000 and 1500 RPM in batch II), the value of shear stress fluctuated between the ultimate tensile stress and the incipient transformation limit of work hardening. However, at high rotational speeds (2500-3500 RPM in batch I and 2000-4500 RPM in batch II) shear stress at beginning of the welding process overcome the tensile strength limit and, before the end of the process, shear stress drops below the incipient strain hardening transformation limit.

The stick-slip mechanism was observed during the early stages of contact during which the tool establishes contact with the workpiece. In this stage, axial stress dominates over shear stress. After the shear stress overcomes axial stress, the condition for a steady-state weld are met. A steady-state weld stage subsequently develops such that the material flow becomes pronounced and, in this state, shear stress takes over the axially applied pressure.

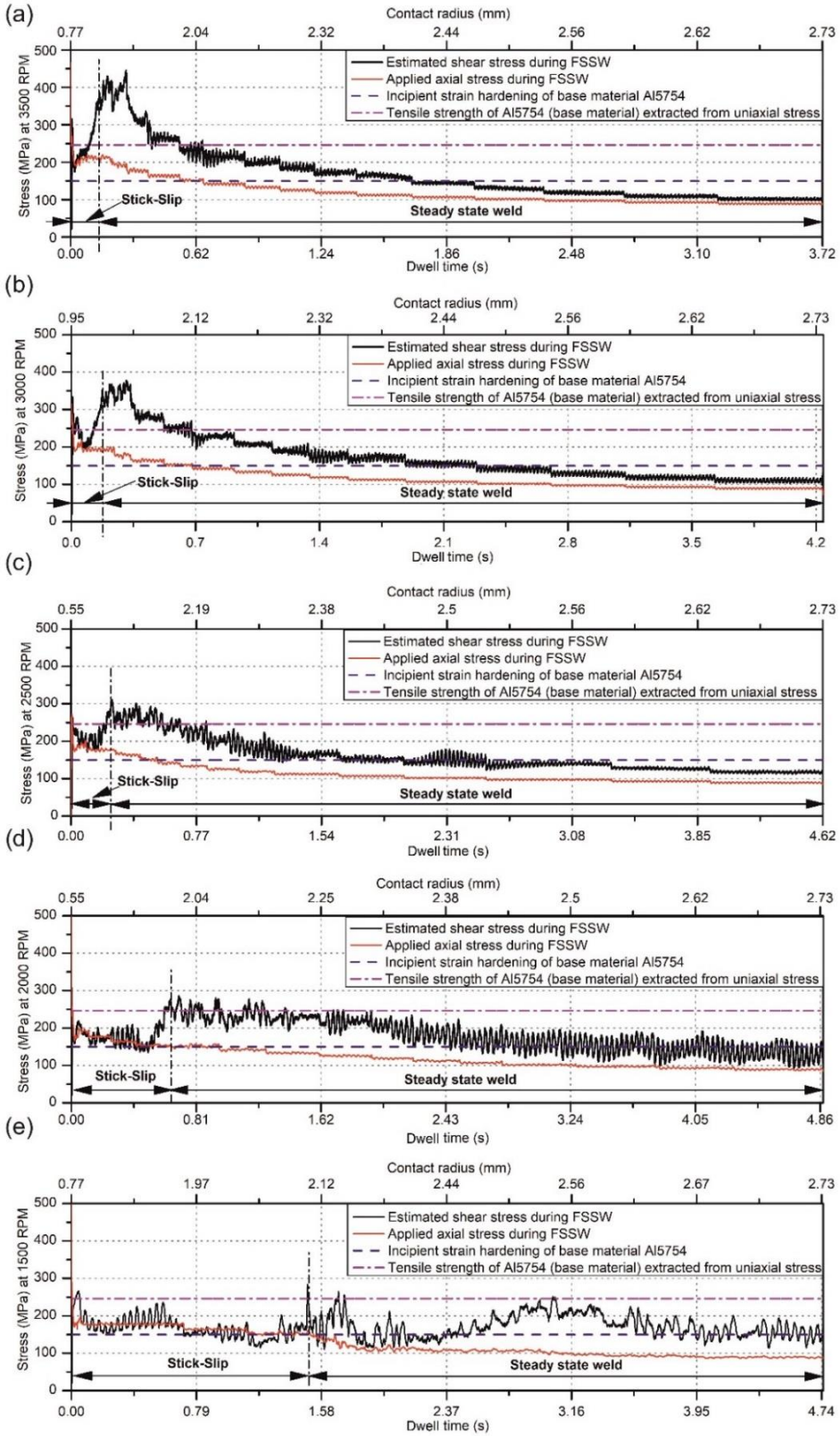

Fig. 4.2 *(a) to (e) Evolution of applied axial stress and shear stress over time measured by using the applied load and estimated torque data at different RPM ranging from 1500 RPM to 3500 RPM*

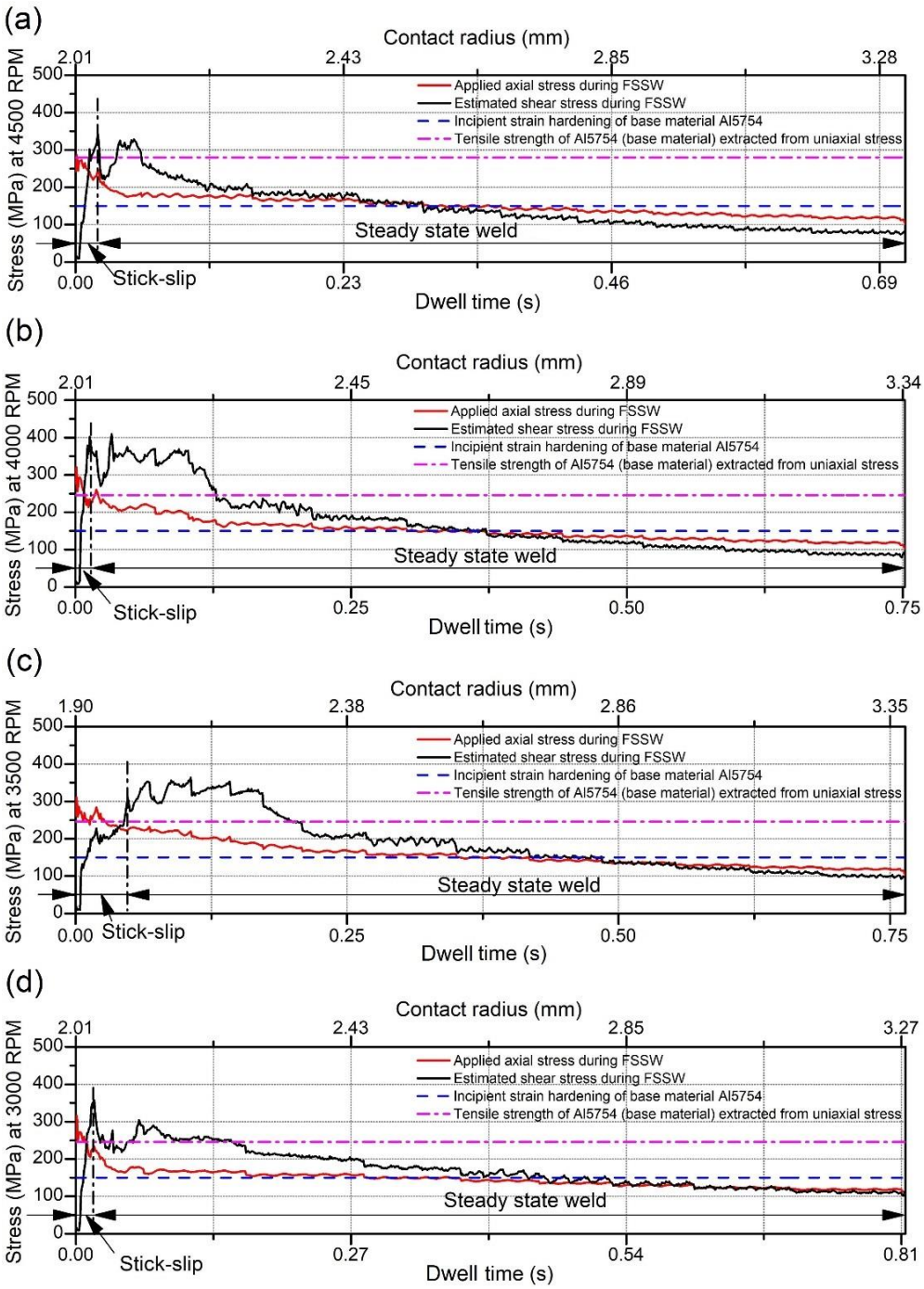

Fig. 4.3 *(a) to (d) Evolution of applied axial stress and shear stress over time measured by using the applied load and estimated torque data at different RPM ranging from 3000 RPM to 4500 RPM*

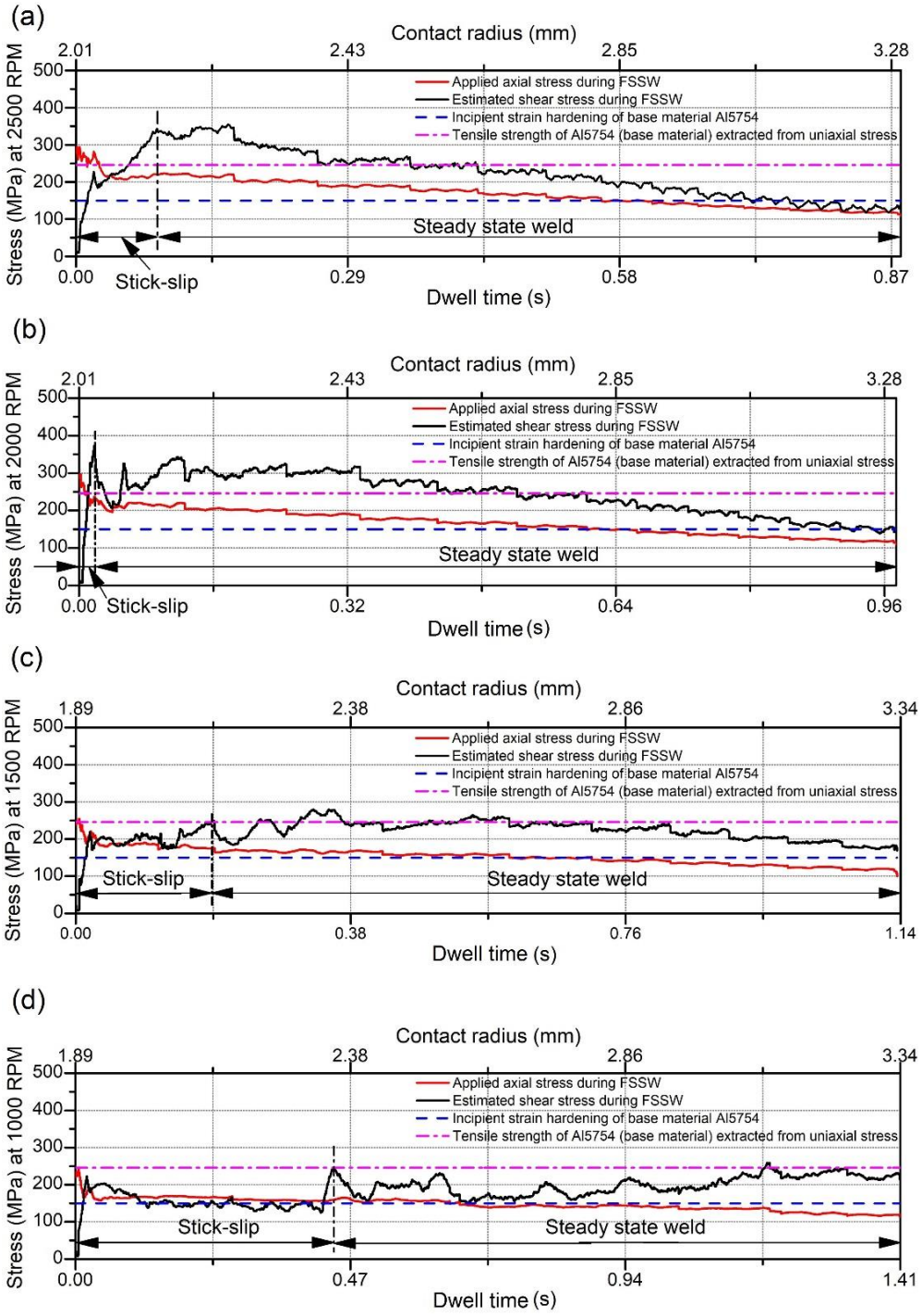

Fig. 4.4 *(a) to (d) Evolution of applied axial stress and shear stress over time measured by using the applied load and estimated torque data at different RPM ranging from 1000 RPM to 2500 RPM*

4.1.2 Coefficient of Friction (CoF)

In **Fig. 4.5** and **Fig. 4.6** the variation in the kinetic coefficient of friction (CoF) calculated by using equation (2.7) for five welding trials for batch I and eight welding trials for batch II has been shown. The horizontal axes in **Fig. 4.5** and **Fig. 4.6** show process times (which include the time needed for clamping, tool approaching, welding, and withdrawal of the tool and clamp). The values of CoF was observed to vary between 0.75 and 2.5 for batch I and between 0.6 and 2 for batch II.

For Batch I, from **Fig. 4.5** it can be seen that the CoF increases from the beginning to the end of the process at low rotational speeds (1500 and 2000 RPM). As for the samples of batch I welded at higher rotational speeds (2500, 3000 and 3500 RPM), the CoF increases up to maximal value immediately after the beginning of the process and afterwards decreases slowly until the end of the process.

For Batch II, as shown in **Fig. 4.6**, different trends of CoF plots were obtained at different rotational speeds. In analogy to batch I on lower rotational speeds (1000 and 1500 RPM), the CoF will increase from the beginning to the end of the process. However, during the welding processes with rotational speeds of 2500, 3000, 3500, 4000 and 4500 RPM, it will reach the peak value at the beginning of the welding and afterwards will decrease at the end of the process. The exception is the welding process obtained with 2000 RPM where CoF slowly increases to the peak value at 2.6 seconds and afterwards slowly decreases to the end of the process.

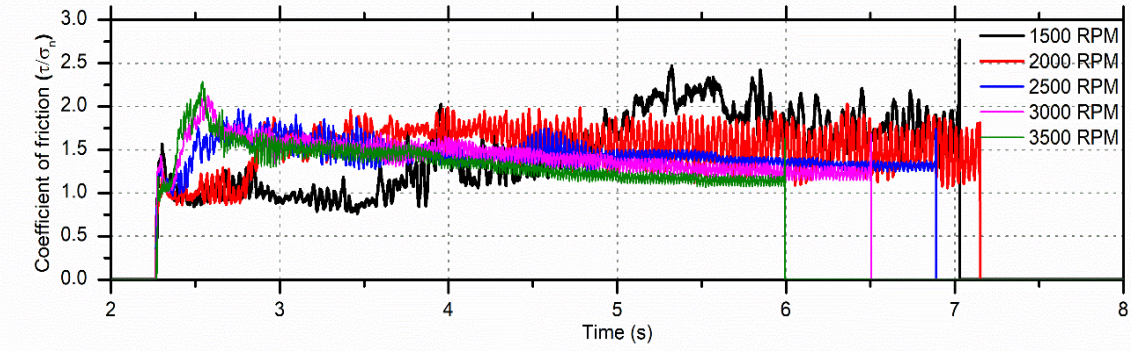

Fig. 4.5 *Variation in the coefficient of friction (CoF) in batch I*

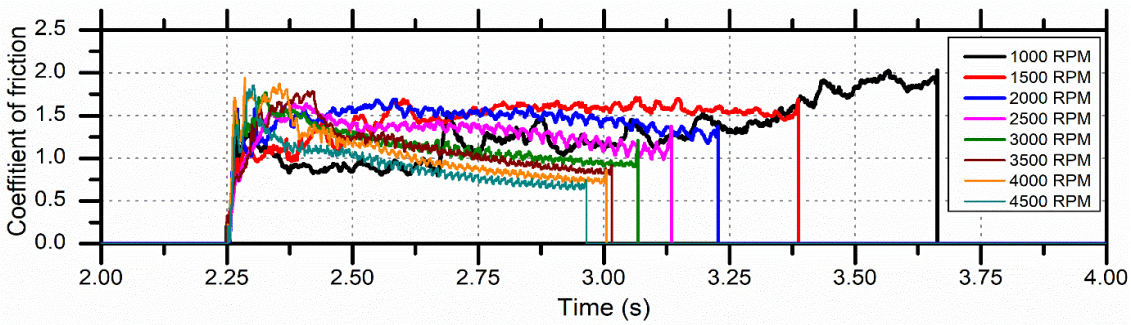

Fig. 4.6 *Variation in the coefficient of friction (CoF) in batch II*

4.1.3 Dwell time and thermal analysis

In **Fig. 4.7a** and **b**, the variation in dwell time (welding time) and maximum temperature measured at the bottom of the sample are respectively shown. A main flaw of the temperature measurements was that they were point measurements taken far from the tool; the lowest temperature is expected in the stir zone. However, at least this data can help to understand and compare heating in the samples welded with different tool geometries and parameters.

From **Fig. 4.7a,** it can be seen that in both batches dwell time decreases with increasing rotational speed. The significant reduction in dwell time of all samples in batch II compared with batch I is particularly notable. Nearly half of the samples from batch II welded at higher rotational speeds (from 3000 to 4500 RPM) were welded in less than one second.

Increasing the rotational speed of the tool increases the process temperature in the stir zone for both batches, as shown in **Fig. 4.7b**. The maximum temperatures in both batches were similar. It seems that dwell time does not influence maximum temperatures. **Fig. 4.7a and b** show that maximum temperature is almost equal for batch I and II even though weld time is approximately three times higher in batch I.

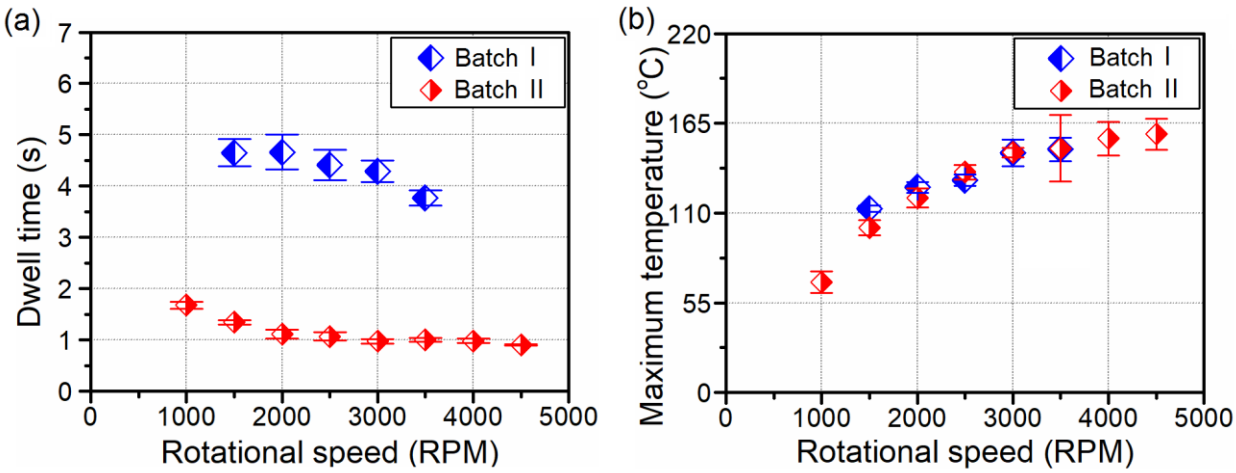

Fig. 4.7 *(a) Dwell time and (b) maximum temperature variation as a function of the rotational speed*

4.2 Surface topography assessment of the top surface of FSSW joints and tools

Both tools (T1 and T2) were produced in the same way, thus the roughness of both tool contact surfaces had a similar trend. Consequently, only the contact surface profile of tool T1 and contact surface profile of weld joints from batch I welded with 3500 RPM were measured and presented in this work. **Fig. 4.8** shows a macrograph of a tested sample (**Fig. 4.8a**) considering the 8.5 mm length of surface topography data congruently laid at the same scale and positions

to show the similarities and influence of the texture of the tool T1 on the FSSW surface shown in **Fig. 4.8b** and **c**. The topography data was produced from the surface profilometer using the steps described in the experimental section. However, the measurement of the welded surface was mirrored, as shown in **Fig. 4.8c,** for representation and comparison at the same scale as the tool shown in **Fig. 4.8b**. It can be seen that the tool surface profile and welded surface profile have identical textures. It can be inferred that the topography irregularities of the tool passes on to the top sheet of the weld surface.

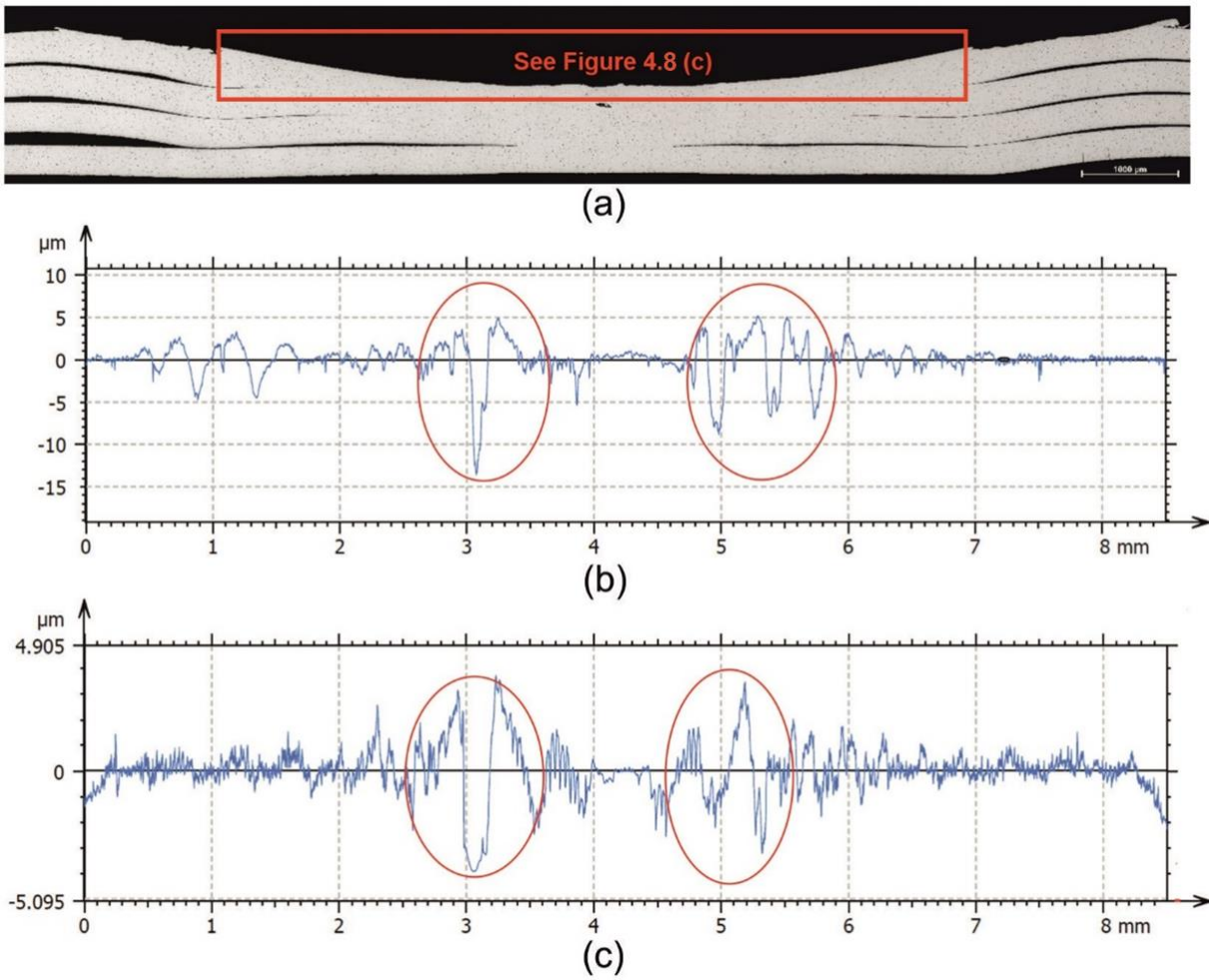

Fig. 4.8 *(a) Light microscope image of the cross-section of the tested FSSW joint; (b) central part of the surface topography of the tool T1 (after form removal and Gaussian filter of 0.8 mm) of length 8.5 mm compared with (c) mirrored view of the top part of the surface topography of the FSSW surface after form removal and Gaussian filter of 0.8 mm*

4.3 Scanning acoustic microscope (SAM) analysis

The SAM results for the sample welded at 1000 RPM from batch II are presented in **Fig. 4.9a-f**. In **Fig. 4.9a**, the surface topography map of the top surface obtained from the SAM is presented. A high degree of plastic deformation on the upper surface from centre of the weld to the periphery can be seen. In **Fig. 4.9b** and **d,** C-scans of the sample in different gate

positions are shown. The scan in **Fig. 4.9b** is a C-scan of the top surface where the material flow pattern can be seen. The second C-scan from **Fig. 4.9d** shows white circles inside the stir zone which can be interpreted as delamination circles (blue arrows). The white ring around the stir zone represents unbonded regions.

In **Fig. 4.9c**, B-scan (A–A cross-section) of the stir zone is presented. Green arrows indicate the presence of an unknown layer further called the *weld faying interface* (WFI). However, this layer needs a detailed analysis because, during the scanning of the sample with SAM in C-scan, some artefacts may occur. In **Fig. 4.9e,** the entire A-scan is shown and **Fig. 4.9f** shows a higher magnification detail from **Fig. 4.9e**.

The first two peaks represent the initial pulse formed between the transducer and the water. The next peak represents the reaction between the water and sample surface and the third peak represents the reaction of the bottom surface and the water. All peaks afterwards are the echo (artefacts) produced from the sample.

In **Fig. 4.10** and **Fig. 4.11** the arrangements of the results are the same as in **Fig. 4.9**. The difference is in the size of the defects and unbonded region in the last sheet. The deformation of the upper contact surface is lowest in the sample welded with 2500 RPM. However, the size of the delamination circles and unbonded ring are the highest in the sample welded with 4500 RPM. They are lowest in sample welded with 1000 RPM; delamination circles can be seen only near the end of the stir zone in the so-called transition zone. In samples welded at 2500 and 4500 RPM, delamination circles spears through the entire stir zone. The WFI is mostly visible in the samples welded at 1000 RPM.

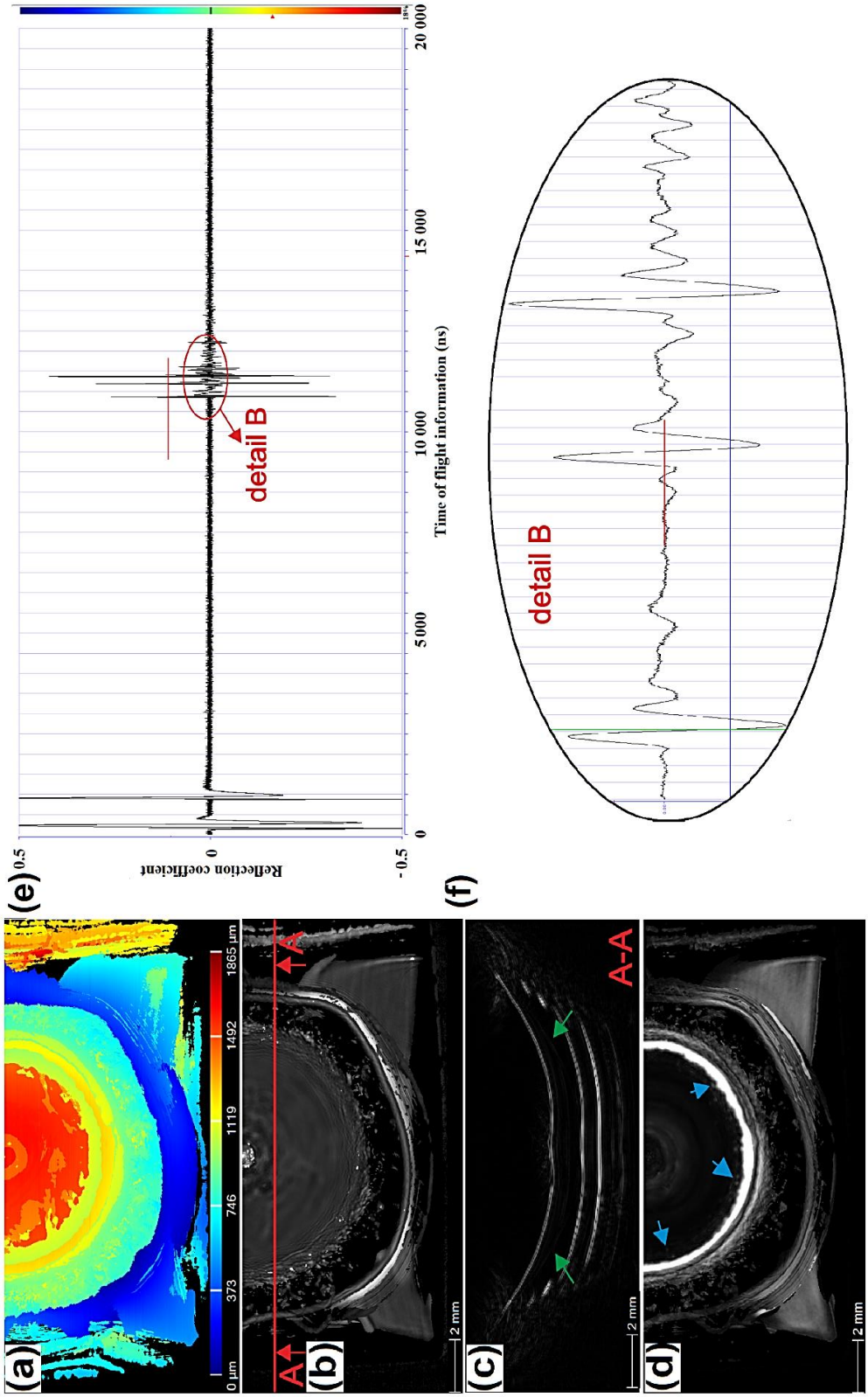

Fig. 4.9 *The sample from batch II welded with 1000 RPM: (a) topography map from the top surface; (b) C-scan with gate position 20 ns and gate length 50 ns with A-A cross-section showing the place where B-scan was obtained; (c) B-scan from A-A cross-section; (d) C-scan with gate position 220 ns and gate length 50 ns as shown in detail B with a red line on A-scan; (e) A-scan with detail showing the gate length of C-scan from (c); green and blue arrow show the WFI and delamination circles, respectively; (f) detail of A-A scan from (e)*

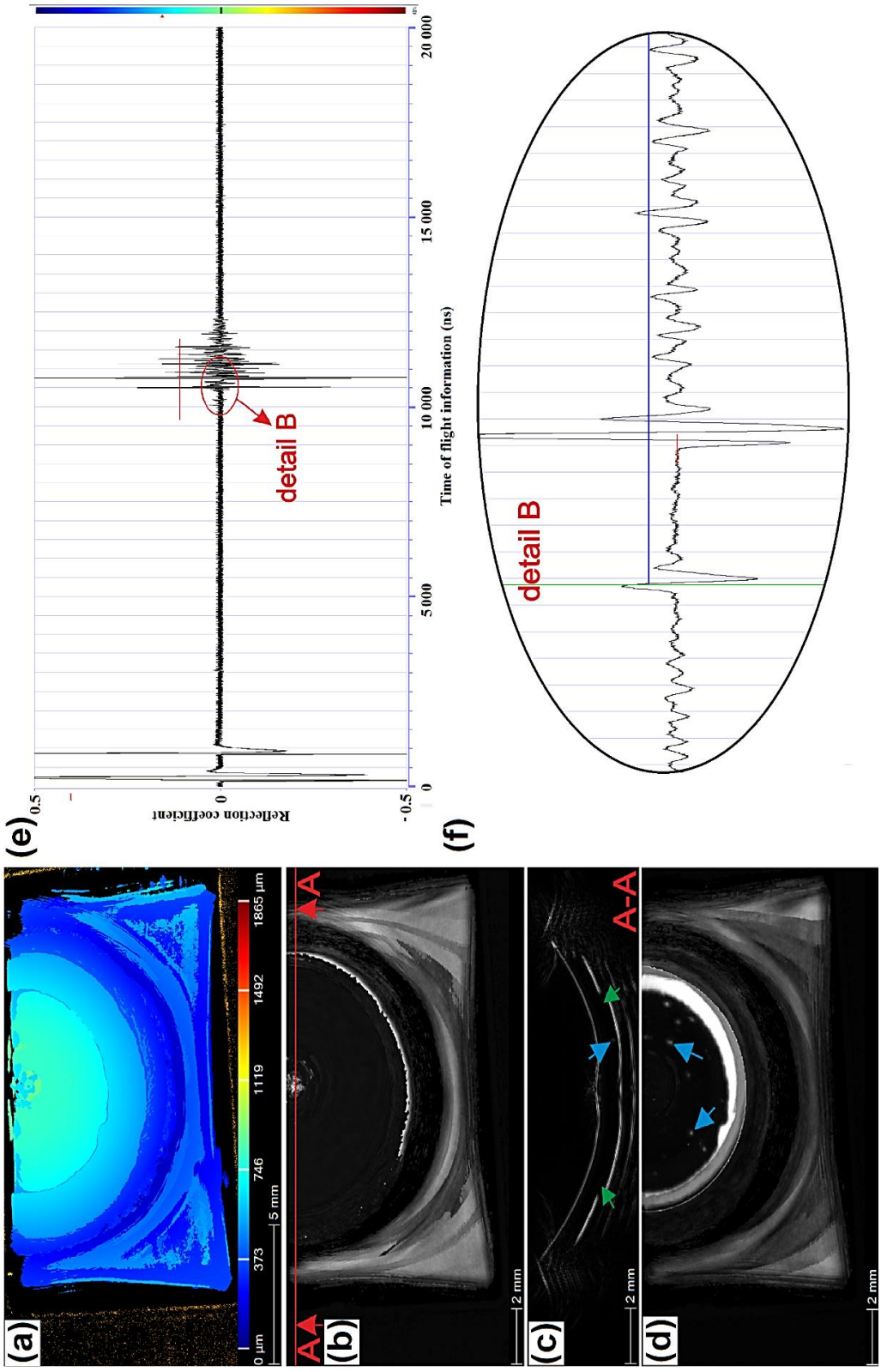

Fig. 4.10 *The sample from batch II welded with 2500 RPM: (a) topography map from the top surface; (b) C-scan with gate position 20 ns and gate length 50 ns with A-A cross-section showing the place where B-scan were obtained; (c) B-scan from A-A cross-section; (d) C-scan with gate position 220 ns and gate length 50 ns as shown in detail B with red line on A-scan; (e) A-scan with detail showing the gate length of C-scan from (c); green and blue arrow show the WFI and delamination circles, respectively; (f) detail of A-A scan from (e)*

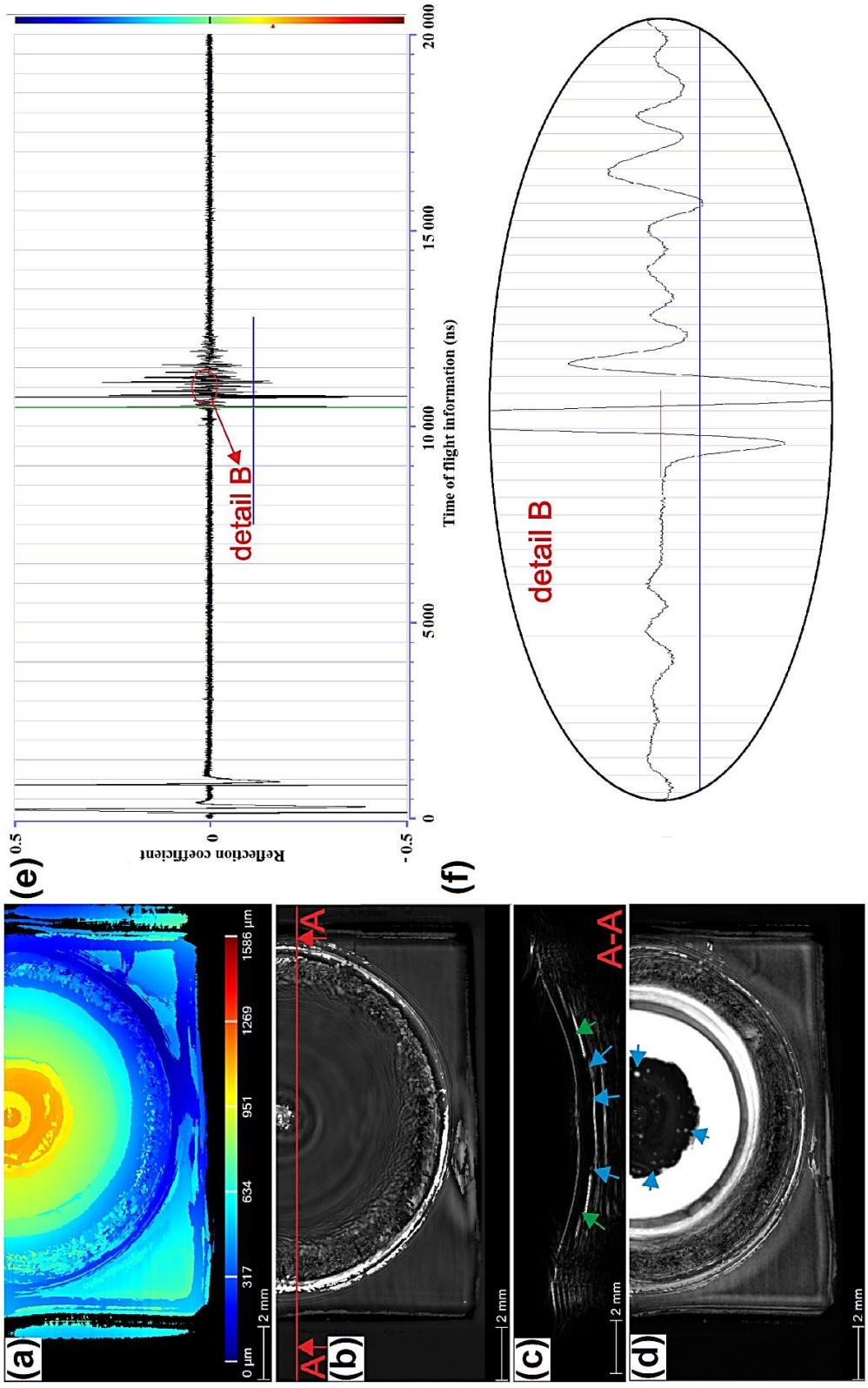

Fig. 4.11 *The sample from batch II welded with 4500 RPM: (a) topography map from the top of the sample; (b) C-scan with gate position 20 ns and gate length 50 ns with A-A cross-section showing the place where B-scan was obtained; (c) B-scan from A-A cross-section; (d) C-scan with gate position 220 ns and gate length 50 ns as shown in detail B with red line on A-scan; (e) A-scan with detail showing the gate length of C-scan from (c); green and blue arrow show the WFI and delamination circles, respectively; (f) detail of A-A scan from (e)*

4.4 Metallographic results

4.4.1 Macrostructural characterization

In **Fig. 4.12a** macrographs of the top view of the welds, in **Fig. 4.12b** cross-sections of polished and in **Fig. 4.12c** etched views of the samples welded at different rotational speeds from batch I are shown. In all macrographs, two different areas can be seen. The first one is the edge-chipping area and is indicated with a white arrow in **Fig. 4.12a**. It is a very rough area with visible marks of fracture and deformation. The second area, which is indicated with a black arrow, is a *stable contact area*. In this zone, the tool was in full contact with the workpiece. In the edge chipping area, the tool was only partly in contact with the upper sheet due to local deformation of the upper sheet caused by the action of the clamping force from one side and radial force of the tool from the other side. These two forces tend to bend the upper sheet, causing unstable low-pressure contact with the outer diameter of the tool. From all macrographs, a different ratio of *edge-chipping area* to *stable contact area* can be seen.

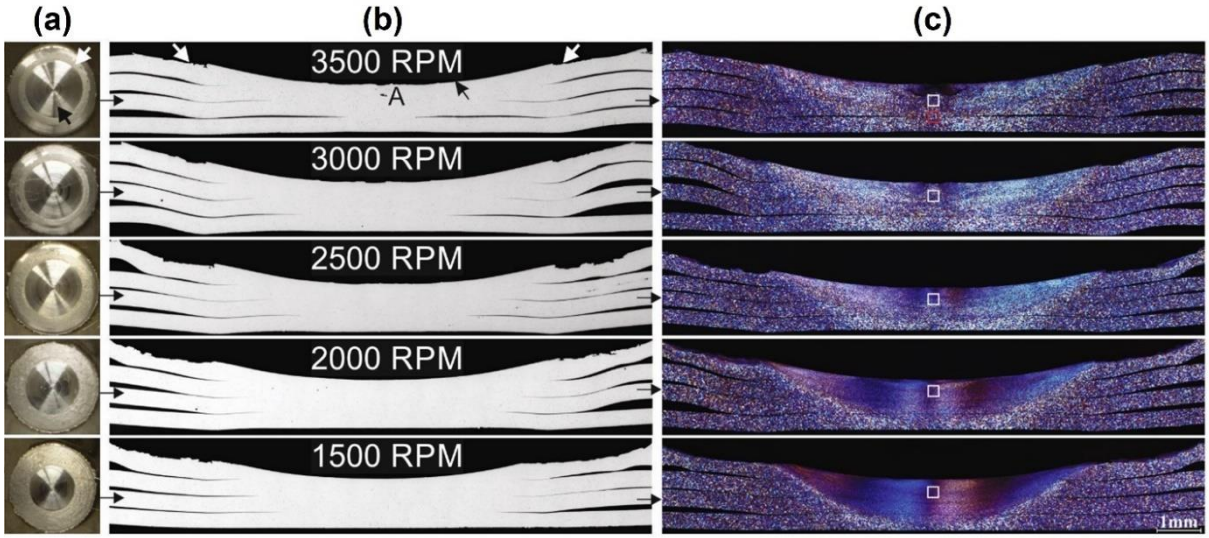

Fig. 4.12 *(a) Macrographs; (b) polished; (c) etched cross-section views of the welded joints from batch I at different RPM (from 3500 to 1500 RPM)*

In polished cross-sections, the *edge-chipping area* is also indicated with a white arrow while *stable contact area* is indicated with a black arrow. The weld zone lies underneath the *stable contact area*. The influence that the RPM or the applied strain rate makes at the shape of the weld can also be seen from the micrographs. The weld shape changes its aspect ratio (width/depth) as a function of rotation speed. From the polished cross-sections, no defects were seen in samples welded from 1500 to 3000 RPM. The sample welded at a rotation speed of 3500 RPM showed a small defect-like void below the surface marked with A in **Fig. 4.12b**. In etched cross-sections, the differences in grain size and orientation at different rotational speeds can be seen. Also, the transition between the stir zone and TMAZ is much clearer in samples welded with low RPM. By contrast, this transition occurs gradually in samples welded with high RPM.

Cognate to the previous section, Figure 4.13 shows the same illustrations for batch II. A few notable differences can be seen:

(i) The weld zone of all samples in batch II is wider than batch I.
(ii) There are no visible defects such as voids or delamination in the stir zone.
(iii) The ratio of the edge-chipping area to stabile contact area for all samples in batch II was lower compared with those of batch I.
(iv) A wide variation in the orientation and size of the grains can be seen.

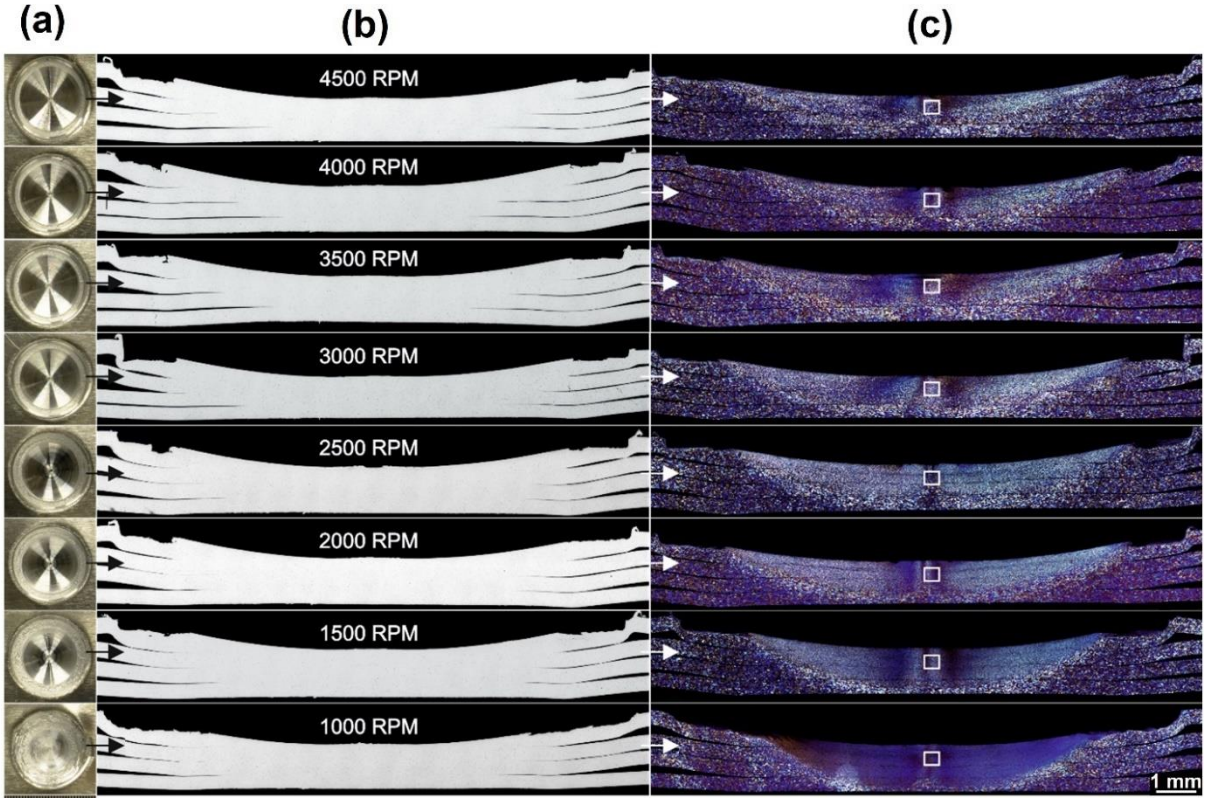

Fig. 4.13 *(a) Macrographs; (b) polished and (c) etched cross-section views of the welded joints from batch II at different RPM (from 4500 to 1000 RPM)*

4.4.2 Microstructural characterisation

4.4.2.1 Stir zone

In **Fig. 4.14**, the microstructures of the base material and stir zones is depicted at a higher magnification. These results shed light on a clear influence of rotation speed on grain size and this calls for the estimation of quantifiable differences. In this spirit, **Fig. 4.15 a** and **b**, show the variation in grain size for the base material and welds obtained at various RPM both for batch I and batch II, respectively. All weld samples were seen to have reduced grain size compared with that of the base material. The grain size significantly decreases at low rotational speeds. The grain size in the transition zone presented in **Fig. 4.15** (TMAZ and HAZ) is analysed in section 4.4.2.2.

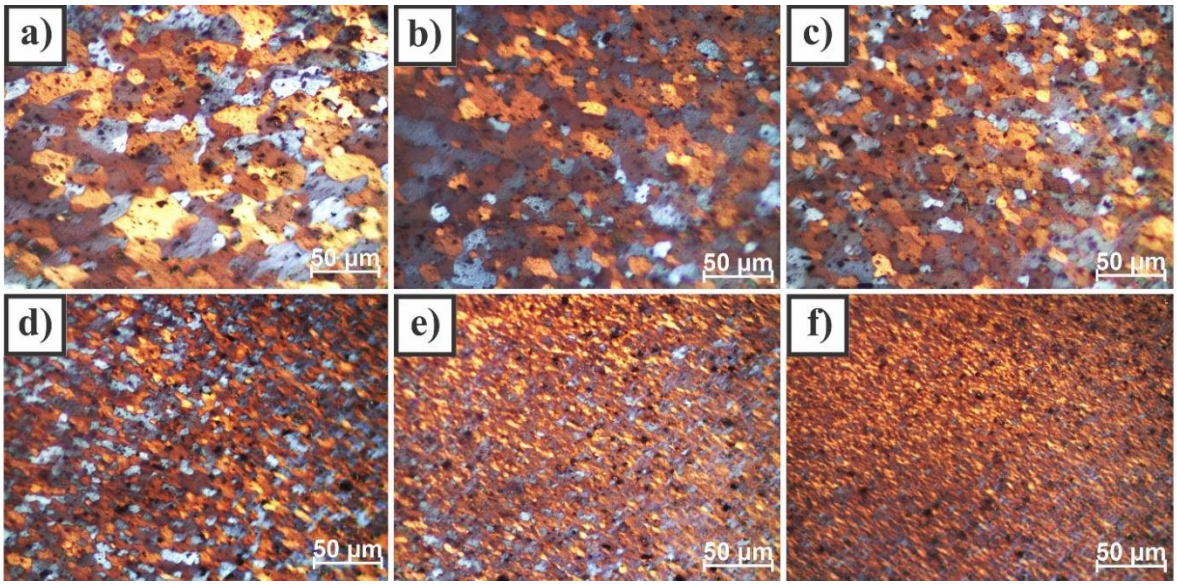

Fig. 4.14 *Cross-section polarized light microscopy images (white squares in* **Fig. 4.12***) revealing grain microstructure of: (a) base material; (b) welded sample with 3500 RPM; (c) with 3000 RPM; (d) with 2500 RPM; (e) with 2000 RPM and (f) with 1500 RPM*

Light micrographs of the base material and stir zones of the welds from batch II produced at rotational speeds ranging from 1000 to 4500 RPM obtained from the centre of the welds (white squares in **Fig. 4.13**) are shown in **Fig. 4.16**. Like batch I, the reduction in grain size compared with that of the base material at higher rotational speeds was seen to be more pronounced. However, by comparing the two batches, the grains were observed to be coarser in the SZs of welds from batch II in the samples with the highest and lowest RPM. However, the sample welded with 2500 RPM showed an opposite trend.

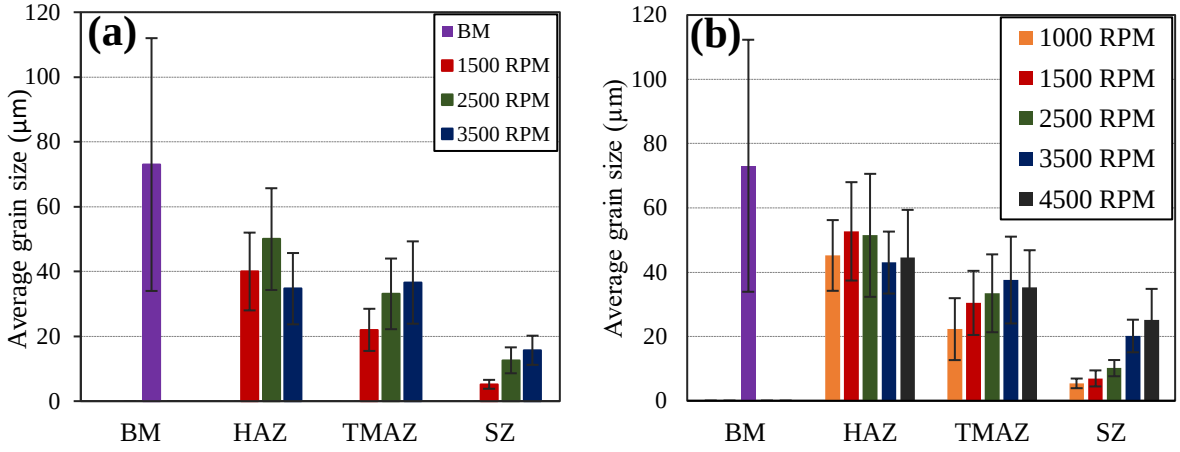

Fig. 4.15 *Variation in grain size between samples welded with different rotational speeds in different weld zones compared with grain size variation of the base material: (a) batch I; (b) batch II*

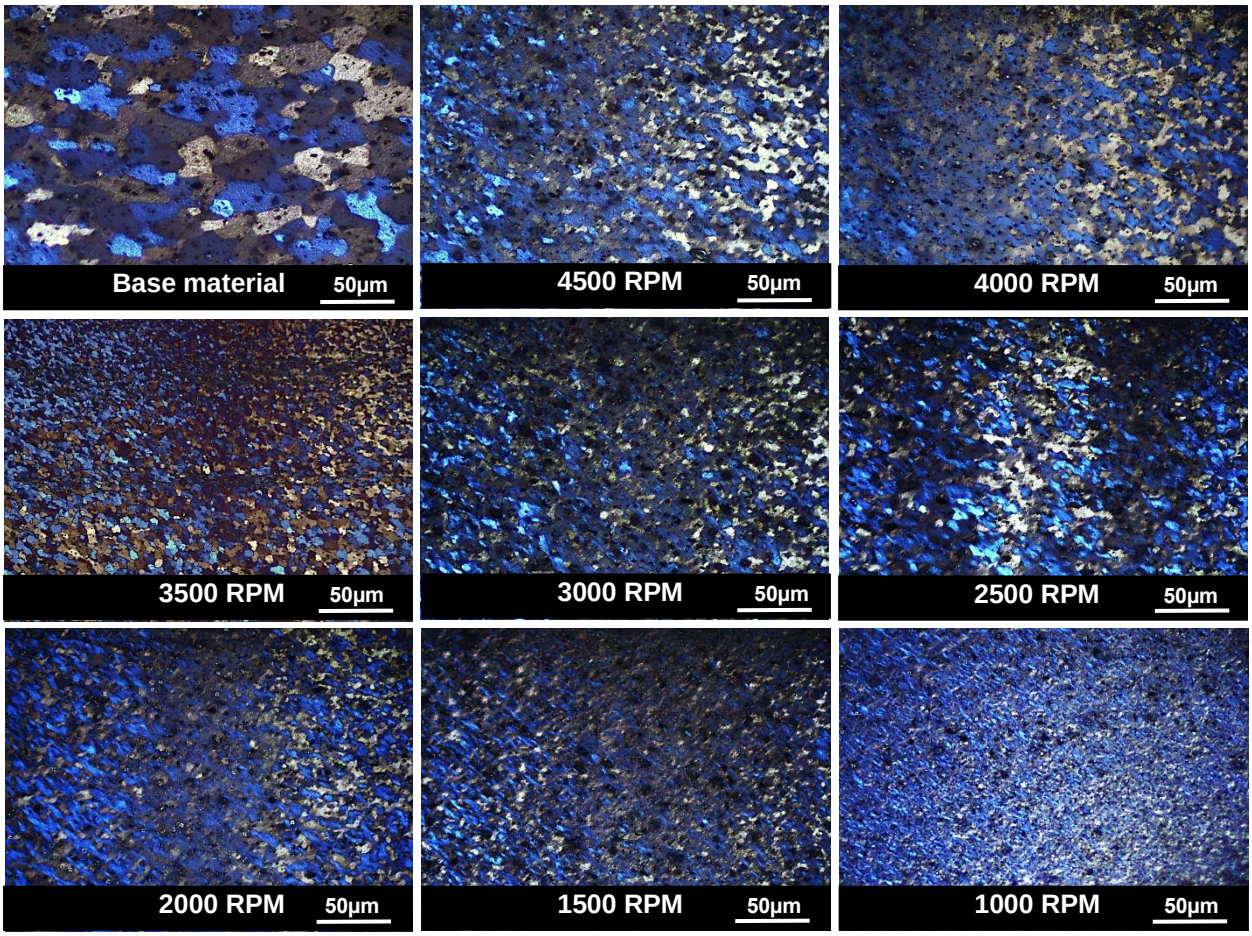

Fig. 4.16 *Cross-section polarized light microscopy images (white squares in* **Fig. 4.13***) comparing the grain microstructures of the base material and of welds produced with rotational speeds of 4500 to 1000 RPM*

4.4.2.2 Transition zone

In **Fig. 4.17** and **Fig. 4.18**, microstructure evaluations of the base material (BM), heat affected zone (HAZ), thermo-mechanically affected zone (TMAZ) and stir zone (SZ) are respectively shown for batch I and batch II. In both batches, a similar trend was observed. In the SZ, the reduced equiaxed grains with uniform size, shape and orientation can be seen in comparison with the base material. The size and shape of the grains vary in samples welded at different rotational speeds. In samples welded at low rotational speeds, the TMAZ is a narrow region with columnar grains orientated in the stir direction. By contrast, in samples welded with higher rotational speed, the shape of the grains in the TMAZ changed from columnar to more equiaxed grains without a clear transition between the SZ and HAZ. The samples welded at 3500 RPM in batch I and at 4500 RPM in batch II only differed in the size and orientation of the grains. The shape of the grains in the HAZ remains same in Batch I and Batch II.

The HAZ is the transition zone between the TMAZ and BM. The shape of the grains in this area corresponds to the shape of the grains in the base material, but they are reduced in size.

The average grain size in all zones (BM, HAZ, TMAZ and SZ) in batch I and batch II were presented previously in **Fig. 4.15a** and **b**. However, the results of the measurements should be taken with caution, especially in columnar grains the TMAZ, due to high anisotropy. This kind of calculation was most convenient for comparing grain size in different zones.

Both **Fig. 4.15a** and **b** showed that, in all welding zones (HAZ, TMAZ and SZ), grain size was reduced compare to the base material. The smallest grain size occurred in the SZ, followed by the TMAZ and HZ. In both batches, the grain size in the SZ and TMAZ increases with the increase of the rotational speed. However, in the HAZ, the grain size increases up to 2500 RPM and then decreases at higher RPM.

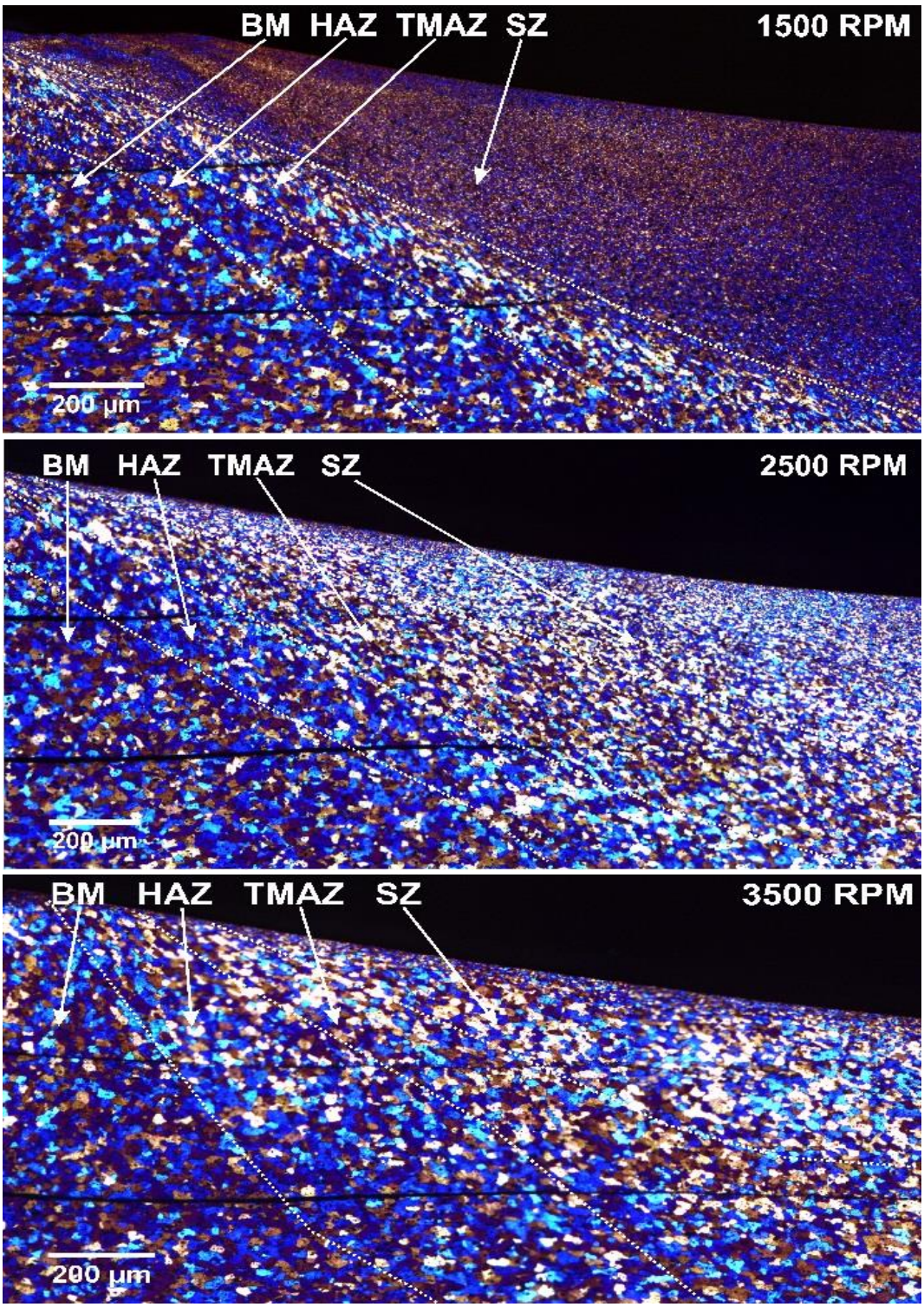

Fig. 4.17 *Micrographs showing the transition between the base material and stir zone for samples welded with 1500, 2500 and 3500 RPM from batch I (polarized LM)*

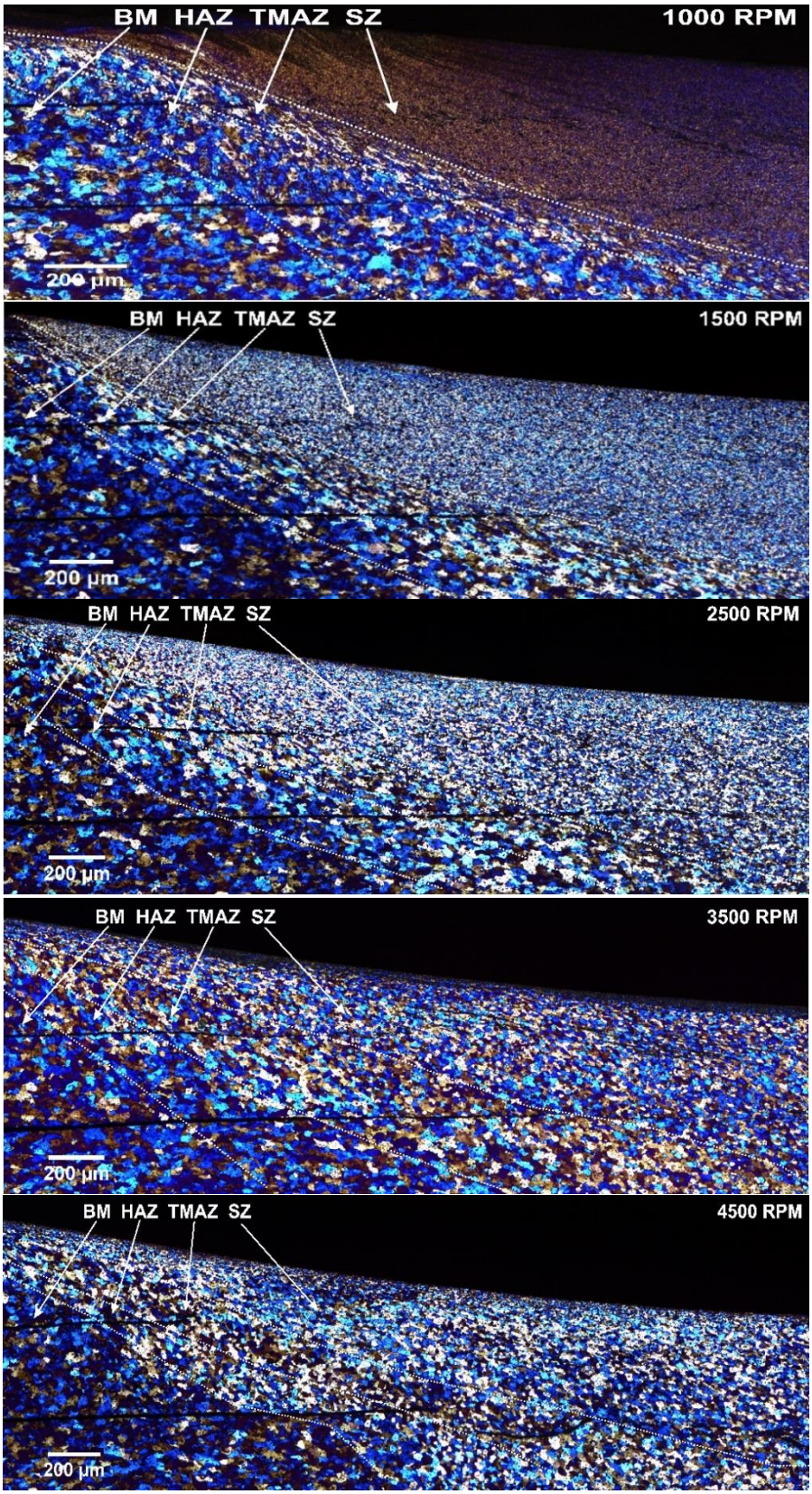

Fig. 4.18 *Macrographs of transition between the base material and stir zone from samples welded with 1000, 1500, 2500, 3500 and 4500 RPM from batch II (polarized LM)*

4.4.3 Dimensional quantification of the weld

In **Fig. 4.19**, variations in several parameters measured as a function of rotational speed for both batches are presented. These parameters include the measurements of *d* (bottom diameter of the lowest welding interface), *D* (top diameter of the topmost welding interface), *H* (axial height of the joint in the centre of the weld) and α (taper angle of the stir zone) and are shown at the bottom of **Fig. 4.19**.

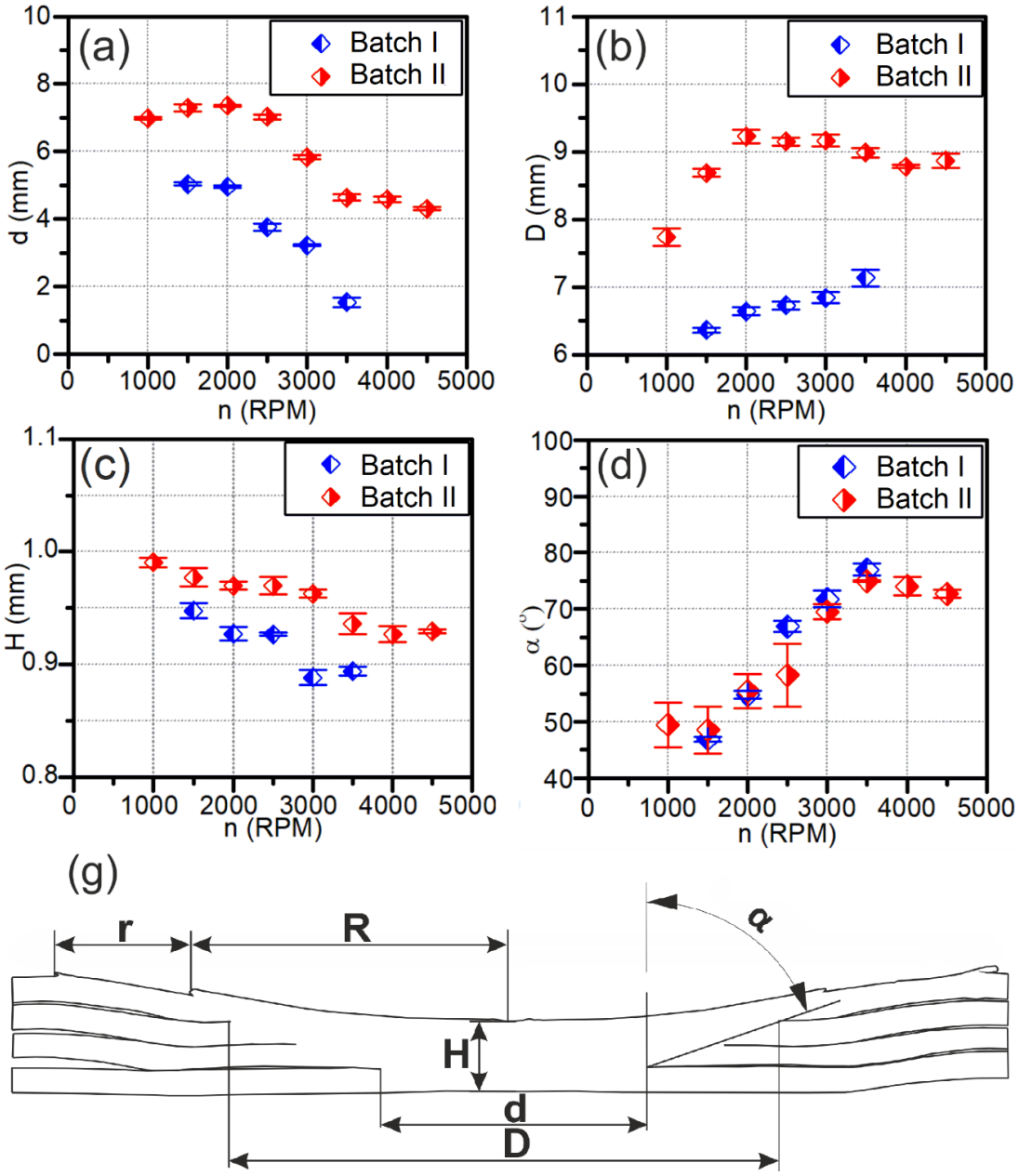

Fig. 4.19 *Dimensional quantification of the weld characteristics measured as a function of the rotational speed of the tool: (a) bottom diameter of the SZ-d; (b) top diameter of the stir zone-D; (c) axial depth of the weld-H; (d) trapper angle of the stir zone-α; (e) schematic of the weld with measured dimension*

An increase in the rotational speed leads to an increase of the *D* parameter. That is the topmost diameter affected, as shown in **Fig. 4.19a**, and comes at the expense of a reduction of *d*, which is diameter of the lowest welding interface (**Fig. 4.19b),** and reduction of *H*, which is the axial depth of the stir zone (**Fig. 4.19c)**. Consequently, the taper angle α from **Fig. 4.19d** scales linearly with an increase of the rotational speed of the tool. The estimated parameters *d*, *D* and *H* are higher in batch II compared with those of batch I.

4.5 Mechanical properties

In this section, results of mechanical tests of the welds, such as a microhardness test and small punch test, are shown. To understand the behaviour of the material and bonding mechanisms during the welding under different welding conditions (parameters and pinless tools), an analysis of the mechanical properties of the welds was carried out. For an improved understanding of the small punch test results, a microstructure evaluation of the fracture samples was also performed.

4.5.1 Microhardness

In **Fig. 4.20**, the results of Vickers microhardness mapping for batch I at rotational speeds ranging from 1500 to 3500 RPM are presented. The hardness of the welded samples in the stir zone was observed to increase at low rotational speeds of 1500, 2000 and 2500 RPM. The highest hardness can be seen in samples welded at a rotational speed of 1500 RPM. However, in samples welded at 3000 and 3500 RPM, the hardness drops compared with that of the base material.

The results in batch II presented in **Fig. 4.21** were similar to Batch I. In batch II, hardness in the stir zone increased compared with that of the base material only in the sample welded at the rotational speed of 1000 RPM. However, in samples welded at 1500 to 4500 RPM, the hardness drops.

In **Fig. 4.20** and **Fig. 4.21**, the hardness reduction in both batches from the top where the weld is in contact with the tool to the bottom where the weld is in contact with the anvil can be seen.

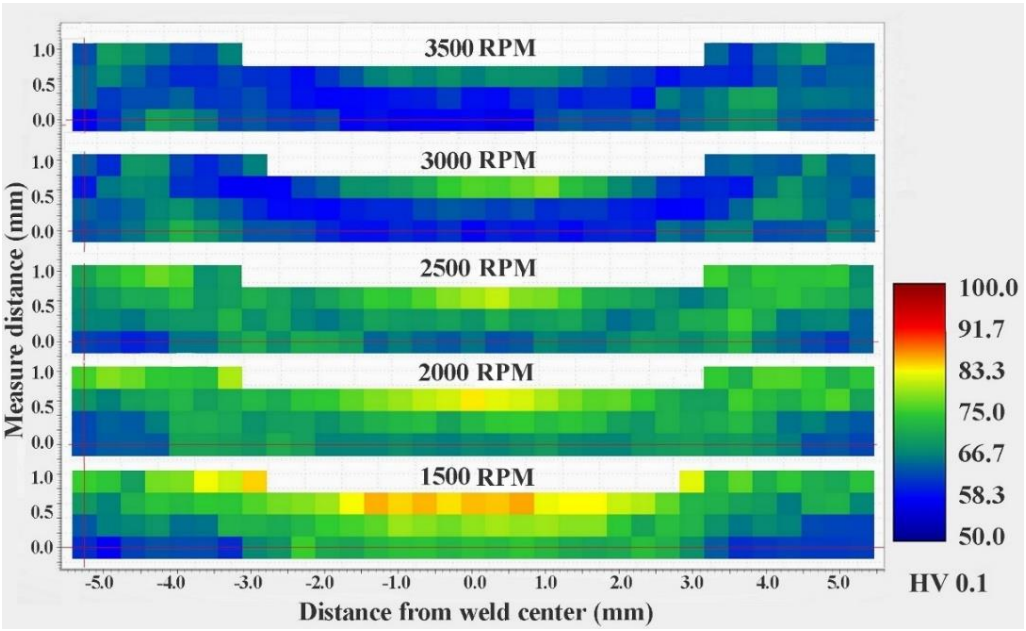

Fig. 4.20 *Microhardness maps obtained by Vickers microhardness test of the samples from batch I processed by FSSW at rotational speeds ranging from 1500 to 3500 RPM*

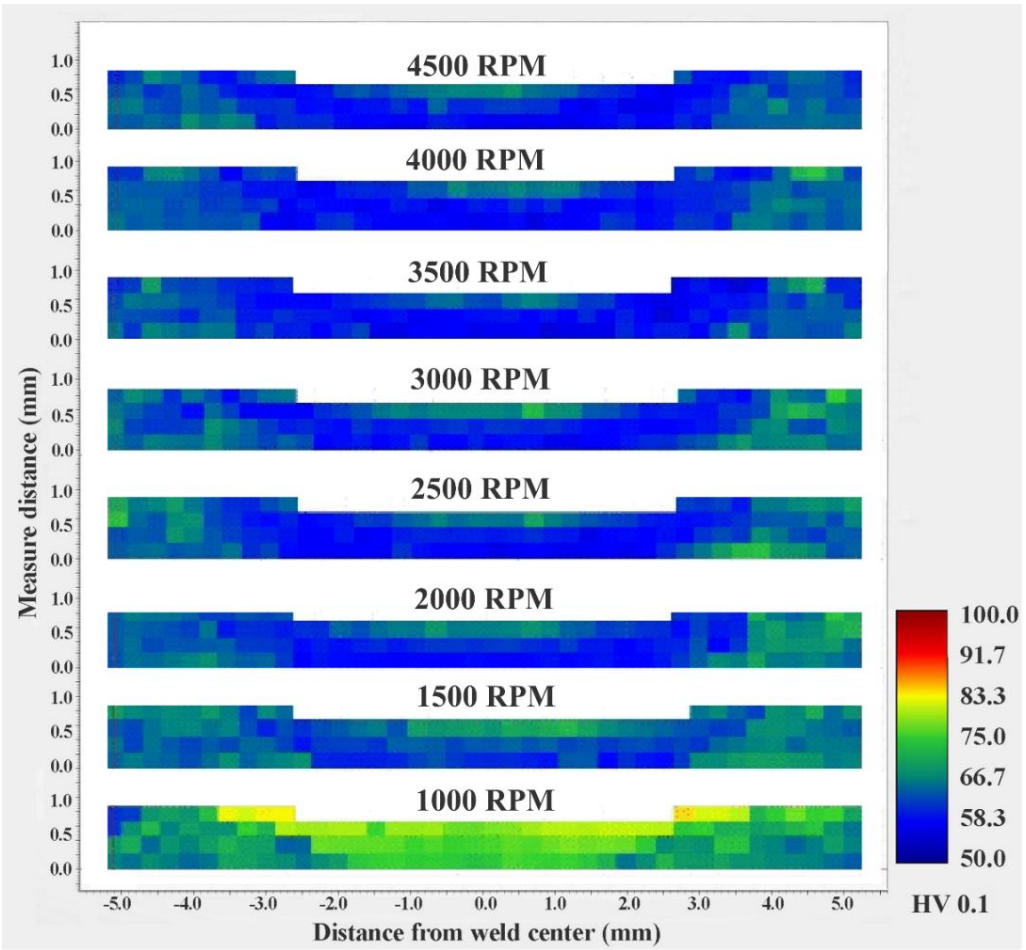

Fig. 4.21 *Microhardness maps obtained by Vickers microhardness test of the samples from batch II processed by FSSW at rotational speeds ranging from 1000 to 4500 RPM*

4.5.2 Small Punch Test Results

In **Fig. 4.22** and **Fig. 4.23**, the small punch test results are presented as load-punch displacement curves of the base material and welds from batch I and batch II. **Fig. 4.24a** shows the variation in the rupture load (F_{max}) and maximum punch displacement (S_{max}) (measured from the beginning of the process to the fracture load) as a function of the rotational speed in batch I. Compared with the strength of the base material (1094.9±21.3 N), the sample welded at 1500 RPM has a higher strength (1162±37.83 N), whereas samples welded at 2000 to 3500 RPM showed lower rupture loads. However, maximal punch displacement showed an opposite behavior. Namely, the samples welded from 2000 to 3500 RPM showed higher maximum punch displacement whereas the sample welded at 1500 RPM showed lower maximum punch displacement compared with that of the base material. The maximal punch displacement (1.87±0.03 mm) was found during testing the sample welded at a rotational speed of 3000 RPM.

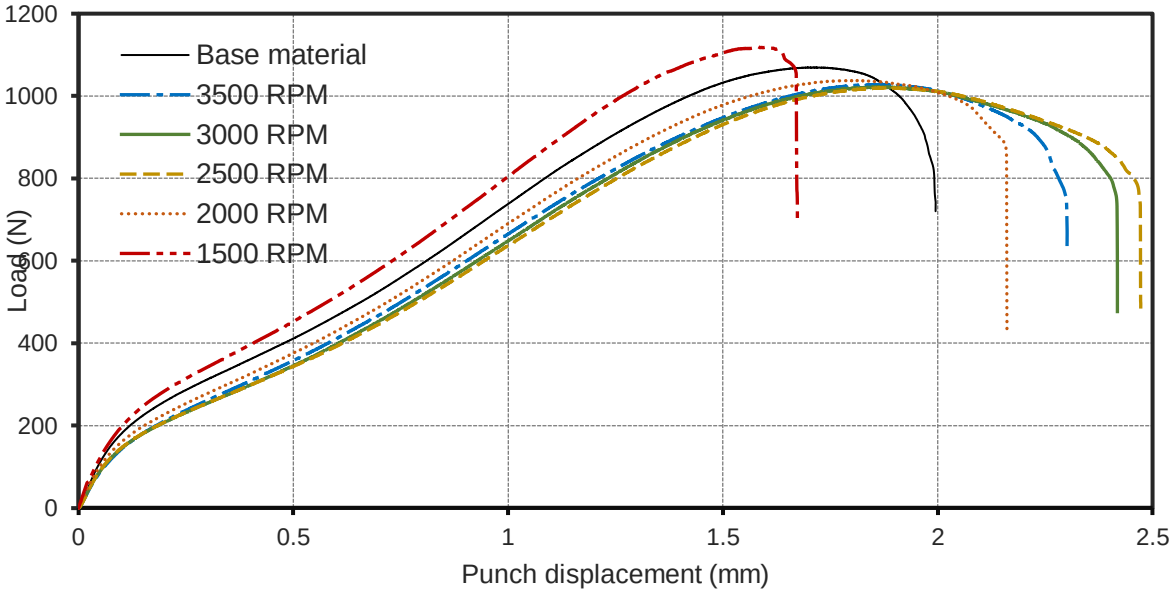

Fig. 4.22 *The load-displacement curves of the base material and weld specimens from batch I with rotational speeds from 1500 to 3500 RPM obtained with a SPT*

In **Fig. 4.24b** rupture load and maximum punch displacement for batch II are shown. In batch II, the specimen at 1000 RPM obtained the highest rupture load (1096.7±33.5 N). However, its value was slightly above the value of the rupture load of the base material (1094.9 ±21.3 N). In batch II, the lowest rupture load (957.2±10.3 N) was in the sample welded at 4500 RPM, while the lowest maximum punch displacement (1.72±0.02 mm) was in the sample welded at 1000 RPM. However, this value is slightly above the value of the base material. The maximum punch displacement was the highest (2.09±0.11 mm) in samples welded at 4000 RPM.

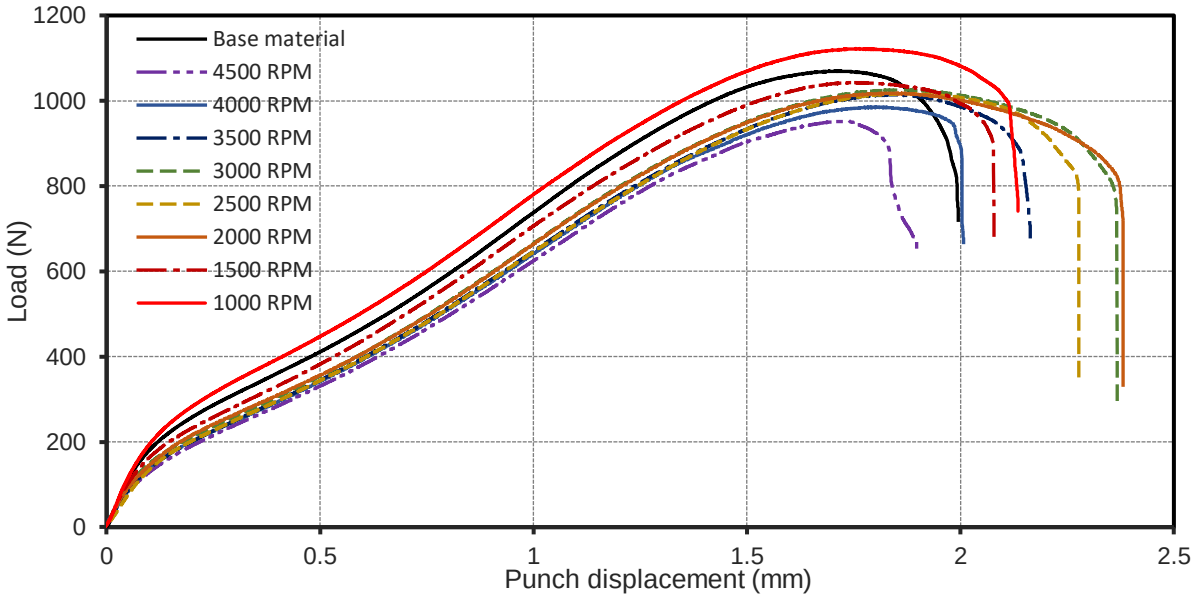

Fig. 4.23 *The load-displacement curves of the base material and weld specimens from batch II with rotational speeds from 1000 to 4500 RPM obtained with a SPT*

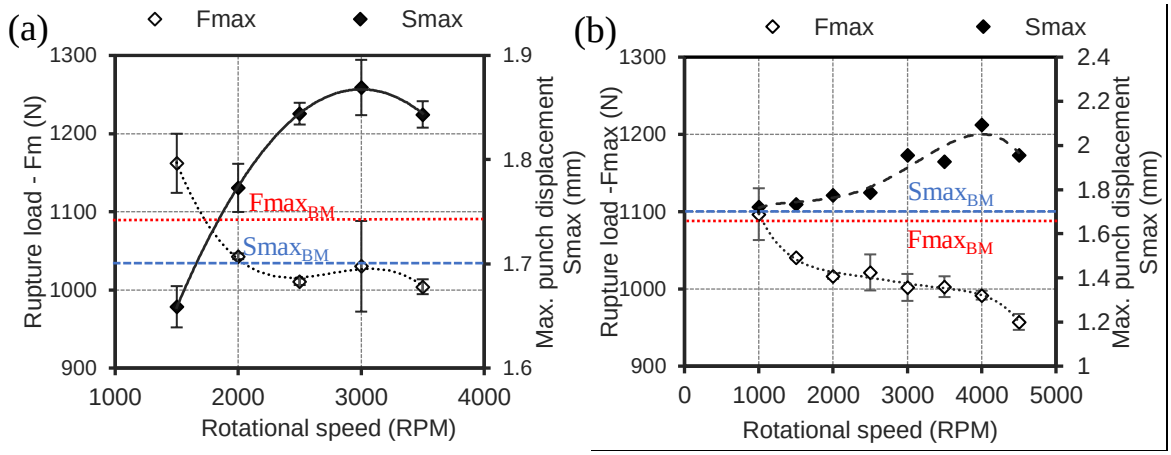

Fig. 4.24 *Rupture load and maximum displacement variation as a function of the rotational speed in (a) batch I and (b) batch II ($Fmax_{BM}$-rupture load of base material with a standard deviation of 21.3N; $Smax_{BM}$-maximum punch displacement of base material with a standard deviation of 0.025 mm)*

During the SPT test, a drop in the load indicated specimen failure. The samples collected after failure were characterized by light microscopy and a scanning electron microscope to analyse the specimen shape, dimensions and fracture mechanisms. The results are presented in this section for a better understanding and overview of the small punch test.

4.5.2.1 Structure and dimensional evaluation of the SPT samples

In **Fig. 4.25** and **Fig. 4.26**, the SPT specimens of the welds from batch I and batch II, respectively, are presented. In some specimens, rupture is visible on the cross-sections (red arrows). One specimen did not show any rupture and that is probably because the SPT was performed until the load reached a drop of 30 % from the rupture load. Therefore, in most specimens, cracks can only be found in one part of the ring-shaped zone, as is indicated with a white arrow in **Fig. 4.27a**. In some macrographs rupture was not seen because the sample cross-section was taken from the other side of the sample. In batch II, a delamination was present in the cross-section, especially in specimens from welds obtained at 1000, 2000 and 4000 RPM (green arrows).

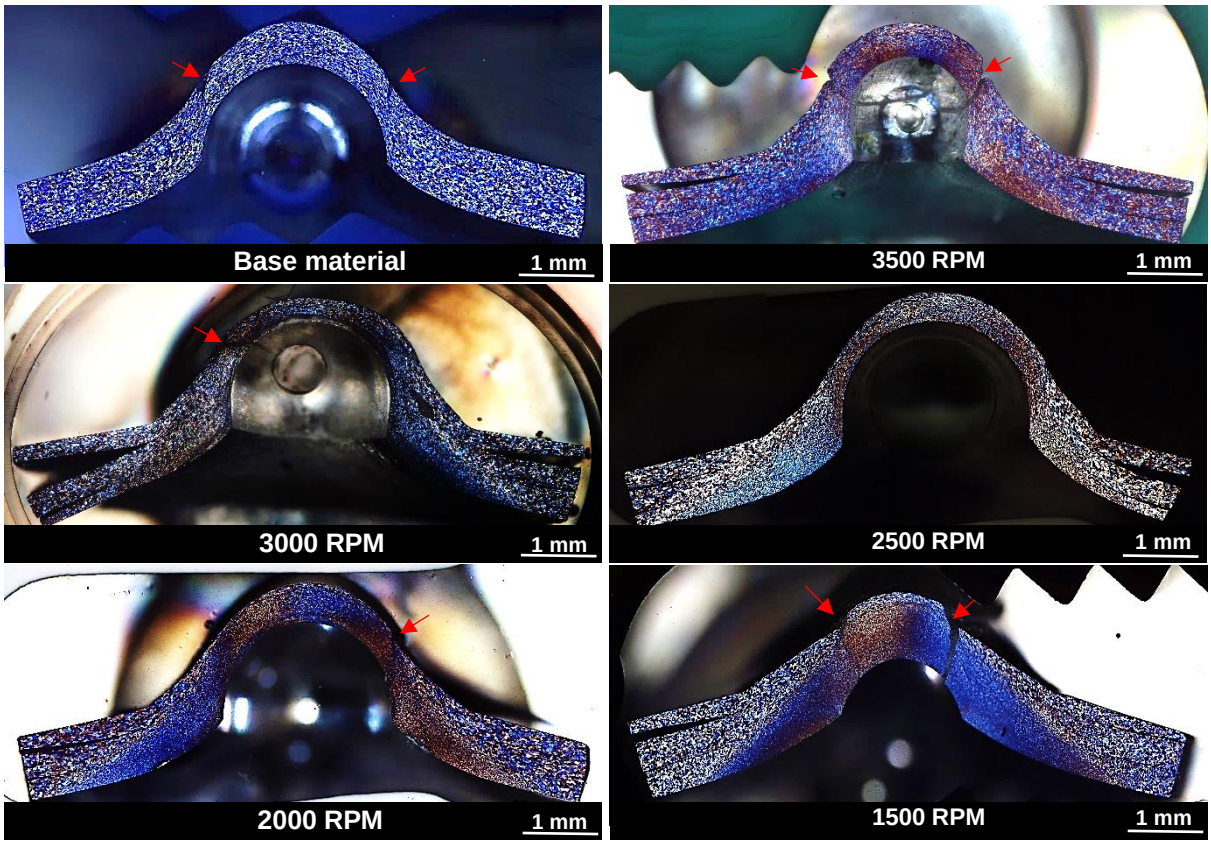

Fig. 4.25 *Macrographs of the base material and SPT samples from batch I for welds produced with rotational speeds from 3500 to 1500 RPM after testing*

Fig. 4.27a shows a sample from batch II welded at a rotational speed of 1000 RPM with a radial crack oriented in the circumferential direction. The delamination of the upper layer can be seen at the higher magnification shown in **Fig. 4.27b** as well as in the micrograph shown in **Fig. 4.26** welded with the same rotational speed of 1000 RPM. After a detailed examination of the rupture in the scanning electron microscope, the weld faying interface (WFI) was observed to cleave at several places, as shown in **Fig. 4.27c**. The thickness of the WFI vary from 1.72 μm to the 4.23 μm as shown in **Fig. 4.27d**. The open surfaces of the crack show evidence of

the void coalescence indicating the ductile fracture mechanism. **Fig. 4.25** shows the cross-section of samples without delamination.

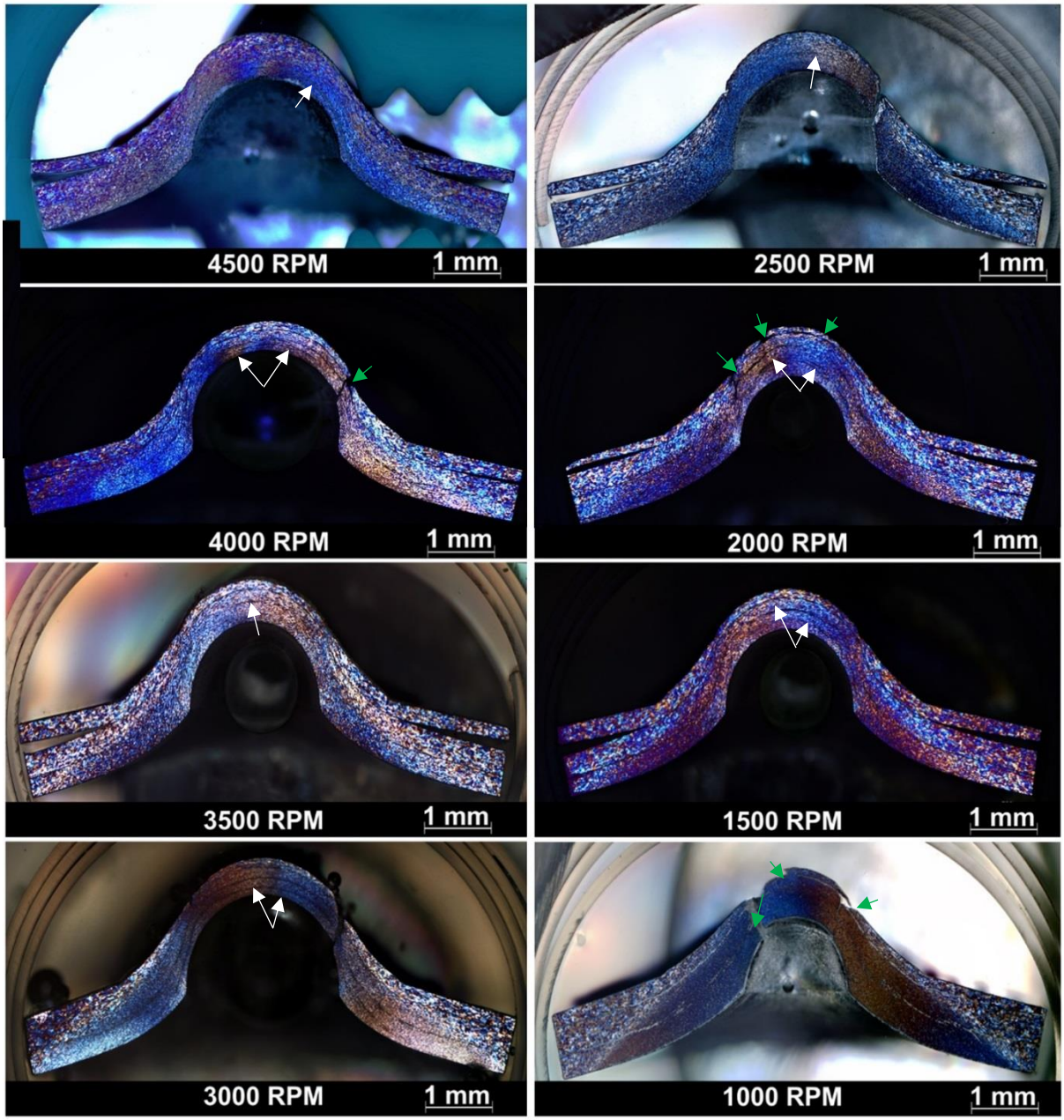

Fig. 4.26 *Macrographs of the SPT samples from batch II for welds produced with rotational speeds from 4500 to 1000 RPM after testing*

A most noteworthy example is the sample welded at 1500 RPM. In this sample, a clear radial crack typical for a SPT can be seen. In batch II, most samples show a trace of a different layer on the welding interface in the form of black lines (indicated with white arrows) showing the existence of a different layer that could not be electrolytically etched. This layer can be correlated with the WFI shown in **Fig. 4.27c**. For a better understanding of the layer and its influence on the mechanical properties of the welds, a detailed analysis of the WFI was carried out in the next section.

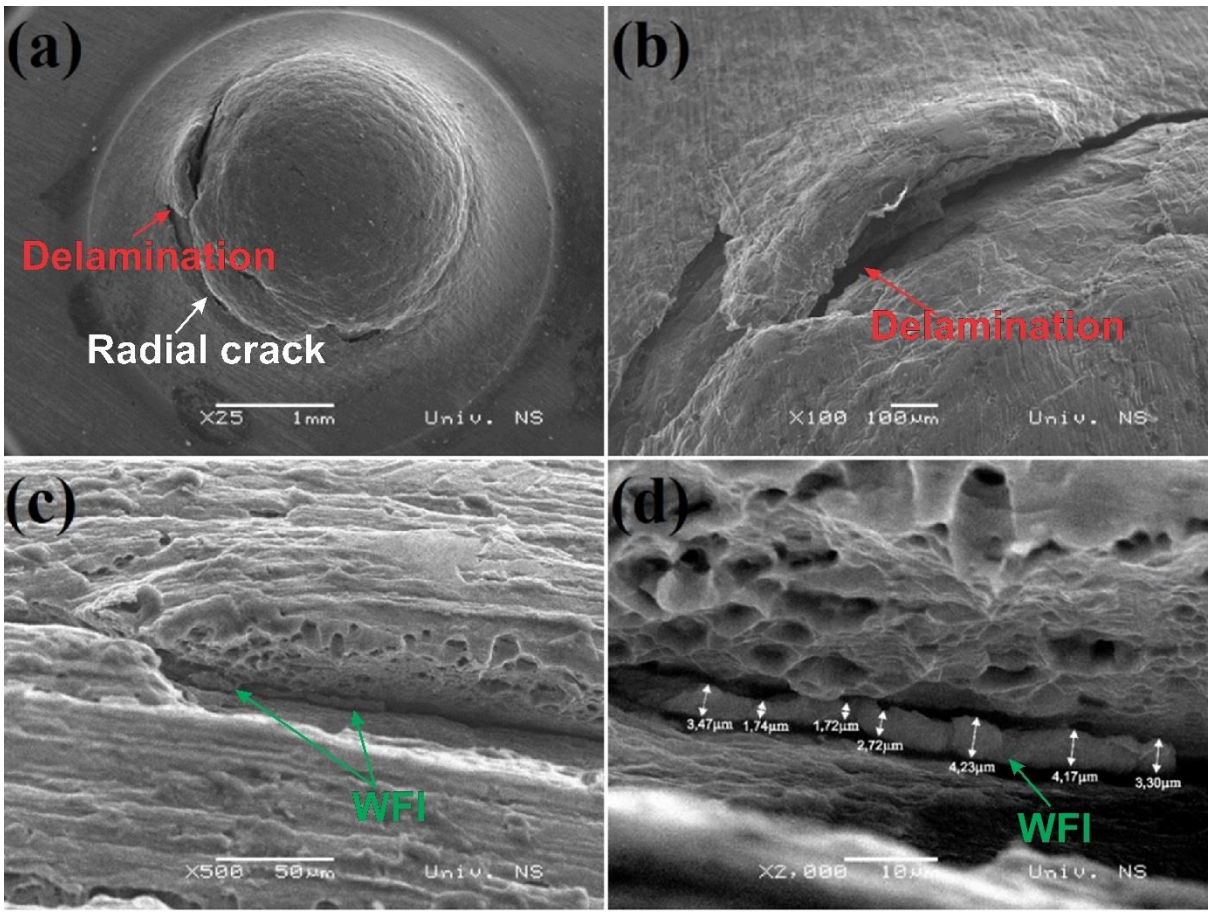

Fig. 4.27 *SEM macro and micrographs of the weld produced with 1000 RPM from batch II after the SPT: (a) SEM macrograph of a ruptured (deformed) sample from a top view; (b) higher magnification of the rupture; (c) SEM micrograph of the WFI trapped in rupture (higher magnification of the WFI with measurements)*

The ruptured specimens differ from each other in the macroscopic morphology of the crack and in the extent of the plastic deformation described with "sample thinning" in **Table 4.1**. Comparing **Fig. 4.22** and **Fig. 4.23** with **Table 4.1,** a correlation between maximal punch displacement and sample thinning can be seen. In both batches, the values of the sample thinning and maximum punch displacement can be well correlated. This result correlates with the maximum displacement of the punch in **Fig. 4.24b**. At the lowest maximum punch displacement, the lowest sample thinning occurred and vice versa; the highest thinning effect can be seen in samples welded at 3000 and 4000 RPM for batches I and II, respectively.

Table 4.1 The specimen thinning (measured from the macrographs in the middle of the stir zone for batch I and II and then subtracted from an initial value of specimen thickness)

Sample thinning	4500 RPM	4000 RPM	3500 RPM	3000 RPM	2500 RPM	2000 RPM	1500 RPM	1000 RPM
Batch I			0.35±0.01	0.48±0.03	0.39±0.02	0.32±0.01	0.12±0.01	
Batch II	0.19±0.03	0.36±0.02	0.28±0.03	0.29±0.01	0.26±0,02	0.26±0,02	0.28±0.01	017±0.01
Base material 0.27±0.3								

4.6 Analysis of welding interfaces

To advance the current understanding on the fracture mechanism that occurred during the small punch test, a detailed analysis of the weld interfaces after welding but before the SPT was carried out. Knowing the structure and chemical composition of the WFI will answer a critical question as to how delamination occurred in batch II and how it reflects on the mechanical properties of the welds. For that reason, nanoindentation mapping (in-situ SPM), transmission electron microscopy (TEM with EDX) and Kelvin probe force microscopy (FM-KPFM) of the weld interfaces were carried out.

4.6.1 In-situ Scanning Probe Microscopy (in-situ SPM)

High-speed property maps (XPM) from the area described in the experimental section in **Fig. 3.21a** are shown in **Fig. 4.28**. **Fig. 4.28a** presents a Young's modulus map of the weld interface obtained from the sample welded at 1000 RPM and **Fig. 4.28b** presents a nano hardness map for the same area. For a better understanding and clear overview of the results, K-means clustering of the modulus was adapted in **Fig. 4.29a** and of hardness in **Fig. 4.29b**. The average values of the three main clusters with standard deviation and error obtained from the maps are presented in **Table 4.2**.

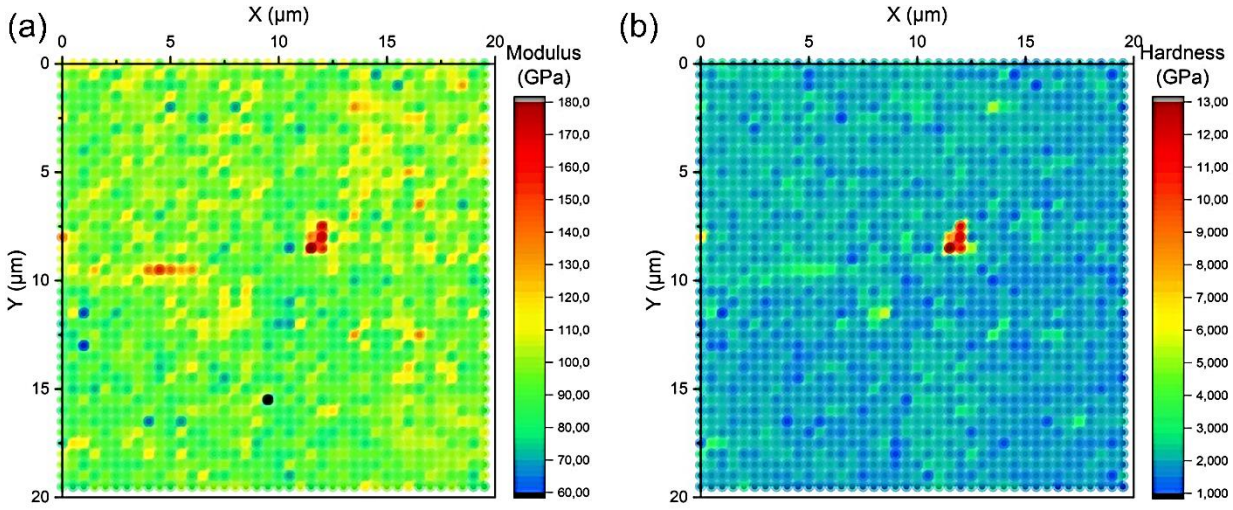

Fig. 4.28 *High-speed property maps showing (a)Young's modulus and (b) nanoindentation hardness distribution on the cross-section of the weld interface obtained from the sample welded at 1000 RPM.. The area where the maps were taken was shown in the experimental section* **Fig. 3.19a**

In **Fig. 4.29**, three main groups of hardness and modulus values can be seen. The soft matrix (cluster 2 green) has the average values of modulus and hardness ~ 88 and 1.87 GPa, respectively. These values are marginally higher than the values of the base material (69 GPa for Young's modulus) Al 5754 alloy. Subsequently, the hard matrix (cluster 1 red) with an

average modulus ~103 GPa and hardness ~2.12 GPa were obtained. Cluster 1 is randomly scattered in the formation of clouds. Inclusion (cluster 3 blue) shows the highest values of the modulus and hardness, ~155 GPa and 10.23 GPa, respectively. By observing the maps of modulus and hardness on the weld interface, no transition or significant changes over the weld interface can be seen. However, the spatial resolution of in-situ SPM is 500 nm so it is not capable of capturing any inclusions, oxides or nanovoids smaller than 500 nm. Therefore, more sensitive methods were adopted to determine further insights on the WFI.

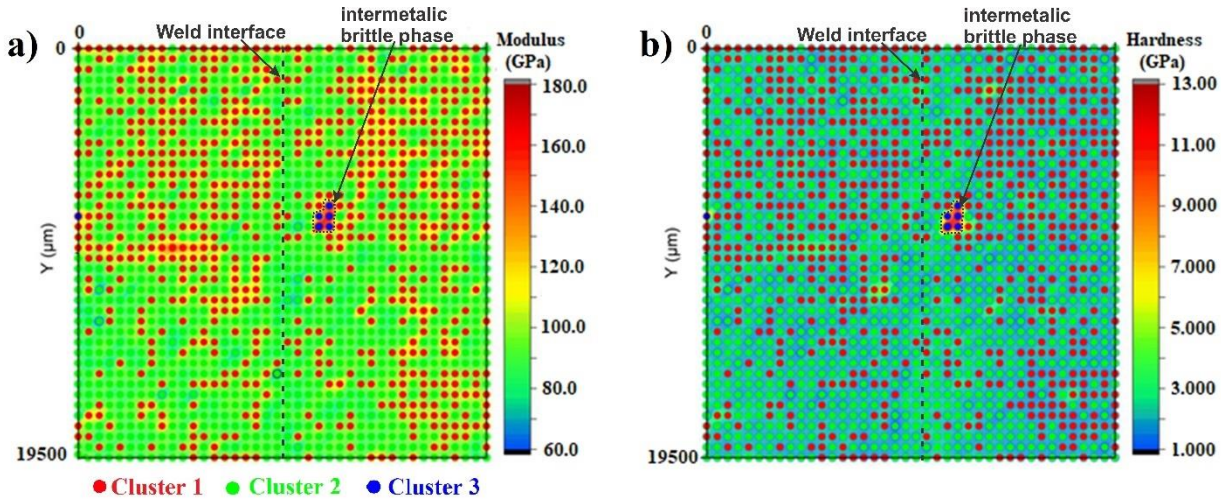

Fig. 4.29 *K-means clustering of the (a)Young's modulus and (b) nano hardness maps obtained from* **Fig. 2.28**

Table 4.2 Values of the Young's modulus and hardness organised in three clusters (blue>red>green) showing the average values of the clusters obtained from the maps from **Fig. 2.29**

Statistic	Cluster 1 Modulus (GPa)	Cluster 1 Hardness (GPa)	Cluster 2 Modulus (GPa)	Cluster 2 Hardness (GPa)	Cluster 3 Modulus (GPa)	Cluster 3 Hardness (GPa)
Mean	103.37	2.1186	88.248	1.8692	154.62	10.23
Standard deviation	6.6549	0.33693	5.8924	0.22696	16.259	1.9906
Standard error	0.25117	0.012716	0.19729	0.0075993	6.6377	0.81266
Number of points	702	702	892	892	6	6
Variance	44.287	0.11352	34.72	0.051513	264.35	3.9625
Skewness	1.7829	3.8779	-1.0754	-0.52025	0.416	-0.10107
Kurtosis	5.2635	29.374	1.4843	0.94858	-1.1111	-0.79584

Outliers removed: 0

4.6.1 Transmission electron microscopy (TEM)

In **Fig. 4.30**, a TEM image of the weld faying interface of the sample welded at 1000 RPM from batch II is presented. The figure shows bright field (BF) in **Fig. 4.30a** and a high angle annular dark field (HAADF) in **Fig. 4.30b.** Furthermore, in **Fig. 4.30c** an EDX spectrum obtained from **Fig. 4.30b** has been presented for detecting the present phase in the recrystallised stir zone (RSZ). **Table 4.3** lists the average grain and precipitates sizes in the RSZ and WFI with standard deviations.

The RSZ contains fine polygonal grains with an average size of 4.90 μm. In polygonal grains, randomly dispersed globular precipitates were found in the grain boundaries with an average size of 0.16 μm. However, the WFI was observed to contain ultrafine fibrous grains with an average size of 0.92 μm which followed the direction vector of the material flow. In the WFI along the grain boundaries, a small globular precipitation with an average size of 0.09 μm can be found. However, inside of the grains, rod-like precipitates can be seen with an average length of 0.076 ±0.016 μm and an average thickness of 0.042 ±0.009 μm (**Fig. 4.31**).

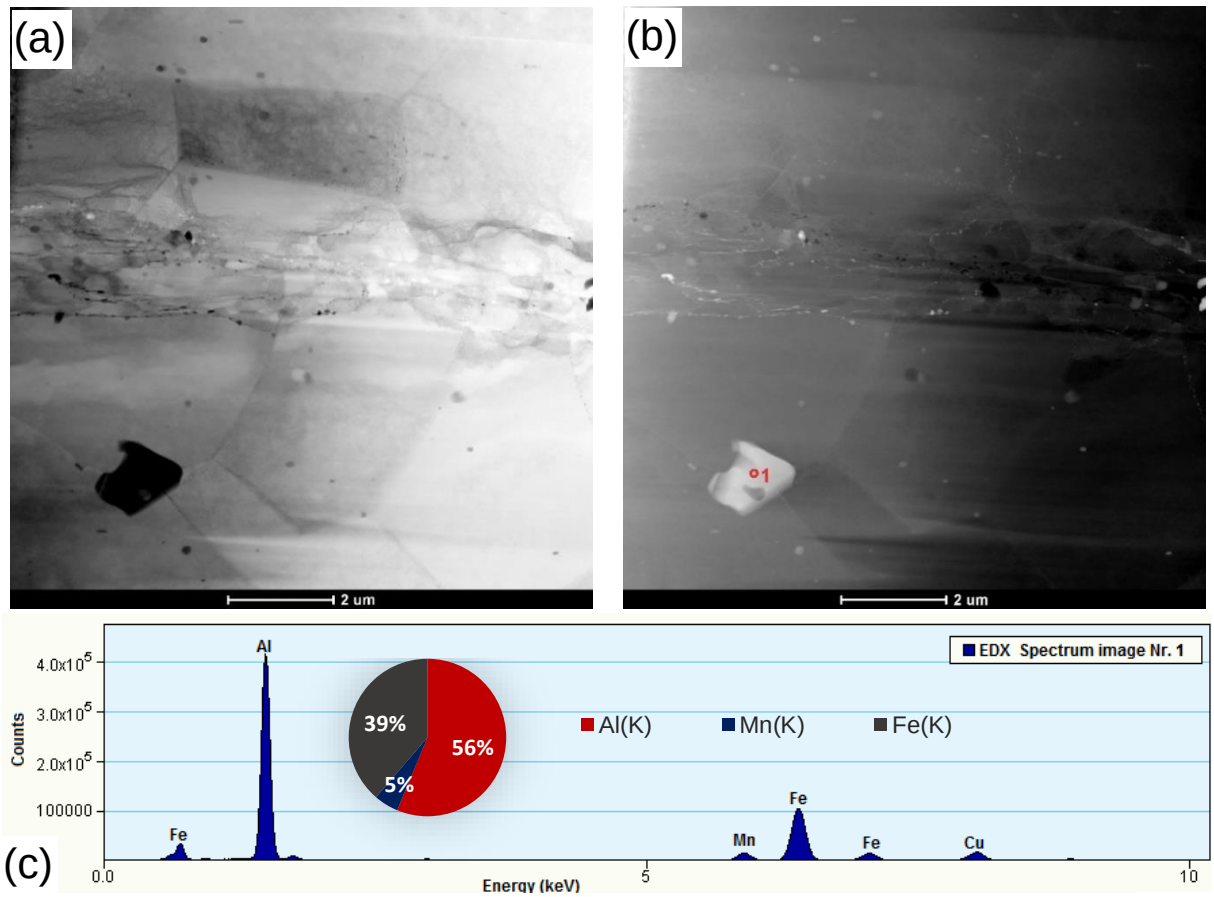

Fig. 4.30 *STEM figure of the weld faying interface of the sample welded with 1000 RPM from batch II: (a) BF; (b) HAADF; (c) spectra obtained from (b) indicated with 1*

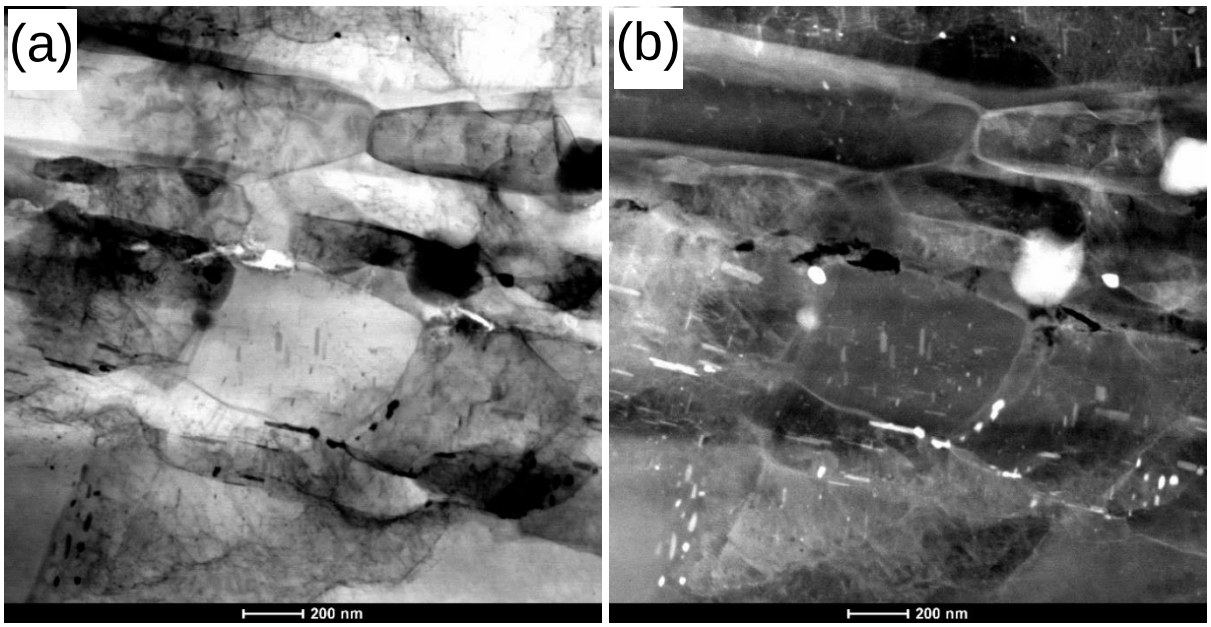

Fig. 4.31 *STEM figure of the weld faying interface of the sample welded with 1000 RPM from batch II with higher magnifications showing needle-like precipitates inside the grains: (a) BF; (b) HAADF*

In the middle of the WFI, a combination of nano pits and an oxide layer dispersed randomly along the interface was seen in (**Fig. 4.32a** and **b)**. The deformed structure of the WFI was heterogeneous while the recrystallized structure can be considered as homogeneous.

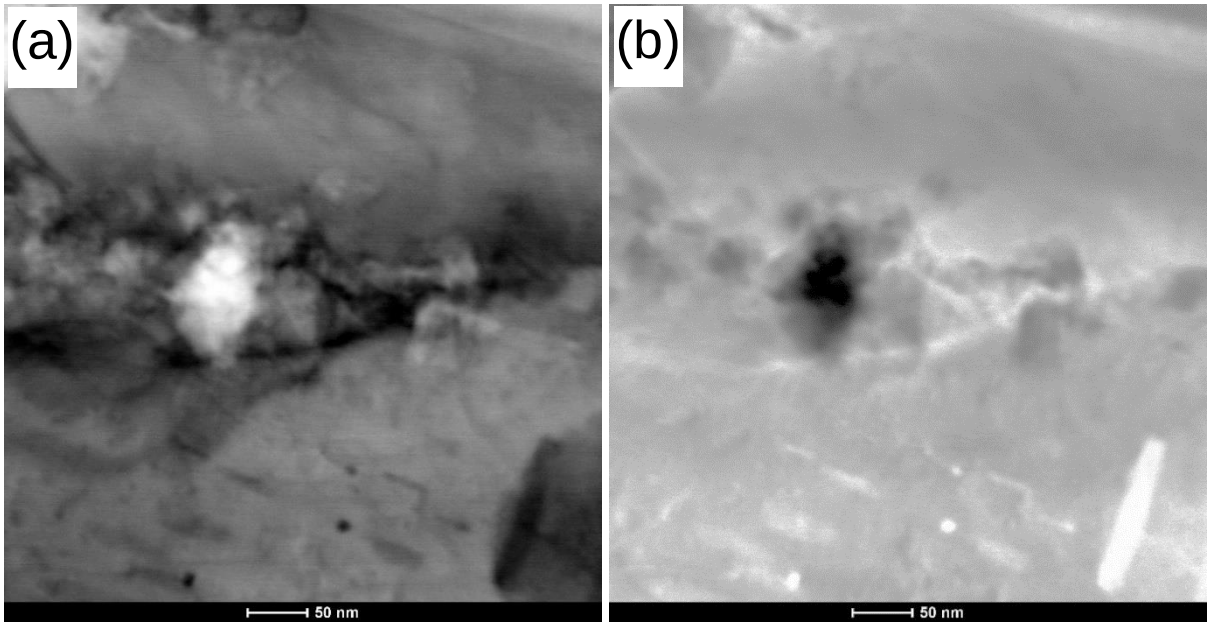

Fig. 4.32 *STEM figure of the weld faying interface of the sample welded with 1000 RPM from batch II with higher magnifications showing nano pits surrounded with trapped oxide: (a) BF; (b) HAADF*

Table 4.3 Grain and precipitates size measured in the weld faying zone and the recrystallized zone (stir zone)

Area of measurement	Average grain size (μm)	Standard deviation (μm)	Average precipitates size (μm)	Standard deviation (μm)
Weld faying interface	0.92	0.81	0.09	0.04
Recrystallised zone	4.90	0.52	0.15	0.07

4.6.1.1 Dislocation cell structure

The initial TEM analysis of the sample welded at 1000 RPM from batch II without objective (**Fig. 4.33a**) and with objective (**Fig. 4.33b)** shows the dislocation tangle inside of the polygonal grains forming dislocation cells (black arrows). The cell structure is composed of cell walls and the cell interior. The dislocation density in the cell walls is significantly higher compared with that of the cell interior.

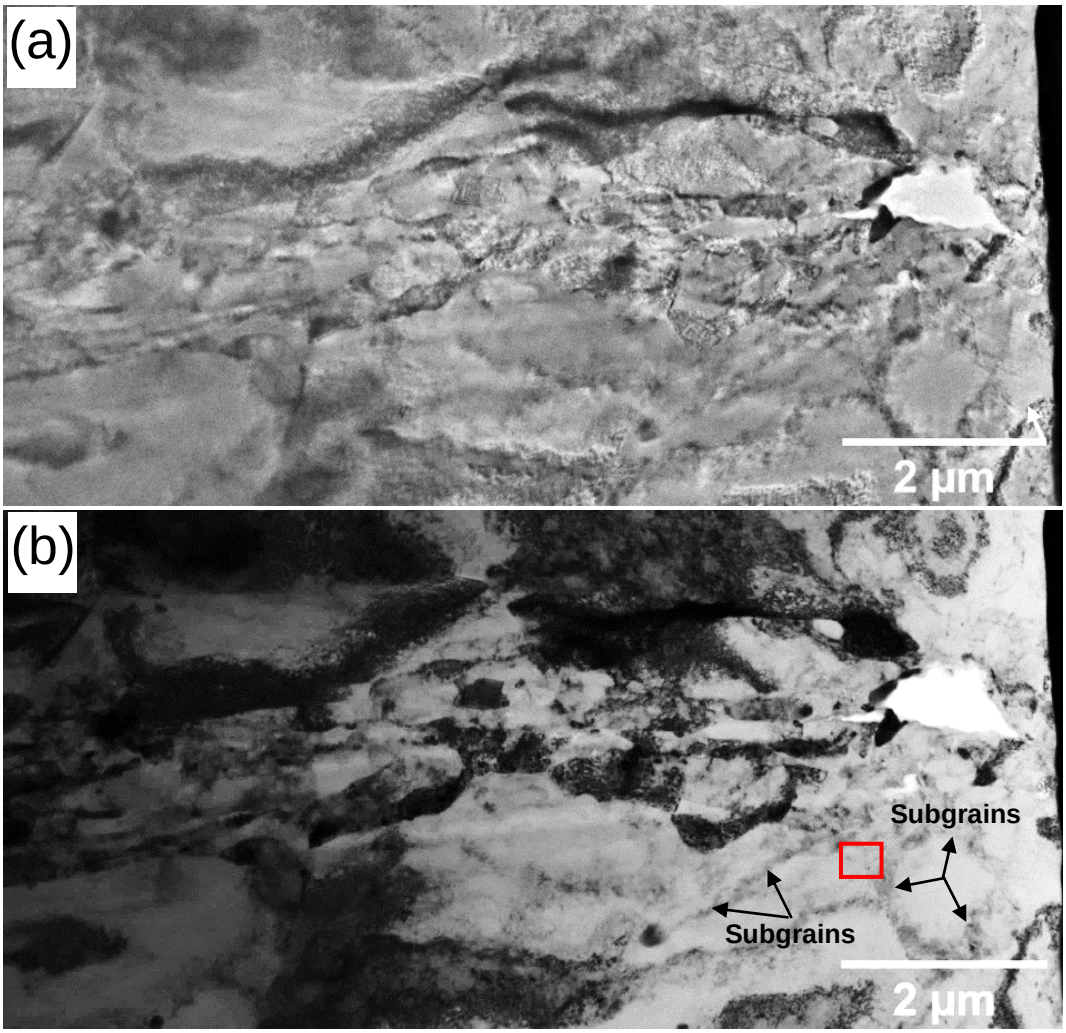

Fig. 4.33 *Weld faying interface: (a) without objective; (b) with objective*

In **Fig. 4.34a,** the image of dislocations, along with the selected area diffraction pattern (SADP) in **Fig. 4.34b** obtained from **Fig. 4.33b** (red square), are presented. From the diffraction pattern, it is observed that the shapes of the diffraction spots are affected by numerous dislocations. The diffraction patterns illustrate streaks on the diffraction spots and many multiple spots can be observed, giving rise of the formation of partial ring appearance. Furthermore, the diffraction spots do not have a circular shape but rather a stretched and irregular shape (disk-type halo).

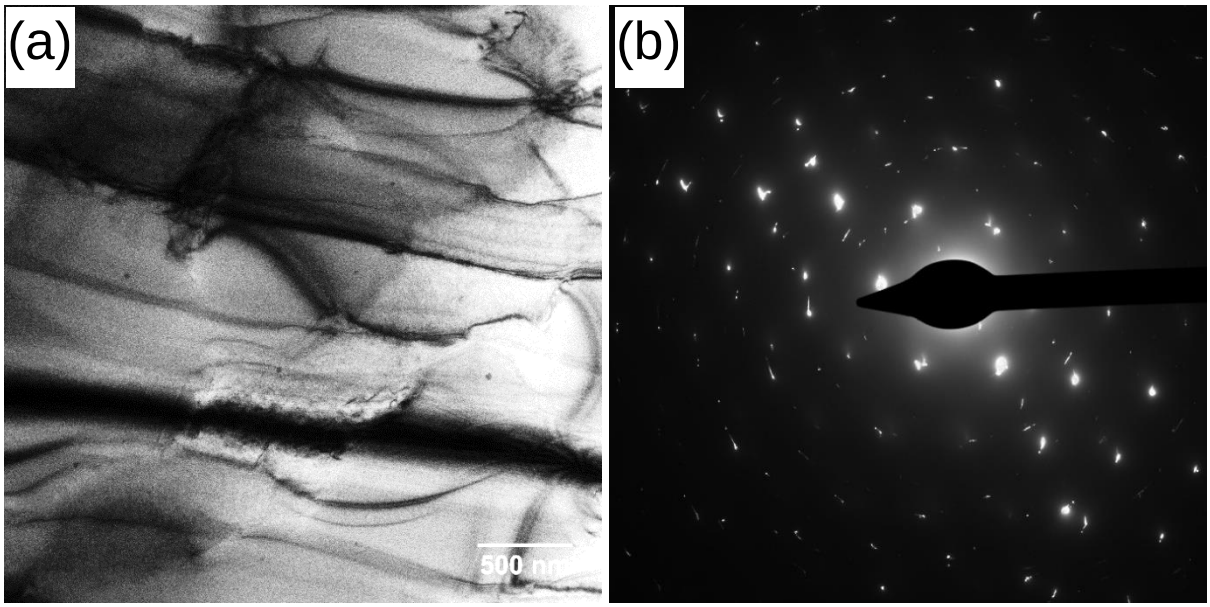

Fig. 4.34 *(a) Dislocations in the sample from batch II welded with 1000 RPM; (b) SADP obtained from (a) illustrating streaks on spots due to a high-density dislocation*

4.6.2 Energy Dispersive X-ray Analysis (EDX)

During the TEM examination, EDX analysis was performed to determine the chemical composition of different phases present in the weld faying interface. In **Fig. 4.35a**, the region indicated with an orange square was used for the EDX analysis. Red numbers show the spots where further EDX analysis was performed. The scanned region consisted of micro-pits, oxides and intermetallics.

In order to identify present phases in the weld faying interface, EDX mapping showing the elemental distribution of detected elements from the region indicated with an orange square in **Fig. 4.35a** is shown in **Fig. 4.35b**. The maps reveal two different chemical compounds. The first is around the micro-pit and in a line parallel to the pit extension which is deformed interface between the sheets. This area is rich in aluminium and oxygen and, in some parts, rich in magnesium too. The second area is rich in aluminium, iron and manganese. A smaller amount of iron can be seen near the micro-pit, which could be contamination of the sheet surfaces before welding.

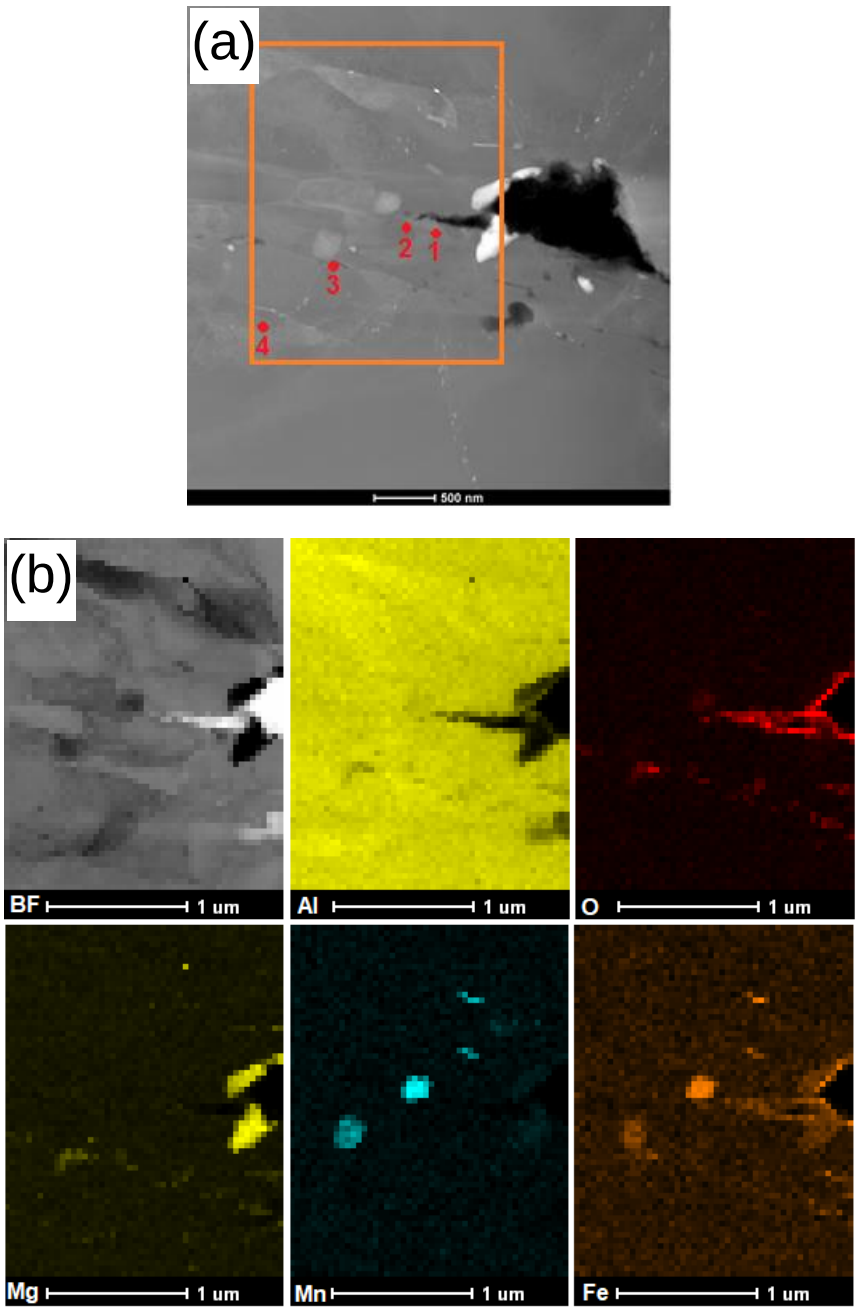

Fig. 4.35 *EDX elemental mapping analysis of the region from a sample obtained with TEM showing the distribution of the oxide and intermetallics: (a) BF image indicating where the scanning was performed; (b) BF and EDX maps of detected elements*

In **Fig. 4.36** and **Table 4.4**, the EDX spectrums with elemental quantification analysis are given for four different spots obtained from **Fig. 4.35b**. The first three spots are chosen in a region where an oxide is expected and the last one is chosen from a region without any observed anomaly for comparison. The first two points showed only the presence of aluminium and oxygen while the third point showed presence of aluminium, oxygen and magnesium. The fourth point showed the presence of only aluminium and magnesium in a ratio that corresponds to the base material.

Fig. 4.37a shows a BF of the region showing the weld interface supported by the EDX maps in **Fig. 4.37b**. The weld interface was seen to contain nano pits. Also, a narrow area around the weld interface rich in magnesium, oxygen and aluminium was observed. Parallel to this region, several rod-like, chemically different zones within grains with different sizes were found. All rod-like zones are parallel or normal to the weld interface following the two main loading directions (from the normal and shear load applied during the welding). In **Fig. 4.38,** a higher magnification of the grains containing rod-like zones is shown. The EDX maps clearly show that rod-like zones contain only magnesium and aluminum.

In **Fig. 4.39a**, HAADF of the boundary between the weld faying interface and RSZ has been shown. The boundaries were seen to contain small precipitates rich in magnesium and aluminium. There are also precipitates rich in iron, manganese and aluminium with a shape similar to the precipitates found in **Fig. 4.35**.

Table 4.4 EDX point analysis at points 1, 2, 3 and 4 in **Fig. 4.35a**

	Element	Weight %	Atomic %	Uncert. %	Correction	k-Factor
Nr. 1	O(K)	23.77	34.47	3.12	0.51	1.889
	Al(K)	76.22	65.52	3.27	0.92	1.030
Nr. 2	O(K)	43.32	56.31	6.27	0.51	1.889
	Al(K)	56.67	43.68	4.74	0.92	1.030
Nr. 3	O(K)	24.01	34.43	2.50	0.51	1.889
	Mg(K)	10.40	9.81	1.19	0.88	1.050
	Al(K)	65.57	55.75	2.69	0.92	1.030
Nr. 4	Mg(K)	2.95	3.27	0.8	0.88	1.05
	Al(K)	97.04	96.72	3.92	0.92	1.03

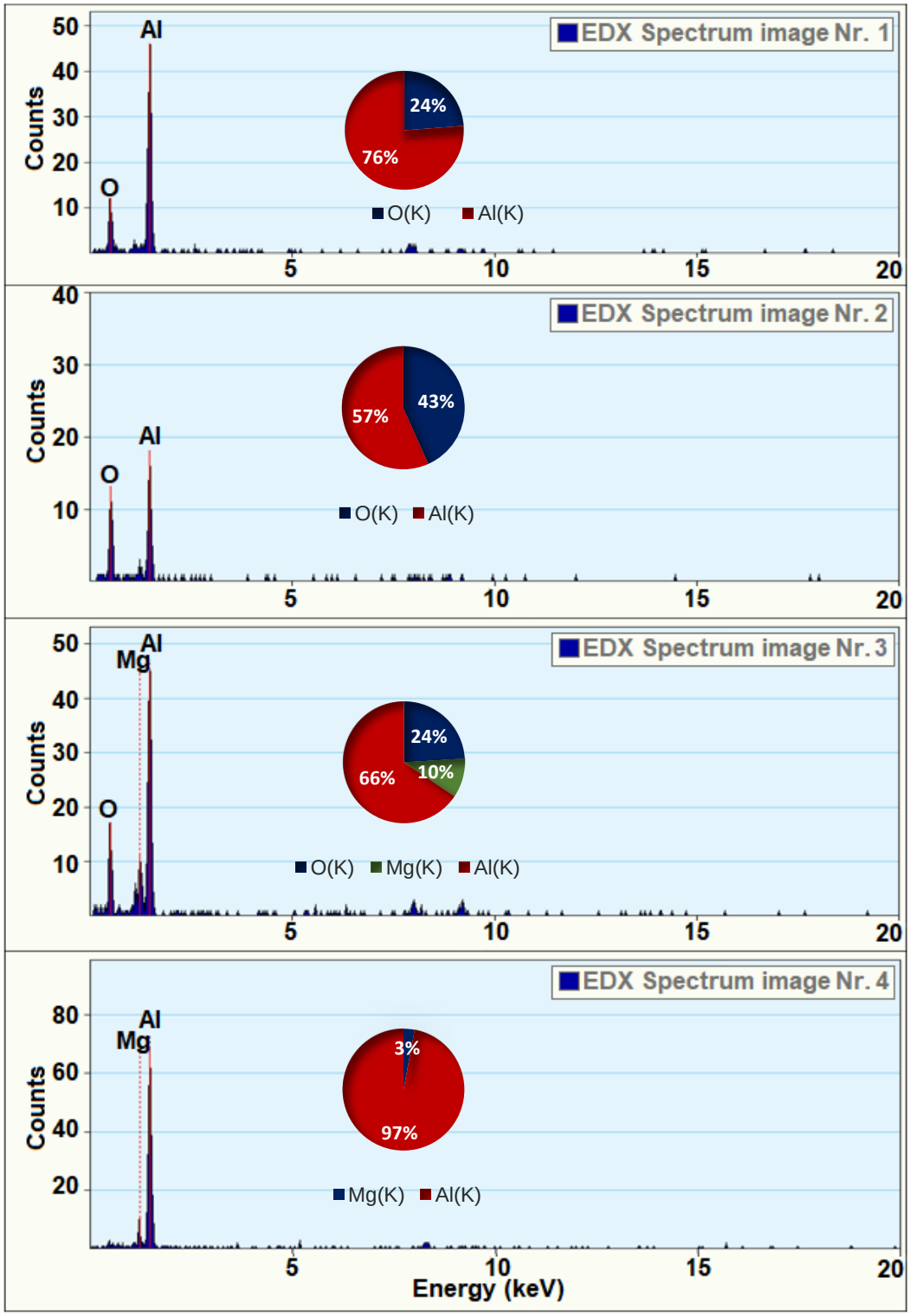

Fig. 4.36 *EDX spectrum obtained from* **Fig. 4.35**

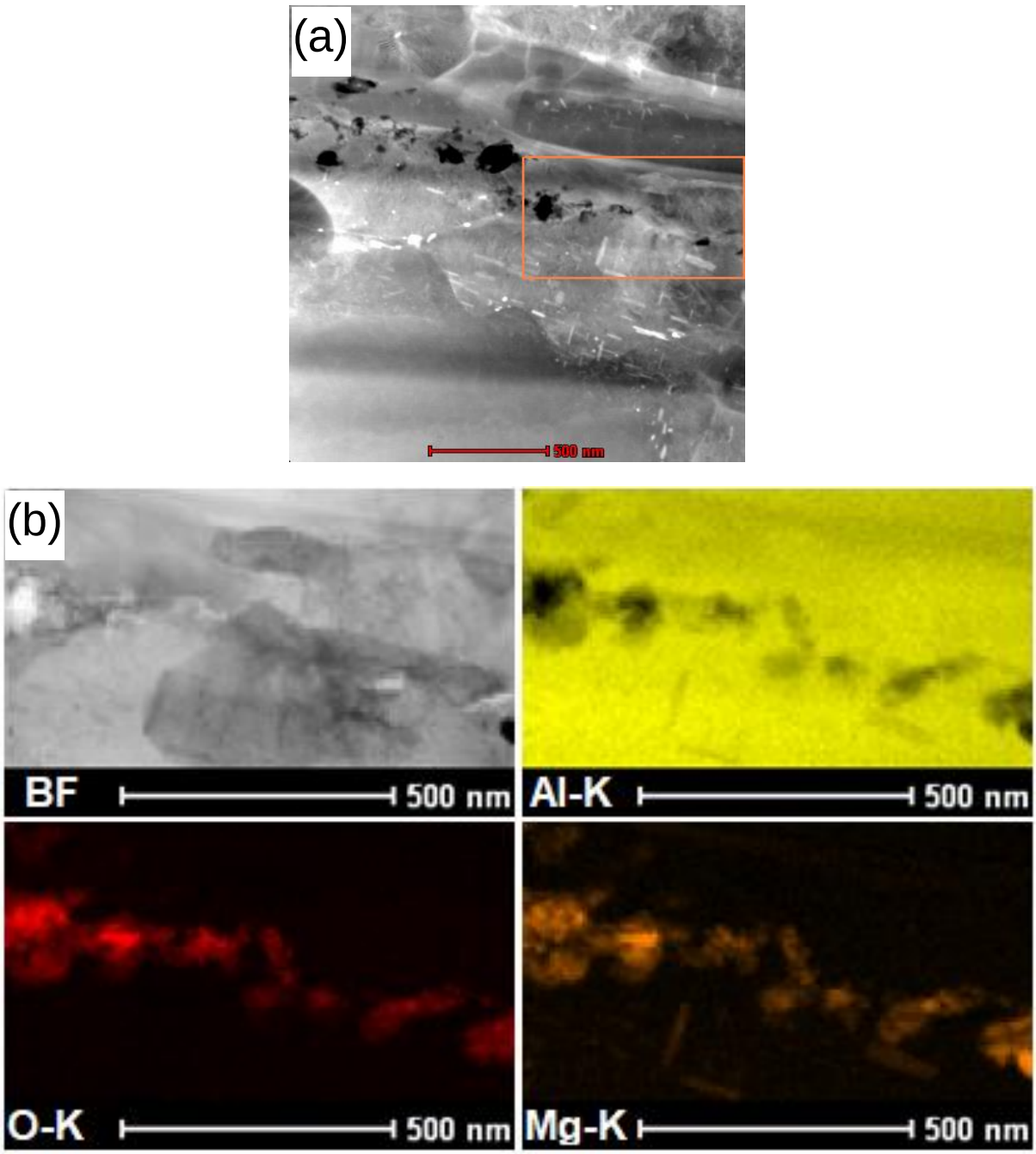

Fig. 4.37 *(a) TEM HAADF of the region of interest within weld interface between two sheets; (b) EDX maps of the region indicated with an orange square in (a)*

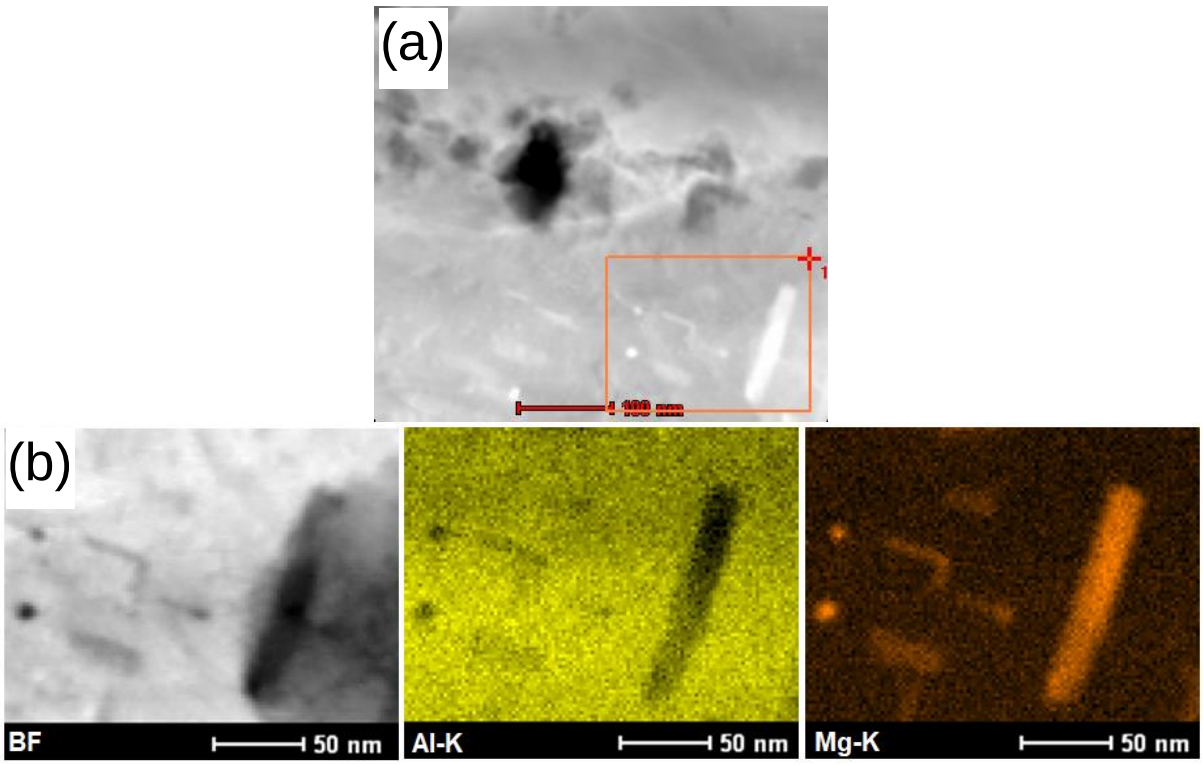

Fig. 4.38 *(a) TEM HAADF with higher magnification of the region containing rod-like inclusions; (b)TEM BF and EDX maps of the scanned area indicated with an orange square in (a)*

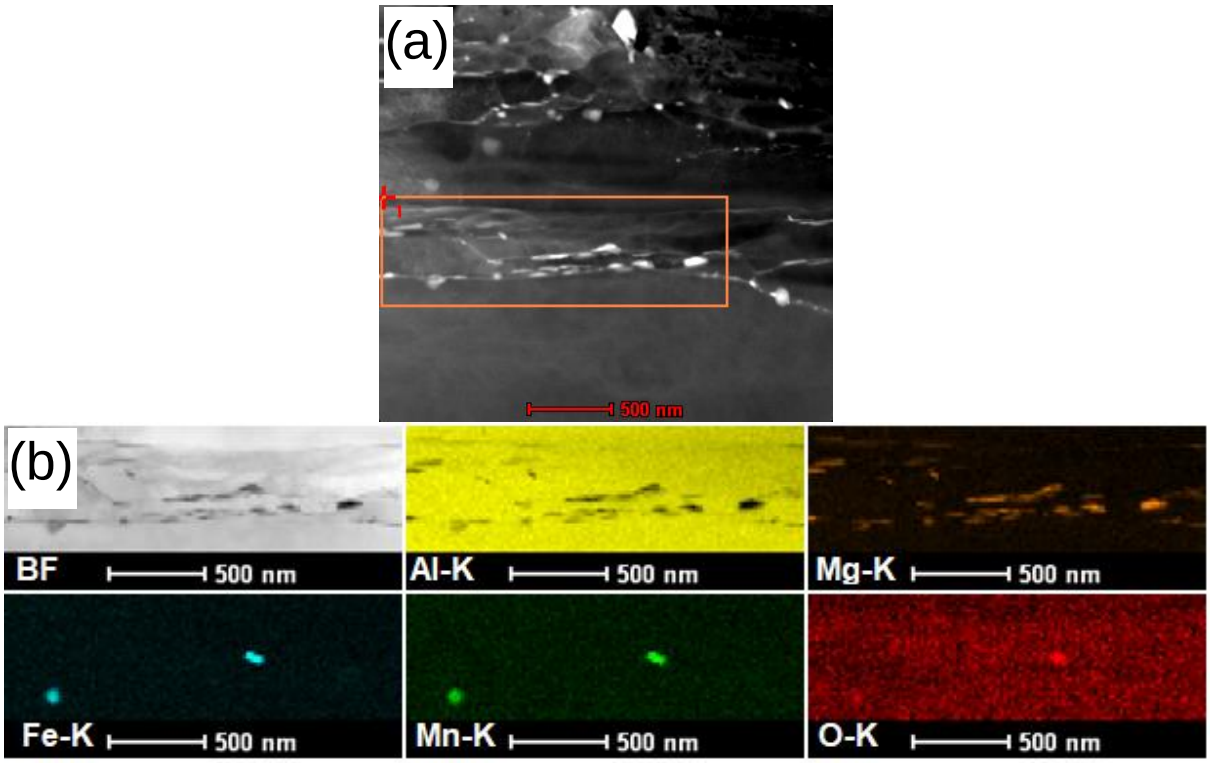

Fig. 4.39 (*a) TEM HAADF of the boundary between the weld faying interface and recrystallized zone; (b) TEM BF image and EDX maps of the area indicated in (a) with an orange square*

4.6.3 Frequency-Modulated Kelvin Probe Force Microscopy (FM - KPFM)

Fig. 4.40 shows the topography map obtained from an AFM for the same sample prepared and studied by TEM shown earlier. An area of 2.5 × 2.5 μm near to the micro-pit was tested for comparison with TEM and EDX and results are presented in **Fig. 4.35**. From the topography map, two micro-pits indicated with white arrows can be seen. Also, the weld interface, which is not a straight line due to a high deformation level, can be seen indicated with black arrows. The stripes along the sample were produced by FIB milling and their average roughness after FIB milling obtained with FM-KPFM was approximately Ra=8.75±3.13 nm

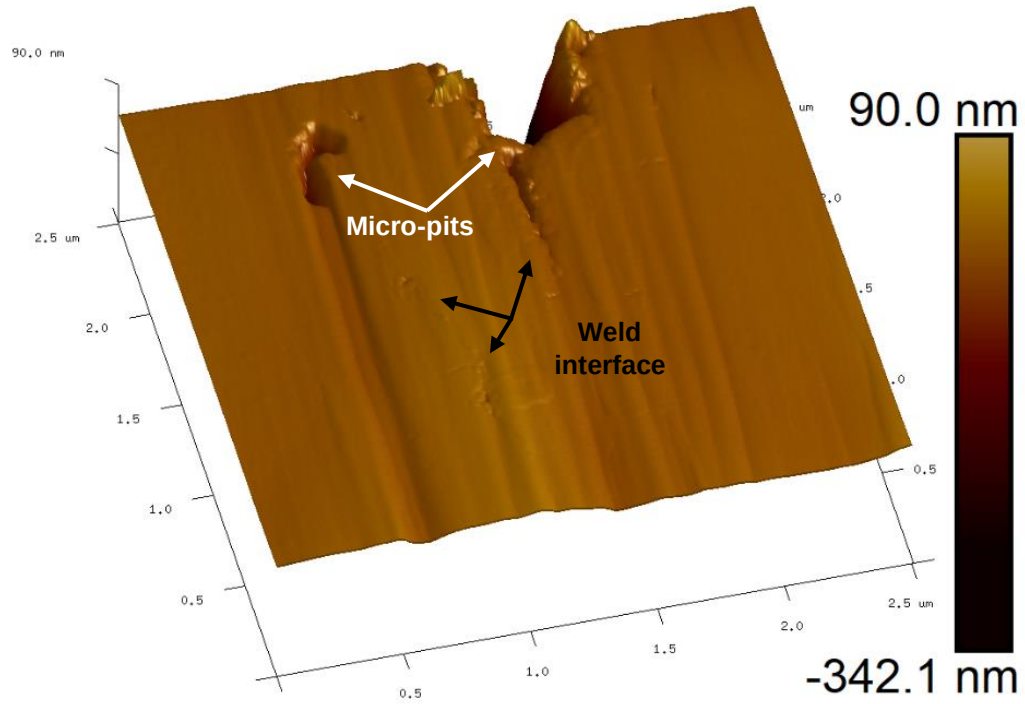

Fig. 4.40 *Topography 3D map obtained with FM-KPFM showing the area near to micro-pit of the sample used in TEM*

Surface potential mapping was further estimated by the FM-KPFM. **Fig. 4.41a** shows a surface potential map of the same area presented in **Fig. 4.40**. The weld interface zone possessed a lower potential compared with that of the rest of the tested zone, which corresponds to the base material. Using the data from the surface potential map, a work function map was generated by using equation (3.3). The blue area corresponds to the area with work potential from 4.350 to 4.480 eV while the yellow area corresponds to a material with work potential from 4.480 to 4.600 eV.

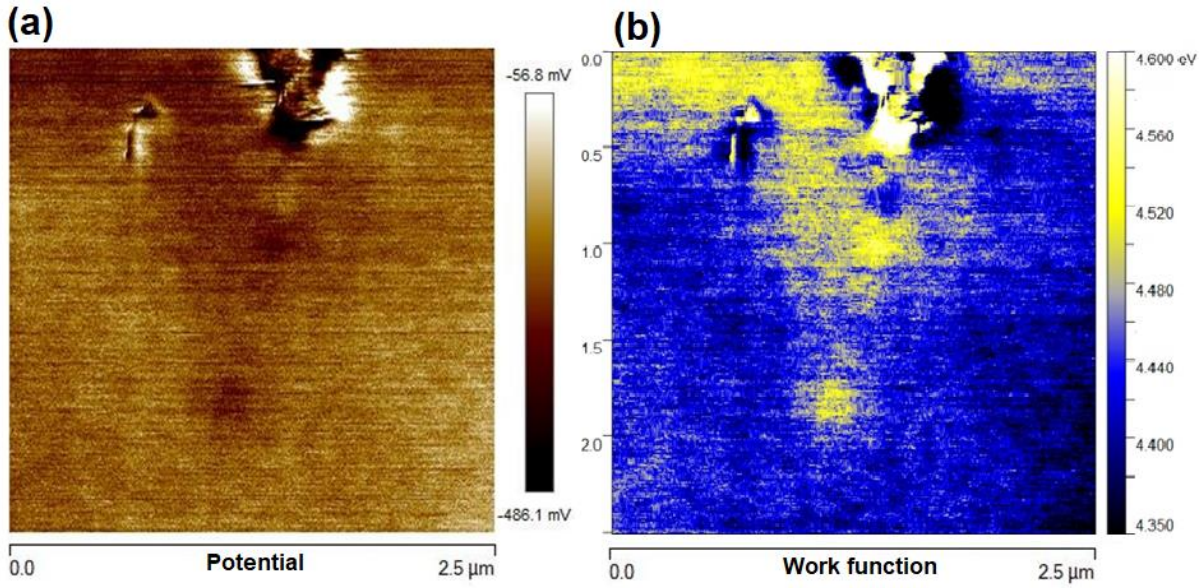

Fig. 4.41 *(a) Surface potential in same area shown in* **Fig. 4.40** *obtained with FM-KPFM; (b) work potential calculated from surface potential in (a)*

5. DISCUSSION

5.1 Influence of process parameters on FSSW

Loading conditions (strain rate, applied stress, strain, and frictional heating) influence mechanical behaviour and thus the quality and life of components. The sensitivity concerning strain, strain rate, and frictional heating varies for different loading conditions and materials. **Fig. 4.2** to **Fig. 4.4** show that the stress behavior of AA 5754 alloy during FSSW is different in welding processes performed at different rotational speeds and with different tool shapes. In both batches at lower rotational speeds, serrated stress-time curves or so-called jerky flow were obtained. According to Yamada *et al.* [168], this happens because solute Mg atoms react with dislocations. This phenomenon is known as the Portevin-Le Chatelier (PLC) effect, which some materials like Al-Mg alloys exhibit when they undergo inhomogeneous plastic deformation. Furthermore, because a local increase in strain rate softens the material locally, a negative strain-rate sensitivity (nSRS) occurs. These effects (PLC and nSRS) are both associated with dynamic strain ageing (DSA). Soare *et al.* [169] explained dynamic strain ageing as a mechanism led by two strengthening mechanisms: (i) solute strengthening and (ii) forest hardening, each being influenced by the same time-dependent mechanism of cross-core solute diffusion proposed by Curtin *et al.* [170]. The diffusion is driven by the enthalpy change $p\Delta V$, where ΔV is solute misfit volume, and p is the dislocation pressure field which makes dislocation motion more difficult. Enhanced diffusion, faster dislocation strengthening and strengthening of material governs nSRS [170]. Solute diffusion simultaneously influences temporary arrested but otherwise mobile dislocations and forest dislocations formed during the plastic deformation. Overall, strain rate dependence is controlled by solute strengthening so that forest hardening is presented as a time-, strain- and strain rate dependent "back-stress" acting on mobile dislocations. The dynamic solute strengthening of the mobile dislocations helps to achieve nSRS by reducing the normal positive SRS to nearly zero and by accounting for the transients during stress-rate jumps. The dynamic forest strengthening mechanism provides nSRS such that overall SRS is negative over a wide range of strain rates and temperatures. This behaviour was analysed by Pucu *et al.* [171].

During FSSW, rotational speed influences strain rate so, in samples welded at higher rotational speeds, a higher strain rate became evident. In this work, strain rate estimation was made in order to get a better understanding of stress-strain behaviour during FSSW. Chang *et al.* [172] proposed to calculate strain rate with a simple linear assumption where the average material flow rate $R_{m,}$ is about half of the rotational speed $R_{p;}$ the material flow strain rate $\dot{\varepsilon}$ during FSSW may be calculated by the torsion typed deformation as:

$$\dot{\varepsilon} = \frac{R_m \cdot 2 \cdot \pi \cdot r_e}{L_e} \tag{5.1}$$

where r_e and L_e are the effective (average) radius and depth of the stir zone (recrystallized zone).

The strain rate was calculated for both batches and is presented in **Fig. 5.1**. Gerlich *et al.* [116] estimated strain rate for different rotational speeds (from 750 to 3000 RPM) in AA 5754 welds obtained with CFSW by using the Zener-Holloman parameter. The strain rate vs rotational speed curves are close to the curves presented in **Fig. 5.1**, which were obtained from the torsion typed deformation equation (**Fig. 2.22**). Also, from **Fig. 5.1**, a small difference between curves obtained with different tools and axial loads can be seen. The most influential parameter on the strain rate was the rotational speed. Strain rate for batch II varies from 170 s^{-1} for 1000 RPM to 650 s^{-1} for 4500 RPM while for batch I it varies from about 230 s^{-1} for 1500 RPM to 520 s^{-1} for 3500 RPM.

With increasing strain rate, the influence of negative SRS on stress-time plots drops and more steady-state deformation was seen, as shown in **Fig. 4.2a-c**, **Fig. 4.3a-d** and **Fig. 4.4a-c**. In samples welded at higher rotational speeds, the highest serration can be seen at the beginning of the *steady-state weld* stage during which the temperature increases and material softens, causing serration to drop and becomes negligible. In batch I, this effect was more pronounced than in batch II, probably due to a lower axial load applied (2 kN) in batch I compared with that of batch II (4 kN), which has a significant influence on deformation, dwell time and strain rate. **Fig. 4.2** also depicts the fact that the time needed for a *steady-state weld* to be achieved depends on rotational speed. With an increase of rotational speed, time in the *stick-slip stage* decreases but initial stress is higher. This time also changes with rotational speed but this is a stochastic behaviour as discussed earlier in **Fig. 4.3** and **Fig. 4.4**.

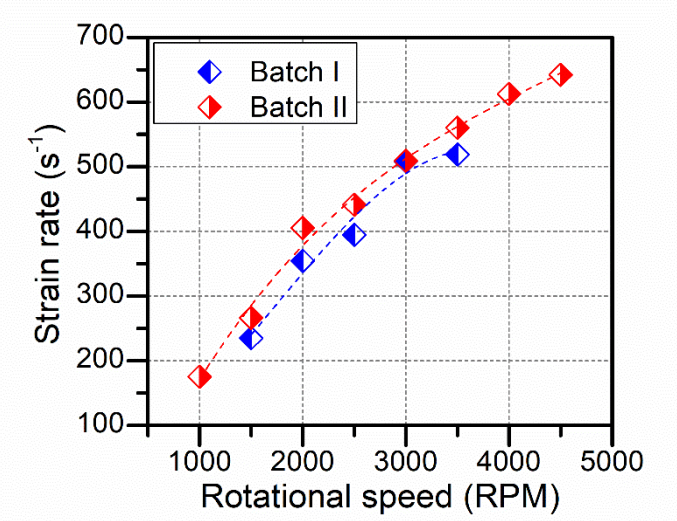

Fig. 5.1 *Relation between estimated strain rate and tool rotational speed*

According to Schmidt *et al.* [173], there are two options for obtaining the CoF during FSSW: (i) exact measurement and (ii) estimation. Due to the complexity of laboratory measuring procedures, the second method is usually used. During FSW, the range of either slip rates (order of 1 $m \cdot s^{-1}$) or strain rates (order 1000 s^{-1}) in combination with the wide range of temperatures from room temperature to the solidus temperature complicate experimental setup significantly, which was the main reason to use the assumed CoF especially for thermal modelling of FSW. Furthermore, assumed CoF is always chosen to be a constant value during the process, which

is not expected in real conditions due to variations in temperature and material properties during the process. For example, in previous works [174,175] a constant value of CoF 0.4 was used for creating the heat generation models. In this work, the CoF was obtained experimentally by measuring torque and axial load and then the equation (2.7) was used to estimate the CoF.

Fig. 4.5 and **Fig. 4.6** show that the CoF fluctuates during the welding process. This effect is most pronounced in batch I during FSSW at 1500 RPM. The CoF slowly rises at the beginning of the process, reaches its peak of CoF ~ 2.5 when dwell time reaches 3.2 s, and then slightly drops and stays almost constant until the end of the process (CoF ~ 2). The sample from the same batch welded at a rotational speed of 2000 RPM acts similarly; CoF increased during the beginning of the process and then remained constant until the end of the process. In batch II similar trends follow the process with 1000 RPM and 1500 RPM. However, the CoF in the process welded at 1000 RPM increased throughout the process, going from 1 to 2. In the sample welded with 1500 RPM, after 0.3 s of dwell time the CoF increased to the maximum value of ~1.7 and remained constant until the end of the process. In all other welding processes from both batches, the CoF behaves conversely. At the beginning of the process, the CoF reaches a peak value and then decreases to the end. Farhat *et al.*[176] and Kumar *et al.*[102] reported that, during the initial interaction between the tool and material surface, friction is influenced by the grains from unprocessed material that are continuously exposed. As the interaction progresses, the material in the subsurface and on the surface deforms and the hardness increases due to a dynamic strain ageing. At the same time, hardening of the material competes against thermal softening. Thus, the two equal and opposite driving forces work against each other to dictate the conditions and microstructure of the material at the end of the process. In samples where the CoF increases at the end of the process, the strain hardening overcomes thermal softening and frictional properties are governed by properties of the hardened metalIn samples where CoF increases at the beginning and then decreases near the end of the process, thermal softening overcame strain hardening after reaching the peak value of the CoF.

It was interesting to observe that the dwell times of samples in batch I welded at different rotational speeds shown in **Fig. 4.7a** are significantly (about three times) higher than the dwell times in batch II for the same rotational speeds. However, the dwell time did not affect the maximum temperatures measured and presented in **Fig. 4.7b**. Temperature profiles of both batches overlap, indicating that temperature does not depend on dwell time, axial load or tool geometry. Rotational speed was the only influence on maximum temperature. With the increase of rotational speed, the temperature increases as well. This was also reported by Kumar *et al*. [102] where temperatures were measured in the FSW process of aluminium alloy 7020-T6 at different rotational speeds (200, 600, 1000 and 1400 RPM) and different axial loads (500, 1000 and 1500 N). It was found that, with the increase of rotational speed, the process temperature increases. Furthermore, with the increase of the axial load, the process temperature increases as well, which is not in agreement with present work. However, the research was done with a different sheet thickness than used in this work. Also, during FSW one more influential parameter is involved, the welding (translator) speed of the tool. Furthermore, the dwell times

reported were of the order of 2500 s [102] while the present work considers this to be about 0.8 to 5 s. It is also important to mention that in present work, the sample areas just below the tool were inaccessible for temperature measurement and measurements were done at the farthest point of stir zone from the source of heat (tool). Thus, the temperature under the tool (top of the joint) may be higher compared with the measured temperature (bottom of the joint). Therefore, the difference between temperature profiles in batch I and II may be more pronounced.

Furthermore, because the temperature profiles in both batches overlap and the values of the CoF are different, it seems that tool geometry (surface area in contact between tool and workpiece) and axial load applied during the process (2 kN in batch I and 4 kN in batch II) are more influential on the CoF than temperature. Incipient hardening is in part an isothermal process which means that heat has less influence during the FSSW process compared with stress or friction assisted plastic deformation.

5.2 The surface topography assessment of contact surface of the tool and the contact surface of the weld joint

All samples were welded with the same tools (batch I with tool T1 and batch II with tool T2) so the influence of tool roughness on CoF cannot be determined. Only an influence of the roughness of the tool contact surface on the joint contact surface roughness could be determined. It was understood through observation on tool T1 only.

The surface roughness of the tool contact surface and joint surface follows the same trend. However, they were different in magnitude considering that the tool material (~235 HV) was about four times harder than the base material (~ 55 HV), as shown in **Fig. 4.8**. The positions of surface topographic features and edge chipping can be seen to have a direct correlation to this behavior. The positions are highlighted by red circles both in **Fig. 4.8b** and **c**. From this simple comparison of topography, it was observed that the smoother area on the contact surface of the tool resulted in a relatively smoother contact area on top of the joined aluminum sheet whilst a rougher surface on the tool contact surface produced a rougher contact area on top of the weld joint.

5.3 Assessment of joint quality obtained with an SAM

FSSW application, especially of thin sheets and foils, can be increasing by improving joint quality assessment. It is preferred for assessment to be carried out with non-destructive examinations concerning the specific nature of the FSSW process. As FSSW has a high potential for applications in electronic components and an SAM has been established as a technique for the fast scanning of electronic parts, it was interesting to combine these two techniques [177–182].

Defect behaviour, such as delamination between the sheets, was similar in both batches with respect to the rotational speed. Therefore, the results presented are focused only on studying

weld quality of samples from batch II concerning the rotational speed which had the highest influence on weld quality. The three samples with the lowest (1000 RPM), middle (2500 RPM) and highest (4500 RPM) rotational speeds were tested for assessing the influence of rotational speed on the deformation of the joint contact surface and on weld defects inside of the stir zone, especially on the interface between the third and fourth sheets, where the weakest bond was expected.

Fig. 4.9 to **Fig. 4.11** shows the difference in surface topography, the volume of the defect and the effective welded area between the two last sheets. In the first two welding interfaces, no delamination was found in any of the three test samples, which can be seen in cross-sections obtained with a B-scan, as shown in **Fig. 4.9c**, **Fig. 4.10c** and **Fig. 4.11c**. An important feature that can be seen in B-scans of the first and second interface is the appearance of a very thin and dashed line, especially in sample welded with 1000 RPM. This WFI has a different wave reflection then rest of the sample as well as a different wave reflection compared with delamination lines (shown with blue arrows). Reilly *et al.*[56] and Yang *et al.* [109] have discussed that, during the welding of aluminium sheets, the natural oxide layer on the surface stays entrapped within the welding interface. Due to the high melting point of oxide, it impedes diffusion bonding. When the tool starts to press and rotate the material, it deforms this interface surface; the tool will stretch the brittle oxide which then disperses into small fragments. The result is diffusion only partly occurs. This could explain the dashed layer obtained in B-scans. Secondly, during FSSW, a high level of deformation combined with increased temperature can cause dynamic precipitation to occur [30,31,183]. This type of behavior was not reported before in FSSW. However, it was reported in processes with similar deformation-temperature conditions such as hot extrusion and equal-channel angular pressing (ECAP). For a better understanding of this layer, a more advanced methodology with higher-resolution techniques will be needed.

In respect to the third weld interface, different rotational speeds produce different sizes of bonded areas and volumes of delamination circles. With an increase of rotational speed, the size of the bonded area in the third interface decreases and volume and size of delamination circles increases. This behaviour is in the function of temperature, deformation and dwell time. In samples welded at higher rotational speeds, due to a high strain rate followed by a fast temperature increase, samples achieve the *steady-state weld* stage significantly earlier than samples with lower rotational speeds. In the *steady-state weld* stage of the samples welded with higher rotational speeds, thermal softening overcome strain hardening and caused the material to soften locally below the tool where the temperature is expected to be the highest. The material flows upwards towards the periphery of the contact area between the tool and the workpiece. Furthermore, the axial load applied to the samples pushes the softened material and does not introduce enough stress in the lower part of the samples. If the stress is not transferred in the lower part of the weld, the interface does not stretch enough, and the oxide layer is partially smashed. Diffusion in some areas does not occur, leaving a partially bonded interface behind. In samples welded at lower rotational speeds, strain hardening dominates over thermal softening and, due to a lower temperature expected just below the tool, stress is more engaged

on the bottom of the workpiece. Stress stretches all interfaces almost equally, providing similar conditions in the whole stir zone.

5.4 Macro- and microstructure characterization of welds in regards to weld dimensions

After the non-destructive characterization of the welded samples, the macro- and microstructure of the joints was studied. **Fig. 4.12a** and **Fig. 4.13a** show two different zones in the top surface of all macrographs. These two zones have different surface roughnesses, which can be seen in the polished cross-sections presented in the same figures with white and black arrows. The white arrows points to the edge-chipping area and the black arrow points to the stable contact area.

Examination of the top view macrograph and cross-section of samples revealed a strong presence of chipping as opposed to plastic deformation. It appears that during the FSSW process, the alloy sheets on the outer part tend to go up but are constrained by the clamping system (shown in **Fig. 5.2**). Consequently, opposite thermal stresses developed radially in the sheets. Due to the continued downward movement of the tool, this radial stress grows further and results in material deforming upwards and coming in contact with the tool under the load F_{EC}. The portion of sheet material in the immediate vicinity of the tool is thus smeared away and leaves fractured sites. It has been shown that the edge chipping contours are rather complex and show no regularity [184]. Also, the parameter "fractal mean square deviation" is quite helpful in the evaluation of contour profile. When the magnitude of tensile stress goes over a certain threshold value and exceeds the fracture toughness of the metal, it causes chipping rather than plastic deformation, as is evident in this work and is shown with black arrows in **Fig. 4.12a** and **Fig. 4.13a**.

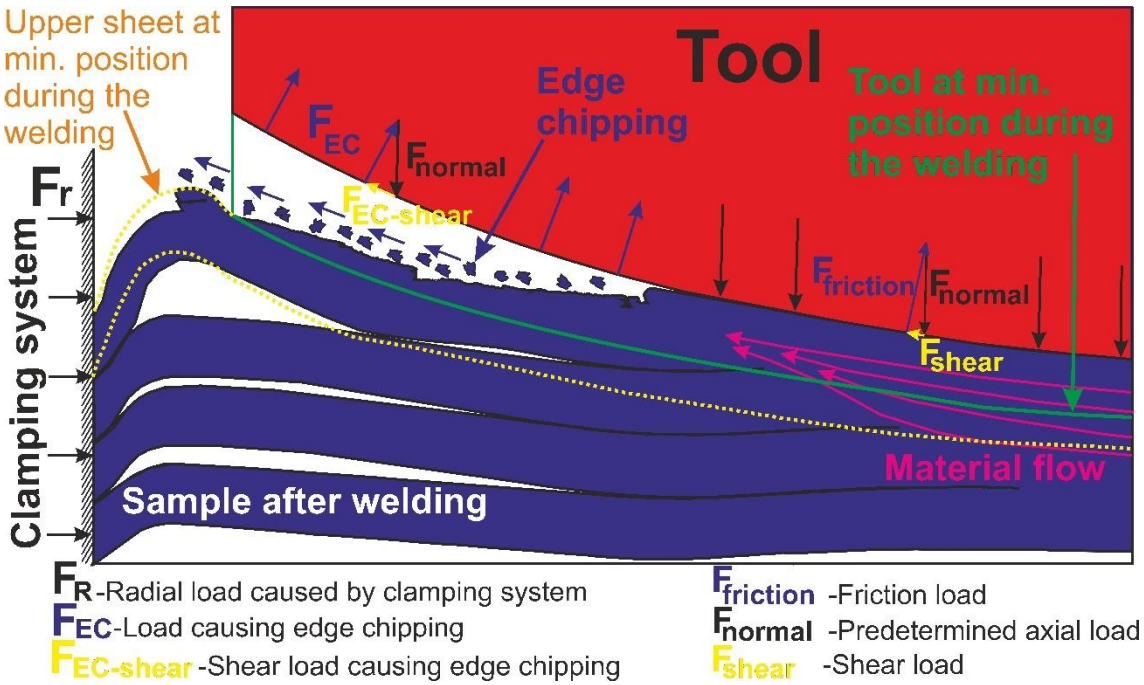

Fig. 5.2 *Schematic of edge chipping effect*

In both batches, the size of these two areas changes with respect to the rotational speed. However, in batch II, the ratio r/R was higher compared with that of batch I. The ratio of these two areas was calculated from radii of both zones (r- radius of *stable contact area* and R- radius of *edge-chipping area*) and is presented in **Fig. 5.3a**. The ratio increases with an increase in rotational speed. Therefore, samples welded at higher rotational speeds have a larger share of smooth surface than fractured (with higher roughness) surface. However, theoretically, the tool should extrude the same volume of material towards the tool periphery within batch because the tool geometry, axial load and plunge depth have been set as constants. Thus, a *stable contact area* theoretically should be the same for all samples within one batch without the influence of rotational speed. However, from **Fig. 4.19c,** it can be seen that the axial depth of the weld zone H is not 0.95 mm, which is the theoretically-expected thickness of all samples, in both batches, in centre of the weld zone after the tool reaches programmed axial displacement of 0.25 mm (number 1 in **Fig. 5.4**) in four sheets with a total thickness of 1.2 mm (**Fig. 5.4**). In reality, the axial depth of the weld decreases with the increase of rotational speed in both batches. In batch II, these values are closer to the theoretical value of 0.95 mm. In batch I, only the sample welded with 1500 RPM is 0.95 mm. Samples welded with rotational speeds ranging from 2000 to 3500 RPM have a lower axial depth of the weld compared with that of the theoretical value. With the decrease of axial depth of the weld, the volume of extruded material to the periphery of the tool increases, which causes r/R ratio to increase.

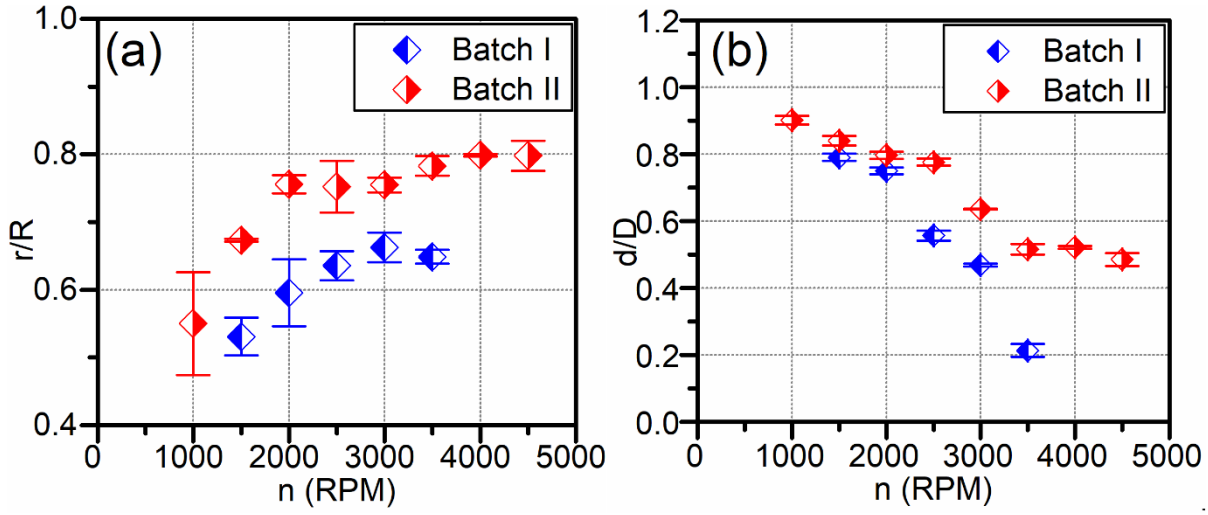

Fig. 5.3 *(a) Ratio of the radius of the edge-chipping area and stable process-pressure area-r/R; (b) ratio of the bottom diameter of the SZ and top diameter of the stir zone-D-d/D*

When the tool reaches the actual axial displacement (number 3 in **Fig. 5.4**) and then retracts, the weld sample will have an axial depth slightly higher than expected due to the elastic recovery of material (number 2 in **Fig. 5.4**). Therefore, in batch II, samples welded with rotational speeds from 1000 to 3000 RPM have a higher axial depth of the weld than their theoretical values. However, material softening is correlated to the decreasing axial depth of the weld to below 0.95 mm. As rotational speed increases, the maximum temperature and thermal softening of the material increases. When the material is softened, a centrifugal force

tends to extrude the material below the tool even when the tool reaches 0.25 mm of penetration depth towards the tool periphery.

For a better understanding of the shape of the stir zone, the ratio of the bottom and top diameter of the SZ, d/D was calculated and presented in **Fig. 5.3b**. The figure shows how, in both batches, d/D significantly decreases when rotational speed increases. This shows that the weld zone changes its shape with rotational speed. This change in the shape of the stir zone was also described with the taper angle of the stir zone (**Fig. 4.19d)**. For different rotational speeds, it varies from approximately 50 to 80^{o}. The trend was identical in both batches. This behaviour confirms the proposed theory that, in samples welded at low rotational speeds, stress is governed towards the the bottom of the stir zone in the sample and thus produces a stir zone with a more cylindrical shape whereas, in samples welded at high rotational speeds, local thermal softening of the material extrudes material up towards the periphery of the tool and causes a stir zone with a more conical shape.

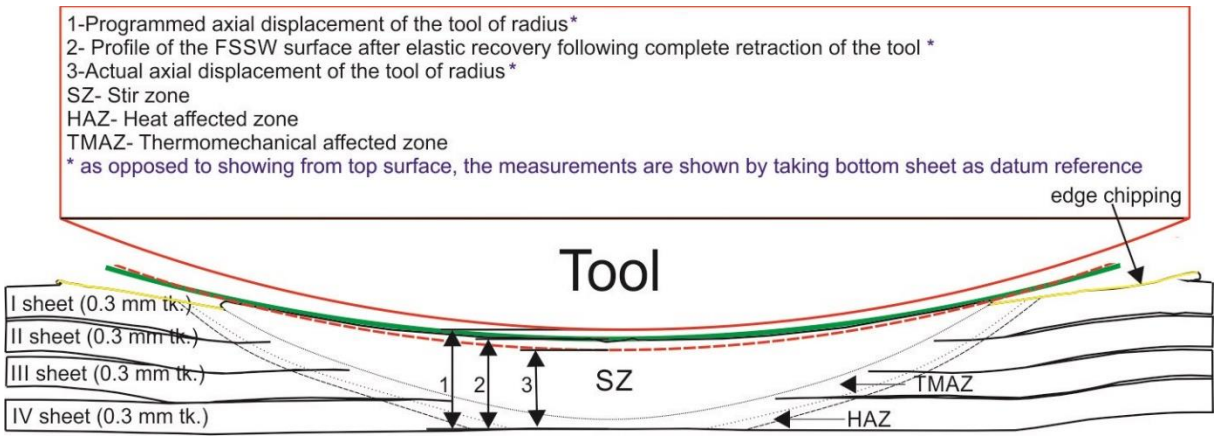

Fig. 5.4 *Schematic illustration of the FSSW process presented in this work*

Etched cross-sections of welds presented in **Fig. 4.12c** and **Fig. 4.13c** show that, within the stir zone, the grain size and orientation are different compared with that of the base material. When the rotational speed increases, the grain size in the stir zone also increases. The grain size range went from less than 5 μm (in welds obtained with 1000 RPM) to 24 μm (for the sample welded with 4500 RPM). Compared with the grain size of the base material (69 μm) significant reduction in grain size within the SZs of all welds was achieved. Until now, a number of studies have been carried out indicating that during FSSW, dynamic recrystallization (DRX) governing the high strain and strain rate, lead to the occurrence of higher temperature [26,114,122,185].

In the schematic illustration in **Fig. 5.4**, different metallurgical zones of weld joints were presented. The stir zone (also called the nugget zone) is the zone that is exposed to intensive plastic deformation and frictional heating during FSSW, resulting in the generation of a recrystallized refined microstructure. The grain size of this zone was mostly influenced by rotational speed, followed by tool geometry and axial load. In **Fig. 4.14** and **Fig. 4.16** it can be seen that decreasing the rotational speed causes a decrease in strain rate, temperature and grain size as well as more uniformly-oriented grains. In this work, an attempt to explain the

mechanism which lead to grain refinement is made. Concerning the base material, subgrain lattice dislocation generated during rolling can remain homogeneously dispersed inside of the grains or they can attain a low energy dislocation structure (LEDS) [186]. During FSSW, the grains and subgrains are replaced with fine, equiaxed recrystallized grains in the stir zone. Jata *et al.* [114] proposed continuous dynamic recrystallization (CDRX) as a grain refinement mechanism during FSSW. This process is driven by temperature, strain and strain rate as well as the interaction between precipitates and solute atoms with dislocations. It appears that a CDRX process analogous to that which gives rise to subgrain formation during high strain rate and frictional heating is operative. Various research papers [27,33,50,114] suggested that the magnitude of misorientation during FSSW/FSW increases significantly compared with that of the base material. Thus, the new grains found in the stir zone are high-misoriented subgrains.

There are three proposed mechanisms of CDRX which can lead to subgrain rotation (twinning) and the appearance of a high-misorientation substructure: (i) lattice rotation associated with slip; (ii) lattice rotation associated with boundary sliding and (iii) subgrain growth. Boundary sliding can be excluded because it is a feature that indicates superplasticity and it is believed not to be operative during high strain rate processes such as FSSW [114]. Subgrain growth can also usually be discarded because of several references reporting that many of the recrystallized grains formed in the DRX region are finer than in the initial subgrains [16,50,114]. Thus, the process that can explain CDRX behaviour is the dislocation-glide-assisted-subgrain rotational model. This model proposes that dislocation glide gives rise to a gradual relative rotation of adjacent subgrains.

Thus, the microstructure of samples welded at different rotational speeds is controlled by competition between: (i) grain size reduction by subgrain rotation induced by dislocation glide and (ii) subgrain coarsening where an amount of subgrain decreases while average subgrain size increases. It is driven by the reduction of local misorientation associated with intercrystalline recovery. The first case is expected in samples where strain hardening overcomes thermal softening (lower rotational speeds). The second case is evident in samples where thermal softening overcomes strain hardening, causing larger grains compared with those in samples welded at lower rotational speed, as seen in **Fig. 4.14** and **Fig. 4.16**. In this case, the stir zone can be seen analogues to the CDRX zone based on dynamic recovery where subgrain growth is associated with the absorption of dislocations into the boundaries.

The TMAZ is a unique transition zone which is located between the SZ and HAZ. It is characterized by a highly deformed structure with columnar grains which follow the pattern around the stir zone. However, it is considered that recrystallization does not occur in this zone due to the low strain rate [16]. **Fig. 4.15** shows that the grain size in the TMAZ in both batches shows a similar trend, meaning that tool geometry, axial displacement and dwell time do not have a significant influence on it. However, rotational speed has a high influence on the shape of the grains in TMAZ, which are equiaxed in samples welded at high rotational speeds and columnar in samples welded at low rotational speeds. Also, rotational speed influences the grain size in TMAZ. The grain size varies from 21 μm (for 1500 RPM) to 36 μm (for 3500 RPM). The most important difference is in the size of the TMAZ. In samples welded at low rotational speeds, the TMAZ is relatively narrow and there is a sharp transition from the SZ to

HAZ. In welds obtained with high rotational speeds, this zone is wide, and the transition is gradual. From a weld quality perspective, gradual transition shows less anisotropy and it is more desirable. Therefore, it can be deduced that samples welded at high rotational speeds have a more uniform microstructure across the weld.

The HAZ is the zone placed beyond the TMAZ. According to Mishra *et al.* [16], this zone experiences only the thermal cycle without any plastic deformation. It has the same grain shape as the base material but with different sizes. Shen *et al.* [108] obtained welds from AA 6061 alloy with FSW where the grain size in the HAZ was higher compared with that of the BM, 22 and 17 μm, respectively. However, during FSW of magnesium alloy AZ31, Sahu *et al.*[187] obtained smaller grains in the HAZ compared with those of the BM. Grains ranged from 53 to 62 μm for different welding conditions in the SZ whereas the grains reached 68 μm in the BM. In this thesis, the HAZ exhibited grain size that is larger than in the TMAZ and smaller than in the BM. In both batches, a similar trend was present: Grain size increases with increasing rotational speed up to 2500 RPM while, beyond that, it decreases.

5.5 Mechanical properties of the welds obtained with a Vickers microhardness test and SPT

The microhardness maps presented in **Fig. 4.20** and **Fig. 4.21** have verified the theory presented in section 5.1 that friction induced plastic deformation and frictional heating lead to competition between strain hardening and thermal softening during FSSW. As reported earlier, in welds obtained at low RPM (1500, 2000 RPM - batch I; 1000 RPM - batch II), a higher hardness in the entire stir zone compared with that of the base material was found. It was proposed that strain hardening overcame thermal softening, which verifies strain hardening behavior. Vice versa, in welds obtained at higher rotational speeds, especially in batch II, the stir zone demonstrated lower microhardness compared with that of the base material. This hardness difference in the stir zones of welds obtained with different rotational speeds can also be correlated to the grain size through the Hall-Petch relationship [188]. In welds obtained at low rotational speeds, grains are smaller, which causes mechanical properties such as strength and hardness to increase. By contrast, with increasing rotational speed, the grain size becomes bigger leading to a decrease in the strength and hardness of welds.

What is also notable here is that, in batch I and batch II, for the same rotational speed, hardness behaves differently. It seems that axial load and dwell time may influence the hardness of the welds. Higher axial load (4 kN in batch II compared with 2 kN in batch I) caused the CoF to be higher in batch I (2.5) than in batch II (1.5), causing more deformation and a higher strain hardening effect. It seems that the relationship between strain hardening and thermal softening depends on the ratio of axial load to rotational speed.Lower axial load also caused dwell time to increase from 1.34 s in batch II (1500 RPM) to 4.65 s in batch I (1500 RPM), which is a significant difference. However, the dwell time in the sample welded with 1000 RPM (1.68 s) was slightly above the values obtained in samples welded with 1500 RPM (1.34 s) in batch II

but almost three times below the dwell time in the sample in batch I welded with 1500 RPM (4.65 s). Hardness in the sample welded with a dwell time of 1.68 s was higher in the entire stir zone than in the other mentioned cases. It is presumed that the hardness of welds depends mostly on the CoF (stress ratio) and not on dwell time. This may lead to the conclusion that decreasing axial load and rotational speed results in a higher strain hardening effect and thus causes hardness to increase.

To explain the variation in hardness over the weld thickness, the Hall-Petch relationship can be applied. In all samples, variations in grain size can be seen from the top surface below the tool where grains are the finest to the bottom of the weld where grains are coarsest. The same trend can be seen in the hardness maps shown in **Fig. 4.20** and **Fig. 4.21**. Even in samples welded at high rotational speed where hardness in the stir zone is below the hardness of the base material, increased hardness is present right below the tool. However, it is important to emphasize that, in samples from batch II welded at rotational speeds from 1500 RPM to 4500 RPM, the grain size is smaller and hardnesss is lower compared with that of the base material. So, the Hall-Petch relationship cannot be applied.

For a more detailed analysis of overall weld quality, a SPT was performed as well. The SPT aimed to compare the mechanical properties of the welds with the base material in order to understand the influence of welding parameters and tool geometry on the weld quality. Also, the fracture mechanism was analysed.

From the load-displacement curves presented in **Fig. 4.22** and **Fig. 4.23** it can be seen that rupture load and maximal punch displacement were in correlation with the microhardness results. The maximal forces (rupture loads) needed to fracture specimens from welds obtained at 1500 RPM (batch I) and 1000 RPM (batch II) were higher compared with those of the BM. All other specimens withstand rupture loads lower than specimens from the BM. This is in correlation with microhardness tests of all specimens with the exception of specimens from welds obtained with 2000 RPM from batch I. These specimens showed higher hardness, but experienced lower rupture loads compared with those of the base material. This is best represented with weld efficiency calculated from the rupture load, as shown in **Table 5.1**. Weld joint efficiency is the ratio of the strengths of the weld and base material:

$$E_s = \frac{Rm_{weld}}{Rm_{BM}} \cdot 100\ (\%) \tag{5.2}$$

where Es represents weld joint efficiency; Rm_{weld}-strength of the weld; $Rm_{base\ material}$-strength of the base material. If the thickness of the specimens cut from welds and base material is the same, weld join efficiency can be calculated by using maximum forces (rupture load):

$$E_s = \frac{Fmax_{weld}}{Fm_{axbase\ material}} \cdot 100\ (\%) \tag{5.3}$$

Table 5.1 showed that, in batch I, specimens from welds produced at rotational speeds from 2000 to 3500 RPM have a lower weld efficiency whereas the specimen welded with 1500 RPM has a higher weld efficiency compared with that of the base material. In batch II, a similar trend can be seen. The specimens from welds obtained with 1500 to 4500 RPM have lower weld

efficiency than the base material. The weld specimen obtained with 1000 RPM has a higher weld efficiency than the base material. However, it is higher by only 0.1%. The highest drop in strength compared with that of the base material is present in the weld produced with 4500 RPM and is 12.6 %

Table 5.1 Rupture loads (*Fm*) with standard deviations used in calculations and weld efficiency (*Es*) of the welds from batch I and II

	Base material	4500 RPM	4000 RPM	3500 RPM	3000 RPM	2500 RPM	2000 RPM	1500 RPM	1000 RPM
Batch I									
Fm (N)	1094.9			1004	1030.2	1010.3	1043	1162	
Standard deviation	21.3			37.83	3.69	4.14	58.01	9.51	
Es (%)	-			91.7	94.1	92.3	95.3	106.1	
Batch II									
Fm (N)	1094.9	957.2	991,9	1002,9	1001.9	1021.3	1016.6	1040.3	1096.7
Standard deviation	21.3	10.3	5.7	13.4	17.4	23.3	3.6	1.9	33.5
Es (%)	-	87.4	90.6	91.6	91.5	93.3	92. 8	95	100.2

Welds obtaining a weld efficiency of above 100 % had higher strength, while the specimens with values below 100% have lower strength compared with the strength of the BM. Weld efficiency in batch I for all RPM was higher compared with the weld efficiency of specimens from batch II. This can be correlated with delamination found in specimens obtained in batch II, which are indicated with green arrows in **Fig. 4.26**. All samples from batch I have narrowly opened a circumferentially-oriented crack, which is a typical crack obtained after a SPT [189] without any sign where the weld interface is and without any trace of delamination. In batch II, delamination seems to be a dominant fracture mechanism in some specimens. The most influential parameter on delamination seems to be dwell time. As mentioned in section 2.8.4, during FSSW of aluminium alloys an oxide layer can get trapped in the weld interface. For diffusion between the sheets to occur, this layer has to be stretched and mixed as much as possible to avoid the delamination effect obtained in samples from batch II in SAM (chapter 4.3). As the dwell time in batch I is approximately three times longer compared with the dwell time in batch II, a better stirring of this WFI layer is provided. A comparison of samples welded with 1500 RPM from batch I (a) and batch II (b) shows that, for the same rotational speed, this trapped WFI is less mixed in a sample from batch II due to significantly lower dwell time as shown in **Fig. *5.5***. In all three interfaces, particularly in the third, a dashed black line can be found. The same dashed lines can be found in specimens in **Fig. 4.26** and are indicated with white arrows. The delamination that was seen in all SPT specimens occurred along those lines leading to believe that the WFI has caused delamination to occur.

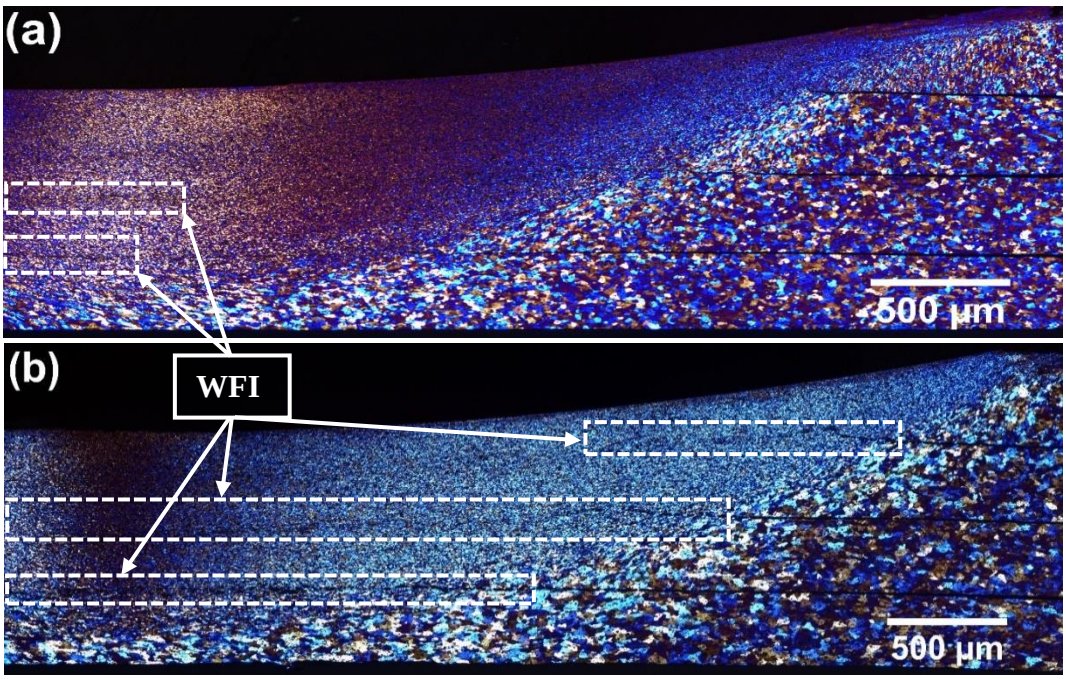

Fig. 5.5 *Comparison of samples welded with 1500 RPM; (a) batch I; (b) batch II*

For a better understanding of delamination behaviour, the SEM micrographs in **Fig. 4.27a** and **b** are shown. These show where the WFI was found in rupture-within cracked surface after the SPT **Fig. 4.27c** and **d**. The thickness of this WFI varies from 1.72 to 4.23 µm, which exceeds the values of the continuous surface oxide layer (CSOL) expected on top of the aluminium sheets before welding. Fishkis *et al*. [153] studied the behaviour of the surface oxide layer after the hot rolling of Al-Mg alloys and found two different oxide zones. The first one is the CSOL with a thickness of 25 to 160 nm. Below the CSOL, a mixed subsurface layer (MSL) with thicknesses of 1.5 to 8 µm was found. The size presented in **Fig. 4.27d** corresponds more with the MSL; it is possible that, during the SPT, a rupture initially occurred in the MSL between the oxide particles and surrounding material. **Fig. 4.27** shows a ductile fracture mechanism full of pits, indicating that fracture occurred between some of the particles and surrounding material, which fits well with this theory. However, further analysis with TEM will give better insight into the composition and size of this layer.

The micrographs in **Fig. 4.25** and **Fig. 4.26** suggest that the ductility of samples welded at different rotational speeds differs. The maximal punch displacements, as well as specimen thinning, show a difference in welds obtained with different rotational speeds. The lowest values of specimen thinning and the lowest *Smax* (**Table 4.1**) can be found in specimens from welds obtained at low rotational speeds. This fact also verifies the theory that the strain hardening mechanism is dominant at low RPM, leading to an increase in surface hardness and reduced ductility.

5.6 Analysis of the WFI

For a closer inspection of the weld interface hardness and modulus, maps over the WFI and RSZ were studied. As seen in **Fig. 4.29**, there was no significant difference in mechanical properties (hardness and modulus) between the RSZ and WFI. The oxide layer which was found in **Fig. 4.35** was not detected due to the insufficient resolution of nanoindentations ~200 nm. However, **Fig. 4.29** and **Table 4.2** show three different clusters of hardness and modulus. The first two clusters correspond to the processed material (stir zone) while the third, which is the highest, corresponds to the hard brittle $Al_6(FeMn)$ phase as detected by the EDX shown in **Fig. 4.30c**. In the case of the stir zone, a 22% drop of modulus and 11% drop of hardness from cluster 1 to cluster 2 can be seen. The hardness and modulus maps show non-uniform distribution over the tested zone but with a similar pattern over the whole area. It can be assumed that higher hardness values correspond to the grain or subgrain boundaries accumulated with dislocation movement, which are found in TEM (**Fig. 4.33**). The TEM figure reveals subgrain formation inside the polygonal grains in both the WFI and RSZ. In **Fig. 4.34a** and **b**, the existence of accumulated dislocations was verified. It is interesting to note that the main dislocations follow the material flow, thus they are parallel to WFI, shown in **Fig. 4.34a**. The diffraction pattern in **Fig. 4.34b** illustrates streaks on spots which are caused by a high accumulation of dislocations and the formation of partial rings due to presence of multiple subgrains and their preferred orientation [190]. Diffraction spots became extended because dislocations change the crystal orientation locally. Due to this heterogeneous dislocation accumulation which causes strain hardening, hardness was heterogeneously increased locally as well.

In **Fig. 5.6**, a clear difference between the RSZ and WFI can be seen. The WFI had a non-uniform thickness which varies from 1.67 to 2.02 μm. This thickness corresponds to the SEM results in **Fig. 4.27d** where the thickness of the WFI varied between 1.72 and 4.73 μm. Also, **Fig. 4.39a** shows a high number of precipitates with an average size of 0.09 μm which are located along the boundary between the WFI and RSZ; these can be initial sites of crack growth. These precipitates made of the chemical composition shown in **Fig. 4.39b** correspond to the Al_3Mg_2 brittle intermetallic phase commonly known for AA 5754 alloy [191]. This phase can be responsible for a number of pits found in the fractured surface between the RSZ and WFI, as shown in **Fig. 4.39a** and **b**.

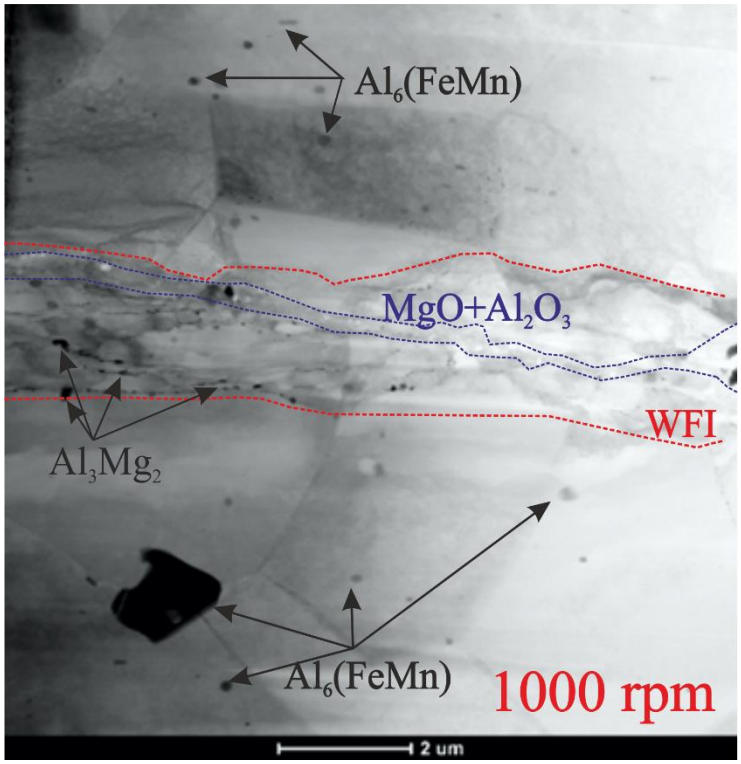

Fig. 5.6 *TEM overall image of weld faying interface*

It is important to note that the WFI is a very complex layer with different grain shapes and sizes as well as different precipitate shapes and sizes in comparison to the RSZ. The variation in the grain size of the WFI compared with that of the RSZ was the result of a high level of microplastic deformation caused by a fairly rough surface of welded sheets in the WFI. This microplastic deformation induces more dislocation in subgrains, thus forming smaller elongated grains which follow the vector of the material flow. In the middle of this zone, a number of nano-pits surrounded by trapped oxide were found. The theory proposed in section 2.8.4 was verified by TEM images shown in **Fig. 4.35** and **Fig. 4.37** indicating that the interface between two sheets, which is covered by oxide during FSSW, gets stretched and diffusion occurs between oxide fragments. A number of oxide fragments in combination with nano and micro pits were found. They followed the direction of the vector of material flow (shear stress). All nano and micro pits were engulfed by an oxide layer, which acts as a diffusion barrier leaving unbonded spots (pits). This was also confirmed by FM-KPFM, which revealed a different work function (**Fig. 5.7b**) in the oxygen-rich zone (**Fig. 5.7a)** compared with that of the aluminium base. The oxide has a higher work function (4.480 to 4.600 eV) than the aluminium base (4.350-4.460 eV). The work function obtained for aluminium varies from 4.06 to 4.41 eV whereas for Al_2O_3 it varies from 4.5 to 4.7 eV [192,193]. This was also confirmed with the EDX spectrums presented in **Fig. 4.36**. It can be seen that, in the zone of interest around the micro-pit indicated in **Fig. 5.7a,** only Al and O were found. Furthermore, mixed Al-Mg-O oxide particles were found in the micro pits. However, it is interesting to note that according to the size and shape of the layer found in **Fig. 4.27d**, delamination was not caused by the oxide layer or by micro or nano pits. It is more likely that delamination was caused by

precipitates found in the boundary between the WFI and RSZ. This is probably because the enitre WFI is strengthened due to a higher deformation level and higher dislocation accumulation. Also, the oxide particles could additionally straighten the WFI by acting as reinforcing particles. Due to a difference in ductility and strength, the WFI was pulled from surrounding material during the SPT.

In WFI, numerous rod-like precipitates were found within the grains. In **Fig. 4.31** and **Fig. 4.38** EDX maps show that precipitates contained only Al and Mg atoms, which indicates that the precipitates were that of Al_3Mg_2. These precipitates can be found only in the WFI and they are orientated in two directions: (i) in the direction of material flow (shear load) and (ii) normal to the material flow (in the direction of axial load). As these precipitates were not found in the RSZ, it is suspected that they are formed only at the WFI during FSSW. The reason for this could be a microplastic deformation induced in grains causing interaction between dislocation and solute atoms causing dynamic precipitation. Hagihara *et al.* [183] proposed that the to-and-fro motion of dislocation induces the precipitation of the ω-phase inside of β-Ti alloy, which is followed by cyclic softening. Precipitations followed a loading orientation and dislocation distribution. With careful investigation, authors manage to confirm that the main axis of precipitates corresponds to the Burgers vector of dislocations. It proves that dislocation motion dynamically induces the precipitation of the ω-phase inside of β-Ti alloy.

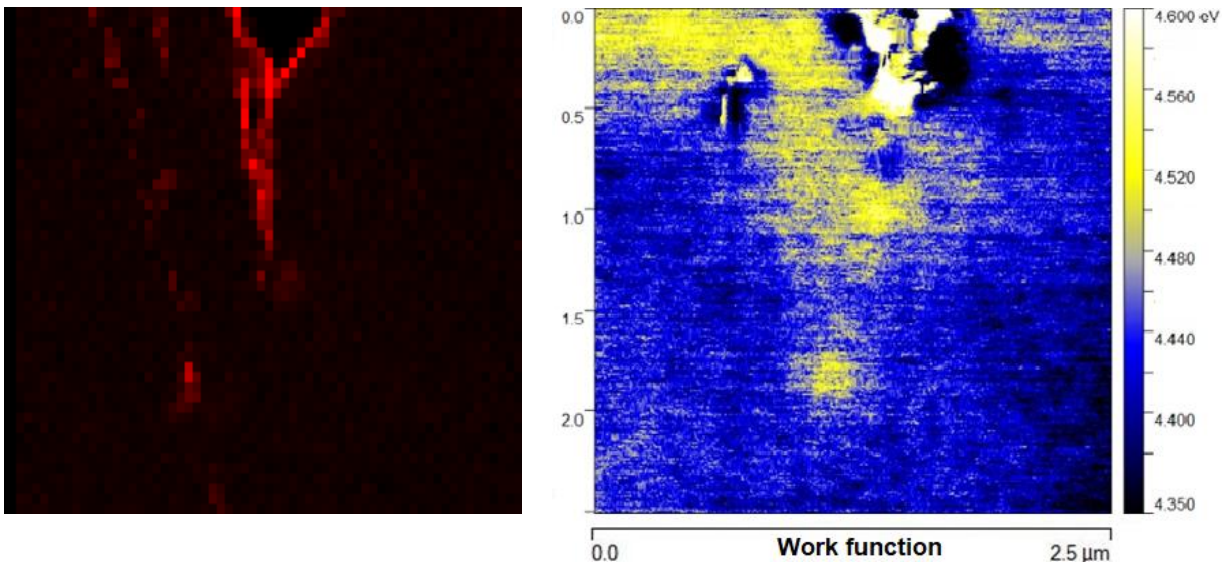

Fig. 5.7 *Comparation between: (a) oxygen distribution obtained from EDX in* **Fig. 4.35** *and (b) work function map showing the distribution of oxide in the same area as in (a)*

The second type of precipitates found in the WFI and at the boundary between the WFI and RSZ was probably the main cause for delamination found during the SPT. Ma *et al.* [30] explained that nucleation of precipitation can be significantly enhanced by mechanical processing at low temperatures during which precipitates growth is suppressed. Crystal defects caused by deformation can enhance nucleation rates by offering a high density of heterogeneous nucleation sites. Those nucleation sites are dislocations, grain boundaries, stacking faults, inclusion and free surface, all of which increase the free energy of the material

[194]. In the WFI beside the grain boundaries and dislocation, the irregularly-shaped free surface caused more deformation and provided more place for nucleation of precipitates, which led to dynamic precipitation. Roven *et al.* [29] investigated dynamic precipitation in Al-Mg-Si alloy during equal-channel angular pressing (ECAP) at 20 and 175 ^{o}C. The high stress imposed during ECAP caused precipitates fragmentation. Tthis was due to the shearing of it into very small pieces. In WFI, fragmentation of the precipitates was found in grain boundaries, especially between the WFI and RSZ. In **Table 4.3** it can be seen that, in the RSZ, size of precipitates is almost twice that of the size of precipitates found in the WFI. Overall, those precipitates were responsible for the delamination between the WFI and RSZ.

6. CONCLUSIONS AND FUTURE WORK

6.1 General conclusions

Friction stir spot welding (FSSW) is one of the emerging spot-welding processes which provides possibilities for joining a wide range of materials with minimal energy consumption. The process is still in its infancy and thus FSSW's applications are limited due to the following constraints:

(i) The minimum thickness of the sheets that can be welded (extant literature reports welding of sheets more than 1 mm thick).
(ii) Lap joining of more than two sheets (extant literature does not show any direct evidence of joining multiple sheets at a time).
(iii) Welding time (to be competitive with RSW).
(iv) Insufficient understanding of the weld faying interface, which has crucial influence on the quality of the weld joints obtained from FSSW.

With the goal of increasing productivity in the electronics sector, the present work addresses these FSSW challenges and aims to find solutions for lap-welding ultrathin sheets and foils. By using two different tool geometries and varying welding parameters such as rotational speed and axial load, welds were obtained with a wide range of mechanical properties and sizes.

To further the current understanding on the different properties of welds obtained with different welding parameters and tool geometry, advanced techniques were used to characterize weld joints. Some of the techniques used were SAM, SEM, TEM with EDX, FM-KPFM, in-situ SPM, and SPT. All these techniques were used to provide a fundamental understanding of the FSSW joints revealing the chemical, geometric and physical (strength) aspects of the FSSW joining process.

To understand the influence of tool geometry and welding parameters on the FSSW process, stress-strain behavior during the process was studied in detail. A strong correlation between the stress-strain behavior during welding, microstructure, and mechanical properties obtained with Vickers microhardness test and small punch test was found. Afterwards, a detailed analysis of the welding interface was done in order to understand the influence deformation and frictional heating developed during the FSSW process have on welds.

The major results obtained in this thesis can be summarized as follows:

1. Two convex tools (T1 and T2) with different tool radius were designed in order to obtain weld joints of four 0.3 mm thick sheets of aluminium alloy with the FSSW process. Both tools produced bonds between four sheets at ranges of rotational speeds. The T1 tool provided the bond between four sheets by setting the axial load at 2 kN, plunge depth 0.25 mm and rotational speeds in the range of 1500 to 3500 RPM. With

the T2 tool, the axial load was set at 4 kN, plunge depth 0.25 mm and the range of rotational speeds was from 1000 to 1500 RPM. Welding with rotational speeds below the minimum (1500 and 1000 RPM for batch I and batch II, respectively) or above the maximum values (3500 and 4500 RPM for batch I and batch II, respectively) did not provide a bond between all sheets or dwell time exceeded maximum time programed (5 s). The axial load was set at the lowest possible load which can provide bonding. Bonding could not be achived at a value above than the applied axial load. When axial load was set to be below the applied, dwell time was increased. Plunge depth was set at the minimum needed for the bond to form and to avoid high dimensional distortion.

2. Two major stresses were found to be present during FSSW: (i) axial stress and (ii) shear stress. Axial stress depends on axial load whereas shear stress depends on rotational speed. Both parameters show significant influence on weld quality. Hence, two different stages during the FSSW process were derived: (i) the stick-slip stage and (ii) steady-state weld. The ratio of these two stages was given by the ratio of axial and shear stress and governs the coefficient of friction during the process.

3. Welds obtained at low rotational speeds had different slopes of stress over time compared with welds obtained at high rotational speeds. This implies a competition between thermal softening and strain hardening during FSSW. During welding at low rotational speeds, strain hardening overcame thermal softening while high rotational speeds caused thermal softening to be more pronounced.

4. The CoF presented as the ratio between shear stress and axial stress was higher in batch I compared with the CoF of batch II. In both batches, a similar trend was present. At low rotational speeds as the strain hardening effect increases over time, CoF increases up to the end of the process. At high rotational speeds, thermal softening softens the material, causing CoF to decrease. This observation goes along with stress behavior and verifies the strain hardening thermal softening theory.

5. Following the CoF, maximal temperature and strain rate were found to increase with increasing rotational speed, which caused thermal softening. However, axial load and tool geometry did not have any influence on the maximum temperature. However, they did have a very high influence on dwell time. It seems that dwell time was three times lower in batch II when tool T2 was used than in batch I when T1 was used. Higher axial load and the wider contact surface between the tool and workpiece are responsible for the drop in dwell time below 1 s, which gives the potential for the FSSW technique to become competitive with RSW.

6. Analysis with a SAM found no defects in the top two interfaces of any of the samples tested. However, in the bottom most interface delamination circles were found. The volume of delamination circles increased with an increase in the rotational speed. It was

also interesting to note that, with increasing rotational speed, the bonded surface area between the last two interfaces reduced.

7. Macrographs revealed defect-less cross-sections in all samples except in the welds obtained at 3500 RPM in batch I, which had a void in the middle of the upper sheet. All samples were bonded successfully. The welds obtained with tool T2 produced a wider stir zone than the welds obtained with tool T1. After measuring the stir zone, it can be concluded that the stir zone is on the shape of a cone with a slope angle varying from approximately 44^o to 77^o for rotational speeds 1500 to 3500 RPM, respectively. Also, higher rotational speeds followed by higher strain rates caused softening of the material below the tool. In the welds obtained with low rotational speeds, strain hardening overcame thermal softening and thus the material became harder.

8. The top surface of the welds consisted of two different zones and the size of these two zones varies depending on rotational speed and follows the conical shape of the welds. The welds obtained at high rotational speeds have a high *r/R* ratio, meaning they have smaller edge-chipping areas and larger smooth areas, due to a higher volume of material suppressed below the tool. Welds obtained with low rotational speeds have a low *r/R* ratio and the welds have almost equal sizes of edge-chipping and smooth areas.

9. The grain size and shape varied within the weld over the SZ, TMAZ, HAZ, and BM. In all welds, grain size was highest in the BM followed by the HAZ, TMAZ and finally the stir zone, which had the lowest grain size. The stir zone consisted of fine recrystallized polygonal grains surrounded by the columnar grains of the TMAZ. The HAZ was between the BM and TMAZ and had the same grains shape as in the BM but smaller. Depending on the rotational speed, a different width of the TMAZ and grain shape inside of it can be seen.

10. The grain size within the stir zone varied for samples welded with different rotational speeds from less than 5μm to 25 μm for 1000 and 4500 RPM, respectively. In all samples, grain size within the stir zone was reduced compared with that of the base material (by about 75 μm). This grain size reduction correlates well with dynamic recrystallization due to high-stress input and frictional heating.

11. Microhardness and weld efficiency showed that, in samples welded at low rotational speeds 1500 and 2000 RPM (batch I) and 1000 RPM (batch II), higher mechanical properties compared with those of the base material were obtained; this is due to the dominating effect of strain hardening in those welds. In samples welded at the higher rotational speeds of 3000 and 3500 RPM (batch I) and from 1500 to 4500 RPM (batch II), a lower microhardness compared with that of the base material was observed, indicating that thermal softening was dominating. Only the sample welded at 2500 RPM (batch I) experienced an equal strength of strain hardening and thermal softening, which resulted in average mechanical properties similar to those of the base material.

This was also verified by sample thinning and maximum punch displacement results. The thinning and *Smax* were found to be minimum in samples welded with the lowest RPM, indicating that those specimens have a lower ductility in comparison to the BM and samples welded with higher RPM, verifying the dominating effect of strain hardening.

12. All specimens without defects in the weld zone during the SPT experienced radial cracking oriented in a circumferential direction. Welds obtained at 1000, 2000 and 4000 RPM (batch II) experienced delamination as well. This cracking followed the path of the WFI. In the rupture between welded sheets, a third non-uniform mixed layer with a thickness ranging from 1.72 to 4.23 μm was found to be responsible for delamination.

13. Closer inspection of the weld interface did not reveal any difference of hardness and modulus inside of the RSZ and WFI. Though, the resolution of nanoindentation was about 200 nm. A different hardness and modulus distributed over the tested area show variation in nano hardness indicating that accumulation of dislocation which was non-uniformly distributed could cause this variation. This observation was verified by TEM, showing a high dislocation accumulation inside of the polygonal grains of the SZ. The dislocation results in the formation of subgrains which cause micrograin rotation and reduced size. This subgrain rotation caused by CDRX was the main recrystallizing mechanism within the stir zone.

14. TEM revealed a different microstructure (shape and size of grains and precipitates) in the RSZ and WFI. The WFI layer varies in thickness from 1.67 to 2.02 μm. This thickness can be correlated to the thickness of the layer found in the rupture, which varied from 1.72 to 4.73 μm. The grains within the WFI were columnarly orientated in the direction of material flow with an average size of 0.92 μm. At the grain boundaries between grains within the WFI and between the WFI and RSZ, precipitates with an average size of 0.09 μm were found. However, in the RSZ polygonal grains with an average size of 4.9 μm and precipitates with an average size of 0.15 μm are present. The reduction of the grain and precipitates size was caused by microplastic deformation which was induced between rough edges of the surface of the sheet before welding. Shear stress caused the rough surface peaks to yield, one over another, causing mechanical fragmentation of grains and precipitates and leaving them smaller and with a columnar shape following the vector of material flow.

15. From the SEM and TEM results, it could be concluded that ductile rupture occurred at the interface between the precipitates found on the boundary between the WFI and RSZ and left a number of small pits behind. The boundary between the WFI and RSZ was oversaturated with Al_3Mg_2 and $Al_6(FeMn)$ precipitates with a low bond energy suitable for crack initiation.

16. In the middle of the WFI zone, a trapped oxide layer distributed in fragments was identified with the TEM (EDX) and FM - KPFM, . All aluminum sheets developed a natural oxide layer on the top surface by reacting with the air. During FSSW, due to the high melting point of oxides, the oxides are entrapped at the interface between the sheets which impedes diffusion between the sheets from occurring. However, when the tool presses the sheets, it stretches the interface. As oxide is a brittle phase, it breaks into fragments causing the formation of diffusion sites. Due to the scattered oxide fragmentation, several nano and micro pits were found to form.

17. Inside of the WFI, rod-like precipitates rich with Al and Mg with an average length of 0.076 ±0.016 μm and an average thickness of 0.042 ±0.009 μm were found within the columnar grains. These precipitates were orientated in two main directions: (i) along the vector of material flow caused by shear stress and (ii) along the direction normal to the applied shear stress. They were produced by microplastic deformation induced in grains which caused interaction between dislocations and solute atoms and trigered dynamic precipitation.

6.2 Recommendations for future work

Until now, the FSSW process was mainly used for welding sheets with a thickness of more than 1 mm. This work provides an opportunity for using FSSW for welding components made from thin sheets and with a short welding time, representing a robust basis for future work. This led FSSW to potentially become a promising technique for the welding of electronic components and battery elements. To overcome present drawbacks and to improve the process, some of the recommendations are outlined as follows:

(i) To improve the relationship between tool geometry and clamping system in order to obtain welds without edge-chipping areas and to reduce welding time below 0.5 s so FSSW can be fully competitive with RSW and UW.
(ii) To evaluate the mechanical properties of the welds by using various testing methods such as tensile, shear and fatigue testing, in order to understand the fracture mechanism in FSSW samples and to assess the fatigue lifetime of weld samples.
(iii) To study the influence of surface roughness of sheets on the size and properties of the weld faying interface.
(iv) To use the EBSD technique to analyse grain and subgrain size and orientation as well as misorientation angle in order to increase the understanding of strain hardening/thermal softening mechanisms.
(v) To use TEM to analyse dynamic precipitation in detail in order to understand the mechanism leading to the formation of the hard phase (rod-like precipitates within the grains).
(vi) To study the influence of preheating and cooling on strain hardening/thermal softening mechanisms.

(vii) To develop a full Molecular Dynamic (MD) model of the FSSW process to understand dynamic recrystallization and diffusion mechanism at the atomic level.

(viii) To use the FSSW technique to weld other combinations of material such as aluminium and copper foils.

7. REFERENCES

[1] A. Regensburg, F. Petzoldt, T. Benss, J.P. Bergmann, Liquid interlayer formation during friction stir spot welding of aluminum / copper, Weld. World. 63 (2018) 117–125. https://doi.org/10.1007/s40194-018-0620-8.

[2] L. Pryor, R. Schlobohm, B. Brownell, A Comparison of Aluminum Vs . Copper As Used in Electrical Equipment, in: Corrosion, 2008: pp. 1–7. http://apps.geindustrial.com/publibrary/checkout/Alum-Copper?TNR=White Papers%7CAlum-Copper%7Cgeneric.

[3] O.O. Ojo, E. Taban, E. Kaluc, Friction stir spot welding of aluminum alloys: A recent review, Mater. Test. 57 (2015) 595–627. doi:10.3139/120.110752.

[4] A. Regensburg, R. Schürer, M. Weigl, J.P. Bergmann, Influence of pin length and electrochemical platings on the mechanical strength and macroscopic defect formation in stationary shoulder friction stir welding of aluminium to copper, Metals (Basel). 8 (2018). doi:10.3390/met8020085.

[5] S.M. Manladan, F. Yusof, S. Ramesh, M. Fadzil, Z. Luo, S. Ao, A review on resistance spot welding of aluminum alloys, Int. J. Adv. Manuf. Technol. 90 (2017) 605–634. doi:10.1007/s00170-016-9225-9.

[6] R. Hajavifard, M. Motahari, H. Özden, H. Miyanaji, S. Kafashi, The Effects of Pulse Shaping Variation in Laser Spot-Welding of Aluminum, Procedia Manuf. 5 (2016) 232–247. doi:10.1016/j.promfg.2016.08.021.

[7] H.Y. Lei, Y.B. Li, B.E. Carlson, Cold metal transfer spot welding of 1 mm thick AA6061-T6, J. Manuf. Process. 28 (2017) 209–219. doi:10.1016/j.jmapro.2017.06.004.

[8] A. Sunwoo, Diffusion bonding of aluminum alloy, 8090, Scr. Metall. Mater. (1994). doi:10.1016/0956-716X(94)90009-4.

[9] Z.L. Ni, F.X. Ye, Ultrasonic spot welding of aluminum alloys: A review, J. Manuf. Process. 35 (2018) 580–594. doi:10.1016/j.jmapro.2018.09.009.

[10] X.W. Yang, T. Fu, W.Y. Li, Friction Stir Spot Welding : A Review on Joint Macro- and Microstructure , Property , and Process Modelling, Adv. Mater. Sci. Eng. 2014 (2014) 1–11.

[11] A. Hill, E.R. Wallach, Modeling solid-state diffusion bonding, Acta Metall. 37 (1989) 2425–2437.

[12] F. Wu, W. Zhou, Y. Han, X. Fu, Y. Xu, H. Hou, Effect of alloying elements gradient on solid-state diffusion bonding between aerospace aluminum alloys, Materials (Basel). 11 (2018). doi:10.3390/ma11081446.

[13] D.R. Cooper, J.M. Allwood, The influence of deformation conditions in solid-state aluminium welding processes on the resulting weld strength, J. Mater. Process. Technol. 214 (2014) 2576–2592. doi:10.1016/j.jmatprotec.2014.04.018.

[14] A. Shirzadi, Diffusion Bonding Aluminium Alloys and Composites : New Approaches and ModelShirzadi, A. (1997) 'Diffusion Bonding Aluminium Alloys and Composites : New Approaches and ModellinG, Univeristy of Cambridge, 1997.

[15] J. Li, S. Lazarevic, S. Miller, W. Wang, W. Cai, L. Xi, K. Wang, M. Banu, The characteristics of interface microstructures in dissimilar materials joints through ultrasonic welding and friction stir processes, in: IWMF2014, 9th Int. Work. MICROFACTORIES, HONOLULU, U.S.A, 2014: pp. 195–201.

[16] R.S. Mishra, Z.Y. Ma, Friction stir welding and processing, Mater. Sci. Eng. R 50. 50 (2005) 1–78. doi:10.1016/j.mser.2005.07.001.

[17] Mazda Develops World's First Steel and Aluminum Joining Technology Using Friction Heat, Maz. News Release. (2003) 1. https://www2.mazda.com/en/publicity/release/2005/200506/050602.html (accessed August 26, 2019).

[18] H. Badarinarayan, Q. Yang, S. Zhu, Effect of tool geometry on static strength of friction stir spot-welded aluminum alloy, Int. J. Mach. Tools Manuf. 49 (2009) 142–148. doi:10.1016/j.ijmachtools.2008.09.004.

[19] W. Li, J. Li, Z. Zhang, D. Gao, W. Wang, C. Dong, Improving mechanical properties of pinless friction stir spot welded joints by eliminating hook defect, Mater. Des. 62 (2014) 247–254. doi:10.1016/j.matdes.2014.05.028.

[20] D. Bakavos, Y. Chen, L. Babout, P. Prangnell, Material interactions in a novel pinless tool approach to friction stir spot welding thin aluminum sheet, Metall. Mater. Trans. A Phys. Metall. Mater. Sci. 42 (2011) 1266–1282. doi:10.1007/s11661-010-0514-x.

[21] Y.C. Chiou, C. Te Liu, R.T. Lee, A pinless embedded tool used in FSSW and FSW of aluminum alloy, J. Mater. Process. Technol. 213 (2013) 1818–1824. doi:10.1016/j.jmatprotec.2013.04.018.

[22] D. Labus Zlatanovic, S. Balos, J.P. Bergmann, T. Köhler, M. Grätzel, L. Sidjanin, S. Goel, An experimental study on lap joining of multiple sheets of aluminium alloy (AA 5754) using friction stir spot welding, Int. J. Adv. Manuf. Technol. 107 (2020) 3093–30107. doi:10.1007/s00170-020-05214-z.

[23] C. Vargel, Corrosion of Aluminium, Elsevier, 2004. doi:10.1016/B978-0-08-044495-6.X5000-9.

[24] I. Polmaer, Light Alloys, Fourth edi, Elsevier, 2006. doi:10.1017/CBO9781107415324.004.

[25] R.N. Lumley, Fundamentals of aluminium metallurgy: Production, processing and applications, Woodhead publishing, 2010. doi:10.1533/9780857090256.

[26] K. Huang, R.E. Logé, A review of dynamic recrystallization phenomena in metallic materials, Mater. Des. 111 (2016) 548–574. doi:10.1016/j.matdes.2016.09.012.

[27] B. Bagheri, M. Abbasi, A. Abdollahzadeh, H. Omidvar, Advanced Approach to Modify Friction Stir Spot Welding Process, Met. Mater. Int. (2019). doi:10.1007/s12540-019-00416-x.

[28] A. Deschamps, M. Niewczas, F. Bley, Y. Brechet, J.D. Embury, L. Le Sinq, F. Livet, J.P. Simon, Low-temperature dynamic precipitation in a supersaturated Al-Zn-Mg alloy and related strain hardening, Philos. Mag. A Phys. Condens. Matter, Struct. Defects Mech. Prop. 79 (1999) 2485–2504. doi:10.1080/01418619908214295.

[29] H.J. Roven, M. Liu, J.C. Werenskiold, Dynamic precipitation during severe plastic deformation of an Al-Mg-Si aluminium alloy, Mater. Sci. Eng. A. 483–484 (2008) 54–58. doi:10.1016/j.msea.2006.09.142.

[30] X.L. Ma, S. Eswarappa Prameela, P. Yi, M. Fernandez, N.M. Krywopusk, L.J. Kecskes, T. Sano, M.L. Falk, T.P. Weihs, Dynamic precipitation and recrystallization in Mg-9wt.%Al during equal-channel angular extrusion: A comparative study to conventional aging, Acta Mater. 172 (2019) 185–199. doi:10.1016/j.actamat.2019.04.046.

[31] Y. Wu, H. Liao, Y. Liu, K. Zhou, Dynamic precipitation of Mg2Si induced by temperature and strain during hot extrusion and its impact on microstructure and mechanical properties of near eutectic Al-Si-Mg-V alloy, Mater. Sci. Eng. A. 614 (2014) 162–170.

doi:10.1016/j.msea.2014.07.023.

[32] Y.M. Hwang, C.H. Lin, Friction Stir Welding of Dissimilar Metal Sheets, Steel Res. Int. 81 (2010) 1076–1079. doi:10.22214/ijraset.2018.13032.

[33] J.Y. Cao, M. Wang, L. Kong, H.X. Zhao, P. Chai, Microstructure, texture and mechanical properties during refill friction stir spot welding of 6061-T6 alloy, Mater. Charact. J. 128 (2014) 54–62. doi:10.1016/j.matchar.2017.03.023.

[34] W.M. Thomas, E.D. Nicholas, J.C. Needham, M.G. Murch, P. Temple Smith, C.J. Dawes, International Patent Application No. PCT/GB92/02203 and GB Patent Application No. 9125978.8, n.d.

[35] R.S. Mishra, M.W. Mahoney, S.X. Mcfadden, N.A. Mara, A.K. Mukherjee, High Strain Rate Superplasticity In a Friction Stir Processed 7075 Al Alloy, Scr. Mater. 42 (2000) 163–168.

[36] N.L. Sukiman, X. Zhou, N. Birbilis, A.E. Hughes, J.M.C. Mol, S.J. Garcia, X. Zhou, G.E. Thompson, Durability and Corrosion of Aluminium and Its Alloys: Overview, Property Space, Techniques and Developments N., in: Alum. Alloy. New Trends Fabr. Appl., 2012: pp. 47–97. doi:http://dx.doi.org/10.5772/57353.

[37] S.T. Amancio-Filho, A.P.C. Camillo, L. Bergmann, J.F. Dos Santos, S.E. Kury, N.G.A. Machado, Preliminary investigation of the microstructure and mechanical behaviour of 2024 aluminium alloy friction spot welds, Mater. Trans. 52 (2011) 985–991. doi:10.2320/matertrans.L-MZ201126.

[38] Y. Tozaki, Y. Uematsu, K. Tokaji, A newly developed tool without probe for friction stir spot welding and its performance, J. Mater. Process. Technol. 210 (2010) 844–851. doi:10.1016/j.jmatprotec.2010.01.015.

[39] S. Hassanifard, M. Mohammadpour, H.A. Rashid, A novel method for improving fatigue life of friction stir spot welded joints using localized plasticity, Mater. Des. 53 (2014) 962–971. doi:10.1016/j.matdes.2013.07.098.

[40] E. Taban, E. Kaluc, Comparison between microstructure characteristics and joint performance of 5086-H32 aluminium alloy welded by MIG, TIG and friction stir welding processes, Kov. Mater. 45 (2007) 241–248.

[41] R.Z. Xu, D.R. Ni, Q. Yang, C.Z. Liu, Z.Y. Ma, Pinless Friction Stir Spot Welding of Mg – 3Al – 1Zn Alloy with Zn Interlayer, J. Mater. Sci. Technol. 32 (2016) 76–88. doi:10.1016/j.jmst.2015.08.012.

[42] F.A. Garcia-Castillo, F. de J. García-Vázquez, F.A. Reyes-Valdés, P. del C. Zambrano-Robledo, G.M. Hernández-Muñoz, E.R. Rodríguez-Ramos, Microstructural evolution in Ti-6Al-4V alloy joints using the process of friction stir spot welding, Weld. Int. 32 (2018) 570–578. doi:10.1080/09507116.2017.1347346.

[43] A.K. Lakshminarayanan, V.E. Annamalai, K. Elangovan, Identification of optimum friction stir spot welding process parameters controlling the properties of low carbon automotive steel joints, J. Mater. Res. Technol. 4 (2015) 262–272. doi:10.1016/j.jmrt.2015.01.001.

[44] E.T. Akinlabi, K.O. Sanusi, E. Muzenda, S.A. Akinlabi, Material behaviour characterization of Friction Stir Spot Welding of Copper, Mater. Today Proc. 4 (2017) 166–177. doi:10.1016/j.matpr.2017.01.010.

[45] M.P. Mubiayi, E.T. Akinlabi, M.E. Makhatha, Current state of friction stir spot welding between aluminium and copper, Mater. Today Proc. 5 (2018) 18633–18640. doi:10.1016/j.matpr.2018.06.208.

[46] J.M. Piccini, H.G. Svoboda, Tool geometry optimization in friction stir spot welding of Al-

steel joints, J. Manuf. Process. 26 (2017) 142–154. doi:10.1016/j.jmapro.2017.02.004.

[47] A. Kar, S. Suwas, S. V. Kailas, Significance of tool offset and copper interlayer during friction stir welding of aluminum to titanium, Int. J. Adv. Manuf. Technol. 100 (2019) 435–443. doi:10.1007/s00170-018-2682-6.

[48] A.R. Patel, C.G. Dalwadi, H.G. Rana, A Review: Dissimilar Material Joining of Metal to Polymer using Friction Stir Welding (FSW), IJSTE -International J. Sci. Technol. Eng. 2 (2016) 702–706.

[49] Refil Friction Stir Spot Welding, (n.d.). https://www.twi-global.com/technical-knowledge/job-knowledge/refill-friction-stir-spot-welding-150 (accessed February 20, 2020).

[50] A. Gerlich, P. Su, M. Yamamoto, T.H. North, Effect of welding parameters on the strain rate and microstructure of friction stir spot welded 2024 aluminum alloy, J. Mater. Sci. 42 (2007) 5589–5601. doi:10.1007/s10853-006-1103-7.

[51] R. Rai, A. De, H.K.D.H. Bhadeshia, T. DebRoy, Review: Friction stir welding tools, Sci. Technol. Weld. Join. 16 (2011) 325–342. doi:10.1179/1362171811Y.0000000023.

[52] Y.F. Sun, H. Fujii, N. Takaki, Y. Okitsu, Microstructure and mechanical properties of dissimilar Al alloy/steel joints prepared by a flat spot friction stir welding technique, Mater. Des. 47 (2013) 350–357. doi:10.1016/j.matdes.2012.12.007.

[53] Z.K. Zhang, Y. Yu, J.F. Zhang, X.J. Wang, Corrosion behavior of keyhole-free friction stir spot welded joints of dissimilar 6082 aluminum alloy and DP600 galvanized Steel in 3.5% NaCl solution, Metals (Basel). 7 (2017). doi:10.3390/met7090338.

[54] S. Hirasawa, H. Badarinarayan, K. Okamoto, T. Tomimura, T. Kawanami, Analysis of effect of tool geometry on plastic flow during friction stir spot welding using particle method, J. Mater. Process. Technol. 210 (2010) 1455–1463. doi:10.1016/j.jmatprotec.2010.04.003.

[55] Y. Tozaki, Y. Uematsu, K. Tokaji, A newly developed tool without probe for friction stir spot welding and its performance, J. Mater. Process. Technol. 210 (2010) 844–851. doi:10.1016/j.jmatprotec.2010.01.015.

[56] A. Reilly, H. Shercliff, Y. Chen, P. Prangnell, Modelling and visualisation of material flow in friction stir spot welding, J. Mater. Process. Technol. 225 (2015) 473–484. doi:10.1016/j.jmatprotec.2015.06.021.

[57] S.R. Yazdi, B. Beidokhti, M. Haddad-Sabzevar, Pinless tool for FSSW of AA 6061-T6 aluminum alloy, J. Mater. Process. Technol. 267 (2019) 44–51. doi:10.1016/j.jmatprotec.2018.12.005.

[58] B. Kuang, Y. Shen, W. Chen, X. Yao, H. Xu, J. Gao, J. Zhang, The dissimilar friction stir lap welding of 1A99 Al to pure Cu using Zn as filler metal with “pinless” tool configuration, Mater. Des. 68 (2015) 54–62. doi:10.1016/j.matdes.2014.12.008.

[59] D.H. Choi, B.W. Ahn, C.Y. Lee, Y.M. Yeon, K. Song, Effect of pin shapes on joint characteristics of friction stir spot welded AA5J32 sheet, Mater. Trans. 51 (2010) 1028–1032. doi:10.2320/matertrans.M2009405.

[60] B. Kuang, Y. Shen, W. Chen, X. Yao, H. Xu, J. Gao, J. Zhang, The dissimilar friction stir lap welding of 1A99 Al to pure Cu using Zn as filler metal with “pinless” tool configuration, Mater. Des. 68 (2015) 54–62. doi:10.1016/j.matdes.2014.12.008.

[61] D. Bakavos, P.B. Prangnell, Effect of reduced or zero pin length and anvil insulation on friction stir spot welding thin gauge 6111 automotive sheet, Sci. Technol. Weld. Join. 14 (2009) 443–456. doi:10.1179/136217109X427494.

[62] H. Conrad, L. Rice, The cohesion of previously fractured Fcc metals in ultrahigh vacuum, Metall. Trans. 1 (1970) 3019–3029. doi:10.1007/BF03038415.

[63] I.J. Ibrahim, G.G. Yapici, Application of a novel friction stir spot welding process on dissimilar aluminum joints, J. Manuf. Process. 35 (2018) 282–288. doi:10.1016/j.jmapro.2018.08.018.

[64] I.J. Ibrahim, G.G. Yapici, Optimization of the intermediate layer friction stir spot welding process, Int. J. Adv. Manuf. Technol. (2019) 993–1004. doi:10.1007/s00170-019-03952-3.

[65] Y.Q. Zhao, H.J. Liu, S.X. Chen, Z. Lin, J.C. Hou, Effects of sleeve plunge depth on microstructures and mechanical properties of friction spot welded alclad 7B04-T74 aluminum alloy, Mater. Des. 62 (2014) 40–46. doi:10.1016/j.matdes.2014.05.012.

[66] B. Parra, V.T. Saccon, N.G. De Alcântara, T. Rosendo, J.F. Dos Santos, An investigation on friction spot welding in AA6181-T4 alloy, Tecnol. Em Metal. Mater. e Mineração. 8 (2011) 184–190. doi:10.4322/tmm.2011.029.

[67] C. Schilling, J.F. Dos Santos, Verfahren und Vorrichtung zum Verbinden von wenigstens zwei aneinanderliegenden Werkstücken nach der Methode des Reibschweissens, Patent Application Amtl. Az. 199 55737.3. 1999, 1999.

[68] B.M.M. Al-Zubaidy, Material Interactions in a Novel Refill Friction Stir Spot Welding Approach to Joining Al-Al and Al-Mg, University of Manchester, 2016.

[69] Z. Shen, X. Yang, Z. Zhang, L. Cui, T. Li, Microstructure and failure mechanisms of refill friction stir spot welded 7075-T6 aluminum alloy joints, Mater. Des. 44 (2013) 476–486. doi:10.1016/j.matdes.2012.08.026.

[70] Z. Xu, Z. Li, S. Ji, L. Zhang, Refill friction stir spot welding of 5083-O aluminum alloy, J. Mater. Sci. Technol. 34 (2018) 878–885. doi:10.1016/j.jmst.2017.02.011.

[71] Y. Ding, Z. Shen, A.P. Gerlich, Refill friction stir spot welding of dissimilar aluminum alloy and AlSi coated steel, J. Manuf. Process. 30 (2017) 353–360. doi:10.1016/j.jmapro.2017.10.006.

[72] Y. Uematsu, K. Tokaji, Y. Tozaki, T. Kurita, S. Murata, Effect of re-filling probe hole on tensile failure and fatigue behaviour of friction stir spot welded joints in Al-Mg-Si alloy, Int. J. Fatigue. 30 (2008) 1956–1966. doi:10.1016/j.ijfatigue.2008.01.006.

[73] S. Fukada, R. Ohashi, M. Fujimoto, H. Okada, Refill friction stir spot welding of dissimilar materials consisting of A6061 and hot dip zinc-coated steel sheets, in: Proc. 1st Int. Jt. Symp. Join. Weld., 2013: pp. 183–187. doi:https://doi.org/10.1533/978-1-78242-164-1.183.

[74] J.A.E. Mazzaferro, T. de S. Rosendo, C.C.P. Mazzaferro, F.D. Ramos, M.A.D. Tier, T.R. Strohaecker, J.F. dos Santos, Preliminary study on the mechanical behavior of friction spot welds, Soldag. Inspeção. 14 (2009) 238–247. doi:10.1590/s0104-92242009000300007.

[75] Y.H. Yin, A. Ikuta, T.H. North, Microstructural features and mechanical properties of AM60 and AZ31 friction stir spot welds, Mater. Des. 31 (2010) 4764–4776. doi:10.1016/j.matdes.2010.05.005.

[76] S. Masaru, O. Kaoru, O. Kohei, T. Yoshihiro, M. Shigeyuki, F. Hidetoshi, Dissimilar spot welding of aluminium alloy and galvannealed steel by metal flow-application of friction anchor welding to aluminium alloy and Zn-coated steel, Weld. Int. 32 (2018) 377–389. doi:10.1080/09507116.2017.1346848.

[77] L. Commin, M. Dumont, J.E. Masse, L. Barrallier, Friction stir welding of AZ31 magnesium alloy rolled sheets: Influence of processing parameters, Acta Mater. 57 (2009) 326–334. doi:10.1016/j.actamat.2008.09.011.

[78] P. Jedrasiak, H.R. Shercliff, Small strain finite element modelling of friction stir spot welding of Al and Mg alloys, J. Mater. Process. Technol. 263 (2019) 207–222. doi:10.1016/j.jmatprotec.2018.07.031.

[79] S.T. Selvamani, K. Umanath, K. Palanikumar, Heat Transfer Analysis during Friction Stir Welding of Al6061-T6 Alloy, Int. J. Eng. Res. Appl. 1 (2014) 1453–1460.

[80] A. Atak, A. Şık, V. Özdemir, Thermo-Mechanical Modeling of Friction Stir Spot Welding and Numerical Solution With The Finite Element Method, Int. J. Eng. Appl. Sci. 5 (2018) 70–75. www.ijeas.org.

[81] G. D'Urso, C. Giardini, Thermo-mechanical characterization of friction stir spot welded AA7050 sheets by means of experimental and FEM analyses, Materials (Basel). 9 (2016) 1–14. doi:10.3390/ma9080689.

[82] P. Su, A. Gerlich, T.H. North, G.J. Bendzsak, Material flow during friction stir spot welding, Sci. Technol. Weld. Join. 11 (2006) 61–71. doi:10.1179/174329306X77056.

[83] A. Roos, Basic investigation about a new joining process called HFDB (Hybrid Friction Diffusion Bonding), TU Ilmenau, Germany, 2010. papers2://publication/uuid/6425D926-4F21-455D-8D26-2558A8562A13.

[84] S. Kalpakijan, Manufacturing Processes for Engineering Materials, Addison Wesley Publishing Company, 1991.

[85] P.P. Benham, R.J. Crawford, C.G. Armstrong, Mechanics of Engineering Materials, Pearson Education Ltd (Longman Group Ltd), 1996.

[86] T.R. McNelley, S. Swaminathan, J.Q. Su, Recrystallization mechanisms during friction stir welding/processing of aluminum alloys, Scr. Mater. 58 (2008) 349–354. doi:10.1016/j.scriptamat.2007.09.064.

[87] M. Awang, V.H. Mucino, Energy generation during friction stir spot welding (FSSW) of Al 6061-T6 plates, Mater. Manuf. Process. 25 (2010) 167–174. doi:10.1080/10426910903206758.

[88] P. Su, A. Gerlich, T.H. North, G.J. Bendzsak, Energy utilisation and generation during friction stir spot welding, Sci. Technol. Weld. Join. 11 (2006) 163–169. doi:10.1179/174329306X84373.

[89] R. Nandan, T. DebRoy, H.K.D.H. Bhadeshia, Recent advances in friction-stir welding - Process, weldment structure and properties, Prog. Mater. Sci. 53 (2008) 980–1023. doi:10.1016/j.pmatsci.2008.05.001.

[90] Z. Lanc, B. Štrbac, M. Zeljković, A. Živković, M. Hadžistević, Emissivity of aluminium alloy using infrared thermography technique, Mater. Tehnol. 52 (2018) 323–327. doi:10.17222/mit.2017.152.

[91] Z. Lanc, M. Zeljkovic, B. Strbac, A. Zivkovic, A. Drstvesek, M. Hadzistevic, The Determination of the Emissivity of Aluminum Alloy Aw 6082 Using Infrared Thermography, J. Prod. Eng. 18 (2015) 23–26.

[92] R. Rajasekaran, A.K. Lakshminarayanan, M. Vasudevan, P. Vasantharaja, Role of welding processes on microstructure and mechanical properties of nuclear grade stainless steel joints, Proc. Inst. Mech. Eng. Part L J. Mater. Des. Appl. 233 (2019) 2335–2351. doi:10.1177/1464420719849448.

[93] D. Kim, H. Badarinarayan, I. Ryu, J.H. Kim, C. Kim, K. Okamoto, R.H. Wagoner, K. Chung, Numerical simulation of friction stir spot welding process for aluminum alloys, Met. Mater. Int. 16 (2010) 323–332. doi:10.1007/s12540-010-0425-9.

[94] C.D. Cox, J.R. Aguilar, M.C. Ballun, A.M. Strauss, G.E. Cook, The application of a pinless tool in friction stir spot welding: An experimental and numerical study, Proc. Inst. Mech. Eng. Part D J. Automob. Eng. 228 (2014) 1359–1370. doi:10.1177/0954407013517374.

[95] C.D. Cox, B.T. Gibson, D.R. Delapp, A.M. Strauss, G.E. Cook, A method for double-sided friction stir spot welding, J. Manuf. Process. 16 (2014) 241–247. doi:10.1016/j.jmapro.2013.10.006.

[96] Z. Gao, J.T. Niu, F. Krumphals, N. Enzinger, S. Mitsche, C. Sommitsch, FE modelling of microstructure evolution during friction stir spot welding in AA6082-T6, Weld. World. 57 (2013) 895–902. doi:10.1007/s40194-013-0083-x.

[97] P. Lacki, Z. Kucharczyk, R.E. Śliwa, T. Gałaczyński, Effect of tool shape on temperature field in friction stir spot welding, Arch. Metall. Mater. 58 (2013) 595–599. doi:10.2478/amm-2013-0043.

[98] P. Jedrasiak, H.R. Shercliff, A. Reilly, G.J. McShane, Y.C. Chen, L. Wang, J. Robson, P. Prangnell, Thermal Modeling of Al-Al and Al-Steel Friction Stir Spot Welding, J. Mater. Eng. Perform. 25 (2016) 4089–4098. doi:10.1007/s11665-016-2225-y.

[99] T. Rosendo, B. Parra, M.A.D. Tier, A.A.M. da Silva, J.F. dos Santos, T.R. Strohaecker, N.G. Alcântara, Mechanical and microstructural investigation of friction spot welded AA6181-T4 aluminium alloy, Mater. Des. 32 (2011) 1094–1100. doi:10.1016/j.matdes.2010.11.017.

[100] Y. Sun, Y. Morisada, H. Fujii, N. Tsuji, Ultrafine grained structure and improved mechanical properties of low temperature friction stir spot welded 6061-T6 Al alloys, Mater. Charact. 135 (2018) 124–133. doi:10.1016/j.matchar.2017.11.033.

[101] K. Wang, H. Ali Khan, Z. Li, S. Lyu, J. Li, Micro friction stir welding of multilayer aluminum alloy sheets, J. Mater. Process. Technol. 260 (2018) 137–145. doi:10.1016/j.jmatprotec.2018.05.029.

[102] K. Kumar, C. Kalyan, S. V Kailas, T.S. Srivatsan, An Investigation of Friction During Friction Stir Welding of Metallic Materials, Mater. Manuf. Process. 24 (2009) 438–445. doi:10.1080/10426910802714340.

[103] Y. Rostamiyan, A. Seidanloo, H. Sohrabpoor, R. Teimouri, Experimental studies on ultrasonically assisted friction stir spot welding of AA6061, Arch. Civ. Mech. Eng. 15 (2015) 335–346. doi:10.1016/j.acme.2014.06.005.

[104] S. Bozzi, A.L. Helbert-Etter, T. Baudin, V. Klosek, J.G. Kerbiguet, B. Criqui, Influence of FSSW parameters on fracture mechanisms of 5182 aluminium welds, J. Mater. Process. Technol. 210 (2010) 1429–1435. doi:10.1016/j.jmatprotec.2010.03.022.

[105] Y. Bozkurt, M.K. Bilici, Application of Taguchi approach to optimize of FSSW parameters on joint properties of dissimilar AA2024-T3 and AA5754-H22 aluminum alloys, Mater. Des. 51 (2013) 513–521. doi:10.1016/j.matdes.2013.04.074.

[106] D. Mitlin, V. Radmilovic, T. Pan, J. Chen, Z. Feng, M.L. Santella, Structure-properties relations in spot friction welded (also known as friction stir spot welded) 6111 aluminum, Mater. Sci. Eng. A. 441 (2006) 79–96. doi:10.1016/j.msea.2006.06.126.

[107] P.C. Lin, J. Pan, T. Pan, Failure modes and fatigue life estimations of spot friction welds in lap-shear specimens of aluminum 6111-T4 sheets. Part 2: Welds made by a flat tool, Int. J. Fatigue. 30 (2008) 90–105. doi:10.1016/j.ijfatigue.2007.02.017.

[108] Z. Shen, X. Yang, S. Yang, Z. Zhang, Y. Yin, Microstructure and mechanical properties of friction spot welded 6061-T4 aluminum alloy, Mater. Des. 54 (2014) 766–778. doi:10.1016/j.matdes.2013.08.021.

[109] Q. Yang, S. Mironov, Y.S. Sato, K. Okamoto, Material flow during friction stir spot welding, Mater. Sci. Eng. A. 527 (2010) 4389–4398. doi:10.1016/j.msea.2010.03.082.

[110] M. Fujimoto, S. Koga, N. Abe, Y. Sato, H. Kokawa, Microstructural analysis of the stir zone of Al alloy produced by friction stir spot welding, Weld. Int. 23 (2009) 403–410. doi:10.1080/09507110802542858.

[111] Z. Zhang, X. Yang, J. Zhang, G. Zhou, X. Xu, B. Zou, Effect of welding parameters on microstructure and mechanical properties of friction stir spot welded 5052 aluminum alloy, Mater. Des. 32 (2011) 4461–4470. doi:10.1016/j.matdes.2011.10.054.

[112] S. Babu, V.S. Sankar, G.D. Janaki Ram, P. V. Venkitakrishnan, G. Madhusudhan Reddy, K. Prasad Rao, Microstructures and mechanical properties of friction stir spot welded aluminum alloy AA2014, J. Mater. Eng. Perform. 22 (2013) 71–84. doi:10.1007/s11665-012-0218-z.

[113] Z. Gao, J. Feng, Z. Wang, J. Niu, C. Sommitsch, Dislocation Density-Based Modeling of Dynamic Recrystallized Microstructure and Process in Friction Stir Spot Welding of AA6082, Metals (Basel). 9 (2019) 672. doi:10.3390/met9060672.

[114] K. V Jata, S.L. Semiatin, Continuous dynamic recrystallization during friction stir welding of high strength aluminum alloys, Scr. Mater. 43 (2000) 743–749. doi:10.1016/S1359-6462(00)00480-2.

[115] H. Andalib, M. Farahani, M. Enami, Study on the new friction stir spot weld joint reinforcement technique on 5754 aluminum alloy, Proc. Inst. Mech. Eng. Part C J. Mech. Eng. Sci. 232 (2018) 2976–2986. doi:10.1177/0954406217729419.

[116] A. Gerlich, M. Yamamoto, T.H. North, Strain rates and grain growth in Al 5754 and Al 6061 friction stir spot welds, Metall. Mater. Trans. A Phys. Metall. Mater. Sci. 38 (2007) 1291–1302. doi:10.1007/s11661-007-9155-0.

[117] Y.F. Sun, H. Fujii, Y. Sato, Y. Morisada, Friction stir spot welding of SPCC low carbon steel plates at extremely low welding temperature, J. Mater. Sci. Technol. 35 (2019) 733–741. doi:10.1016/j.jmst.2018.11.011.

[118] T. Sakai, A. Belyakov, R. Kaibyshev, H. Miura, J.J. Jonas, Dynamic and post-dynamic recrystallization under hot, cold and severe plastic deformation conditions, Prog. Mater. Sci. 60 (2014) 130–207. doi:10.1016/j.pmatsci.2013.09.002.

[119] Y.S. Sato, H. Kokawa, M. Enomoto, S. Jogan, Microstructural evolution of 6063 aluminum during friction-stir welding, Metall. Mater. Trans. A Phys. Metall. Mater. Sci. 30 (1999) 2429–2437. doi:10.1007/s11661-999-0251-1.

[120] A. Garg, A. Bhattacharya, Characterizing Various Zones Formed in Friction Stir Spot Welding With, in: Proc. 16th Int. Alum. Alloy. Conf., Canadian Institute of Mining, Metallurgy & Petroleum CHARACTERIZING, 2018: pp. 1–10.

[121] Y.S. Sato, M. Urata, H. Kokawa, Parameters Controlling Microstructure and Hardness during Friction-Stir Welding of Precipitation-Hardenable Aluminum Alloy 6063, Metall. Mater. Trans. A. 33A (2002) 625–635.

[122] J.Q. Su, T.W. Nelson, R. Mishra, M. Mahoney, Microstructural investigation of friction stir welded 7050-T651 aluminium, Acta Mater. 51 (2003) 713–729. doi:10.1016/S1359-6454(02)00449-4.

[123] G. Li, L. Zhou, L. Luo, X. Wu, N. Guo, Microstructural evolution and mechanical properties of refill friction stir spot welded alclad 2A12-T4 aluminum alloy, J. Mater. Res. Technol. 8 (2019) 4115–4129. doi:10.1016/j.jmrt.2019.07.021.

[124] H. Badarinarayan, Y. Shi, X. Li, K. Okamoto, Effect of tool geometry on hook formation and

static strength of friction stir spot welded aluminum 5754-O sheets, Int. J. Mach. Tools Manuf. 49 (2009) 814–823. doi:10.1016/j.ijmachtools.2009.06.001.

[125] N. Farmanbar, S.M. Mousavizade, M. Elsa, H.R. Ezatpour, AA5052 sheets welded by protrusion friction stir spot welding: High mechanical performance with considering sheets thickness at low dwelling time and tool rotation speed, Proc. Inst. Mech. Eng. Part C J. Mech. Eng. Sci. 0 (2019) 1–12. doi:10.1177/0954406219850202.

[126] T.A. Freeney, S.R. Sharma, R.S. Mishra, Effect of welding parameters on properties of 5052 Al friction stir spot welds, SAE Tech. Pap. (2006). doi:10.4271/2006-01-0969.

[127] D. Klobčar, J. Tušek, A. Smolej, S. Simončič, Parametric study of FSSW of aluminium alloy 5754 using a pinless tool, Weld. World. 59 (2014) 269–281. doi:10.1007/s40194-014-0208-x.

[128] T.S. Mahmoud, T.A. Khalifa, Microstructural and mechanical characteristics of aluminum alloy AA5754 friction stir spot welds, J. Mater. Eng. Perform. 23 (2014) 898–905. doi:10.1007/s11665-013-0828-0.

[129] M.D. Tier, T.S. Rosendo, J.F. Dos Santos, N. Huber, J.A. Mazzaferro, C.P. Mazzaferro, T.R. Strohaecker, The influence of refill FSSW parameters on the microstructure and shear strength of 5042 aluminium welds, J. Mater. Process. Technol. 213 (2013) 997–1005. doi:10.1016/j.jmatprotec.2012.12.009.

[130] A. Abdollahzadeh, A. Shokuhfar, J.M. Cabrera, A.P. Zhilyaev, H. Omidvar, In-situ nanocomposite in friction stir welding of 6061-T6 aluminum alloy to AZ31 magnesium alloy, J. Mater. Process. Technol. 263 (2019) 296–307. doi:10.1016/j.jmatprotec.2018.08.025.

[131] M. Fujimoto, S. Koga, N. Abe, Y. Sato, H. Kokawa, Microstructural analysis of the stir zone of Al alloy produced by friction stir spot welding, Sci. Technol. Weld. Join. 13 (2008) 663–670. doi:10.1080/09507110802542858.

[132] Z.M. Su, Q.H. Qiu, P.C. Lin, Design of friction stir spot welding tools by using a novel thermal-mechanical approach, Materials (Basel). 9 (2016). doi:10.3390/ma9080677.

[133] M. Enami, M. Farahani, M. Farhang, Novel study on keyhole less friction stir spot welding of Al 2024 reinforced with alumina nanopowder, Int. J. Adv. Manuf. Technol. 101 (2019) 3093–3106. doi:10.1007/s00170-018-3142-z.

[134] D.M. Rodrigues, A. Loureiro, C. Leitao, R.M. Leal, B.M. Chaparro, P. Vilaça, Influence of friction stir welding parameters on the microstructural and mechanical properties of AA 6016-T4 thin welds, Mater. Des. 30 (2009) 1913–1921. doi:10.1016/j.matdes.2008.09.016.

[135] Y. Hu, H. Liu, H. Fujii, Improving the mechanical properties of 2219-T6 aluminum alloy joints by ultrasonic vibrations during friction stir welding, J. Mater. Process. Technol. 271 (2019) 75–84. doi:10.1016/j.jmatprotec.2019.03.013.

[136] S. Venukumar, S. Muthukumaran, S.G. Yalagi, S. V. Kailas, Failure modes and fatigue behavior of conventional and refilled friction stir spot welds in AA 6061-T6 sheets, Int. J. Fatigue. 61 (2014) 93–100. doi:10.1016/j.ijfatigue.2013.12.009.

[137] A.M.S. Malafaia, M.T. Milan, M.F. Oliveira, D. Spinelli, Fatigue behavior of friction stir spot welding and riveted joints in an Al alloy, Procedia Eng. 2 (2010) 1815–1821. doi:10.1016/j.proeng.2010.03.195.

[138] S. Joy-A-Ka, T. Hirano, H. Akebono, M. Kato, A. Sugeta, Fatigue Properties and Crack Growth Behavior of Friction Stir Spot Welded 300 MPa-Class Automobile Steel Sheets, (2013) 1–9.

[139] Y. Uematsu, K. Tokaji, Comparison of fatigue behaviour between resistance spot and friction stir spot welded aluminium alloy sheets, Sci. Technol. Weld. Join. 14 (2009) 62–71.

doi:10.1179/136217108X338908.

[140] V.X. Tran, J. Pan, T. Pan, Fatigue behavior of aluminum 5754-O and 6111-T4 spot friction welds in lap-shear specimens, Int. J. Fatigue. 30 (2008) 2175–2190. doi:10.1016/j.ijfatigue.2008.05.025.

[141] Z.M. Su, R.Y. He, P.C. Lin, K. Dong, Fatigue analyses for swept friction stir spot welds in lap-shear specimens of alclad 2024-T3 aluminum sheets, Int. J. Fatigue. 61 (2014) 129–140. doi:10.1016/j.ijfatigue.2013.11.021.

[142] A.R. Shahani, A. Farrahi, Experimental investigation and numerical modeling of the fatigue crack growth in friction stir spot welding of lap-shear specimen, Int. J. Fatigue. 125 (2019) 520–529. doi:10.1016/j.ijfatigue.2019.04.026.

[143] A. Shahani, A. Farrahi, Effect of stirring time on the mechanical behavior of friction stir spot weld of Al 6061-T6 lap-shear configuration, Proc. Inst. Mech. Eng. Part C J. Mech. Eng. Sci. 233 (2019) 3583–3591. doi:10.1177/0954406218818606.

[144] Y.H. Yin, N. Sun, T.H. North, S.S. Hu, Hook formation and mechanical properties in AZ31 friction stir spot welds, J. Mater. Process. Technol. 210 (2010) 2062–2070. doi:10.1016/j.jmatprotec.2010.07.029.

[145] W. Yuan, B. Carlson, R. Verma, R. Szymanski, Study of top sheet thinning during friction stir lap welding of AZ31 magnesium alloy, Sci. Technol. Weld. Join. 17 (2012) 375–380. doi:10.1179/1362171812Y.0000000018.

[146] S. Ji, Z. Li, Y. Wang, L. Ma, L. Zhang, Material flow behavior of refill friction stir spot welded LY12 aluminum alloy, High Temp. Mater. Process. 36 (2017) 495–504. doi:10.1515/htmp-2015-0254.

[147] Y. Wang, P. Chai, H. Ma, X. Cao, Y. Zhang, Formation mechanism and fracture behavior in extra-filling refill friction stir spot weld for Al–Cu–Mg aluminum alloy, J. Mater. Sci. (2019) 358–374. doi:10.1007/s10853-019-03940-8.

[148] P.H.F. Oliveira, S.T. Amancio-Filho, J.F. Dos Santos, E. Hage, Preliminary study on the feasibility of friction spot welding in PMMA, Mater. Lett. 64 (2010) 2098–2101. doi:10.1016/j.matlet.2010.06.050.

[149] D. Bakavos, P.B. Prangnell, Effect of the Pin Length and the Anvil Insulation on Friction Stir Spot welding Thin Gauge 6111 Automotive Sheet, in: 2009: pp. 1–10. doi:10.1179/136217109X427494.

[150] D.R. Cooper, J.M. Allwood, Influence of diffusion mechanisms in aluminium solid-state welding processes, Procedia Eng. 81 (2014) 2147–2152. doi:10.1016/j.proeng.2014.10.300.

[151] A. Sunwoo, R. Lum, Superplastic deformation enhanced diffusion bonding of aluminum alloy 7475, Scr. Metall. Mater. 33 (1995) 639–644. doi:10.1016/0956-716X(95)00224-J.

[152] M.F. Ashby, R.A. Verrall, Diffusion-accommodated flow and superplasticity, Acta Metall. (1973). doi:10.1016/0001-6160(73)90057-6.

[153] M. Fishkis, J.C. Lin, Formation and evolution of a subsurface layer in a metalworking process, Wear. 206 (1997) 156–170. doi:10.1016/S0043-1648(96)07480-7.

[154] A.P. Semenov, The phenomenon of seizure and its investigation, Wear. 4 (1961) 1–9. doi:10.1016/0043-1648(61)90236-8.

[155] A.A. Shirzadi, H. Assadi, E.R. Wallach, Interface evolution and bond strength when diffusion bonding materials with stable oxide films, Surf. Interface Anal. 31 (2001) 609–618. doi:10.1002/sia.1088.

[156] Z. Shen, X. Yang, Z. Zhang, L. Cui, Y. Yin, Mechanical properties and failure mechanisms of friction stir spot welds of AA 6061-T4 sheets, Mater. Des. 49 (2013) 181–191. doi:10.1016/j.matdes.2013.01.066.

[157] R. Leach, The Measurement of Surface Texture using Stylus Instruments, Measurement Good Practice Guide No. 37, 2014.

[158] C.A. Schneider, W.S. Rasband, K.W. Eliceiri, NIH Image to ImageJ: 25 years of image analysis, Nat. Methods. 9 (2012) 671–675. doi:10.1038/nmeth.2089.

[159] ZEISS Crossbeam Family - Product information, (n.d.). https://www.zeiss.com/microscopy/int/products/fib-sem-instruments/crossbeam.html (accessed February 20, 2020).

[160] PFQNE-AL- Bruker, (n.d.). https://www.brukerafmprobes.com/p-3817-pfqne-al.aspx (accessed January 19, 2020).

[161] V. Panchal, R. Pearce, R. Yakimova, A. Tzalenchuk, O. Kazakova, Standardization of surface potential measurements of graphene domains, Sci. Rep. 3 (2013). doi:10.1038/srep02597.

[162] S. William, Application Note # 140 PeakForce Kelvin Probe Force Microscopy, 1898.

[163] W.C. Oliver, G.M. Pharr, An improved technique for determining hardness and elastic modulus using load and displacement sensing indentation experiments, J. Mater. Res. 7 (1992) 1564–1583.

[164] S. Goel, G. Cross, A. Stukowski, E. Gamsjäger, B. Beake, A. Agrawal, Designing nanoindentation simulation studies by appropriate indenter choices: Case study on single crystal tungsten, Comput. Mater. Sci. 152 (2018) 196–210. doi:10.1016/j.commatsci.2018.04.044.

[165] CEN CWA 15627: Small Punch Test Method for Metalic Materials, European Committee for Standardization CEN, Brussels, Belgium, 2006.

[166] S. Rasche, M. Kuna, Improved small punch testing and parameter identification of ductile to brittle materials, Int. J. Press. Vessel. Pip. 125 (2015) 23–34. doi:10.1016/j.ijpvp.2014.09.001.

[167] S. Rasche, Bestimmung von Materialparametern der elastish-plastischen Verformung und des spröden Versagens aus Smal-Punch-Lkeinstproben, Technische Universität Bergakademie Freiberg, 2013.

[168] H. Yamada, T. Kami, R. Mori, T. Kudo, M. Okada, Strain rate dependence of material strength in aa5xxx series aluminum alloys and evaluation of their constitutive equation, Metals (Basel). 8 (2018) 1–15. doi:10.3390/met8080576.

[169] M.A. Soare, W.A. Curtin, Solute strengthening of both mobile and forest dislocations: The origin of dynamic strain aging in fcc metals, Acta Mater. 56 (2008) 4046–4061. doi:10.1016/j.actamat.2008.04.027.

[170] W.A. Curtin, D.L. Olmsted, L.G. Hector, A predictive mechanism for dynamic strain ageing in aluminium-magnesium alloys, Nat. Mater. 5 (2006) 875–880. doi:10.1038/nmat1765.

[171] R.C. Picu, A mechanism for the negative strain-rate sensitivity of dilute solid solutions, Acta Mater. 52 (2004) 3447–3458. doi:10.1016/j.actamat.2004.03.042.

[172] C.I. Chang, C.J. Lee, J.C. Huang, Relationship between grain size and Zener-Holloman parameter during friction stir processing in AZ31 Mg alloys, Scr. Mater. 51 (2004) 509–514. doi:10.1016/j.scriptamat.2004.05.043.

[173] H.B. Schmidt, J.H. Hattel, Thermal modelling of friction stir welding, Scr. Mater. 58 (2008) 332–337. doi:10.1016/j.scriptamat.2007.10.008.

[174] M. Song, R. Kovacevic, Thermal modeling of friction stir welding in a moving coordinate system and its validation, Int. J. Mach. Tools Manuf. 43 (2003) 605–615. doi:10.1016/S0890-6955(03)00022-1.

[175] Frigaard, Grong, O.T. Midling, A process model for friction stir welding of age hardening aluminum alloys, Metall. Mater. Trans. A Phys. Metall. Mater. Sci. 32 (2001) 1189–1200. doi:10.1007/s11661-001-0128-4.

[176] Z.N. Farhat, Y. Ding, D.O. Northwood, A.T. Alpas, Effect of grain size on friction and wear of nanocrystalline aluminum, Mater. Sci. Eng. A. 206 (1996) 302–313.

[177] F. Javier Aparicio Rebollo, How it works Scanning Acoustic Microscopy (C-SAM), (n.d.). https://wpo-altertechnology.com/how-it-works-scanning-acoustic-microscopy-c-sam/ (accessed December 2, 2019).

[178] K. Dizon, Enhancement of root crack detection in friction stir welds using ultrasonic non-destructive testing and signal processing technique., University of Windsor, Ontario, Canada, 2007.

[179] Q. Ahsan, H. Kato, Ultrasonic Evaluation at the Interface of Aluminum/Steel Obtained by TIG Welding, IOP Conf. Ser. Mater. Sci. Eng. 554 (2019). doi:10.1088/1757-899X/554/1/012010.

[180] R.W. Martin, S. Sathish, K. V Jata, A. Force, Friction Stir Welded Ti-6Al-4V Using Scanning Acoustic Microscopy, 34th Annu. Rev. Prog. Quant. Nondestruct. Eval. (AIP Conf. Proc. 975). 27 (2008) 1050–1057.

[181] S.P. Sagar, C. Miyasaka, M. Ghosh, B.R. Tittmann, NDE of friction stir welds of Al alloys using high-frequency acoustic microscopy, Nondestruct. Test. Eval. 27 (2012) 375–389. doi:10.1080/10589759.2012.656638.

[182] P. Lacki, W. Więckowski, P. Wieczorek, Assessment of joints using friction stir welding and refill friction stir spot welding methods, Arch. Metall. Mater. 60 (2015) 2297–2306. doi:10.1515/amm-2015-0377.

[183] K. Hagihara, T. Nakano, M. Todai, Unusual dynamic precipitation softening induced by dislocation glide in biomedical beta-titanium alloys, Sci. Rep. 7 (2017) 1–9. doi:10.1038/s41598-017-08211-7.

[184] S. Wei, Y. Liu, X. Liu, H. Zhao, Investigation on edge chipping evaluation of Si 3 N 4 ceramics milling surface, Meas. J. Int. Meas. Confed. 133 (2019) 241–250. doi:10.1016/j.measurement.2018.10.015.

[185] D. Yadav, R. Bauri, Effect of friction stir processing on microstructure and mechanical properties of aluminium, Mater. Sci. Eng. A. 539 (2012) 85–92. doi:10.1016/j.msea.2012.01.055.

[186] D. Kuhlmann-Wilsdorf, H.G.F. Wilsdorf, J.A. Wert, LEDS theory of workhardening stages and “planar” versus “distributed” glide, Scr. Metall. Mater. 31 (1994) 729–734. doi:10.1016/0956-716X(94)90218-6.

[187] P.K. Sahu, N.P. Vasudevan, B. Das, S. Pal, Assessment of self-reacting bobbin tool friction stir welding for joining AZ31 magnesium alloy at inert gas environment, J. Magnes. Alloy. 7 (2019) 661–671. doi:10.1016/j.jma.2019.05.011.

[188] B.S. Naik, D.L. Chen, X. Cao, P. Wanjara, Microstructure and fatigue properties of a friction stir lap welded magnesium alloy, Metall. Mater. Trans. A Phys. Metall. Mater. Sci. 44 (2013) 3732–3746. doi:10.1007/s11661-013-1728-5.

[189] A. Jan, J. Siegl, P. Hau, Small punch test evaluation methods for material characterisation, 481 (2016). doi:10.1016/j.jnucmat.2016.09.015.

[190] M. Asadi Asadabad, M. Jafari Eskandari, Chapter I, in: Electron Diffr., Intech, 2016: p. 13. doi:http://dx.doi.org/10.5772/57353.

[191] D.H. Choi, B.W. Ahn, D.J. Quesnel, S.B. Jung, Behavior of β phase (Al3Mg2) in AA 5083 during friction stir welding, Intermetallics. 35 (2013) 120–127. doi:10.1016/j.intermet.2012.12.004.

[192] T. Ronnhult, U. Rilby, I. Olefjord, The Surface State and Weldability of Aluminium Alloys, 42 (1980) 329–336.

[193] Work function table, (n.d.). https://www.fh-muenster.de/ciw/downloads/personal/juestel/juestel/Work_function.pdf (accessed May 15, 2020).

[194] D.A. Porter, K.E. Easterling, Phase Transformations in Metals and Alloys, Chapman and Hall, London, 1996. doi:10.1017/CBO9781107415324.004.

APPENDICES

A. Dwell time and maximum temperature variation as a function of the rotational speed

Table 1. Dwell time and maximum temperature variation within batch I presented in **Fig. 4.7a** and **b**

Sample	Dwell time (s)	Standard deviation (s)	Maximum temperature (^oC)	Standard deviation (^oC)
RW1	4.65	0.26771	112.66667	2.0548
RW2	4.66	0.34029	125.66667	3.39935
RW3	4.41	0.29811	130	3.55903
RW4	4.29	0.21229	146.66667	8.17856
RW5	3.77	0.1484	149	7.11805

Table 2. Dwell time and maximum temperature variation within batch II presented in **Fig. 4.7a** and **b**

Sample	Dwell time (s)	Standard deviation (s)	Maximum temperature (^oC)	Standard deviation (^oC)
RWA1	1.67667	0.07024	67.6667	6.65833
RWA2	1.34333	0.04163	101	4.58258
RWA3	1.11333	0.08145	119.333	5.85947
RWA4	1.07	0.0755	135	4.3589
RWA5	0.97333	0.04041	147	3
RWA6	1.00333	0.03786	149.6667	20.20726
RWA7	0.98333	0.04163	155.6667	10.2632
RWA8	0.90667	0.01528	158.3333	9.45161

B. Grain size measurements

Table 3. Estimated grain size presented in **Fig. 4.15**

Sample	Grain size (μm)					
	HAZ		**TMAZ**		**SZ**	
Batch I						
RW1	40.158	12.174	22.451	6.640	5.534	1.897
RW3	50.119	15.652	33.518	11.225	12.806	4.091
RW5	35.099	11.713	36.364	12.648	16.126	4.826
Batch II						
RWA1	44.940	10.677	22.311	9.562	5.618	1.614
RWA2	52.590	15.139	30.598	10.199	7.052	2.570
RWA4	51.315	18.805	33.307	12.112	10.100	2.629
RWA6	43.187	9.402	37.769	13.564	20.199	4.960
RWA8	44.622	14.980	35.378	11.315	25.159	9.681
Base material	73.09712628 ± 39.24006					

C. Dimensional quantification of the weld

Table 5. Bottom diameter of the stir zone presented in **Fig. 4.19a**

Batch I Sample	d (mm)	Standard deviation (mm)	Batch II Sample	d (mm)	Standard deviation (mm)
RW1	5.04	0.05292	**RWA1**	6.975	0.03294
RW2	4.95667	0.03512	**RWA2**	7.294	0.10063
RW3	3.76233	0.10055	**RWA3**	7.354	0.02654
RW4	3.22833	0.02888	**RWA4**	7.027	0.07235
RW5	1.53833	0.13322	**RWA5**	5.827	0.06325
			RWA6	4.638	0.1003
			RWA7	4.583	0.0745
			RWA8	4.309	0.04526

Table 6. Top diameter of the stir zone presented in **Fig. 4.19b**

Batch I Sample	D (mm)	Standard deviation (mm)	Batch II Sample	D (mm)	Standard deviation (mm)
RW1	6.36233	0.03459	**RWA1**	7.739	0.13063
RW2	6.64333	0.05686	**RWA2**	8.69	0.05654
RW3	6.72667	0.05508	**RWA3**	9.228	0.09924
RW4	6.84267	0.081	**RWA4**	9.151	0.06325
RW5	7.134	0.12705	**RWA5**	9.165	0.09003
			RWA6	8.986	0.0745
			RWA7	8.785	0.02526
			RWA8	8.872	0.1054

Table 7. Axial depth of the weld presented in **Fig. 4.19c**

Batch I Sample	H (mm)	Standard deviation (mm)	Batch II Sample	H (mm)	Standard deviation (mm)
RW1	0.94767	0.00643	**RWA1**	0.99051	0.00679
RW2	0.927	0.00608	**RWA2**	0.97735	0.00806
RW3	0.92667	0.00153	**RWA3**	0.95275	0.00725
RW4	0.88833	0.01677	**RWA4**	0.96979	0.01677
RW5	0.894	0.00361	**RWA5**	0.96285	0.00361
			RWA6	0.93605	0.01608
			RWA7	0.92682	0.00173
			RWA8	0.9593	0.01677

Table 8. Trapper angle of the stir zone-*α* presented in **Fig. 4.19**

Batch I Sample	α (mm)	Standard deviation (mm)	Batch II Sample	α (mm)	Standard deviation (mm)
RW1	46.91	0.40037	**RWA1**	49.45	3.94566
RW2	54.76667	0.68069	**RWA2**	48.53	4.15183
RW3	66.9	0.95394	**RWA3**	55.43	3.09339
RW4	71.75	1.47102	**RWA4**	58.285	5.59321
RW5	76.96667	1.0504	**RWA5**	69.52	1.32936
			RWA6	74.935	0.12021
			RWA7	74.005	1.61927
			RWA8	72.66	0.69296

Table 9. Ratio of the radius of the edge-chipping area to stable process-pressure area **Fig. 5.3a**

Batch I Sample	r/R	Standard deviation	Batch II Sample	r/R	Standard deviation
RW1	0.53063	0.02786	**RWA1**	0.55007	0.07586
RW2	0.59541	0.04922	**RWA2**	0.67321	0.00224
RW3	0.63568	0.02154	**RWA3**	0.75591	0.01342
RW4	0.66224	0.02188	**RWA4**	0.75232	0.03788
RW5	0.64868	0.01003	**RWA5**	0.75473	0.011
			RWA6	0.78293	0.0142
			RWA7	0.79854	0.00188
			RWA8	0.79782	0.022

Table 10. Ratio of the bottom diameter of the stir zone to top diameter of the stir zone presented with diagram in **Fig. 5.3b**

Batch I Sample	d/D	Standard deviation	Batch II Sample	d/D	Standard deviation
RW1	0.79033	0.01091	**RWA1**	0.90128	0.01291
RW2	0.7503	0.01027	**RWA2**	0.83936	0.01427
RW3	0.55658	0.01555	**RWA3**	0.79692	0.01055
RW4	0.46838	0.0047	**RWA4**	0.77638	0.01047
RW5	0.21316	0.01926	**RWA5**	0.63579	0.00193
			RWA6	0.51614	0.01555
			RWA7	0.52168	0.0047
			RWA8	0.48569	0.01926

D. Rupture load and maximum displacement variation as a function of the rotational speed

Table 11. Maximum rupture load presented in **Fig. 4.24a** and **b**

Batch I Sample	Maximum rupture load (N)	Standard deviation (N)	Batch II Sample	Maximum rupture load (N)	Standard deviation (N)
RW1	1162.0	37.83	**RWA1**	1096.7	33.5
RW2	1043.0	3.69	**RWA2**	1040.3	1.9
RW3	1010.3	4.14	**RWA3**	1016.6	3.6
RW4	1030.2	58.01	**RWA4**	1021.3	23.3
RW5	1004.0	9.51	**RWA5**	1001.9	17.4
			RWA6	1002.9	13.4
			RWA7	991.9	5.7
Base material	1094.9	21.3	**RWA8**	957.2	10.3

Table 12. Maximum rupture load presented in **Fig. 4.24a** and **b**

Batch I Sample	Maximum displacement (mm)	Standard deviation (mm)	Batch II Sample	Maximum displacement (mm)	Standard deviation (mm)
RW1	1.6588	0.0198	**RWA1**	1.70944	0.02528032
RW2	1.77288	0.02311838	**RWA2**	1.720336	0.02052142
RW3	1.84412	0.01045196	**RWA3**	1.73411733	0.00788189
RW4	1.86922	0.02653702	**RWA4**	1.77562733	0.03201788
RW5	1.84336667	0.01269444	**RWA5**	1.78767467	0.04733043
			RWA6	1.95581333	0.23495208
			RWA7	1.926736	0.12556167
Base material	1.70944	0.02528032	**RWA8**	2.092816	0.11269081

E. Estimated strain rate

Table 13. Estimated strain rate presented in **Fig. 5.1**

Batch I Sample	Strain rate	Batch II Sample	Strain rate
RW1	235.1357	**RWA1**	175.27404
RW2	354.20582	**RWA2**	266.48173
RW3	394.48634	**RWA3**	405.25025
RW4	508.32622	**RWA4**	441.18444
RW5	518.94264	**RWA5**	508.66532
		RWA6	560.07385
		RWA7	612.42165
		RWA8	642.00486

Raw data supporting the findings within PhD thesis are available from the author Danka Labus Zlatanović at Email address danlabus@uns.ac.rs on request.